

Nonempirical hybrid functionals for advanced electronic-structure calculations

Présentée le 23 avril 2021

Faculté des sciences de base
Chaire de simulation à l'échelle atomique
Programme doctoral en physique

pour l'obtention du grade de Docteur ès Sciences

par

Thomas BISCHOFF

Acceptée sur proposition du jury

Prof. P. Ricci, président du jury
Prof. A. Pasquarello, directeur de thèse
Dr F. Bruneval, rapporteur
Dr A. Alkauskas, rapporteur
Prof. U. Röthlisberger, rapporteuse

Abstract

Electronic-structure calculations based on hybrid functionals have emerged as a standard technique used in physics, chemistry, and material science. Despite this success, hybrid functionals have the drawback of containing undetermined parameters. To overcome this deficiency, two different nonempirical determination schemes are being investigated at present, namely dielectric-dependent hybrid (DDH) functionals and hybrid functionals that satisfy Koopmans' condition. This thesis is dedicated to the examination and further development of these approaches. In particular, we show that a precise description of band gaps in condensed-matter systems can be achieved with these functionals. Moreover, we demonstrate that their accuracy is comparable to state-of-the-art *GW* methods while requiring substantially lower computational cost.

First, we focus on the development of hybrid functionals satisfying Koopmans' condition. We show that the construction of those functionals can be optimized through suitably defined potential probes. By monitoring the delocalized screening charge, we achieve a measure of the degree of hybridization with the band states, which can be used to improve the band-gap estimate. We show that the application of this methodology to common semiconducting and insulating materials yields band gaps differing by less than 0.2 eV from experiment. These conceptual developments are an important step towards establishing hybrid functionals satisfying Koopmans' condition as a robust approach for band-gap predictions.

Second, we examine DDH functionals and hybrid functionals satisfying Koopmans' condition for band gaps of more sophisticated materials. In particular, we focus on inorganic metal-halide perovskites which have recently drawn great scientific attention. For this class of materials, we show that both nonempirical hybrid-functional schemes yield band gaps of comparable accuracy (~ 0.2 eV) with respect to *GW* reference calculations. Furthermore, we discuss the suitability of nonempirical hybrid-functional schemes for the application to the screening of large sets of perovskite materials.

Third, we investigate the fundamental band gap of liquid water and hexagonal ice. These materials are particularly challenging since experimental studies have not reached a consensus on the band gap yet. Therefore, we first deduce robust benchmarks on the basis of a critical review of various experimental studies in the literature. Then, we compute the band gap through state-of-the-art *GW* methods as well as nonempirical hybrid functionals. We show

Abstract

that theoretical calculations and experimental references are in good agreement with each other and we discuss critical aspects which are essential to ensure a consistent description of the band gap.

Finally, we investigate band-edge levels as obtained with hybrid-functional calculations. The $\text{CaF}_2/\text{Si}(111)$ interface serves thereby as an ideal test case to examine the accuracy of different theoretical schemes. The comparison with experiment reveals that global hybrid functionals and self-consistent GW methods provide the most accurate description of the interfacial band alignment.

Keywords: Nonempirical hybrid functionals, GW approximation, dielectric response, Koopmans' condition, point defects, band gap, band edges

Zusammenfassung

Berechnungen der elektronischen Struktur von Materialien auf Basis von Hybrid-Funktionalen haben sich zu einer weit verbreiteten Technik entwickelt, die sowohl in Physik, Chemie als auch in der Materialwissenschaft Anwendung findet. Trotz dieses Erfolges besitzen Hybrid-Funktionale den Nachteil, dass sie unbestimmte Parameter beinhalten. Um diesen Mangel zu überwinden, werden derzeit zwei verschiedene nicht-empirische Bestimmungsschemata untersucht, nämlich dielektrisch-abhängige Hybrid-Funktionale [engl. dielectric-depedent hybrid (DDH) functionals] und Hybrid-Funktionale, welche die Koopmans-Bedingung erfüllen. Die vorliegende Doktorarbeit widmet sich der Evaluierung und Weiterentwicklung dieser Methoden. Insbesondere zeigen wir, dass eine präzise Beschreibung der Bandlücke von Systemen kondensierter Materie erreicht werden kann. Außerdem demonstrieren wir, dass diese Funktionale die Genauigkeit von hoch entwickelten *GW*-Methoden erreichen, dafür jedoch nur einen Bruchteil des numerischen Aufwands bedürfen.

Zunächst konzentrieren wir uns auf die Weiterentwicklung von Hybrid-Funktionalen, welche Koopmans-Bedingung erfüllen. Wir zeigen, dass die Konstruktion dieser Funktionale mittels geeignet definierter Defekte optimiert werden kann. Durch die Überwachung der delokalisierten Abschirm-Ladung entwickeln wir ein Maß für den Hybridisierungsgrad mit den Bandkanten, welches verwendet werden kann, um die Bandlücke genauer zu berechnen. Wir demonstrieren, dass die Anwendung dieser Methodik für übliche halbleitende und isolierende Materialien Bandlücken ergibt, die sich vom Experiment um weniger als 0.2 eV unterscheiden. Diese konzeptionellen Entwicklungen representieren einen wichtigen Schritt zur Etablierung von nicht-empirischen Hybrid-Funktionalen als robuste Methode für Bandlücken-Berechnungen.

Anschließend untersuchen wir DDH-Funktionale und Hybrid-Funktionale, welche Koopmans-Bedingung erfüllen, für Bandlücken von anspruchsvolleren Materialien. Insbesondere konzentrieren wir uns auf anorganische Metall-Halogen-Perowskite, die kürzlich große wissenschaftliche Aufmerksamkeit erregt haben. Für diese Materialklasse zeigen wir, dass beide nicht-empirischen Schemata Bandlücken von vergleichbarer Genauigkeit (~ 0.2 eV) ergeben, wenn *GW*-Methoden als Referenz herangezogen werden. Darüber hinaus diskutieren wir die Eignung der vorliegenden Funktionale für die Analyse einer großen Anzahl von Perowskit-Materialien.

Drittens untersuchen wir die Bandlücke von flüssigem Wasser und hexagonalem Eis. Diese Materialien sind besonders herausfordernd, da experimentelle Studien noch keinen Konsens über die Bandlücke erzielt haben. Daher leiten wir zunächst robuste Referenzwerte auf Grundlage einer kritischen Überprüfung verschiedener experimenteller Studien her. Anschließend berechnen wir die Bandlücke mit modernsten *GW*-Methoden sowie mit nicht-empirischen Hybrid-Funktionalen. Wir zeigen, dass theoretische Berechnungen und experimentelle Referenzen gut miteinander übereinstimmen, und diskutieren kritische Aspekte, die wesentlich sind, um eine konsistente Beschreibung der Bandlücke zu gewährleisten.

Zuletzt untersuchen die Vorhersage von Bandkanten, wie sie mit Hilfe von Hybrid-Funktionalen erhalten werden. Die $\text{CaF}_2/\text{Si}(111)$ -Grenzfläche dient dabei als idealer Testgegenstand, um die Genauigkeit verschiedener theoretischer Schemata zu evaluieren. Der Vergleich mit dem Experiment zeigt, dass globale Hybrid-Funktionale und selbstkonsistente *GW*-Methoden die genaueste Beschreibung der Bandkanten ermöglicht.

Schlüsselwörter: Nicht-empirische Hybrid-Functionale, *GW* Approximation, Dielektrische Funktion, Koopmans-Bedingung, Punktdefekt, Bandlücke, Bandkante

Contents

Abstract (English/Deutsch)	i
1 Introduction	1
1.1 Electronic-structure calculations	1
1.2 Parameter dependence of hybrid functionals	3
1.3 Nonempirical hybrid functionals	5
1.4 Objectives	6
1.5 Organization of the thesis	7
2 Theoretical background	11
2.1 Many-electron problem	12
2.2 Density-functional theory	13
2.3 Hybrid functionals	19
2.4 Many-body perturbation theory in the <i>GW</i> approximation	21
2.5 Other computational methods in this thesis	29
3 Construction schemes for nonempirical hybrid functionals	35
3.1 Dielectric-dependent hybrid (DDH) functionals	36
3.1.1 Motivation of DDH functionals	36
3.1.2 Overview of DDH functionals	38
3.1.3 Construction scheme adopted in this thesis	39
3.2 Hybrid functionals satisfying Koopmans' condition	41
3.2.1 Koopmans' condition and related theorems	41
3.2.2 Overview of hybrid functionals satisfying Koopmans' condition	43
3.2.3 Construction scheme adopted in this thesis	45
4 Developments for hybrid functionals satisfying Koopmans' condition	47
4.1 Open questions	48
4.2 Definition of adjustable potential probes	49
4.3 Computational aspects	50
4.4 Application of adjustable potential probes	52
4.5 Summary	55

5	Band gaps of inorganic metal-halide perovskites	57
5.1	Motivation	58
5.2	Theoretical schemes and band-gap references	58
5.3	Computational aspects	59
5.3.1	Computational details	59
5.3.2	Role of semicore electrons	61
5.4	Band gaps	63
5.4.1	Dielectric-dependent hybrid functionals	63
5.4.2	Hybrid functionals satisfying Koopmans' condition	65
5.5	Summary	68
6	Band gaps of liquid water and hexagonal ice	71
6.1	Motivation	72
6.2	Experimental band-gap references	73
6.3	Theoretical schemes	76
6.4	Computational aspects	77
6.4.1	Structural models	77
6.4.2	Computational details	79
6.5	Band gaps of liquid water and hexagonal ice	81
6.5.1	Quasiparticle self-consistent <i>GW</i>	81
6.5.2	Dielectric-dependent hybrid functionals	83
6.5.3	Hybrid functionals satisfying Koopmans' condition	87
6.6	Summary	93
7	Band alignment at the $\text{CaF}_2/\text{Si}(111)$ interface	97
7.1	Motivation	98
7.2	Computational aspects	99
7.2.1	Electronic-structure methods	99
7.2.2	Computational details	100
7.2.3	Band-alignment scheme	101
7.2.4	Strain effects	103
7.3	Band gaps and band-edge levels of bulk materials	105
7.4	Band offsets at the $\text{CaF}_2/\text{Si}(111)$ interface	109
7.4.1	Interfacial line-up potential	109
7.4.2	Band offsets at the interface	112
7.5	Effect of interfacial Si-F bonding	113
7.6	Summary	115
8	Conclusions	117
A	Band alignment at the water/vacuum interface	121
	Bibliography	126

Acknowledgements	147
List of Acronyms	149
Curriculum Vitae	151

1 Introduction

1.1 Electronic-structure calculations

The electronic structure is among the most relevant physical properties of each material. Indeed, the interaction of electrons with each other and with different particles (such as nuclei, photons, etc.) entirely characterizes a material at the microscopic level. Therefore, various material properties can be subsequently determined based on the knowledge of the electronic structure. Moreover, the mathematical description of the electrons is given by the fundamental equations of quantum mechanics. As a consequence, the electronic structure (and thus many deduced properties) can in principle be determined relying only on quantum mechanics and a few physical constants. The prediction of materials based only on these *first principles* of nature has inevitably stimulated great scientific effort. Interestingly, these developments encompass various scientific disciplines such as physics, chemistry, biology, and material science. Thus, electronic-structure theory exhibits generally a great interdisciplinary character.

However, the computation of the electronic structure is not a trivial task. It is therefore not surprising, that a large variety of computational methods have been developed within the last century. Early approaches have been invented simultaneously to the development of quantum mechanics in the beginning of the 20th century. Indeed, the prominent Hartree-Fock (HF) [1, 2] and Thomas-Fermi (TF) [3] theories date back almost one hundred years. The predictive power of these schemes remained however limited due to the lack of computational resources and to the approximations involved.

A major breakthrough has been achieved with the advent of density-functional theory (DFT) in the 1960s [4]. The central idea of this method is to describe the electronic structure using a simple quantity: the electron density. Based on this approach, DFT enabled electronic-structure calculations with reasonable accuracy at low computational cost. Due to this promising combination, DFT has developed into the most widely used techniques for electronic-structure calculations. A simple way to quantify this development, is the number of scientific articles which employ DFT as shown in Fig. 1.1. Starting with not even hundred per year in the 1980s, the use of DFT has grown almost exponentially, resulting in more than ten thousand articles

within the last years. The enormous success of DFT is also reflected in the fact that Walter Kohn, one of the founders of DFT, received the Nobel prize in 1998.

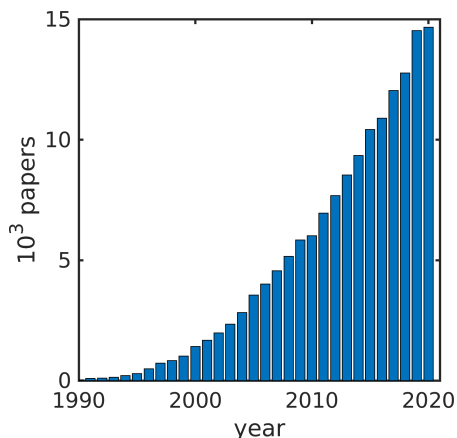


Figure 1.1 – Number of papers per year when DFT is searched as a topic in the Web of Knowledge.

Nevertheless, local and semilocal density functionals such as the widely used Perdew-Burke-Ernzerhof (PBE) functional [5] suffer from important deficiencies. While the prediction of ground-state properties (such as total energies, electron densities, lattice constants and compressibilities) are already reasonably accurate, the description of the excited-state properties remains still unsatisfactory [6]. In particular, the prediction of band gaps indicates generally a severe underestimation by up to 50 %. For some narrow-gap semiconductors, such as Ge or InN, this can lead to an even qualitatively wrong metallic character [7]. As a consequence of the band-gap underestimation, also the computation of defect levels as well as of interfacial band offsets suffers tremendously [8]. These limitations of local and semilocal DFT have led to an extensive search for more advanced electronic-structure methods.

The generally accepted approach to overcome the band-gap underestimation consists in many-body perturbation theory (MBPT). This highly sophisticated scheme relies on a set of equations proposed by Hedin in 1965, together with the so called *GW* approximation to them [9]. Based on this theoretical foundation, various flavours of *GW* methods have been developed in the last decades. The earliest *GW* calculations in the 1960s and 1970s remained limited to the electron gas as a model system [10]. The first applications to semiconductors have been presented in the 1980s by Hybertsen and Louie [11, 12] as well as by Godby and coworkers [13]. In this approach, the underestimated band gaps as obtained with (semi)local DFT are corrected in a perturbative fashion resulting in a better agreement with respect to the experimental references. In the 2000s, this one-shot procedure has been conceptually expanded to self-consistent *GW* calculations [14, 15, 16]. More recently, the incorporation of vertex corrections [17, 18] has led to advanced *GW* approaches with a even higher predictive power. It is noteworthy, that the improved description of the electronic structure is not limited to the band gap. Indeed, also defect levels [19, 20], ionization potentials [18], and band offsets [21] have been predicted with a remarkable accuracy.

The main drawback of *GW* methods are their high computational cost with respect to DFT calculations. Despite, implementations with increasing efficiency [22] and various numerical techniques [23], the application of *GW* calculations remained limited to rather small molecules or crystals with small unit cells. Moreover, a practical *GW* based scheme to perform structural relaxations is still missing. Therefore, it was (and still remains) highly desirable to develop alternative computational schemes yielding the same accuracy as self-consistent *GW* methods but requiring a lower computational cost.

Hybrid functionals have the potential to fill this gap. These functionals aim at combining the advantages of Hartree-Fock (HF) theory with those of DFT [24]. Indeed, the former provides an exact treatment of exchange and the latter enables an efficient computation of correlation effects [24]. An early approach to unify both aspects has been proposed by Kleinman and Bylander in 1990 [25]. This method, later termed as sX-LDA [26], yields an improved description of band gaps with respect to semilocal functionals [7]. In a different context, also Becke proposed a combined approach in 1993 [24]. Based on the adiabatic connection formula and adopting a linear interpolation, Becke invented the so called half-and-half hybrid functional [24]. The name refers thereby to the 50%:50% mixing ratio between semilocal and Fock exchange. Following Becke’s pioneering work, numerous hybrid functionals have been proposed in the literature. In chemistry, hybrid-functional calculations have been used regularly since the 1990s. In particular, the most popular B3LYP functional [27, 24] has been adopted in numerous studies for the computation of molecular properties. Instead, the application of hybrid functionals in condensed-matter physics has been hampered notably. The origin of this delay is the substantial increase in computational cost of hybrid functionals when adopting plane-wave basis sets. Therefore, semilocal functionals provided for long time a more appropriate combination of accuracy and computational burden. However, in the last decades several methodological advances [28, 29, 30] drastically reduced the cost of hybrid-functional calculations for periodic systems. As a consequence, hybrid functionals have been used intensively for the modelling of phenomena in solid-state physics.

1.2 Parameter dependence of hybrid functionals

Among the most popular hybrid functional used for extended condensed matter systems is the PBE0 functional [31]. This functional is deduced from the semilocal PBE functional by replacing a fraction α of the semilocal exchange with nonlocal Fock exchange. As a generalization of PBE0, one could consider the hybrid functional proposed by Heyd, Scuseria, and Ernzerhof (HSE) [32, 33]. This functional additionally incorporates a range-separation length by which Fock exchange is treated explicitly only at short-range distances whereas the semilocal expression is adopted in the long range. Recently, as previously done by Yanai *et al.* [34] for the B3LYP functional, the expression of this hybrid functional has been extended to allow for distinct fractions of Fock exchange to be admixed at short and long range through the incorporation of yet another parameter [35]. The rationale behind this decomposition is that spatial variations in the screening might be better accounted for in this way.

Intuitively, the question arises how to fix the undetermined parameters incorporated in hybrid functionals. Early strategies in searching for the optimal parameter focused on the validation against experimental data sets [7]. More specifically, the mean absolute error in the prediction of particular properties is minimized when considering large sets of materials. For the case of the PBE0 functional, this has led to a default fraction of Fock exchange of 0.25 on the basis of energetic considerations for molecular systems [31]. However, this way of proceeding yields accurate results only “on average”, whereas for specific cases significant deviations can be observed. Moreover, an arbitrariness arises due to the selective choice of the dataset and the properties against which the parameters are fitted [7]. In this perspective, default hybrid-functional parameters represent only an educated guess rather than a general solution.

Another aspect of the parameter dependence of hybrid functionals is the fact, that the incorporated parameters should depend on the system under consideration. Indeed, the optimal ratio between semilocal and Fock exchange is apparently different for a narrow-gap semiconductor and a wide-gap insulator. Therefore, a uniquely defined set of parameters for all materials is not achievable. Nevertheless, the system dependence of the optimal parameters provides clear advantages for the practical application of hybrid functionals.

In the study of solids, hybrid functionals are particularly appreciated for the capability of reproducing the experimental band gap [8]. In particular when considering defect levels, this aspect is crucial to avoid ambiguities in the comparison of theory and experiment. To achieve this goal, the free parameters are commonly adjusted empirically in order to produce a calculated band gap that corresponds to the experimental one [36]. Here, one takes advantage of the dependence of the band gap on the hybrid-functional parameter. For the case of the PBE0 functional, this is shown in Fig. 1.2 for typical materials investigated in this thesis.

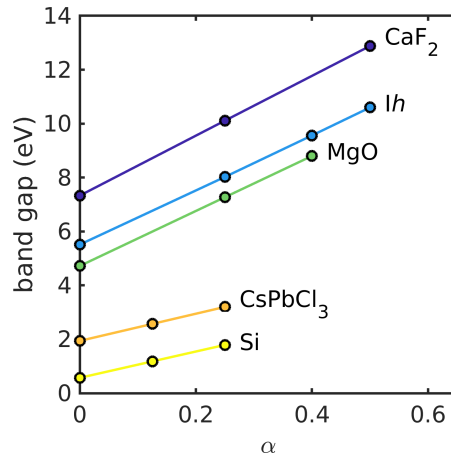


Figure 1.2 – Linear dependence of the theoretical band gap on the fraction of Fock exchange α incorporated in the PBE0(α) functional for several materials investigated in this thesis.

For each specific material an optimal fraction of Fock exchange can be determined in case the experimental band gap is known. This specific empirical choice appears to offer also the additional benefit that calculated band offsets at interfaces [8, 21] and ionization potentials at

surfaces [18] are in good agreement with their experimental counterparts. Furthermore, total-energy differences [8] and basic structural properties [37] generally do not depend strongly on the amount of Fock exchange. However, setting the functional parameters in an empirical way remains unsatisfactory from a conceptual point of view.

1.3 Nonempirical hybrid functionals

To overcome this drawback, considerable scientific effort has been devoted to the development of nonempirical and still system-dependent definitions of the hybrid-functional parameters. A promising strategy is the consideration of exact physical constraints which are not *a priori* fulfilled by the approximate functional. The hybrid functional is then denoted as nonempirical, if the free parameters are fixed in such a way that the exact condition is fulfilled or at least residual deviations are minimized. At present, two main branches of development can be identified, namely dielectric-dependent hybrid (DDH) functionals [38, 39, 40, 41, 42, 43, 44, 45, 35, 46, 47] and hybrid functionals enforcing Koopmans' condition [48, 49, 50, 51, 52, 53, 54, 55]. Both approaches exhibit great potential due to their promising combination of accuracy and computational cost.

In the DDH approach, the dielectric response of the considered material is used to determine the free hybrid-functional parameters. In particular, the inverse high-frequency dielectric constant $1/\epsilon_\infty$ has shown to be in close relation with the incorporated amount of Fock exchange [36, 41]. From a conceptual perspective, this connection corresponds to enforcement of the asymptotically correct Kohn-Sham potential [56] within the approximate hybrid functional. Through adopting this exact property, one can determine one hybrid-functional parameter for each investigated material and without resorting to an empirical adjustment. The application of this basic idea has stimulated the development of various DDH schemes within the last decade. These approaches differ mostly in technical aspects such as global [36, 41, 43] or range-separated functional form [35, 57, 47], one-shot [41, 58] or self-consistent workflow [39, 43, 44], as well as the spatial variability of the DDH functionals [59]. The most elaborate schemes represent the recently developed DD-RSH of Skone *et al.* [35], DD-RSH-CAM of Chen *et al.* [47], and DSH of Cui *et al.* [57]. In practice, these schemes have shown to provide an accurate description of band gaps and dielectric constants for a variety of organic and inorganic crystals [35, 47, 57]. Furthermore, specific DDH functionals have been successfully applied to polaronic distortions [45], aqueous solutions [60, 61], and heterogeneous systems [59].

The second category of nonempirical hybrid functionals particularly focuses on the enforcement of Koopmans' condition. This constraint represents a property of the exact density functional and states that a single-particle energy level does not change upon electron occupation. Interestingly, this property can be equivalently expressed as the piecewise linearity of the total energy as a function of fractional electron number [62, 63]. In the same perspective, Koopmans' condition can be related to a variety of other theoretical concepts such as the so

called IP theorem [62, 64] or the many-electron self-interaction error [62, 63]. However, in practice it turned out that most of the commonly used electronic-structure methods do not fulfil Koopmans' condition (and thus the equivalent exact constraint) [65]. In order to overcome this deficiency, considerable efforts have been devoted to enforce these exact conditions within a hybrid-functional framework [66, 67, 42, 68, 48, 49, 51, 52, 69, 50, 53, 55]. The first successful applications of this idea have been reported for finite systems (such as atoms and molecules). Indeed, for such systems an improved description of the band gaps, the ionisation potential and the spectra of excited states has been achieved [66, 67, 42, 65]. The application of the same concept to infinite systems (such as solids) has been shown to be more challenging because of the fact that a localized state is necessary while band edges of solids are usually delocalized. This drawback has been overcome, for instance, through the analysis of localized defect states [68, 48, 49, 51, 50, 53, 55].

Overall, the nonempirical construction of hybrid functionals has become a widely used technique in numerous scientific studies. Either by means of the dielectric response or through the enforcement of Koopmans' condition, the unsatisfactory parameter dependence of hybrid functionals can be circumvented without relying on empirical adjustments. Therefore, such functionals exhibit great potential to overcome the limitations of semilocal DFT in a fully nonempirical fashion. Even more, their moderate computational cost makes them a valuable alternative to highly demanding *GW* calculations. However, a variety of open questions remain to be answered before nonempirical hybrid functionals will have achieved this goal.

1.4 Objectives

In this thesis, we set out to explore various routes for improving electronic-structure calculations by focusing on nonempirical hybrid functionals. In particular, we are interested to what extent an accurate description of band gaps and band-edge levels can be achieved through these functionals. We specifically ask the questions: Which nonempirical hybrid functional is going to perform best? Is the obtained accuracy dependent on the investigated material? So far, these questions have been addressed only separately for DDH functionals [41, 43, 35, 47, 57] and hybrid functionals satisfying Koopmans' condition [42, 51]. A comparative study of both approaches has only been reported for the case of alkali halides in Ref. [51]. Therefore, it is our goal to examine both schemes in a systematic fashion for a more extended set of materials.

In order to ensure the overall consistency among electronic-structure methods, we address this problem also from the side of many-body perturbation theory. Here, it is our special interest to confront nonempirical hybrid functionals with state-of-the-art *GW* calculations. Are these functionals indeed able to compete with the most sophisticated *GW* techniques? And if not, which further developments are necessary to achieve this goal?

Additionally, we want to address the possible benefits due to different classes of hybrid functionals. This comprises both global as well as range-separated hybrid functionals. For the

former, we generally consider the widely used PBE0(α) functional [31]. For the latter, we adopt the so called CAM($\alpha_s, \alpha_\ell, \mu$) functional [70] which provides a substantial amount of flexibility due to the three incorporated parameters. Are both functional forms adequate for the construction of nonempirical hybrid functionals? Which accuracy can be achieved in each case? It is noteworthy that for DDH functionals it has already been shown, that the range-separated form enables more accurate band-gap predictions than the global one [35, 47]. For hybrid functionals satisfying Koopmans' condition, it is not clear to what extent the same statement holds [51, 55]. Therefore, we systematically apply the two nonempirical construction schemes to both global and range-separated hybrid functionals and evaluate the obtained accuracy in each case.

Another very interesting question concerns the possibility of combining both nonempirical schemes. So far, hybrid functionals determined by the dielectric response and those enforcing Koopmans' condition have been treated as distinct techniques. However, a few studies in the literature have already implied a combination of both approaches [71, 51]. It is our interest, to continue these promising results and to investigate to what extent a hybrid functional can be constructed that enforces both the correct long-range screening and Koopmans' condition. Are both nonempirical schemes compatible with each other? Are the underlying exact physical constraints equivalent?

Finally, we want to remark that both nonempirical hybrid-functional schemes exhibit a different level of conceptual development. Indeed, DDH functionals are already an established technique for band-gap predictions [43, 35, 47, 57]. In contrast, hybrid functionals satisfying Koopmans' condition have not yet reached such an elaborated stage. Most studies have applied these functionals for the investigation of specific defects such as polaronic distortions [48, 51, 50, 53]. The application of hybrid functionals satisfying Koopmans' condition as a predictive tool for band-gap calculations has been proposed just recently by Miceli *et al.* [51]. Therefore, open questions have to be answered before these functionals can be applied in a systematic way. Which defect should be used for the enforcement of Koopmans' condition? Are all defects equivalent for this purpose? Is there maybe an optimal defect applicable to every material? We set out, to address these questions in a comprehensive way. This allows us to establish hybrid functionals satisfying Koopmans' condition as an accurate method for band-gap calculations and thus to perform a meaningful comparison with DDH functionals.

1.5 Organization of the thesis

This thesis is organized as follows.

In **Chapter 2**, we describe the theoretical background of the electronic-structure methods adopted in this thesis. This comprises DFT in semilocal and hybrid-functional formulations as well as many-body perturbation theory in the *GW* approximation. In addition, we describe computational aspects and practical implementations of these methods. Finally, we devote special attention to finite-size corrections for charged defects and to the computation of

the dielectric function since these computational methods are of great importance for the construction of nonempirical hybrid functionals.

In **Chapter 3**, we introduce the construction schemes for nonempirical hybrid functionals adopted in this thesis. First, we address dielectric-dependent hybrid functionals. We describe the relationship between the dielectric function and the amount of incorporated Fock exchange and show how this connection can be used to determine free hybrid-functional parameters in a nonempirical manner. Second, we consider hybrid functionals which satisfy Koopmans' condition. We introduce Koopmans' condition as an exact physical constraint and describe its connection to equivalent theorems. Based on this conceptual preface, we then describe the nonempirical construction of a hybrid functional based on single-particle energy levels of localized states. For both schemes, we present related approaches in the literature and discuss similarities and differences with the ones adopted in this thesis.

In **Chapter 4**, we present conceptual developments for hybrid functionals that satisfy Koopmans' condition. More specifically, we introduce adjustable potential probes for determining band gaps of extended systems. This allows us to study the band-gap prediction as the defect level varies within the band gap. In particular, we examine the relation between the estimated band gaps and the hybridization with the band-edge states, which we describe through the delocalized screening charge in the simulation cell. We apply the proposed scheme to aluminium phosphide (AlP), diamond (C) and magnesium oxide (MgO), which cover a large range of band gaps and show both covalent and ionic bonding character. The accuracy of the band-gap estimate corresponding to the lowest degree of hybridization is assessed and compared to that achieved with point defects or with the interstitial hydrogen probe. We underline that the concepts presented in this chapter are a crucial step to establish hybrid functionals satisfying Koopmans' condition as a serious alternative with respect to DDH functionals.

A systematic comparison between both nonempirical hybrid-functional schemes is presented in **Chapter 5**. In particular, we evaluate the performance of various nonempirical hybrid functionals for inorganic metal-halide perovskites. We consider the cubic phase of CsBX_3 perovskites, where B represents Pb or Sn and X stands for Cl, Br, or I. These compounds serve as a representative set of metal-halide perovskites and additionally show sufficiently small unit cells to make high-level reference calculations affordable. The parameters in the hybrid functionals constructed here are determined both through the static dielectric response and through the enforcement of Koopmans' condition. Our work carefully goes through the construction process highlighting all critical issues encountered, thereby allowing clear insight into the viability of the two approaches. To achieve reference band gaps, we additionally perform state-of-the-art *GW* calculations within a consistent computational set-up. The present analysis allows us to determine the accuracy of the investigated schemes in a comparative fashion and to discuss their suitability for application to the screening of large sets of perovskite materials.

In **Chapter 6**, we calculate the fundamental band gap of liquid water and hexagonal ice through several advanced electronic-structure methods. These comprise state-of-the-art *GW* schemes as well as nonempirical hybrid functionals. In particular, we consider QSGW calculations that account for vertex corrections in the screening and hybrid functionals in which the free parameters are fixed either through the dielectric response of the material or through enforcing Koopmans' condition to localized states. Both nonempirical procedures are applied to global and range-separated hybrid functionals. The evaluation of such a variety of different approaches within a consistent computational setup allows us to achieve a robust band-gap estimate and to overcome the spread of previous results in the literature. The comparison with available experimental references confirms the validity of our results.

In **Chapter 7**, we determine band offsets at the $\text{CaF}_2/\text{Si}(111)$ interface using various advanced electronic-structure schemes to examine their accuracy in comparison with the experimental characterization. Our investigation includes both hybrid-functional and *GW* calculations. In particular, we use both global and range-separated hybrid functionals and consider self-consistency and vertex corrections in the *GW* calculations. Our study also encompasses the effect of strain in the CaF_2 overlayer to ensure that it does not affect the comparison with experiment. In this way, we expect to be able to identify the most suitable theoretical approach for the band alignment. We then address the variation of the band offset upon the occurrence of extra fluorine at the interface.

We draw the conclusions of this thesis in **Chapter 8**.

2 Theoretical background

In this chapter, we describe the theoretical background of the electronic-structure methods adopted in this thesis. First, we present the quantum mechanical many-body problem for interacting electron and nuclei together with the Born-Oppenheimer approximation. Then, we introduce density functional theory (DFT) in local and semilocal approximations. The hybrid-functional formulation of DFT is described subsequently. In the last part of this chapter, we turn to many-body perturbation theory. In particular, we present Hedin's equations, the prominent *GW* approximation, and the widely used self-consistent *GW* schemes. In addition to the theoretical concepts, we also describe computational aspects and practical implementations of the adopted electronic-structure methods. Finally, we devote special attention to finite-size corrections for charged defects and to the computation of the dielectric function.

2.1 Many-electron problem

Many-body Hamiltonian

Atoms, molecules, and solids represent quantum mechanical systems composed of interacting electrons and nuclei. The Hamiltonian of such systems can be written in a non-relativistic and spin-unpolarized form as [72]

$$\hat{H}_{\text{tot}} = \underbrace{-\sum_i \frac{\nabla_i^2}{2}}_{\hat{T}_e} - \underbrace{\sum_I \frac{\nabla_I^2}{2M_I}}_{\hat{T}_N} + \underbrace{\frac{1}{2} \sum_{i \neq j} \frac{1}{|\mathbf{r}_i - \mathbf{r}_j|}}_{\hat{V}_{ee}} + \underbrace{\frac{1}{2} \sum_{I \neq J} \frac{Z_I Z_J}{|\mathbf{R}_I - \mathbf{R}_J|}}_{\hat{V}_{NN}} - \underbrace{\sum_{i,I} \frac{Z_I}{|\mathbf{r}_i - \mathbf{R}_I|}}_{\hat{V}_{eN}}. \quad (2.1)$$

Here, a formulation in Hartree atomic units ($\hbar = m_e = e = 1/(4\pi\epsilon_0) = 1$) is adopted. The properties of the electrons (coordinates \mathbf{r}_i) and the nuclei (coordinates \mathbf{R}_I , masses M_I , charges Z_I) are distinguished through lower and upper case letters, respectively. Every term of the Hamiltonian \hat{H}_{tot} represents a part of the total energy, namely the kinetic energy of the electrons \hat{T}_e , the kinetic energy of the nuclei \hat{T}_N , the potential energy of the electron-electron interaction \hat{V}_{ee} , the potential energy of the nuclei-nuclei interaction \hat{V}_{NN} , and the potential energy of the electron-nuclei interaction \hat{V}_{eN} . The ground-state energy E and the wave function Ψ of this system are then determined by the time-independent Schrödinger equation

$$\hat{H}_{\text{tot}} \Psi(\underline{\mathbf{r}}, \underline{\mathbf{R}}) = E \Psi(\underline{\mathbf{r}}, \underline{\mathbf{R}}). \quad (2.2)$$

Here, the wave function Ψ depends on the positions of the electrons $\underline{\mathbf{r}} = \{\mathbf{r}_i\}$ and the nuclei $\underline{\mathbf{R}} = \{\mathbf{R}_I\}$. With these equations, the physics of a quantum mechanical system composed of interacting electrons and nuclei is in principle captured. However, obtaining solutions for systems of $\sim 10^{23}$ particles is practically impossible. Indeed, analytical solutions are only known for very simple systems and direct calculations suffer from the enormous computational burden. Therefore, reasonable approximations to this problem are needed.

Born-Oppenheimer approximation

The first simplification is the Born-Oppenheimer (BO) approximation [73], which uses the fact that electrons and nuclei exhibit largely different masses. Indeed, the mass of a proton is ~ 1800 times larger than the mass of an electron. Therefore, it is justified to decouple the description of both constituents. Mathematically, this corresponds to the development of a perturbation series based on the small parameter $1/M_I$ [74]. The many-body wave function Ψ (and thus the Hilbert space) is then separated into an electronic and an ionic part. To simplify the discussion, M_I can be set to infinity thereby neglecting the kinetic energy of the nuclei \hat{T}_N . Also the potential energy of the nuclei-nuclei interaction \hat{V}_{NN} can be disregarded. This term represents only an additive constant to the total energy and is not relevant here since we are only interested in the electronic states of the many-body problem. Overall, one can write the

Hamiltonian of the electronic system as

$$\hat{H} = \hat{T}_e + \hat{V}_{ee} + \hat{V}_{eN}. \quad (2.3)$$

This Hamiltonian (and thus the wave function Ψ) still depends on the coordinates of the nuclei \mathbf{R} but only in a parametrical fashion. With the present approximations, one can reduce the “many-body problem” to a (still challenging) “many-electron problem”. To tackle the latter, different theoretical approaches have been developed which will be introduced in the next section.

2.2 Density-functional theory

Electron density

Density-functional theory (DFT) is one of the most prominent approaches to tackle the many-electron problem. As the name suggests, the electron density $n(\mathbf{r})$ plays an important role within DFT. This quantity is a scalar function of the position in space \mathbf{r} and is therefore much more tractable compared to the multi-dimensional many-electron wave function $\Psi(\mathbf{r})$. Moreover, the electron density for a system of N electrons can be deduced from the wave function via [72]

$$n(\mathbf{r}) = N \int |\Psi(\mathbf{r}, \mathbf{r}_2, \dots, \mathbf{r}_N)|^2 d\mathbf{r}_2 \dots d\mathbf{r}_N. \quad (2.4)$$

The normalization of Ψ ensures that $n(\mathbf{r})$ integrates to the integer number of N electrons, i.e.

$$\int n(\mathbf{r}) d\mathbf{r} = N. \quad (2.5)$$

Hohenberg-Kohn theorems

Based on this simple quantity, Hohenberg and Kohn laid the foundation for DFT in their pioneering work in 1964 [75]. The authors considered a system of electrons subject to an external potential \hat{W}_{ext} . Analogous to Eq. (2.3), the Hamiltonian of this system can be formulated as

$$\hat{H} = \hat{T}_e + \hat{V}_{ee} + \hat{W}_{\text{ext}} = \hat{T}_e + \hat{V}_{ee} + \sum_i V_{\text{ext}}(\mathbf{r}_i). \quad (2.6)$$

The external potential comprises the interaction of the electrons with the nuclei (\hat{V}_{eN}), electromagnetic fields, etc. and can be written in the identical functional form $V_{\text{ext}}(\mathbf{r})$ for all electrons. For such an electronic system, Hohenberg and Kohn proved a twofold theorem. First, it was shown that there is a one-to-one correspondence between the external potential \hat{W}_{ext} and the ground-state electron density $n(\mathbf{r})$. This bijection has far reaching consequences. In particular, it guarantees that the expectation value of the electron kinetic energy \hat{T}_e and the electron-electron interaction \hat{V}_{ee} on the ground-state wave function Ψ can be written as a functional of the electron density. Moreover, also the total energy E of the ground state can be

Chapter 2. Theoretical background

written as such a functional which represent the second part of the Hohenberg-Kohn (HK) theorem. Mathematically, this can be expressed as [75]

$$E[n] = F^{\text{HK}}[n] + \int V_{\text{ext}}(\mathbf{r}) n(\mathbf{r}) d\mathbf{r}, \quad (2.7)$$

where $F^{\text{HK}}[n]$ is a universal functional of the density, independent of both the considered system and the external potential. The HK theorems proof that this functional exists and that it is uniquely defined. Moreover, the total-energy functional $E[n]$ reaches it's minimum at the exact ground-state density with the exact ground-state energy [76]. These exciting properties indicate a way to solve the many-electron problem using variational calculus, although the HK functional itself is not explicitly known. It is noteworthy that the presented theorems can be rigorously generalized for spin-polarized electronic systems.

Kohn-Sham equations

The minimization of the total-energy functional with respect to the electron density was then performed by Kohn and Sham [4]. The authors used the assumption that the system of interacting electrons can be substituted by an auxiliary system of non-interacting electrons that yields the same ground-state density. Adopting orthonormal orbitals $\phi_i(\mathbf{r})$, one can then write the ground-state density as

$$n(\mathbf{r}) = \sum_i \phi_i^*(\mathbf{r}) \phi_i(\mathbf{r}). \quad (2.8)$$

One can argue that this decomposition is in principle exact and unique for any well behaved density $n(\mathbf{r})$ [76]. Moreover, it allows one to write the kinetic energy of the non-interacting electron system in a simple form as

$$T_0[n] = \sum_i \langle \phi_i | -\frac{\nabla^2}{2} | \phi_i \rangle. \quad (2.9)$$

Also, the Hartree energy, which is the classical energy of the electron-electron interaction, can be expressed with the orbital ϕ_i as

$$E_{\text{H}}[n] = \frac{1}{2} \sum_{i,j} \langle \phi_i \phi_j | \frac{1}{|\mathbf{r} - \mathbf{r}'|} | \phi_i \phi_j \rangle = \frac{1}{2} \iint \frac{n(\mathbf{r}) n(\mathbf{r}')}{|\mathbf{r} - \mathbf{r}'|} d\mathbf{r} d\mathbf{r}'. \quad (2.10)$$

Assuming that the non-interacting electron system mimics the fully interacting one, the given expressions for $T_0[n]$ and $E_{\text{H}}[n]$ can serve as reasonable approximations to $T_{\text{e}}[n]$ and $V_{\text{ee}}[n]$, respectively. Adopting these simplifications, the HK functional can be recast to

$$F^{\text{HK}}[n] = T_0[n] + E_{\text{H}}[n] + E_{\text{xc}}[n]. \quad (2.11)$$

The last term in Eq. (2.11) represents the so-called exchange-correlation (xc) functional

$$E_{\text{xc}}[n] = T_e[n] - T_0[n] + V_{\text{ee}}[n] - E_{\text{H}}[n]. \quad (2.12)$$

In contrast to $T_0[n]$ and $E_{\text{H}}[n]$, this functional is not given through an explicit expression. Indeed, it remains as an unknown term and can be interpreted as the error induced by disregarding the full electron-electron interaction. Nevertheless, $E_{\text{xc}}[n]$ amounts only to a minor contribution of the total energy insofar as the Hartree term has already been separated out [72]. Therefore, the xc functional can be reasonably approximated in a local or semilocal fashion as discussed at a later point in this section. The variational minimization of the total-energy functional under the constraint of orthonormalized orbitals ($\langle \phi_i | \phi_j \rangle = \delta_{ij}$) leads to the prominent Kohn-Sham (KS) equations [4]

$$\left[-\frac{\nabla^2}{2} + \underbrace{V_{\text{ext}}(\mathbf{r}) + V_{\text{H}}(\mathbf{r}) + V_{\text{xc}}(\mathbf{r})}_{V_{\text{eff}}(\mathbf{r})} \right] \phi_i(\mathbf{r}) = \varepsilon_i \phi_i(\mathbf{r}). \quad (2.13)$$

Here, $V_{\text{H}}(\mathbf{r})$ represents the Hartree potential as obtained by the functional derivative of the Hartree energy, which is given by

$$V_{\text{H}}(\mathbf{r}) = \frac{\delta E_{\text{H}}[n]}{\delta n(\mathbf{r})} = \int \frac{n(\mathbf{r}')}{|\mathbf{r} - \mathbf{r}'|} d\mathbf{r}' = \sum_i \langle \phi_i | \frac{1}{|\mathbf{r} - \mathbf{r}'|} | \phi_i \rangle. \quad (2.14)$$

Analogously, $V_{\text{xc}}(\mathbf{r})$ denotes the xc potential derived from the xc functional

$$V_{\text{xc}}(\mathbf{r}) = \frac{\delta E_{\text{xc}}[n]}{\delta n(\mathbf{r})}. \quad (2.15)$$

The sum over the three potentials in Eq. (2.13) can then be considered as an effective potential $V_{\text{eff}}(\mathbf{r})$. In this perspective, the KS equations can be interpreted as single-particle Schrödinger equations combined with a mean-field approach. More specifically, the energy of each individual electron is determined by the effective potential induced by the other electrons. It is also noteworthy that the quantities ε_i are Lagrangian multipliers adopted within the variational procedure. Therefore, they have, in principle, no physical meaning. Nevertheless, ε_i are generally interpreted as single-particle energy levels. This way of proceeding can be justified within the more general quasiparticle picture, which will be discussed later.

Local density approximation

As mentioned earlier, the exact xc functional is not known. Therefore it is necessary to find approximate xc functionals in order to solve the KS equations. Within the last fifty years a large variety of such functionals have been developed differing in complexity and predictive power [77]. One of the first approximations for the xc functional was the local density approximation (LDA). Indeed, this approach was already proposed by Kohn and Sham in 1965 [4]. Its main simplification is to locally refer the xc energy of the considered (inhomogeneous) electronic

Chapter 2. Theoretical background

system to the one obtained for the homogeneous electron gas (HEG) with the same density $n(\mathbf{r})$. This can be expressed as

$$E_{xc}^{LDA}[n] = \int n(\mathbf{r}) \epsilon_{xc}^{HEG}(n(\mathbf{r})) d\mathbf{r}, \quad (2.16)$$

where ϵ_{xc}^{HEG} is the xc energy density of the HEG. To obtain analytical expressions for ϵ_{xc}^{HEG} , one decomposes exchange (ϵ_x) and correlation (ϵ_c) contributions as $\epsilon_{xc}^{HEG} = \epsilon_x^{HEG} + \epsilon_c^{HEG}$. Both parts are then considered separately. First, the exchange energy density of the HEG can be written as [78]

$$\epsilon_x^{HEG}(n) = -\frac{3}{4\pi} (3\pi^2 n)^{1/3} = -\frac{3}{4\pi} \left(\frac{9\pi}{4}\right)^{1/3} \frac{1}{r_s}, \quad (2.17)$$

where r_s denotes the Wigner-Seitz radius. This quantity describes a typical length scale within the HEG and is defined as the radius of the sphere occupied on average by each electron [72]:

$$\frac{4\pi}{3} r_s^3 = \frac{1}{n}. \quad (2.18)$$

Second, the correlation energy density of the HEG is considered. In contrast to the exchange energy density, ϵ_c^{HEG} is analytically known only in the extreme limits of high and low electron densities [78]. Nevertheless, one can deduce rather complicated expressions which encompass both limits [79, 80, 81]. Such parametrizations quantify $\epsilon_c^{HEG}(r_s)$ based on numerical parameters which are (i) extracted from the analytical high-density expressions and (ii) obtained by fitting to the quantum Monte-Carlo calculations of Ceperley and Alder [82]. One prominent example is the parametrization reported by Perdew and Zunger [80] which reads as

$$\epsilon_c^{HEG}(r_s) = \begin{cases} -0.0480 - 0.0116 r_s + 0.0311 \ln(r_s) + 0.002 r_s \ln(r_s) & \text{for } r_s < 1 \\ -0.1423 / (1 + 1.0529 \sqrt{r_s} + 0.3334 r_s) & \text{for } r_s \geq 1 \end{cases}. \quad (2.19)$$

In conclusion, $\epsilon_{xc}^{HEG}(n)$ and thus $E_{xc}^{LDA}[n]$ can be computed. It is noteworthy that LDA can be rigorously generalized for spin-polarized systems, resulting in the local spin density approximation (LSDA) [78]. For the collinear case, the xc functional can then be expressed as

$$E_{xc}^{LSDA}[n_\uparrow, n_\downarrow] = \int n(\mathbf{r}) \epsilon_{xc}^{HEG}(n_\uparrow(\mathbf{r}), n_\downarrow(\mathbf{r})) d\mathbf{r}, \quad (2.20)$$

where n_\uparrow and n_\downarrow denote the electron densities in both spin polarizations and $n = n_\uparrow + n_\downarrow$ holds. The presented parametrizations for $\epsilon_{xc}^{HEG}(n)$ are also thereby generalized to a spin-polarized formulation as given for instance in Ref. [78].

Generalized gradient approximation

Although, the LDA is only exact for the HEG, it performs surprisingly well for systems with slowly varying densities. In particular, structural properties such as bond lengths are typically underestimated by only 1 – 2 % with respect to experimental references. Despite this success,

great scientific effort has been devoted to overcome the conceptual limitations of the LDA.

A natural extension of the local density approximation is the incorporation of higher derivatives such as the gradient of the electron density ∇n . Thus, the resulting density functionals represent not only local but semilocal approximations. However, first approaches including ∇n yield less accurate results than those obtained with the LDA [78]. Indeed, these so-called gradient expansion approximations (GEA) suffered from various unphysical assumptions which are further described in Ref. [78]. The GEA was succeeded by the generalized gradient approximation (GGA) which overcame these obstacles and represents a milestone in the development of DFT. Analogous to the LDA, the xc functional of the GGA can be generally expressed as [77]

$$E_{xc}^{GGA}[n] = \int n(\mathbf{r}) \epsilon_{xc}^{GGA}(n(\mathbf{r}), \nabla n(\mathbf{r})) d\mathbf{r}. \quad (2.21)$$

It is noteworthy that a substantial amount of physical intuition and craftsmanship is required for the construction of the function $\epsilon_{xc}^{GGA}(n, \nabla n)$ [77]. Therefore it is not surprising, that numerous different expressions have been proposed over the last decades [77]. The most widely used GGA functional is the Perdew-Burke-Ernzerhof (PBE) functional [5] which is also adopted for all semilocal DFT calculations in this thesis. A detailed description of the construction of the PBE functional is given in Refs. [5, 78].

It is of interest, that the incorporation of higher order derivatives has not remained restricted to the gradient of the density $\nabla n(\mathbf{r})$. Indeed, so called meta-GGA functionals consider also the Laplacian of the density $\nabla^2 n(\mathbf{r})$ as well as the kinetic energy density $\tau(\mathbf{r})$, which is further explained in Ref. [77]. However, such functionals are not the scope of this thesis and are therefore mentioned here for completeness. In this work, we focus on another class of approximate density functionals, namely hybrid functionals, which will be introduced in Sec. 2.3.

Practical aspects of DFT calculations

For practical DFT calculations, different numerical techniques are instrumental in order to ensure an efficient computation. First, the KS equations have to be solved for all electrons. Insofar as these equations are non-linear and coupled with each other, one generally addresses this task by resorting to self-consistent computational schemes. More specifically, based on an initial guess for the electron density, the effective potential is computed and is subsequently adopted to solve the KS equations. The orbitals obtained in this way, are used to calculate a new charge density which is feed backed until self-consistent description is reached.

For such calculations, it is advantageous to incorporate more information about the considered physical system. In particular, the periodicity of the crystal (which frequently occurs in this thesis) can be accounted for within the computational setup. This stems from the fact that a periodic potential can be expressed as $V(\mathbf{r}) = V(\mathbf{r} + \mathbf{R})$, where \mathbf{R} denotes a crystal lattice

Chapter 2. Theoretical background

vector. Thanks to Bloch's theorem [74], one can then write the KS wave functions as

$$\phi_{n,\mathbf{k}}(\mathbf{r}) = e^{i\mathbf{k}\mathbf{r}} u_{n,\mathbf{k}}(\mathbf{r}), \quad (2.22)$$

where \mathbf{k} is a wave vector within the first Brillouin zone and n is a band index. The Bloch functions $u_{n,\mathbf{k}}(\mathbf{r})$ indicate the same periodicity as the crystal and can be expanded in a plane-wave basis set. Thus, the KS wave functions can then be expressed as [83]

$$\phi_{n,\mathbf{k}}(\mathbf{r}) = \frac{1}{\sqrt{\Omega}} \sum_{\mathbf{G}} c_{n,\mathbf{k}}(\mathbf{G}) e^{i(\mathbf{k}+\mathbf{G})\mathbf{r}}, \quad (2.23)$$

where Ω denotes the volume of the unit cell, \mathbf{G} represents a reciprocal lattice vector and $c_{n,\mathbf{k}}$ are the expansion coefficients. To ensure that the calculations are numerically feasible, the present expansion is restricted to a finite number of plane waves. In practice, this can be achieved by means of a cutoff energy E_{cut} .

Beside the plane-wave basis, the reciprocal lattice plays an important role in DFT calculations for periodic systems. In particular, an integration over the first Brillouin zone is required for the evaluation of many physical quantities such as the electron density, density of states, etc. Numerically, this is achieved by replacing the integral with a sum over a finite grid. An efficient integration scheme has been proposed by Monkhorst and Pack [84]. It provides a uniform \mathbf{k} -point sampling adjusted to the primitive vectors of the reciprocal lattice [74] and is used throughout this thesis.

Another very useful numerical method to reduce the computational cost of DFT calculations is the use of pseudopotentials. This technique is motivated by the fact that the description of core-electron wave functions is numerically expensive due to strong oscillations in the vicinity of the nucleus. Moreover, such deep electrons are insignificant for the chemical bonds, which are mainly determined by the valence electrons. Therefore, it is appropriate to separate the core from the valence electrons. The former are treated in an effective manner together with the nucleus, whereas the latter are computed explicitly. Proceeding in this way leads to a significant reduction of the computational cost which speeds up the DFT calculations and enables the treatment of larger systems. In this thesis, we generally use either the normconserving Troullier-Martins pseudopotentials [85] (taken from Ref. [86]) or the recently developed optimized norm-conserving Vanderbilt pseudopotentials (ONCVPSP) [87] (taken from Ref. [88]).

The presented numerical techniques are typically implemented in sophisticated electronic-structure codes. In this thesis, we used the software packages ABINIT [22] and Quantum ESPRESSO [89]. We generally adopted a consistent computational setup to ensure a meaningful comparison between the results of the two codes.

2.3 Hybrid functionals

The density functional theory in the local and semilocal approximations, which we have presented in the preceding section, is one of the most widely used approaches to tackle the many-electron problem. However, the prediction of band gaps as obtained with DFT calculations remained highly unsatisfactory [6]. To overcome this drawback, considerable effort has been devoted to the development of more sophisticated electronic-structure methods. Hybrid functionals are a promising representative of such advanced techniques. These functionals have in common that they admix a certain fraction of nonlocal Fock exchange together with a complementary fraction of semilocal exchange. For the purposes of this thesis, the PBE0 [31] and the CAM [70] functional are of great importance. Therefore, these hybrid functionals are briefly introduced in the following section.

PBE0(α) and CAM($\alpha_s, \alpha_\ell, \mu$)

First, we consider the PBE0, or more specifically PBE0(α), functional which can be written as

$$E_{xc}^{\text{PBE0}(\alpha)} = \alpha E_x^{\text{Fock}} + (1 - \alpha) E_x^{\text{PBE}} + E_c^{\text{PBE}}. \quad (2.24)$$

Here, α denotes the fraction of incorporated Fock exchange. In the original work of Perdew, Burke, and Ernzerhof, this parameter was empirically set to $\alpha = 0.25$ in order to provide accurate atomization energies of typical molecules [31]. However, this empirical definition can be generalized to a generic fraction α between 0 and 1. For the specific case of $\alpha = 0$, the PBE0 functional reverts back to the semilocal PBE functional. It is noteworthy that the correlation energy is independent of the mixing parameter α and generally obtained at the PBE level of theory.

Second, we describe the CAM($\alpha_s, \alpha_\ell, \mu$) functional which is derived from the PBE0(α) functional following the Coulomb-attenuating method (CAM) of Yanai *et al.* [70]. This range-separated hybrid functional offers a substantial amount of flexibility through the appearance of three parameters. The range-separation parameter μ determines the partitioning of the Coulomb potential through an error function

$$\frac{1}{|\mathbf{r} - \mathbf{r}'|} = \frac{\text{erfc}(\mu|\mathbf{r} - \mathbf{r}'|)}{|\mathbf{r} - \mathbf{r}'|} + \frac{\text{erf}(\mu|\mathbf{r} - \mathbf{r}'|)}{|\mathbf{r} - \mathbf{r}'|}. \quad (2.25)$$

First and second term of the right-hand side of Eq. (2.25), define the short-range (SR) and the long-range (LR) part of the exchange respectively. For both limits of the range separation, the exchange is then determined through admixing a certain fraction of nonlocal Fock exchange to the semilocal PBE exchange. In the short range this fraction amounts to α_s whereas in the long range a value of α_ℓ is considered. In analogy to Eq. (2.24), one can express this xc

functional as [56]

$$E_{xc}^{\text{CAM}(\alpha_s, \alpha_\ell, \mu)} = \alpha_s E_x^{\text{Fock,SR}}(\mu) + (1 - \alpha_s) E_x^{\text{PBE,SR}}(\mu) + \alpha_\ell E_x^{\text{Fock,LR}}(\mu) + (1 - \alpha_\ell) E_x^{\text{PBE,LR}}(\mu) + E_c^{\text{PBE}} \quad (2.26)$$

Once again, the correlation energy contribution is taken entirely from the PBE functional. A schematic visualization of the range-separated $\text{CAM}(\alpha_s, \alpha_\ell, \mu)$ functional is given in Fig. 2.1 together with the global $\text{PBE0}(\alpha)$ functional.

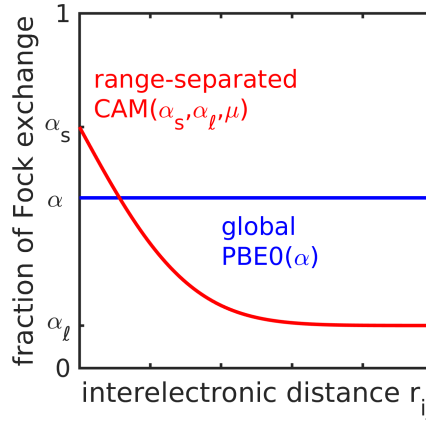


Figure 2.1 – Schematic illustration of the fraction of Fock exchange vs. the interelectronic distance r_{ij} for the hybrid functionals $\text{PBE0}(\alpha)$ and $\text{CAM}(\alpha_s, \alpha_\ell, \mu)$.

It is noteworthy that in the original work of Yanai *et al.*, the three parameters have been set empirically to $\alpha_s = 0.18$, $\alpha_\ell = 0.65$ and $\mu = 0.33 \text{ bohr}^{-1}$ [70]. However, the expression given in Eq. (2.26) provides a substantially larger amount of flexibility. Therefore, various commonly used functionals can be derived from the CAM functional form. Indeed, for $\mu \rightarrow 0$, the $\text{CAM}(\alpha_s, \alpha_\ell, \mu)$ functional reverts back to $\text{PBE0}(\alpha_s)$. Also for $\mu \rightarrow \infty$, the PBE0 functional is obtained, but with a mixing parameter $\alpha = \alpha_\ell$. If $\alpha_s = \alpha_\ell = 0$, the PBE functional is recovered. For $\alpha_s = 0$ and specific definitions for α_ℓ and μ , various long-range corrected hybrid functionals can be obtained [90, 91, 92, 93, 94]. Furthermore, the prominent Heyd-Scuseria-Ernzerhof (HSE) functional [32, 33] is recovered through $\alpha_s = 0.25$, $\alpha_\ell = 0$ and $\mu = 0.11 \text{ bohr}^{-1}$. Overall, the range-separated $\text{CAM}(\alpha_s, \alpha_\ell, \mu)$ functional represents a natural generalization of various commonly used hybrid functionals.

Fock exchange

Technically, it shall be mentioned that irrespective of the hybrid-functional form, Fock exchange is not computed through a HF calculation. Indeed, the Fock exchange is defined as

$$E_x^{\text{Fock}} = -\frac{1}{2} \sum_{i,j} \iint \frac{\phi_i^*(\mathbf{r}) \phi_j^*(\mathbf{r}') \phi_j(\mathbf{r}') \phi_i(\mathbf{r})}{|\mathbf{r} - \mathbf{r}'|} d\mathbf{r} d\mathbf{r}' \quad (2.27)$$

2.4. Many-body perturbation theory in the *GW* approximation

and is self-consistently evaluated with the KS orbitals ϕ_i . The corresponding Fock exchange potential can then be expressed as

$$V_x^{\text{Fock}}(\mathbf{r}, \mathbf{r}') = - \sum_i \frac{\phi_i^*(\mathbf{r}') \phi_i(\mathbf{r})}{|\mathbf{r} - \mathbf{r}'|}. \quad (2.28)$$

This potential (and thus the xc potential V_{xc}) are nonlocal within hybrid-functional formulations. As shown by Seidl *et al.* [26], these nonlocal potentials can be rigorously embedded within a generalized KS theory. The corresponding generalized Kohn-Sham (gKS) equations can then be written as

$$\left[-\frac{\nabla^2}{2} + V_{\text{ext}}(\mathbf{r}) + V_H(\mathbf{r}) \right] \phi_i(\mathbf{r}) + \int V_{xc}(\mathbf{r}, \mathbf{r}') \phi_i(\mathbf{r}') d\mathbf{r}' = \varepsilon_i \phi_i(\mathbf{r}). \quad (2.29)$$

It is apparent that the gKS equations incorporate the standard KS equations in the special case of a (semi)local xc potential.

Practical aspects of hybrid-functional calculations

For practical calculations based on hybrid functionals, it is necessary to evaluate the Fock exchange. Within a plane-wave basis [cf. Eq. (2.23)], one can express the corresponding matrix elements as [83]

$$\langle \mathbf{k} + \mathbf{G} | V_x | \mathbf{k} + \mathbf{G}' \rangle = -\frac{4\pi}{\Omega} \sum_n \sum_{\mathbf{q}} \sum_{\mathbf{G}''} \frac{c_{n,\mathbf{q}}^*(\mathbf{G}' + \mathbf{G}'') c_{n,\mathbf{q}}(\mathbf{G} + \mathbf{G}'')}{|\mathbf{k} - \mathbf{q} - \mathbf{G}''|^2}. \quad (2.30)$$

The evaluation of this expression is a very time-consuming step in hybrid-functional calculations. Moreover, Eq. (2.30) contains a singularity for $\mathbf{k} - \mathbf{q} = \mathbf{G}''$ [83]. Gygi and Baldereschi proved that this integrable divergence can be circumvented by means of an auxiliary function [83]. We adopt this approach for all hybrid-functional calculations presented in this thesis. Further information and insightful explanations on the Coulomb singularity can be found in Ref. [37].

2.4 Many-body perturbation theory in the *GW* approximation

Green's function formalism

A highly sophisticated method to overcome the infamous band-gap problem of semilocal DFT consists in many-body perturbation theory (MBPT). In contrast to DFT, this approach is not centered on the electron density n but on the one-particle Green's function G . As explained in Ref. [10], G is conceptually superior to n . While from both quantities one can obtain the ground-state energy and the expectation values for any one-particle operator in the ground-state, only the Green's function provides the single-particle excitation spectrum of the system [10]. Nonetheless, G still represents an approximation to the full many-body wave function.

Chapter 2. Theoretical background

Within a second quantization formalism, the one-particle Green's function G can be written as [10]

$$G(\mathbf{r}t, \mathbf{r}'t') = -i\langle N | \hat{T}[\hat{\Psi}(\mathbf{r}t)\hat{\Psi}^\dagger(\mathbf{r}'t')] | N \rangle = \begin{cases} -i\langle N | \hat{\Psi}(\mathbf{r}t)\hat{\Psi}^\dagger(\mathbf{r}'t') | N \rangle & \text{for } t > t' \\ i\langle N | \hat{\Psi}^\dagger(\mathbf{r}'t')\hat{\Psi}(\mathbf{r}t) | N \rangle & \text{for } t < t' \end{cases}, \quad (2.31)$$

where $|N\rangle$ is the exact N -particle ground-state wave function, i is the imaginary unit, $\hat{\Psi}^\dagger$ and $\hat{\Psi}$ are the electron creation and annihilation field operators and \hat{T} is the time-ordering operator [9]. The Green's function is also called propagator due to the physical interpretation of Eq. (2.31). Indeed, for $t > t'$, G describes the probability amplitude for the propagation of an electron from \mathbf{r}' at time t' to \mathbf{r} at time t . Instead, for $t < t'$, G describes analogously the propagation of a hole [10].

The physical meaning of G also becomes clear when Eq. (2.31) is recast through inserting the closure relation in between the two field operators [95]. Taking the Fourier transformation in time, one finds the so called Lehmann representation of G which reads as [10]

$$G(\mathbf{r}, \mathbf{r}', \omega) = \sum_i \frac{\psi_i(\mathbf{r}, \omega) \psi_i^*(\mathbf{r}', \omega)}{\omega - E_i(\omega)}. \quad (2.32)$$

Here, ψ_i are the so-called Lehmann amplitudes which are defined as given in Ref. [95]. More relevant is the fact that the excitation energies $E_i(\omega)$ of the electronic systems represent the poles of the Green's function G . Therefore, G incorporates the exact ionization energies, electron affinities and thus the band gap of the investigated system. More than that, one can make a direct comparison between the poles of the Green's function and the peaks obtained in photoemission and inverse photoemission experiments [95].

Due to these fascinating properties of the Green's function, great scientific effort has been devoted to the evaluation of G in the many-body context [95]. However, this goal represents a challenging theoretical task. Indeed, by adopting the Heisenberg equation for the field operators, one can derive an equation which defines the one-particle Green's function G . Unfortunately, this specific equation also involves the two-particle Green's function $G^{(2)}$ [10]. Adopting the same procedure for $G^{(2)}$, one finds an equation which depends on the three-particle Green's function $G^{(3)}$, and so on. Overall, one can derive an infinite hierarchy of equations defining the one-particle Green's function G . This structure describes the physical phenomenon, that the propagation of one electron/hole (G) causes an electron-hole pair ($G^{(2)}$) that further polarizes the medium ($G^{(3)}, \dots$).

In order to break this hierarchy, one can formally introduce an effective operator, called the self-energy Σ [95]. This new operator is supposed to incorporate all the many-body effects associated to the many-particle Green's functions. Therefore, Σ is generally a nonlocal, dynamical and non-Hermitian operator [95]. With this sophisticated object, one can derive

the famous Dyson equation for the one-particle Green's function [95]

$$G(\mathbf{r}, \mathbf{r}', \omega) = G_0(\mathbf{r}, \mathbf{r}', \omega) + \int G_0(\mathbf{r}, \mathbf{r}_1, \omega) \Sigma(\mathbf{r}_1, \mathbf{r}_2, \omega) G(\mathbf{r}_2, \mathbf{r}', \omega) d\mathbf{r}_1 d\mathbf{r}_2. \quad (2.33)$$

In a shorthand notation, Eq. (2.33) can be also expressed as $G = G_0 + G_0 \Sigma G$. The first term refers to the Hartree Green's function G_0 , which corresponds to the specific case of a vanishing self-energy ($\Sigma = 0$) [10, 95].

Quasiparticles

The Lehmann representation already hints at the more general interpretation of the one-particle Green's function G . This picture is called quasiparticle approximation and is described in more detail in Refs. [10, 96]. One of the most relevant results of quasiparticle approximation is the reformulation of the Dyson equation (2.33) to the so called quasiparticle equation [10]

$$\left[-\frac{\nabla^2}{2} + V_{\text{ext}}(\mathbf{r}) + V_{\text{H}}(\mathbf{r}) \right] \psi_i(\mathbf{r}, \omega) + \int \Sigma(\mathbf{r}, \mathbf{r}', \omega) \psi_i(\mathbf{r}', \omega) d\mathbf{r}' = E_i(\omega) \psi_i(\mathbf{r}, \omega). \quad (2.34)$$

It is noteworthy that the quasiparticle energies E_i are generally complex. The real part describes the energy of an excitation, whereas the imaginary part can be interpreted as the inverse of the lifetime [10]. Furthermore, the quasiparticle wave functions ψ_i are in general not orthogonal since Σ is non-Hermitian. These properties are in contrast to the non-interacting system for which Σ is Hermitian, and thus the wave functions are orthogonal and the eigenstates have infinite lifetime. The similarities between the quasiparticle equation (2.34) and the KS [cf. Eq. (2.13)] or the gKS [cf. Eq. (2.29)] equations are apparent. Therefore, one can interpret the xc potential V_{xc} (local or nonlocal) as a static and Hermitian approximation to the *GW* self-energy Σ . In addition, the single-particle orbitals ϕ_i can be seen as approximations to the quasiparticle wave functions ψ_i .

Thanks to the Dyson equation and its insightful reformulation, it is possible to compute the one-particle Green's function, provided that the self-energy can be approximated appropriately. However, this constraint has proven to be challenging, in particular, when considering periodic systems [96, 95]. This drawback can be circumvented through considering a modified Coulomb interaction as shown by Hedin in 1965 [9].

Screened Coulomb interaction

Periodic systems such as solids generally invoke numerous interacting electrons. For the modelling of such systems, it is physically more meaningful to consider a screened Coulomb interaction W instead of the bare repulsion $v(\mathbf{r}, \mathbf{r}') = 1/|\mathbf{r} - \mathbf{r}'|$. The attribute 'screened' refers to the fact, that the interaction between two electrons is always shielded by other electrons. This screening effect is typically described by means of a dielectric function ϵ . One can connect the

Chapter 2. Theoretical background

three quantities via [95]

$$W(\mathbf{r}, \mathbf{r}', \omega) = \int \varepsilon^{-1}(\mathbf{r}, \mathbf{r}_1, \omega) v(\mathbf{r}_1, \mathbf{r}') d\mathbf{r}_1 = \int \frac{\varepsilon^{-1}(\mathbf{r}, \mathbf{r}_1, \omega)}{|\mathbf{r}_1 - \mathbf{r}'|} d\mathbf{r}_1, \quad (2.35)$$

or in a more compact notation $W = \varepsilon^{-1} v$.

It is noteworthy that the nonlocal and dynamical $\varepsilon(\mathbf{r}, \mathbf{r}', \omega)$ in Eq. (2.35) should be interpreted as a microscopic dielectric function. It is, in principle, not a measurable quantity, in contrast to the macroscopic dielectric function ε_M [95]. The connection between microscopic and macroscopic scale is given by [97]

$$\varepsilon_M(\mathbf{q}, \omega) = \frac{1}{\varepsilon_{00}^{-1}(\mathbf{q}, \omega)}, \quad (2.36)$$

where $\varepsilon_{\mathbf{G}\mathbf{G}'}^{-1}(\mathbf{q}, \omega)$ is the Fourier transformation of the inverse microscopic dielectric function. Note that the full matrix has to be inverted before taking the reciprocal of the $\mathbf{G} = \mathbf{G}' = 0$ component. The thereby obtained ε_M is a measurable quantity which can be compared to experimental data from, e.g., electron loss spectroscopy (EELS) or inelastic X-ray scattering (IXS) [95].

Hedin's equations and the *GW* approximation

The Green's function G , the self-energy Σ and the screened interaction W are important quantities to describe the excitation characteristics of a many-electron system. In order to find suitable approximations for their practical calculation, Hedin proposed a system of five equations in 1965 [9]. The major step forward in Hedin's work was the incorporation of the screened Coulomb interaction W instead of the bare interaction v . In a graphical illustration (and employing shorthand notation), one can summarize Hedin's equations as shown in Fig. 2.2.

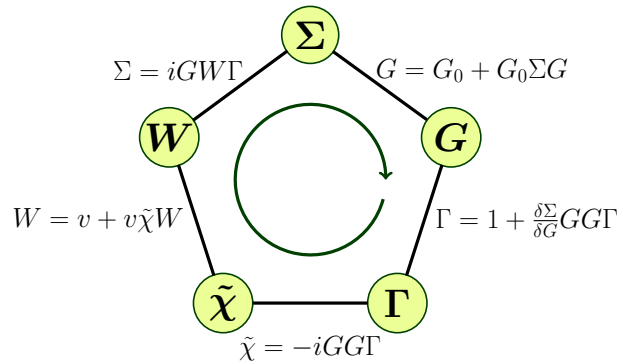


Figure 2.2 – Hedin's equations illustrated in an pentagonal form.

In addition to the previously introduced quantities, the irreducible polarizability $\tilde{\chi}$ and the vertex function Γ also appear in Hedin's equations. The former describes the response of the

2.4. Many-body perturbation theory in the *GW* approximation

system to an additional electron/hole and the latter contains the information how electrons and holes interact [96]. Overall, Hedin's equations represent five coupled integral equations for five quantities, which have to be solved self-consistently. Starting with a given expression for Σ , the above set of equations provides a way to generate higher order approximations [10]. However, this procedure is not feasible for practical calculations and it is also challenging due to functional derivative in the equation of the vertex function Γ . Therefore, further simplifications are required.

The so called *GW* approximation has already been proposed by Hedin in his pioneering work in 1965 [9]. Through retaining only the zero-order term in the vertex function ($\Gamma = 1$), he obtained a simplified set of equations [95]. In analogy to Fig. 2.2, this is shown in Fig. 2.3.

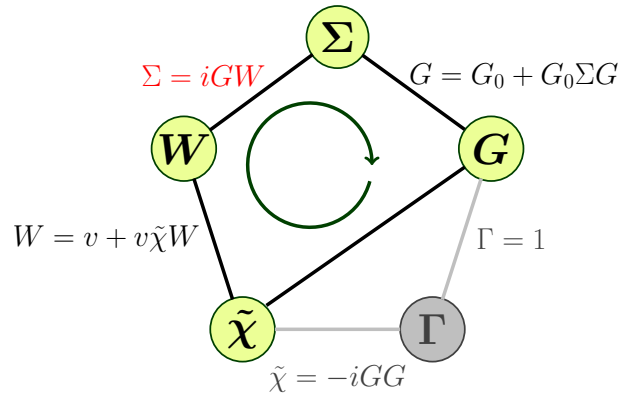


Figure 2.3 – Illustration of Hedin's equations employing the *GW* approximation.

It is noteworthy that the self-energy becomes the product of G and W (in the time domain), which explains the name *GW* approximation. In the frequency domain, Σ becomes a convolution which can be expressed as [10]

$$\Sigma(\mathbf{r}, \mathbf{r}', \omega) = \frac{i}{2\pi} \int G(\mathbf{r}, \mathbf{r}', \omega + \omega') W(\mathbf{r}, \mathbf{r}', \omega') d\omega'. \quad (2.37)$$

Furthermore, the irreducible polarizability $\tilde{\chi}$ becomes a simple product of Green's functions which is known as the random-phase approximation (RPA) [95]. Due to the connection $\varepsilon = 1 - v\tilde{\chi}$, equivalent RPA expressions can be derived for the irreducible polarizability $\tilde{\chi}$ and for the dielectric function ε . In case these representations are written in terms of single-particle energies and orbitals, one obtains the well-known expressions proposed by Adler [97] and Wiser [98].

Overall, the *GW* approximation represents a notable simplification of Hedin's equations. However, the practical implementation of these equations is not trivial. Therefore, it is not surprising that various different flavours of *GW* calculations have been developed over the last decades.

G_0W_0 calculations

Technically, GW calculations are often carried out subsequently to preliminary DFT or HF calculations [12, 99]. The rationale behind this procedure is the assumption that single-particle orbitals ϕ_i and eigenvalues ε_i provide already a good description of the investigated electronic system. One can then reconstruct the independent-particle Green's function G_0 and thus compute the polarizability ($\tilde{\chi}_0$), the screened interaction (W_0) and self-energy (G_0W_0) according to Hedin's equations. This is called the one-shot GW (G_0W_0) approach since the self-consistent loop shown in Fig. 2.3 is truncated after the first iteration.

By considering the quasiparticle equation (2.34) within the G_0W_0 framework, one can calculate the quasiparticle energies E_i as first-order perturbative correction to the single-particle energies ε_i . This reads as [95]

$$E_i = \varepsilon_i + \langle \phi_i | \Sigma(E_i) - V_{xc} | \phi_i \rangle. \quad (2.38)$$

The implicit occurrence of E_i in Eq. (2.38), is generally overcome through a linearization of Σ . This yields [95]

$$E_i = \varepsilon_i + Z_i \langle \phi_i | \Sigma(\varepsilon_i) - V_{xc} | \phi_i \rangle, \quad (2.39)$$

with a renormalization factor

$$Z_i = \left[1 - \langle \phi_i | \frac{\partial \Sigma(\omega)}{\partial \omega} \bigg|_{\omega=\varepsilon_i} | \phi_i \rangle \right]^{-1}. \quad (2.40)$$

In most G_0W_0 calculations, the perturbative corrections are obtained through Eq. (2.39). This approach yields generally improved band gaps [37, 100] with respect to the underestimated results from semilocal DFT [6]. However, G_0W_0 remains unsatisfactory since it is highly dependent on the adopted starting point [37]. Indeed, G_0W_0 results, as obtained from semilocal DFT, hybrid functional or HF calculations as starting points, indicate notable differences. In the case where initial wave functions are insufficient, the G_0W_0 corrections might fail entirely [101, 102].

Self-consistent GW calculations

To overcome the dependence on a specific starting point, different self-consistent GW schemes have been developed in the last decades. Intuitively, the self-consistent solution of Hedin's equations in the GW approximation is the natural solution to the starting-point problem. This approach is called fully self-consistent GW (sc GW) and has been shown to suffer from critical limitations. First, the computational cost of this scheme is very high. Indeed, since the self-energy is non-Hermitian, one should distinguish left and right eigenvectors, which do not form a orthogonal basis, and are associated with complex eigenvalues [95]. Therefore, practical sc GW calculations are subject to stringent computational limitations. The second and even more severe drawback of sc GW is of conceptual nature. As further explained in

2.4. Many-body perturbation theory in the *GW* approximation

Refs. [103, 95], *scGW* incorporates an unbalanced renormalization factor in the irreducible polarizability. As a consequence, the screening becomes unreasonable and subsequently computed quantities deteriorate [104, 105].

To overcome the limitations of *scGW*, Schilfgarde, Kotani and Faleev proposed an alternative method which is called quasiparticle self-consistent *GW* (QSGW) [103, 15, 16]. This approach is based on an Hermitian ansatz for the *GW* self-energy. More specifically, the matrix elements of the self-energy in the QSGW approximation are expressed as

$$\langle \phi_i | \Sigma^{\text{QSGW}} | \phi_j \rangle = \frac{1}{2} \text{Re} [\langle \phi_i | \Sigma(\epsilon_i) | \phi_j \rangle + \langle \phi_j | \Sigma(\epsilon_j) | \phi_i \rangle], \quad (2.41)$$

where Re denotes the Hermitian part. The diagonalization of Σ^{QSGW} yields a new set of orthogonal orbitals ϕ_i , which is then used to construct a new Σ^{QSGW} [37]. This procedure is carried out until a self-consistent description is reached. Interestingly, the specific ansatz in Eq. (2.41) can also be justified as a way to find an optimal one-body Hamiltonian [15, 95]. Due to the Hermitian self-energy, QSGW is computationally more efficient than *scGW* (but still notably more demanding than G_0W_0). Furthermore, it has been shown that QSGW yields improved band gaps compared to those obtained with semilocal functionals or G_0W_0 calculations [15].

It is noteworthy that alternative self-consistent *GW* schemes have also been developed, such as eigenvalue-only self-consistent *GW* [106] or self-consistent versions of the Coulomb-hole plus screened exchange (COHSEX) method [107, 108]. However, for the purpose of this thesis it is sufficient to focus on the QSGW approach which is one of the most widely used methods for self-consistent *GW* calculations.

Vertex corrections

Despite the great success of QSGW in overcoming the starting-point problem, also this approach has been shown to have limitations. In particular, it has been observed that QSGW systematically overestimates the band gap by $\sim 20\%$ [103, 15, 18]. The origin of this observation is the lack of electron-hole interaction in the polarizability when calculated within the RPA [17, 18]. This obstacle can be circumvented through the incorporation of so-called vertex corrections. The polarizability χ is then expressed through a Dyson equation

$$\chi = \chi^0 + \chi^0(\nu + f_{\text{xc}})\chi, \quad (2.42)$$

where χ^0 is the independent-particle polarizability as calculated with the one-particle wave functions and energies [18]. The exchange-correlation kernel f_{xc} is the functional derivative of the exchange-correlation potential with respect to the density, and accounts for the many-body interactions [18]. For the specific case of a vanishing f_{xc} , the RPA polarizability is recovered.

Chapter 2. Theoretical background

Various expressions for f_{xc} have been proposed over the last few years [96]. Throughout this thesis, we adopt the bootstrap kernel of Sharma *et al.* [109] in the efficient implementation of Chen *et al.* [18]. This kernel makes use of the exact relation between f_{xc} and ϵ^{-1} [109], and iterates the RPA screening and the f_{xc} kernel until the convergence is reached [18]. In reciprocal space, the bootstrap kernel f_{xc}^{boot} can be expressed as [18]

$$f_{xc,GG'}^{\text{boot}}(\mathbf{q}, \omega) = \frac{\nu_{\mathbf{G}}^{1/2}(\mathbf{q}) \epsilon_{GG'}^{-1}(\mathbf{q}, 0) \nu_{\mathbf{G}'}^{1/2}(\mathbf{q})}{1 - \epsilon_{00}^{\text{RPA}}(\mathbf{q}, 0)}, \quad (2.43)$$

where ϵ^{RPA} is the RPA dielectric function. The expression given in Eq. (2.43) requires no empirical parameters and it ensures the correct scaling behaviour as further discussed in Ref. [18]. A comprehensive overview of various other xc kernels can be found in Ref. [110].

The screened interaction including vertex corrections is then denoted as \tilde{W} and the corresponding self-consistent GW scheme is named $QSG\tilde{W}$. The accuracy of this method has been verified for numerous materials including common semiconductors and insulators [17, 18, 111], transition-metal compounds [18, 112, 113], alkali halides [51], metal-halide perovskites [114, 115], as well as liquid water [116]. $QSG\tilde{W}$ is therefore acknowledged as one of the most reliable GW approaches for band-gap predictions. Throughout this thesis, we therefore consider the results obtained with $QSG\tilde{W}$ as a benchmark for other electronic-structure methods.

Practical aspects of GW calculations

A critical aspect of many GW calculations is the variety of incorporated parameters which affect the final result. It is therefore of major importance to carefully converge all parameters which are required for the investigated quantity. The GW calculations performed in this thesis are mainly focused on the band-edge levels and thus on the band gap. To obtain converged results for these quantities, the cutoff in the dielectric matrix $E_{\text{cut}}^{\text{eps}}$ and the total number of bands n_{band} are highly relevant. Depending on the considered supercell size, the band gap as a function of these parameters can indicate a very slow convergence. In order to retain computationally feasible calculations, it is good practice to separately extrapolate the band gap with respect to $E_{\text{cut}}^{\text{eps}}$ and/or n_{band} . In terms of $E_{\text{cut}}^{\text{eps}}$, an extrapolation with an exponential function is adequate. In terms of n_{band} , generally an extrapolation with a hyperbolic function

$$f(n_{\text{band}}) = \frac{a}{n_{\text{band}} - \tilde{n}_{\text{band}}} + b, \quad (2.44)$$

is performed, where a , b , and \tilde{n}_{band} are fitting parameters [117]. Overall, the sum of these extrapolations typically amounts to $\sim 0.1\text{--}0.2$ eV which is then added as an posteriori correction to the computed band gaps.

Another important aspect of GW calculations is the treatment of the frequency dependence of key quantities such as self-energy, screened exchange, and dielectric function. In this thesis, we adopt a full frequency approach as given by the contour deformation technique

[118]. This method has been shown to yield more adequate results for states far away from the Fermi level [119] than those obtained with standard plasmon-pole models [12, 119]. The contour deformation technique incorporates results from complex analysis in order to efficiently compute the convolution of the self-energy. More specifically, the cumbersome integration over the real frequency axis is replaced by an integration along the imaginary axis plus contributions arising from the poles lying inside the contour [118]. Further information on the technicalities of this method can be found in Refs. [118, 16, 22]. For the materials investigated in this thesis, it was generally sufficient to account for 8 real and 4 imaginary frequencies. Only for Si and CaF_2 in chapter 7, we adopted very conservative values of 10 real and 10 imaginary frequencies.

2.5 Other computational methods in this thesis

In this section, computational methods are presented which are of great importance for this thesis. More specifically, finite-size corrections for charged defects and different techniques for the computation of the dielectric constant are presented. We remark that these methods are applicable irrespective of the considered density functional approach (semilocal or hybrid). Therefore, we generally refer to DFT calculations within the following section.

Finite-size corrections for charged defects

For the purposes of this thesis, the investigation of point defects is of great importance. We aim at describing such defects in an isolated manner. However, due to the periodic-boundary conditions adopted in the electronic-structure calculations, the simulations are performed in practice for an infinite array of point defects. This way of proceeding is justified as long as sufficiently large supercells are considered. In particular, for charged defects, this constraint cannot be fulfilled due to the long-ranged Coulomb potential which inevitably leads to spurious defect-defect interactions. The resulting divergence of the electrostatic energy is treated in the self-consistent DFT procedure through a neutralizing charge background. However, the total energy and thus the single-particle defect levels still suffer from the spurious interactions with image charges.

To overcome these finite-size effects, various correction schemes have been developed within the last decades [120, 121, 122, 123, 19, 124]. In particular, the scheme proposed by Freysoldt, Neugebauer and van de Walle (FNV) [122] has achieved accurate results irrespective of the considered defect [125]. The central idea of this scheme is the (formally exact) partition of the defect potential into a long-range and a short-range contribution [20]. The former can be approximated by the potential of a localized model charge repeated in an infinite array. The latter is then given through a simple potential shift obtained from the difference between the actual and the model potential. In the specific case of a point-charge model for a defect within

a cubic supercell, the FNV correction can be expressed in a simple form as [20]

$$E_{\text{corr}}^{\text{FNV}} = \frac{\alpha q^2}{2\epsilon L} - q\Delta V. \quad (2.45)$$

The physical quantities included are the Madelung constant α , the total defect charge q , the dielectric constant ϵ , and the supercell size L . The first term of Eq. (2.45) represents the well-known Madelung energy for an array of point charges within a compensating background and immersed in a dielectric medium. The second term is given by the potential alignment ΔV . The practical computation of ΔV is illustrated in Fig. 2.4 for a hydrogen interstitial H_i^+ in MgO. It is noteworthy that the obtained finite-size corrections are independent of the adopted model charge [122]. Further information about the FNV scheme can be found in Refs. [125, 20].

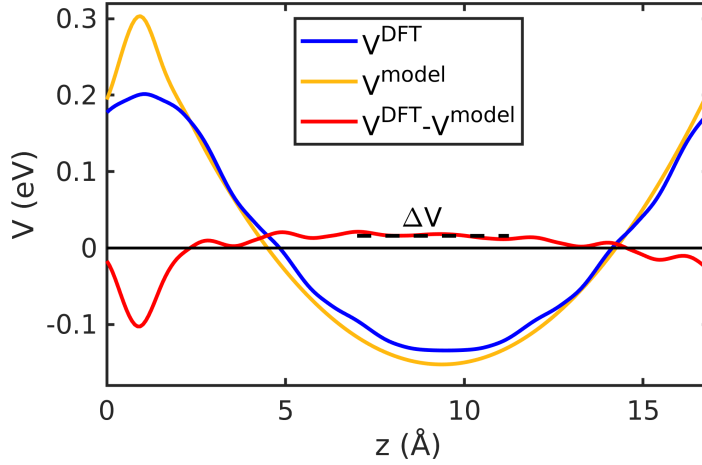


Figure 2.4 – Planar averaged electrostatic potential for a hydrogen interstitial H_i^+ in MgO. The defect is located at $z = 0.9 \text{ Å}$ with periodic images according to the supercell size $L = 16.9 \text{ Å}$. The potential as obtained through a DFT calculation V^{DFT} and the potential associated to a point-charge model V^{model} are shown. The difference between the two potentials far away from the defect site determines the potential alignment ΔV (in this case $\sim 0.02 \text{ eV}$).

We note, that the present FNV scheme provides accurate corrections to the total energy of a considered defective supercell. For the purposes of this thesis, we are however interested in single-particle defect levels. To this end, one can deduce a KS level correction $E_{\text{corr}}^{\text{KS}}$ from the total-energy correction $E_{\text{corr}}^{\text{FNV}}$ via [19, 124]

$$E_{\text{corr}}^{\text{KS}} = -\frac{2}{q} E_{\text{corr}}^{\text{FNV}}. \quad (2.46)$$

The accuracy of these KS level corrections have been demonstrated for various defects in semiconducting and insulating materials [19, 20, 124]. Therefore, we apply this correction scheme throughout this thesis to all DFT calculations of charged defects. We remark that Eq. (2.46) is only valid for defects which do not involve ionic polarizations as described in more detail in Ref. [124].

Computation of the high-frequency dielectric constant

The high-frequency dielectric constant ϵ_∞ of an investigated material is of major importance for the purposes of this thesis. For the calculation of this quantity, three different approaches have been instrumental, namely the application of a sawtooth potential [126, 127], the finite-electric field approach [128], and the linear response theory [97, 98]. The specific choice in favour of one of these techniques has been made conveniently according to the investigated materials and the electronic-structure methods compared. Furthermore, the three different approaches yield generally dielectric constants in close agreement with each other thereby ensuring the consistency of the conclusion drawn in the following sections. Here, a brief introduction to the three techniques is given.

The first approach consists in the application of an external sawtooth-like potential V^{saw} to an elongated cell of the considered material [126, 127]. In response to this potential, the average electrostatic potential V^{DFT} , as obtained through a DFT calculation, indicates also a sawtooth-like shape, but screened by the dielectric constant ϵ_∞ [129]. This fact is visualized in Fig. 2.5 for the case of MgO.

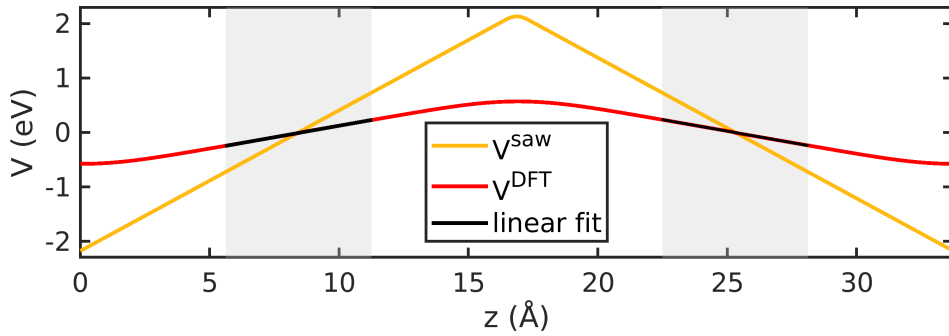


Figure 2.5 – Planar-averaged electrostatic potential V^{DFT} across a $1 \times 1 \times 8$ supercell of MgO in the presence of a sawtooth potential V^{saw} . For simplicity, the displayed potential V^{DFT} has been broadened with a Gaussian of width 2.5 Å in the z direction. The shaded areas correspond to the regions far away from the extrema of the sawtooth potential. The linear fit to the potential in both regions is indicated in black.

The dielectric constant ϵ_∞ is then determined by the ratio of the slopes of sawtooth and electrostatic potential. This can be expressed as [129]

$$\epsilon_\infty = \frac{\partial V^{\text{saw}} / \partial z}{\partial V^{\text{DFT}} / \partial z}. \quad (2.47)$$

It is good practice to deduce the slopes in the region far away from the extrema of the sawtooth potential. Moreover, the total height of the potential must be smaller than the band gap of the considered material to avoid a dielectric breakdown [129]. Further technical details of this technique are summarized in Ref. [129]. The computation of the dielectric constant through the sawtooth procedure is straightforward and yields generally very robust results. Indeed, residual deviations associated to different cell sizes, different amplitudes, and rising/falling

part of the potential amount to only 1–2% [129]. The drawback of this method is the high computational burden due to the treatment of an elongated supercell. The dielectric constant ϵ_∞ as calculated with a sawtooth potential is shown in Fig. 2.6 for the case of MgO. We observe a good agreement with the experimental counterpart irrespective of the employed approximate density functional.

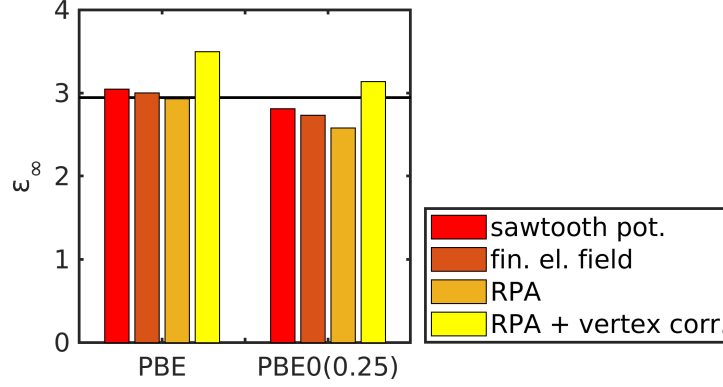


Figure 2.6 – High-frequency dielectric constant ϵ_∞ as calculated with a sawtooth potential, a finite electric field, and the RPA with and without vertex corrections. Calculations performed with the semilocal functional PBE and the hybrid functional PBE0(0.25) are distinguished. The value of ϵ_∞ as obtained in experiment [130] is indicated through a black line.

The second technique for the determination of the dielectric constant considered in this thesis consists in a finite-electric field approach [131]. This method relies on the fact, that differences in the electric polarization P can be defined also for periodic systems, independent of the surface termination [132]. Indeed, based on the modern theory of polarization [133, 134], P can be related to a Berry phase computed from the valence wave functions [132]. Therefore, one can model the presence of a finite electric field \mathcal{E} through a variational energy functional $E^\mathcal{E} = E^0 - \mathcal{E} \cdot P$ [132, 131, 135]. Here, E^0 denotes the usual energy functional in the absence of the electric field and P is the polarization along the direction of \mathcal{E} . The functional $E^\mathcal{E}$ can be minimized for finite values of the electric field. Based the present theory, one can then express the high-frequency dielectric constant through [131, 128]

$$\epsilon_\infty = 1 + \frac{4\pi}{\Omega} \frac{P^\mathcal{E} - P^0}{\mathcal{E}}, \quad (2.48)$$

where Ω is the volume of the unit cell and $P^\mathcal{E}$ and P^0 are the polarizations with and without electric field, respectively. It is noteworthy that also for this technique, a critical electric field shall not be overcome in order to avoid numerical instabilities [131]. The calculation of ϵ_∞ using Eq. (2.48) yields results in good agreement with those of the sawtooth potential as shown in Fig. 2.6. Moreover, the sawtooth potential and the finite electric field yield in principle the same results provided all numerical parameters are carefully converged. This is due to the fact that in both methods the electronic structure in the presence of an electric field (or potential) is computed explicitly. Apart from the considered approximate density functional, both methods do not rely on any further approximation for the determination of the dielectric constant.

From a computational point of view, the finite electric field method is more appropriate than the sawtooth potential insofar as the calculations can be performed with the primitive unit cells.

The third approach considered in this thesis, namely linear response theory, has already been discussed in the context of *GW* calculations and shall therefore not be repeated here. In particular, the random-phase approximation (RPA) has been introduced for the computation of the dielectric constant. We remark that this method incorporates a further approximation in addition to the adopted density functional. Therefore, the computed values of ϵ_∞ are not necessarily equal to the ones obtained with the sawtooth potential and the finite electric field. However, in practice it turned out that the differences between the various methods amount to only a few percent as shown in Fig. 2.6 for case of MgO.

It is noteworthy that the RPA does not incorporate electron-hole interactions, which is generally overcome through the use of vertex corrections. We show the effect of such corrections in Fig. 2.6 for the bootstrap xc kernel [109, 18]. The somewhat overestimated results in Fig. 2.6 can be attributed to the fact that the xc kernel should correspond to the functional derivative of the xc potential with respect to the density. Therefore, we should in principle use vertex corrections obtained with a xc kernel associated to the PBE and the PBE0(0.25) functional. However, for the purposes of this demonstration the application of the bootstrap kernel shall be sufficient.

Overall, we adopted three different approaches to compute the high-frequency dielectric constant ϵ_∞ . The different methods yield generally results in good agreement with each other and with experimental references.

3 Construction schemes for nonempirical hybrid functionals

This chapter is devoted to the detailed description of nonempirical hybrid functionals. First, we consider dielectric-dependent hybrid (DDH) functionals. We motivate the development of these functionals through describing the relationship between the dielectric constant and the amount of incorporated Fock exchange. Then, we provide an overview of existing DDH functionals in the literature. The construction scheme for DDH functionals adopted in this thesis is given subsequently. In the second part of this chapter, we turn to hybrid functionals satisfying Koopmans' condition. We introduce this exact physical constraint and describe its connection to equivalent theorems. Then, we summarize existing hybrid functionals satisfying Koopmans' condition in the literature and conclude this chapter with the construction scheme used in this thesis.

Parts of this chapter have been published in peer-reviewed articles [54, 115] or have been submitted to Physical Review Research.

3.1 Dielectric-dependent hybrid (DDH) functionals

3.1.1 Motivation of DDH functionals

An important step towards nonempirical hybrid functionals has been the identification of the connection between the dielectric constant and the amount of Fock exchange in the global PBE0(α) functional. This was first described by Alkauskas *et al.* [36] and shortly afterwards by Marques *et al.* [41]. In the former study, it has been shown that the optimal fraction of Fock exchange α_{opt} (which reproduces the experimental band gap) and the inverse high-frequency dielectric constant $1/\epsilon_{\infty}$ are closely related to each other [36]:

$$\alpha_{\text{opt}} \approx 1/\epsilon_{\infty}. \quad (3.1)$$

Interestingly, this dependence has also been implied in the early works of Bylander and Kleinman [25], and Shimazaki and Asai [38, 39, 40].

A graphical illustration of the connection expressed in Eq. (3.1) is given in Fig. 3.1. Note, that we show here α_{opt} as deduced from the slightly larger data set of Marques *et al.* [41]. Nevertheless, the results of Alkauskas *et al.* [36] are almost identical thereby confirming the conclusion drawn in their work. The adopted set of materials amounts to 21 compounds comprising semiconductors (Si, Ge, GaAs, etc.), insulators (MgO, SiO₂, etc.), alkali halides (LiF, LiCl, etc.), 2D materials (BN, MoS₂), as well as noble-gas crystals (Ne, Ar, etc.).

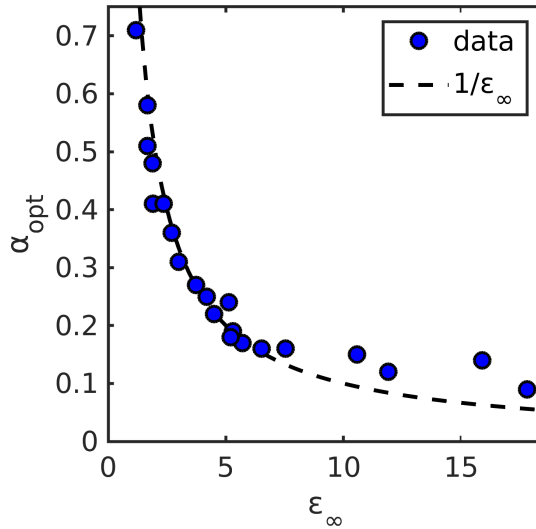


Figure 3.1 – Optimal mixing parameter α_{opt} within the PBE0(α) functional vs. the high-frequency dielectric constant ϵ_{∞} for various materials. The curve associated to $\alpha_{\text{opt}} = 1/\epsilon_{\infty}$ is shown as a dashed line. The data for α_{opt} have been deduced from Table I in Ref. [41]. The experimental data for ϵ_{∞} have been taken from Ref. [47] and the references therein.

In Fig. 3.1, a clear correlation between α_{opt} and $1/\epsilon_{\infty}$ is apparent. The residual scattering can be attributed to various simplifications such as neglecting the frequency dependence

and the anisotropy of the dielectric function [36]. Also materials including d electrons have been identified as typical outliers [36]. Nevertheless, the manifest correlation shown in Fig. 3.1 remains unaffected by these minor deviations.

The empirical connection between α_{opt} and $1/\epsilon_\infty$ can be also explained adopting physical arguments. Semiconductors with a narrow band gap indicate typically a strong dielectric screening. In contrast, wide band-gap insulators show only a weak dielectric screening. Whereas this observation is already qualitatively reproduced at the PBE level, the hybrid functional PBE0($1/\epsilon_\infty$) yields also a quantitatively correct description. Indeed, for semiconductors $1/\epsilon_\infty$ becomes small and thus the band-gap estimate $E_g^{\text{PBE0}(1/\epsilon_\infty)}$. Analogously for insulators, $1/\epsilon_\infty$ assumes much larger values and therefore the band gap $E_g^{\text{PBE0}(1/\epsilon_\infty)}$ increases.

One can also provide some theoretical support for Eq. (3.1) by considering the COHSEX approximation to the GW self energy. This static approximation is composed of two parts: the Coulomb hole (COH) and the screened exchange (SEX) contribution [10]. One can write the COHSEX self-energy as the sum of the following terms:

$$\Sigma^{\text{COH}}(\mathbf{r}, \mathbf{r}') = -\frac{1}{2} \delta(\mathbf{r}, \mathbf{r}') [\nu(\mathbf{r}, \mathbf{r}') - W(\mathbf{r}, \mathbf{r}', 0)], \quad (3.2)$$

$$\Sigma^{\text{SEX}}(\mathbf{r}, \mathbf{r}') = -\sum_i \phi_i(\mathbf{r}) \phi_i^*(\mathbf{r}') W(\mathbf{r}, \mathbf{r}', 0) \quad (3.3)$$

Here, ϕ_i are the single-particle wave functions and ν and W are the bare and the screened Coulomb interaction, respectively. Assuming that the dielectric function acts as a constant scaling of the electron-electron interaction, one finds $W(\mathbf{r}, \mathbf{r}', 0) \approx \nu(\mathbf{r}, \mathbf{r}')/\epsilon_\infty$ and thus [7]

$$\Sigma^{\text{SEX}}(\mathbf{r}, \mathbf{r}') \approx -\frac{1}{\epsilon_\infty} \sum_i \phi_i(\mathbf{r}) \phi_i^*(\mathbf{r}') \nu(\mathbf{r}, \mathbf{r}') = \frac{1}{\epsilon_\infty} V_x^{\text{Fock}}(\mathbf{r}, \mathbf{r}'), \quad (3.4)$$

where in the last step, Eq. (2.28) is used. It becomes apparent, that a hybrid functional including a fraction of Fock exchange $\alpha = 1/\epsilon_\infty$ yields the same asymptotic behaviour as Σ^{SEX} given in Eq. (3.4). This conclusion is valid since the fraction of semilocal exchange is only short ranged and Σ^{COH} can be sufficiently well approximated through the correlation term within the hybrid functional [99].

Interestingly, a somewhat similar reasoning can be found in the works of Kronik and collaborators [71, 56]. In Ref. [56], these authors discuss that within exact KS theory, the KS potential for a finite neutral system decays as $-1/r$ for large distances r from the center of the system [56]. This exact property is denoted as the asymptotically correct potential for finite systems [64, 56]. For the extension of this property to infinite systems, it is then argued, that the exact KS potential decays as $-1/(\epsilon_\infty r)$ [71, 56]. Under the justified assumption that the asymptotically correct potential is the same for exact KS and gKS theory, one can transfer this result to the hybrid-functional framework. The resulting fraction of Fock exchange is then the well known $\alpha = 1/\epsilon_\infty$ [71]. For a more extensive discussion on the exact properties in KS and gKS theory, we refer here to Ref. [56].

Overall, the connection between the amount of Fock exchange and the high-frequency dielectric constant is well supported through statistical, physical, and theoretical arguments. The practical incorporation of this concept into nonempirical hybrid-functional schemes will be discussed in the following.

3.1.2 Overview of DDH functionals

Based on the fundamental idea of dielectric-dependent hybrid (DDH) functionals, various construction schemes have been proposed in the last years. These approaches have in common, that the inverse dielectric constant is an integral part of the adopted procedure. However, the technical details of the schemes exhibit notable differences.

Only a few works, such as the study of Conesa [58], utilized the experimental dielectric constant $\epsilon_{\infty}^{\text{Expt}}$ and then determined the mixing parameter as $\alpha = 1/\epsilon_{\infty}^{\text{Expt}}$. However, this way of proceeding relies on experimental data and is therefore comparable to adopting the empirical α_{opt} . It is apparent that also the dielectric constant has to be calculated from first principles in order to construct nonempirical hybrid functionals. This constraint raises the question: Which electronic-structure method shall be employed for this task? For instance, Marques *et al.* computed the dielectric constant at the PBE level of theory [41]. The resulting PBE0($1/\epsilon_{\infty}^{\text{PBE}}$) functional was then instrumental to obtain an estimate for the band gap. However, this choice remains kind of arbitrary, even if the computed dielectric constant depends only weakly on the considered functional.

In order to answer this open question, several iterative procedures have been proposed. In these workflows, the dependence of the dielectric constant on the specific electronic-structure method is overcome through a simple feedback loop. Further details on such workflows, are presented in the next section. The application of an iterative scheme to a global hybrid functional has first been performed by Skone *et al.* and denoted as sc-hybrid approach [43]. Similar schemes were also proposed later by Gerosa *et al.* [44] and He *et al.* [136]. The sc-hybrid approach has been applied to a variety of semiconductors, insulators, and transition-metal oxides and has led to notably improved band gaps with respect to semilocal DFT and PBE0(0.25) [43, 44, 136]. However, this method has also some limitations which have been attributed to the underlying global hybrid functional.

As a remedy, range-separated hybrid functionals have been investigated. These functionals offer a substantial amount of flexibility due to the distinct fraction of Fock exchange in the short range (α_s) and in the long range (α_ℓ) mediated through the range-separation parameter (μ). The long-range fraction α_ℓ is generally set to $1/\epsilon_{\infty}$ in order to enforce the correct long-range screening. For the remaining parameters α_s and μ further approximations are required, which have shown to be less straightforward [47]. Interestingly, the range-separated framework

allows us to approximate the static Coulomb interaction as [35]

$$W(\mathbf{r}, \mathbf{r}') \approx \frac{\varepsilon_{\infty}^{-1}}{|\mathbf{r} - \mathbf{r}'|} + \frac{(\alpha_s - \varepsilon_{\infty}^{-1}) \operatorname{erfc}(\mu|\mathbf{r} - \mathbf{r}'|)}{|\mathbf{r} - \mathbf{r}'|}. \quad (3.5)$$

Here, the first term is the same as for a global DDH functional and the second term represents a short-range correction to the Coulomb interaction. In this perspective, one can interpret range-separated DDH functionals as a natural generalization of global DDH functionals.

Among the first range-separated DDH schemes was the RS-DDH method of Skone *et al.* In this approach, the screening parameter μ has been determined through different nonempirical definitions [35]. Instead, the short-range fraction of Fock exchange α_s has been set to 0.25 following the seminal PBE0 paper [31]. It has been argued, that this definition of α_s represents an attenuated short-range exchange which amounts in practice for an approximate form of short-range correlation in the functional [35]. However, this semi-empirical setting of α_s has remained rather unsatisfactory.

To overcome this drawback of RS-DDH, Chen *et al.* proposed the DD-RSH-CAM method [47]. In this approach, the full Fock exchange is considered in the short-range, i.e. $\alpha_s = 1$. This definition has been rationalized by a comparison between the range-separated Coulomb interaction and a model dielectric function [47]. The range-separation parameter μ is then computed by fitting the model to the inverse dielectric function [47]. It is noteworthy that in DD-RSH-CAM the dependence of the hybrid-functional parameters on the dielectric constant has been embedded in more general dependence on the dielectric function. Since the dielectric function can be calculated with *ab-initio* methods, DD-RSH-CAM is in principle free of empirical parameters [47]. We remark, that simultaneously to the work of Chen *et al.* [47], Cui *et al.* proposed the doubly screened hybrid (DSH) approach [57]. This method is essentially the same as DD-RSH-CAM, differing only in some technical aspects and the physical motivation [57]. Consequently, both range-separated DDH schemes yield very similar results as shown in Ref. [137].

3.1.3 Construction scheme adopted in this thesis

In this thesis, we employ some of the DDH schemes described in the previous section. Furthermore, we develop new flavours of DDH functionals in order to overcome drawbacks of the established approaches. Generally, we determine DDH functionals by adopting the self-consistent workflow visualized in Fig. 3.2. The scheme consists in an iterated update of an initial guess for the hybrid-functional parameters. Within each iteration step, the gKS equations [26] are solved and the dielectric constant ε_{∞} of the considered material is calculated (cf. Sec. 2.5). Subsequently, improved values of the parameters are determined using the calculated dielectric properties. This process is performed until a self-consistent description is reached. We note that the parameter update in Fig. 3.2 is specific to the adopted class of hybrid functional. We discuss this separately for the different classes investigated in this thesis.

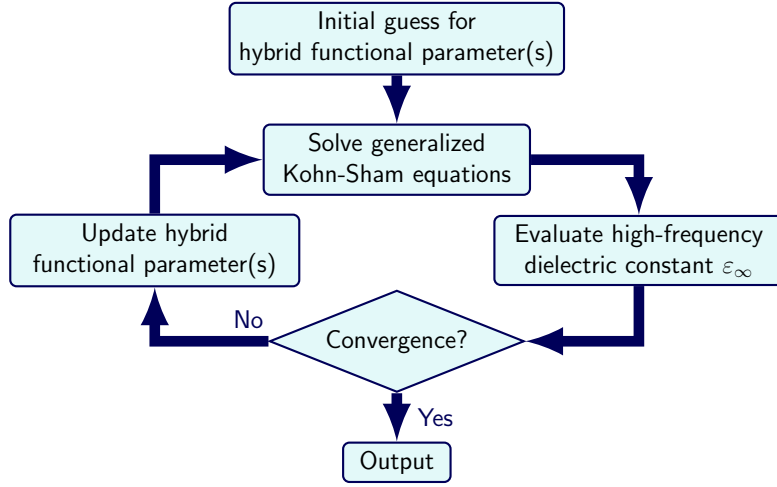


Figure 3.2 – Workflow for the construction of dielectric-dependent hybrid (DDH) functionals. The procedure for updating the free parameters depends on the considered hybrid-functional form and is described in the text.

First, we consider the $\text{PBE0}(\alpha)$ functional which depends on the global fraction of incorporated Fock exchange α [31]. This parameter is updated in the standard fashion through $\alpha = 1/\epsilon_\infty$. The self-consistent procedure in Fig. 3.2 then converges to a dielectric constant $\epsilon_\infty^{\text{sc}}$ and a mixing parameter $\alpha = 1/\epsilon_\infty^{\text{sc}}$. The hybrid functional determined in this way is denoted $\text{PBE0}(1/\epsilon_\infty^{\text{sc}})$.

Second, we examine the $\text{CAM}(\alpha_s, \alpha_\ell, \mu)$ functional which incorporates different fractions of Fock exchange in the short (α_s) and in the long range (α_ℓ), connected via the inverse range-separation length μ [70]. These three parameters are treated differently. The short-range fraction α_s is taken as a constant and is set according to different definitions proposed in the literature. We specifically consider α_s equals to 1 [47], 0.25 [35], or 0 [90, 91, 92, 93, 94]. The long-range fraction of Fock exchange α_ℓ is determined analogously to the global mixing parameter by setting $\alpha_\ell = 1/\epsilon_\infty^{\text{sc}}$. Finally, the inverse range-separation length μ is fixed either through the fitting procedure of Chen *et al.* [47] or through the Thomas-Fermi (TF) screening parameter

$$\mu_{\text{TF}} = \sqrt[6]{\frac{3n_v}{\pi}}, \quad (3.6)$$

where n_v is the valence-electron density [35].

Overall, we investigate five distinct DDH functionals in this thesis which are denoted as $\text{PBE0}(1/\epsilon_\infty^{\text{sc}})$, DD-RSH-CAM, $\text{CAM}(1, 1/\epsilon_\infty^{\text{sc}}, \mu_{\text{TF}})$, $\text{CAM}(0.25, 1/\epsilon_\infty^{\text{sc}}, \mu_{\text{TF}})$, and $\text{CAM}(0, 1/\epsilon_\infty^{\text{sc}}, \mu_{\text{TF}})$. A comparison of these functionals is given in Table 3.1.

3.2. Hybrid functionals satisfying Koopmans' condition

Table 3.1 – Comparison of the DDH functionals examined in this thesis. The comparison is made in terms of the fraction of short-range Fock exchange α_s , the fraction of long-range Fock exchange α_ℓ , and the range-separation parameter μ .

	α_s	α_ℓ	μ
PBE0($1/\epsilon_\infty^{\text{sc}}$)	$1/\epsilon_\infty^{\text{sc}}$	$1/\epsilon_\infty^{\text{sc}}$	-
DD-RSH-CAM [47]	1	$1/\epsilon_\infty^{\text{sc}}$	μ_{fit}
CAM($1, 1/\epsilon_\infty^{\text{sc}}, \mu_{\text{TF}}$)	1	$1/\epsilon_\infty^{\text{sc}}$	μ_{TF}
CAM($0.25, 1/\epsilon_\infty^{\text{sc}}, \mu_{\text{TF}}$)	0.25	$1/\epsilon_\infty^{\text{sc}}$	μ_{TF}
CAM($0, 1/\epsilon_\infty^{\text{sc}}, \mu_{\text{TF}}$)	0	$1/\epsilon_\infty^{\text{sc}}$	μ_{TF}

3.2 Hybrid functionals satisfying Koopmans' condition

3.2.1 Koopmans' condition and related theorems

The second class of nonempirical hybrid functionals investigated in this thesis, are determined through enforcing Koopmans' condition. This constraint describes a physical property within exact DFT and will be introduced in this section. In addition, we describe several well known theorems which are equivalent but not identical to Koopmans' condition. We note, that beside the nomenclature adopted in this thesis, various different names for these theorems can be found in the literature.

In 1982, Perdew and collaborateurs showed that the HK theorems can be extended to systems with fractional electron numbers [62]. Such systems are not described by a single many-body wave function but through a statistical enesemble of wave function associated to integer electron numbers [62]. Adopting Levy's constrained search formulation [138], one can then proof that within exact DFT the total energy E satisfies

$$E(N + f) = (1 - f)E(N) + fE(N + 1), \quad (3.7)$$

where N is an integer and f is a real number between 0 and 1 [62]. This represents a series of linear functions in between integer values of the electron number. Therefore, Eq. (3.7) is also denoted as piecewise-linearity condition. Interestingly, this constraint was later also derived by Yang *et al.* [34] based on a different interpretation of fractional charges invoking replicas of pure states [56]. A graphical illustration of the piecewise-linearity condition is given in Fig. 3.3.

In practice, it turned out that most of the commonly used electronic-structure methods do not fulfil the piecewise-linearity condition. Indeed, semilocal functionals typically give a convex curve whereas HF yields a concave one [63, 65]. For this violation of the piecewise-linearity condition different terms have been coined in the literature such as deviation-from-the-straight-line-error [139], localization/delocalization error [140] or many-electron self-interaction error [63]. In particular, the latter term has to be distinguished from the one-electron self-interaction

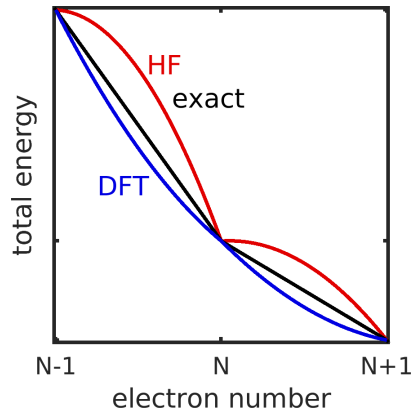


Figure 3.3 – Schematic illustration of the piecewise-linearity condition. The total energy is shown as a function of the electron number of the system. The curves corresponding to exact DFT (exact), a semilocal xc functional (DFT) and Hartree-Fock theory (HF) are indicated.

error [80], which is related to another property of the exact xc functional [56].

The piecewise-linearity condition can be equivalently expressed in terms of the single-particle levels. This can be achieved through Janak's theorem, $\varepsilon_i = \partial E / \partial f_i$, which states that the single-particle energies ε_i are equal to the derivative of the total energy E with respect to the occupation f_i [141]. Employing this theorem, one can deduce that the highest occupied single-particle energy level does not change upon its occupation [142]. This is the so called Koopmans' condition which is illustrated in Fig. 3.4.

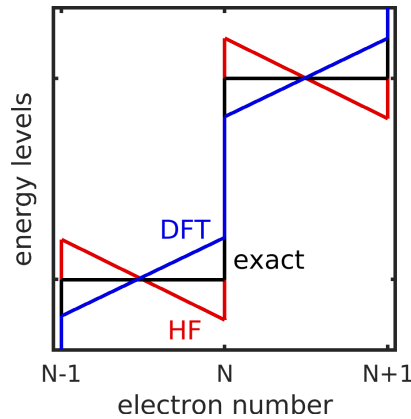


Figure 3.4 – Schematic illustration of Koopmans' condition. The highest occupied single-particle level is shown as a function of the electron number of the system. The curves corresponding to exact DFT (exact), a semilocal xc functional (DFT) and Hartree-Fock theory (HF) are indicated.

In analogy to the observations made for the piecewise-linearity condition, many commonly used electronic-structure methods also violate the Koopmans' condition [65]. Indeed, the spurious convexity (concavity) in the total-energy curve of semilocal DFT (HF) translates into an almost linear increase (decrease) of the highest occupied single-particle level as a

function of the fractional occupation [65]. At integer values of the electron number, finite steps are apparent which are underestimated (overestimated) with respect to exact DFT [65]. It is noteworthy that these finite steps represent discontinuities in the derivative of the total energy. Moreover, these steps are of great importance for the interpretation of the fundamental band gap and have stimulated significant scientific effort [62, 140, 142, 143].

Another equivalent exact property is the so called IP theorem [62, 64]. It states that the highest occupied single-particle level corresponds to the negative ionization potential (IP). It can be proved by simply adopting the piecewise linearity, Janak's theorem and the definition of the IP [56]. The violation of the IP theorem by most of the commonly used electronic-structure methods is a direct consequence of the previous explanations and is therefore not discussed again. We remark that in the early work of Koopmans [144] the same statement as in the IP theorem has been made. However, Koopmans' result is an approximate theorem since it is derived from a frozen-orbital HF theory [56]. In contrast, the IP theorem is a physical constraint derived within exact DFT. In order to preserve a consistent nomenclature, we refer to the study of Koopmans as to the "original Koopmans' condition" to distinguish it from the "Koopmans condition" shown in Fig. 3.4.

3.2.2 Overview of hybrid functionals satisfying Koopmans' condition

As shown in the previous section, Koopmans' condition and its related theorems are violated by most of the commonly used electronic-structure methods. Therefore, great scientific effort has been devoted to incorporate these exact constraints within approximate density functionals. In particular, hybrid functionals exhibit great potential to achieve this goal. Indeed, their incorporated free parameters can be varied systematically in order to enforce a specific constraint or at least to minimize the deviations from it. Moreover, as seen in Figs. 3.3 and 3.4, semilocal density functionals and HF theory typically show an opposite behaviour with respect to exact DFT. Therefore, hybrid functionals, which incorporate a certain fraction of Fock exchange, represent an ideal compromise between both limits and are thus an intuitive starting point for the incorporation of exact constraints. It is noteworthy that the previously discussed properties of exact KS DFT can be rigorously generalized to gKS DFT [56]. Therefore, it is meaningful to enforce these constraints within a hybrid-functional framework.

The enforcement of previously presented exact constraints through hybrid functionals has been first achieved for molecular systems. Indeed, the presence of localized orbitals enables the enforcement of the IP theorem [42, 71] and the piecewise-linearity [65] in a straightforward manner. The application of the same idea to extended systems such as solids is more challenging and will be described later.

Among the first nonempirical hybrid-functional schemes for molecular systems was the optimally tuned range-separated hybrid (OT-RSH) method of Baer, Kronik and coworkers [66, 67, 42]. In this scheme, the exchange energy is decomposed into pure Fock exchange in the long-range and pure semilocal exchange in the short-range. The range-separation parameter

is “optimally tuned” through minimizing the deviation from the IP theorem [66]. Despite the success of OT-RSH for various molecular systems, the application to extended systems proved to be difficult. The origin of these complications lies in the fact that IPs for extended systems are not directly accessible from periodic bulk calculations. Indeed, the computation of IPs requires calculations for an adequate surface model which would result in a rather impractical nonempirical scheme. In the investigation of molecular crystals, this problem has been circumvented by first fixing the optimal parameters through calculations of individual molecules in the gas phase and then adopting the determined parameters for the molecular crystal [71]. However, this procedure is apparently not applicable to inorganic crystals. This limitation is also apparent in the further generalized OT-SRSH approach [71], which requires an empirical parameter adjustment in case inorganic crystals are investigated.

The application of hybrid functionals satisfying Koopmans’ condition to solids has been mostly achieved within the last decade. In particular, the investigation of defects in semiconductors was key to overcome the limitations outlined before. Indeed, defects naturally induce localized states, which can be considered analogously to the localized orbitals in molecular systems. Various authors adopted this basic idea in order to enforce Koopmans’ condition within a hybrid-functional framework [68, 48, 49, 51, 52, 69, 50, 53, 55]. This development was accelerated by the fact that the study of defects through hybrid functionals was already a well established technique, which allowed for a fast adaption of the computational procedure. It is noteworthy that most studies employ these nonempirical hybrid functionals in order to achieve an accurate description of the defect under investigation [68, 49, 55]. In particular, the modelling of polaronic distortions has shown to be sensitively affected by the fulfilment of the piecewise linearity condition [48, 51, 50, 53]. Miceli *et al.* [51] were among the first, to employ hybrid functionals that satisfy Koopmans’ condition as a predictive tool for band-gap calculations. These authors showed that the exact constraint is satisfied across a series of defects, which in turn enables a robust band-gap estimate for the specific host material [51]. Moreover, the hydrogen-interstitial defect has been proposed as a universal probe for achieving accurate band gaps [51]. These promising results guide the way towards a nonempirical hybrid-functional scheme which is generally applicable to semiconducting and insulating materials. Therefore, we adopt the construction procedure of Miceli *et al.* throughout this thesis. A more detailed description of the workflow is given in the next section.

Before closing this section, we briefly summarize closely related computational methods which also rely on Koopmans’ condition. First, it is noteworthy that the incorporation of Koopmans’ condition (and the equivalent theorems) has not been limited to hybrid functionals. Indeed, similar nonempirical approaches have been proposed within the DFT+ U [145, 146, 68] and the hybrid+ U framework [147, 148]. Also one-shot GW corrected hybrid functionals have been considered as a starting point for the enforcement of exact constraints [149, 139, 65]. All these approaches have in common that they incorporate undetermined parameters. In analogy to the case of hybrid functionals, these free parameters are fixed in such a way that the exact constraint is satisfied. A second possible strategy to enforce Koopmans’ condition is the incorporation of additional terms in the Hamiltonian. This way of proceeding can be

interpreted as a generalization of the one-electron self-interaction correction (SIC) scheme [80] to the more general many-electron self-interaction error [63]. The application of this idea to extended systems typically requires the use of maximally-localized Wannier functions. The resulting schemes are therefore denoted as Wannier-Koopmans method [150] or Koopmans' compliant functionals [151, 152]. Such corrections are in principle also applicable to hybrid functionals, but lie outside of the scope of this thesis. In the following, we focus again on hybrid functionals without resorting to SIC schemes anymore.

3.2.3 Construction scheme adopted in this thesis

In this thesis, we construct hybrid functionals that satisfy Koopmans' condition through the procedure outlined in the work of Miceli *et al.* [51]. Here, we illustrate the workflow for the specific case of the global PBE0(α) functional. For range-separated functionals, the procedure can be applied analogously.

First, we consider a supercell of the investigated material in which a point defect D is introduced. The associated single-particle energy level is then computed in the occupied and in the unoccupied charge configuration. For an arbitrary mixing parameter α , both PBE0(α) calculations yield generally different defect levels due to the violation of Koopmans' condition. This is shown schematically in Fig. 3.5. The energy difference between the single-particle level in the two charge configurations is denoted as Δ_K . Since a single-particle level evolves linearly with α , the same holds for Δ_K . Therefore, one can identify a unique value $\alpha = \alpha_K$ for which Δ_K vanishes, i.e. $\Delta_K(\alpha_K) = 0$. In this case, Koopmans' condition is fulfilled as shown in Fig. 3.5. The PBE0(α_K) functional is then instrumental to obtain a band-gap estimate for the host material.

It is worth noting that α_K is independent of the specific occupation of the single-particle level. The crossing point can therefore also be determined through every pair of fractional occupations between 0 and 1. However, it is good practice to use the two extreme cases of occupation in order to minimize numerical errors associated with the determination of the intersection. Furthermore, we remark that we show here D^0 as occupied and D^+ as unoccupied. Of course, the analogous situation of unoccupied D^0 and occupied D^- is equivalent.

Technically, one should bear in mind, that the present construction scheme relies predominantly on defect calculations. We note that upon the creation of the defect we generally calculated the electronic structure fully self-consistently and without allowing for structural relaxations. This is justified insofar we are interested in an accurate band-gap prediction of the host material rather than the correct modelling of the defect structure. Furthermore, this way of proceeding carries the advantage that the long-range screening is described entirely by the high-frequency dielectric constant ϵ_∞ . The spurious interactions with periodically repeated image charges is overcome through accurate finite-size corrections to the single-particle levels [20, 124] as described in Sec. 2.5. It is noteworthy that these corrections incorporate the specific value of ϵ_∞ [cf. Eq. (2.45)]. In order to ensure a consistent application of the finite-size

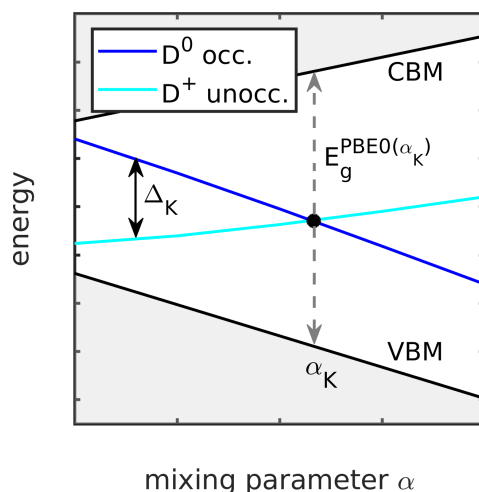


Figure 3.5 – Occupied and unoccupied single-particle energy levels as a function of the mixing parameter α used in the PBE0(α) functional. The energy difference Δ_K between both charge configurations is indicated for an arbitrary value of α . The point of intersection corresponds to the enforcing of Koopmans’ condition. The dashed vertical line indicates the resulting band-gap estimate. The band-edge levels of the host material vs. α are also shown.

corrections, we systematically consider dielectric constants as calculated with the same hybrid functional used in the defect calculations.

The outlined procedure has been applied to various defects and host materials throughout this thesis. In order to visualize our results in a understandable fashion, we simplify the presentation of Fig. 3.5. In particular, we show in the following only the crossing point as obtained for each specific defect. This point contains all the relevant information for the enforcement of Koopmans’ condition.

4 Developments for hybrid functionals satisfying Koopmans' condition

In this chapter, we describe a nonempirical procedure for achieving accurate band gaps of extended systems through the insertion of suitably defined potential probes. By enforcing Koopmans' condition on the resulting localized electronic states, we determine the optimal fraction of Fock exchange to be used in the adopted hybrid functional. As potential probes, we consider point defects, the hydrogen interstitial, and various adjustable potentials that allow us to vary the energy level of the localized state in the band gap. By monitoring the delocalized screening charge, we achieve a measure of the degree of hybridization with the band states, which can be used to improve the band-gap estimate. Application of this methodology to AlP, C, and MgO yields band gaps differing by less than 0.2 eV from experiment.

The results presented in this chapter have been published in Ref. [54]. Further information can be found in the corresponding archive on the Materials Cloud [153].

4.1 Open questions

The determination of nonempirical hybrid functionals through the enforcement of Koopmans' condition has recently drawn great scientific attention [68, 48, 49, 51, 50, 52]. In particular, Koopmans' condition applied to defect states and interstitial hydrogen probes has been successful in accurately describing band gaps [49, 51, 52] and polaronic states [48, 69, 51, 50, 53]. However, open questions concerning the use of defects within this procedure still remain. Indeed, it is unclear to what extent the band-gap estimate depends on the selected defect. This uncertainty is visualized in Fig. 4.1 for the oxygen vacancy V_O and the two different charge transition levels for the hydrogen interstitial H_i in MgO.

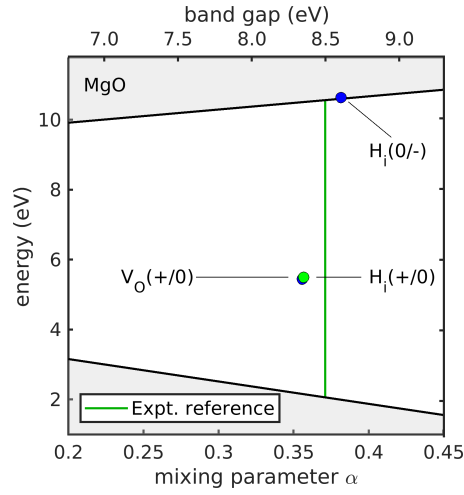


Figure 4.1 – Band edges and defect energies at the points of intersection displayed versus mixing parameter α , as obtained with the $PBE0(\alpha)$ functional for native defects in MgO. The defects comprise the oxygen vacancy V_O and the two different charge transition levels for the hydrogen interstitial H_i . The indicated band gaps correspond to those obtained with the $PBE0(\alpha)$ functional. The vertical green line corresponds to the experimental reference (see text).

We observe that the nonempirical construction procedure (cf. Sec. 3.2.3) applied to the three defects yields mixing parameter in overall agreement with each other. Also the comparison with respect to the empirically adjusted mixing parameter reveals acceptable deviations. However, the corresponding band-gap estimates differ by ~ 0.3 eV. This deviation is not negligible and raises the question of how to assess the reliability of a specific defect for band-gap predictions. Moreover, it might be possible to identify an optimal defect for this task. On the other hand, we should bear in mind that we aim at calculating the band gap of a specific material without performing an extended defect study. These open issues call for further clarification.

4.2 Definition of adjustable potential probes

To overcome these drawbacks, we introduce adjustable potential probes. These are defects that allow us to study the band-gap prediction as the defect level varies within the band gap. More specifically, rather than relying on immutable physical defects, we aim at controlling the energy level of a localized electron state in the band gap. For this purpose, we consider parameter-dependent potentials that correspond to generalizations of the standard Coulomb potential of the hydrogen atom. These flexible potential probes are achieved by suitably modifying the local or the nonlocal part of the hydrogen pseudopotential.

As a first type of potential probe, we take the local potential

$$V_{\text{loc}}(r) = -\frac{1}{r} \operatorname{erf}\left(\frac{r}{\sqrt{2}\sigma}\right), \quad (4.1)$$

which corresponds to the solution of the Poisson equation for a Gaussian charge distribution of width σ . For a vanishing σ , the local potential coincides with the standard Coulomb potential $V_C(r) = -1/r$. The use of a finite width leads to the transformation of the central divergence into a finite global minimum. The asymptotic r^{-1} behavior is ensured irrespective of the value of σ . A graphical visualization of such local potentials is given in Fig. 4.2.

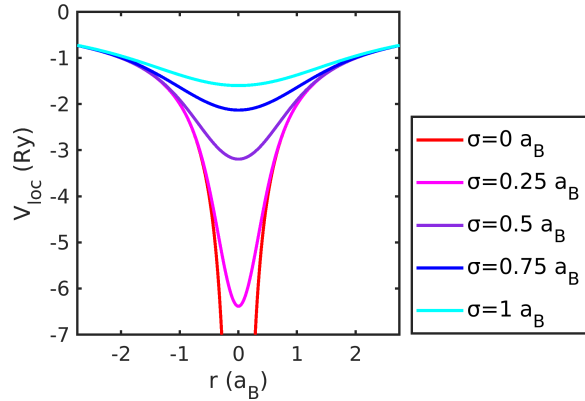


Figure 4.2 – Local potential as a function of the distance to the origin for various width parameter σ .

The energy level associated with the local potential V_{loc} shifts upwards for increasing σ accompanied by an electronic state of larger extent. The parameter dependence is found to be almost linear when the defect level lies close to the middle of the band gap, as shown in Fig. 4.3 for a local potential probe in C. Upon varying σ , it is possible to position the energy level between the neutral hydrogen level and the conduction-band edge of the host material.

The second type of parametrized potentials that we take under consideration in this chapter are nonlocal. We define such potentials as

$$V_{\text{nonloc}} = \tilde{V}_{\text{loc}}(r) + D|\beta\rangle\langle\beta|, \quad (4.2)$$

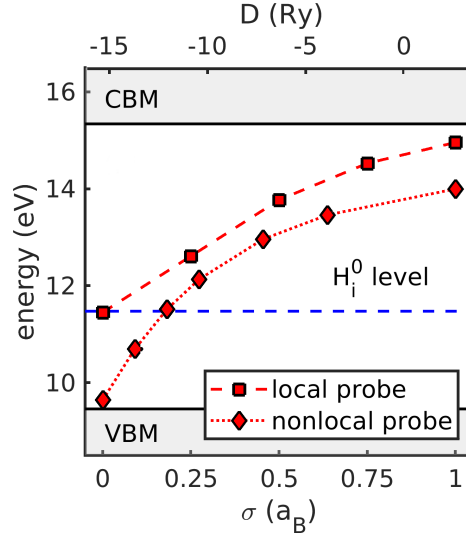


Figure 4.3 – Defect energy eigenvalue of the local and the nonlocal potential probe in C as a function of the internal parameters σ and D , respectively. The energy eigenvalue of the neutral hydrogen interstitial H_i^0 is also indicated. The defect eigenvalues and the band-edge levels are obtained with the functional $PBE0(\alpha_{opt})$, which reproduces the experimental reference for the band gap (see text).

where $\tilde{V}_{loc}(r)$ is a local Coloumb-like potential, D is a controllable parameter, and $|\beta\rangle$ is a projector on a localized orbital of s symmetry. For a specific value of D ($D = -12.5$ Ry), the potential probe V_{nonloc} corresponds to a viable pseudopotential for hydrogen and the eigenvalue describes that of the hydrogen interstitial, as can be seen in Fig. 4.3. The parameter D is then varied to continuously displace the energy level of the nonlocal potential probe either to higher or lower energies compared to the neutral hydrogen level. The energy level is found to shift monotonically with D . The use of these two types of adjustable potential probes allow us to generalize the hydrogen-probe concept of Miceli *et al.* [51] providing an instrument to tune the associated defect level to a desired energy.

4.3 Computational aspects

To examine the performance of the adjustable probes, we consider three materials, namely AlP, C, and MgO. These compounds cover a large range of band gaps and show either covalent or ionic bonding character. The conventional unit cells of the three materials are shown in Fig. 4.4. We adopt experimental lattice constants taken from Ref. [130]. For the electronic-structure calculations, we use energy cutoffs of 50, 80, 100 Ry for AlP, C, and MgO, respectively, by which the total-energy convergence is assured within 1 meV/atom. Converged results for the band gaps are achieved with a $4 \times 4 \times 4$ \mathbf{k} -point sampling. It is noteworthy that the three considered compounds show different kinds of band gaps, namely indirect for AlP and C, and direct for MgO. The different positions of the band-edge levels are visualized in Fig. 4.5 as obtained at the PBE level of theory.

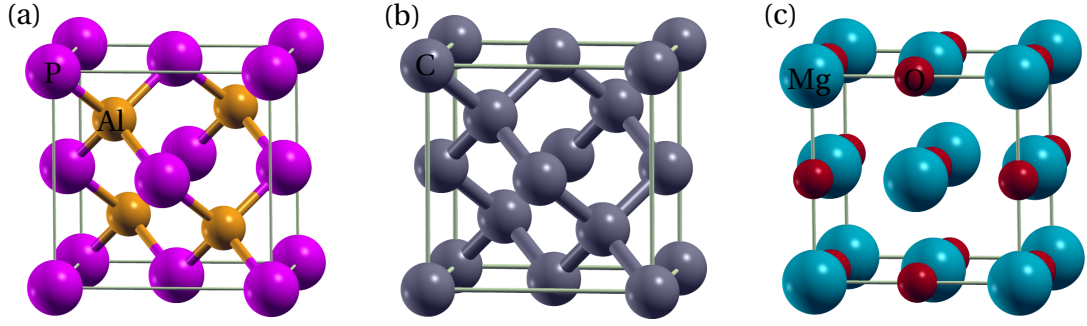


Figure 4.4 – Conventional unit cells of (a) AlP in zincblende structure, (b) C in diamond structure, and (c) MgO in rocksalt structure. Al, P, C, Mg, and O atoms are shown in violet, orange, gray, blue, and red, respectively.

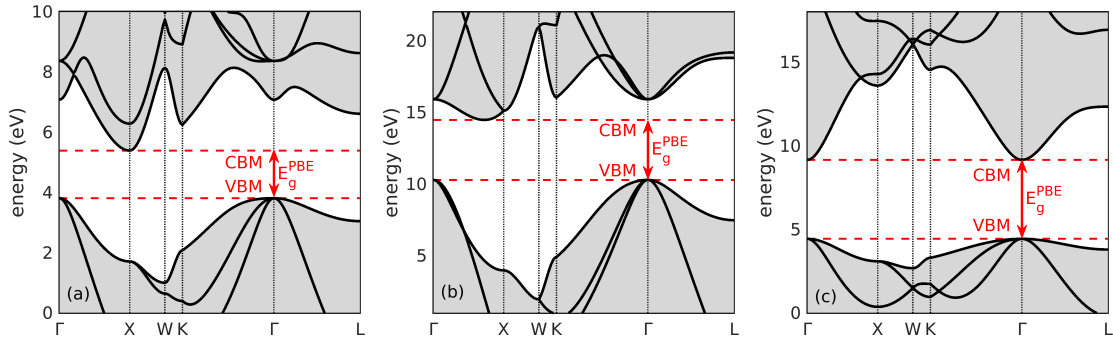


Figure 4.5 – PBE band structure of (a) AlP, (b) C, and (c) MgO. The valence-band maximum (VBM), the conduction-band minimum (CBM), and the corresponding band gap are indicated.

For the construction of hybrid functionals satisfying Koopmans' condition, we consider in this chapter the global PBE0(α) functional. The mixing parameter α is determined through the analysis of point defects modelled within a 64-atom supercell together with a $2 \times 2 \times 2$ Brillouin zone sampling. A graphical visualization of the defective supercells is given in Fig. 4.6 for the case of an adjustable potential probe at an interstitial position. We account for the spurious interactions with image charges arising from the periodic boundary conditions (PBC) through finite-size corrections as described in Sec. 2.5. The dielectric constants are calculated separately through the application of a sawtooth potential to a $1 \times 1 \times 8$ supercell [126, 127].

It is important to set the references for the band gaps against which we benchmark our calculations. For AlP, C, and MgO, we take experimental band gaps E_g^{Expt} of 2.50 [154], 5.48 [154], and 7.97 eV [130], respectively. These values correspond to fundamental electronic gaps. To ensure a proper comparison between theory and experiment, we add to the experimental band gaps renormalizations due to phonons, i.e. 0.02 eV for AlP, 0.37 eV for C, and 0.53 eV for MgO, where the former two estimates are based on experimental data [154] and the latter corresponds to a theoretical value [155] and includes the effect of lattice polarization [156]. Further effects such as spin-orbit coupling are neglected. We estimate that the experimental references obtained in this way are subject to a global uncertainty of 0.1 eV.

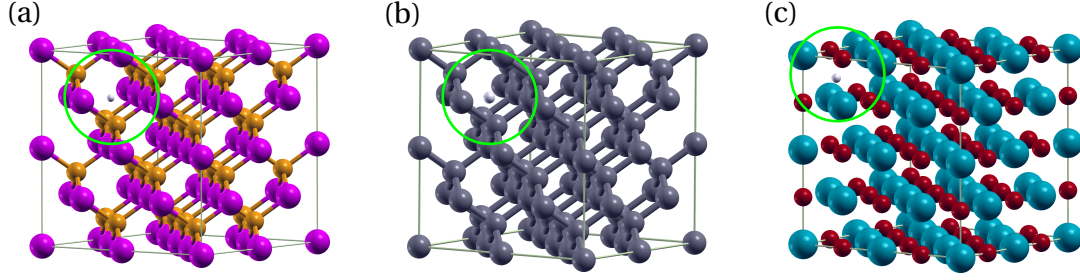


Figure 4.6 – Defective supercell with an adjustable potential probe at an interstitial position in (a) AlP, (b) C, and (c) MgO. The defect sites are highlighted with green circles. Al, P, C, Mg, and O atoms are shown in violet, orange, gray, blue, and red, respectively. The adjustable potential probes are visualized in white.

4.4 Application of adjustable potential probes

For various point defects, the hydrogen interstitial, and the two types of adjustable potential probes, we construct hybrid functionals satisfying Koopmans' condition following the procedure illustrated in Sec. 3.2.3. As defect levels, we consider the $(+/0)$ level for the P_{Al} antisite in AlP, the substitutional N_C in C, and the oxygen vacancy V_O in MgO. For the hydrogen interstitial, which is inserted at the center of the largest void, we take under consideration both the $(+/0)$ and $(0/-)$ charge transitions. As far as both the local and nonlocal potential probes are concerned, we position their centers at the same location as that of the hydrogen interstitial. We focus on the $(+/0)$ transition and use parameters for which the defect levels sample the band gap. The results of our calculations are given in Fig. 4.7.

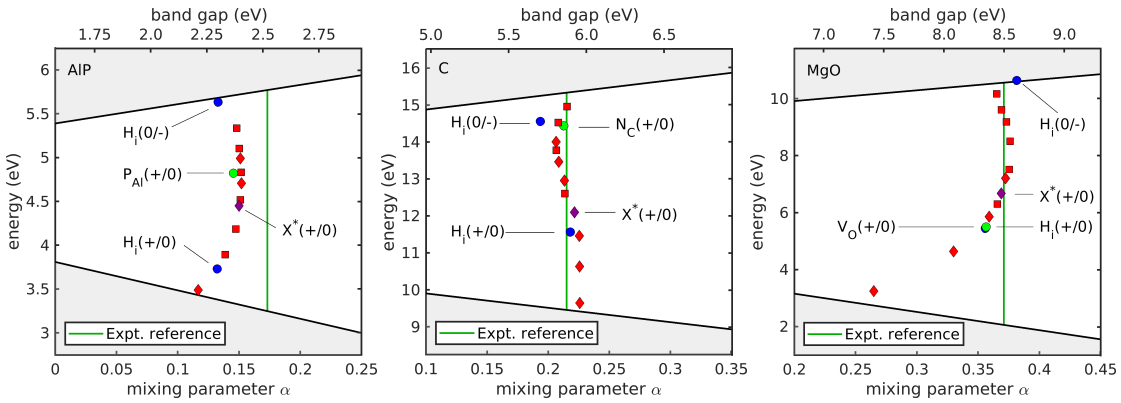


Figure 4.7 – Band edges and defect energies at the points of intersection displayed versus mixing parameter α , as obtained for various defects in AlP, C, and MgO. The results for the parametrized local and nonlocal potentials are indicated by red squares and red diamonds, respectively. Additionally, labeled defects comprise P_{Al} in AlP, N_C in C, and V_O in MgO, together with two different charge transition levels for the hydrogen interstitial H_i . X^* refers to the potential probe with the smallest degree of hybridization δ . The vertical green lines correspond to experimental references (see text).

We observe that the mixing parameters α_K satisfying Koopmans' condition for the various defects and probes fall in a narrow range for each of the three considered materials, supporting the robustness of the proposed scheme. In particular, the derived α_K values achieved with the two types of adjustable potential probes almost coincide when the associated energy level is the same, and this holds to some extent also for the other defects. More generally, the adjustable potential probes allow us to visualize trends resulting from the continuous variation of the defect energy level in the band gap. We detect a systematic tendency of deviating from the ideal vertical line for defect energies close to the band-edges. This deviation is especially evident in the vicinity of the valence band of MgO [cf. Fig. 4.7(c)]. For each value of α , Fig. 4.7 also provides the band gap achieved with the PBE0(α) functional. We note that the band gaps corresponding to α_K values resulting from defect levels close to the middle of the band gap fall within about 0.2 eV from the experimental reference (cf. Fig. 4.7), consistent with previous observations [51]. However, the behavior close to the band edges leads to a deterioration of this agreement.

It is natural to assign the deviations observed for defect levels falling in the vicinity of the band edges to the hybridization of the defect state with the delocalized band-edge states. To verify this connection, we adopt a criterion for describing the degree of hybridization on the basis of the delocalized screening charge, as proposed in Ref. [125]. Indeed, the polarization charge that screens a charged defect is drawn in a uniform way from the periodically repeated simulation cell [125, 146]. Far from the defect, this gives an average charge density of $(1 - 1/\epsilon)q/\Omega$, where ϵ is the dielectric constant, q the total defect charge, and Ω the volume of the supercell. In the presence of hybridization, the observed charge density is found to deviate from this reference value [125]. We define the degree of hybridization δ through this deviation, as shown in Fig. 4.8(a). We use a Gaussian broadening with a width of 1 Å to smoothen the defect charge density prior to the evaluation of δ .

To demonstrate its direct connection with the deviations in Fig. 4.7, we evaluate the degree of hybridization δ for all considered defects versus the corresponding defect energy level within the band gap. The calculated values in the case of MgO are shown in Fig. 4.8(b). We observe that the lowest degree of hybridization is found for defect states in the middle of the band gap. The hybridization increases noticeably when the defect level is located in the vicinity of either the valence or the conduction band. Considering both local and nonlocal potential probes, we identify the highlighted defect X^* yielding the minimal degree of hybridization. For the three considered materials, the energy level of X^* is found to lie close to the middle of the band gap (cf. Fig. 4.7). The corresponding mixing parameter α_K then gives an accurate description of the band gap. We note that the hybridization between band-edge and defect states depends critically on the host material. In particular, we observe in MgO a strong interaction with the valence band, which shows a high density of states due to the localized nature of the O 2p states [157]. Such a dramatic behavior is seen neither for ALP nor for C. These results allow us to understand the dependence of the mixing parameter α_K on the considered defect and to improve our selection criteria for identifying the most suitable defect states.

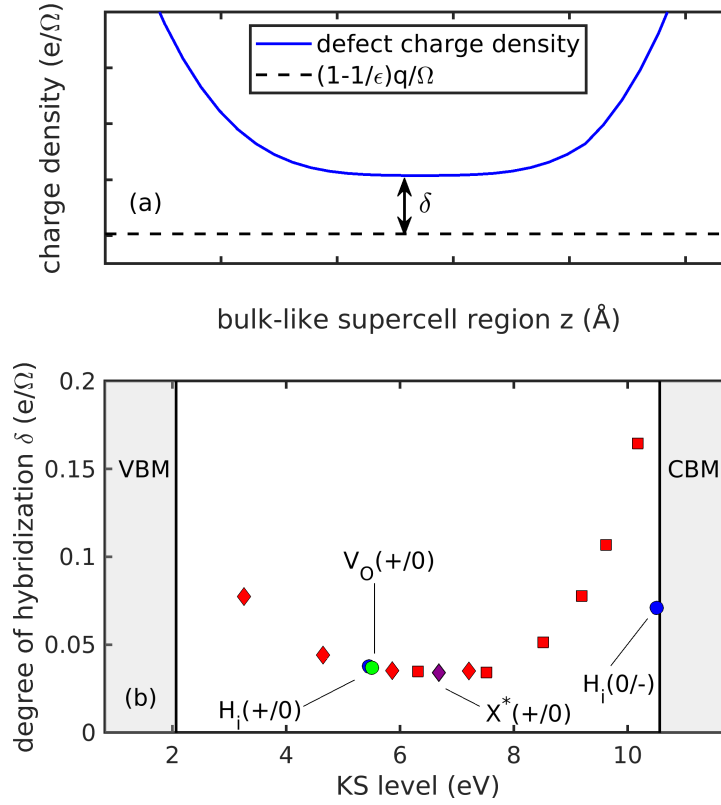


Figure 4.8 – (a) Schematic view of the degree of hybridization δ defined in this work as the deviation of the smoothened defect charge density from the delocalized screening charge density (horizontal dashed line) at a large distance from the defect site. (b) Degree of hybridization for various potential probes in MgO as a function of the defect energy level. The results for the parametrized local and nonlocal potentials are indicated by red squares and red diamonds, respectively. The indicated band-edge energies correspond to the functional $PBE0(\alpha_{opt})$, which reproduces the experimental reference for the band gap (see text).

Table 4.1 – Band gaps (in eV) of AlP, C, and MgO obtained with the $PBE0(\alpha_K)$ functional, in which the mixing parameter is set through enforcing Koopmans' condition for the two different charge transition levels of the hydrogen interstitial, $H_i(+0)$ and $H_i(0/-)$, as well as for the potential probe $X^*(+0)$ showing the minimal degree of hybridization. The corresponding mixing parameters α_K are given in parentheses. The mean absolute errors (MAE) are determined with respect to the experimental references (Expt. in last column). These correspond to fundamental band gaps corrected for phonon renormalization.

	$H_i(+0)$	$H_i(0/-)$	$X^*(+0)$	Expt.
AlP	2.30 (0.13)	2.30 (0.13)	2.40 (0.15)	2.52
C	5.90 (0.21)	5.71 (0.19)	5.93 (0.22)	5.85
MgO	8.35 (0.36)	8.61 (0.38)	8.48 (0.37)	8.50
MAE	0.14	0.16	0.07	

In Table 4.1, we give the band gaps of AlP, C, and MgO obtained from the (+/0) defect level of the potential probe X^* showing the minimal degree of hybridization, in comparison with those obtained from the (+/0) and (0/−) charge transitions of the hydrogen interstitial H_i . All hybrid functionals that result from these nonempirical constructions give band gaps in good agreement with experimental references (Table 4.1). The mean absolute errors are within 0.20 eV, which is comparable to other state-of-the-art methods for band-gap evaluation [17, 18, 47, 35, 43]. Noticeably, the MAE of the potential probe X^* is lower than those for H_i indicating that minimizing the degree of hybridization generally improves the band gap estimate. This property is particularly valuable when the natural defect levels associated to H_i lie close to the band edges or even outside the band gap. More generally, these results validate a rational procedure for identifying a suitable localized state for band-gap evaluation through the fulfillment of Koopmans' condition. In view of the results in Ref. [52], we expect that such a procedure should also be applicable to systems of lower dimensions.

4.5 Summary

In this chapter, we present two types of adjustable potential probes for band-gap evaluations through the application of Koopmans' condition. Through the use of these potential probes, the hybridization with the band-edge states can be minimized to yield band gaps within 0.2 eV or lower from experimental values. The dependence on the parameters of the potential probes is smooth and thus suitable to be implemented in an automated minimization process. The present results provide guidelines for the selection of suitable potential probes even when natural defect states cannot be used, thereby enlarging the application scope of the methodology based on the enforcement of Koopmans' condition. This is an important step towards establishing the present technique as a serious alternative with respect to many-body perturbation theory schemes and dielectric-dependent hybrid functionals for robust and accurate band-gap predictions.

5 Band gaps of inorganic metal-halide perovskites

In this chapter, we investigate nonempirical hybrid functionals for band-gap predictions of inorganic metal-halide perovskites belonging to the class CsBX_3 , with $\text{B} = \text{Ge}, \text{Sn}, \text{Pb}$ and $\text{X} = \text{Cl}, \text{Br}, \text{I}$. We consider both global and range-separated hybrid functionals and determine the parameters through two different schemes. The first scheme is based on the static screening response of the material and thus yields dielectric-dependent hybrid functionals. The second scheme defines the hybrid functionals through the enforcement of Koopmans' condition for localized defect states. We also carry out quasiparticle self-consistent GW calculations with vertex corrections to establish state-of-the-art references. For the investigated class of materials, dielectric-dependent functionals and those fulfilling Koopmans' condition yield band gaps of comparable accuracy (~ 0.2 eV), but the former only require calculations for the primitive unit cell and are less subject to the specifics of the material.

The results presented in this chapter have been published in Ref. [115]. Further information can be found in the corresponding archive on the Materials Cloud [158].

5.1 Motivation

Solar cells based on metal-halide perovskites have recently drawn great scientific attention [159, 160, 161, 162, 163]. In fact, within one decade their power conversion efficiencies increased tremendously [159, 161] and reached 22.1% in 2017 [163] with potential for improving even further. This makes them stand out as a promising alternative to today's best thin-film photovoltaic devices [160, 162]. The further improvement of perovskite solar cells relies greatly on the ability of exploring the immense space of possible compositions and structures. For this task, one naturally resorts to automated computational methods [164, 165, 166]. This requires a critical trade off between aspired accuracy and bearable effort. The most accurate technique for band-gap evaluation consists of quasiparticle self-consistent GW calculations including vertex corrections [9, 15, 17, 18]. However, this technique demands a high computational effort and is practically limited to materials with small unit cells. In particular, a recent study by Wiktor *et al.* on perovskite compounds accounting for spin-orbit and thermal effects showed that this level of theory is needed to achieve a good comparison with experimental band gaps [114]. Therefore, it is highly desirable to develop alternative computational schemes yielding the same accuracy as self-consistent GW methods but requiring a lower computational cost. Electronic-structure calculations based on nonempirical hybrid functionals have the potential to fill this gap. In this chapter, we evaluate the performance of such functionals for inorganic metal-halide perovskites.

5.2 Theoretical schemes and band-gap references

In this chapter, we apply nonempirical construction schemes to different classes of hybrid functionals. In particular, we consider the global PBE0(α) and the range-separated CAM($\alpha_s, \alpha_\ell, \mu$) functional. First, we determine the free parameters through the dielectric response of the perovskites materials. For the global functional this leads to the PBE0($1/\epsilon_\infty^{\text{sc}}$) functional (cf. Sec. 3.1.3). For the case of the range-separated functional CAM($\alpha_s, \alpha_\ell, \mu$), we adopt the DD-RSH-CAM approach of Chen *et al.* (cf. Sec. 3.1.3). In analogy, we also fix the free parameters of the global and the range-separated functional through the enforcement of Koopmans' condition (cf. Sec. 3.2.3).

To evaluate the performance of the nonempirical hybrid functionals, we carry out comparisons with state-of-the-art methods for band-gap evaluation. Quasiparticle self-consistent GW (QSG \tilde{W}) including vertex corrections in the screening (\tilde{W}) can serve as such a high-level reference [9, 15, 17, 18]. A detailed QSG \tilde{W} study of inorganic metal-halide perovskites has recently been carried out by Wiktor *et al.* [114]. Here, we calculate QSG \tilde{W} band gaps in a similar fashion but with the pseudopotentials considered in this work and with nonlocal commutators for the optical matrix element in the long-wavelength limit as described in Ref. [167]. Our QSG \tilde{W} band gaps are given in Table 5.1. In comparison to the results in Ref. [114], the present band gaps agree within ~ 0.2 eV on average and thereby confirm the conclusions drawn previously.

The comparison with experiment requires the consideration of thermal effects and spin-orbit coupling [114]. For the perovskites based on Pb and Sn, this can be achieved by relying on the corrections given in Ref. [114]. The calculated band gaps corrected in this way are compared with experimental band gaps in Table 5.1. We generally consider experimental data for the same cubic phase when available, but report values referring to other phases otherwise. We observe that the QSG \tilde{W} band gaps generally agree well with experiment after the consideration of thermal effects and spin-orbit coupling [114]. The case of CsSnCl₃ shows a deviation of about 0.6 eV, but this could at least partially result from the consideration of a cubic phase in the calculation and of a monoclinic one in the experiment. In the following, we do not refer to experimental data any more and use our QSG \tilde{W} results to benchmark the band gaps obtained through the nonempirical hybrid-functional schemes.

Table 5.1 – Band gaps (in eV) as calculated through QSG \tilde{W} . Following Ref. [114], we include corrections for finite temperature effects (Δ_T) and for spin-orbit coupling (Δ_{SOC}) before comparing with experimental band gaps.

	QSG \tilde{W}	QSG $\tilde{W} + \Delta_T + \Delta_{\text{SOC}}$	Expt.
CsPbI ₃	2.27	1.79	1.67 [168], 1.73 [169]
CsPbBr ₃	3.01	2.24	2.25 [170], 2.36 [171]
CsPbCl ₃	3.41	2.70	2.85 [170]
CsSnI ₃	1.10	1.46	1.31 ^a [172], 1.3 ^a [173]
CsSnBr ₃	1.32	1.75	1.75 [172]
CsSnCl ₃	1.79	2.17	2.8 ^b [172]
CsGeI ₃	1.67	-	1.6 ^c [174], 1.63 ^c [175]
CsGeBr ₃	2.13	-	2.38 ^d [176]
CsGeCl ₃	2.67	-	3.43 ^d [176]

^a orthorhombic phase, ^b monoclinic phase, ^c trigonal phase, ^d rhombohedral phase.

5.3 Computational aspects

5.3.1 Computational details

The calculations presented in this chapter are carried out using experimental lattice constants for the cubic phase as given in Refs. [177, 114]. A graphical representation of the primitive unit cell is given in Fig. 5.1(a) for the case of CsPbI₃. In this crystal structure, all the nine considered perovskites show a direct gap at the R point as shown in Fig. 5.1(b).

In our calculations, we use two sets of normconserving pseudopotentials to describe core-valence interactions [87, 88] to examine the role of exchange interactions with core states [178] (see Sec. 5.3.2). The first set (denoted PP1) incorporates only the outermost shells among the valence states, whereas the second set (denoted PP2) additionally includes semicore shells. The pseudopotential of Cs includes the semicore states in both sets. The reference GW calculations have been performed with the set PP2. We used cutoffs of 70 and 100 Ry for the sets

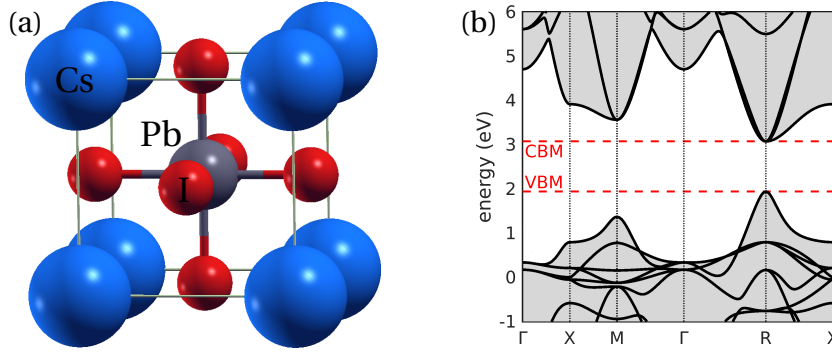


Figure 5.1 – (a) Primitive unit cell of cubic CsPbI₃. Cs, Pb, I atoms are shown in blue, gray, and red, respectively. (b) PBE band structure of CsPbI₃. Band-edge levels as determined at the *R* point are indicated with vertical dashed lines.

PP1 and PP2, respectively. The valence electrons for all the elements in the pseudopotential sets are specified in Table 5.2.

Table 5.2 – Atomic shells treated among the valence electrons in the two different sets of pseudopotentials considered in this work.

	PP1	PP2
Cs	$5s^2 5p^6 6s^1$	$5s^2 5p^6 6s^1$
Ge	$3d^{10} 4s^2 4p^2$	$3s^2 3p^6 3d^{10} 4s^2 4p^2$
Sn	$4d^{10} 5s^2 5p^2$	$4s^2 4p^6 4d^{10} 5s^2 5p^2$
Pb	$5d^{10} 6s^2 6p^2$	$5s^2 5p^6 5d^{10} 6s^2 6p^2$
Cl	$3s^2 3p^5$	$2s^2 2p^6 3s^2 3p^5$
Br	$4s^2 4p^5$	$3s^2 3p^6 3d^{10} 4s^2 4p^5$
I	$5s^2 5p^5$	$4s^2 4p^6 4d^{10} 5s^2 5p^5$

The QSGW calculations in this chapter are performed with computational parameters consistent with Ref. [114]. In particular, we use a plane-wave cutoff of 100 Ry. We include 800 bands and achieve results in the infinite basis-set limit through linear extrapolation with respect to the inverse number of bands [117]. For the materials investigated here, we find that such an extrapolation generally leads to a band-gap opening of ~ 0.1 eV.

For the construction of DDH functionals, we calculate the dielectric function through a linear response approach. The irreducible polarization is evaluated with the formula of Adler and Wiser [97, 98], for which 500 bands and an energy cutoff of 16 Ry are found to give converged results. For a more realistic description, we calculate the reducible polarizability including the bootstrap exchange-correlation kernel [109] for treating vertex corrections [47]. For the proper evaluation of the high-frequency dielectric constants a dense **k**-point sampling of $8 \times 8 \times 8$ for the Pb compounds and of $10 \times 10 \times 10$ for the Sn and Ge compounds are used. The convergence of the high-frequency dielectric constant with respect to the **k**-point mesh is shown in Fig. 5.2 for the representative cases CsPbCl₃ and CsSnCl₃. It is noteworthy that samplings without

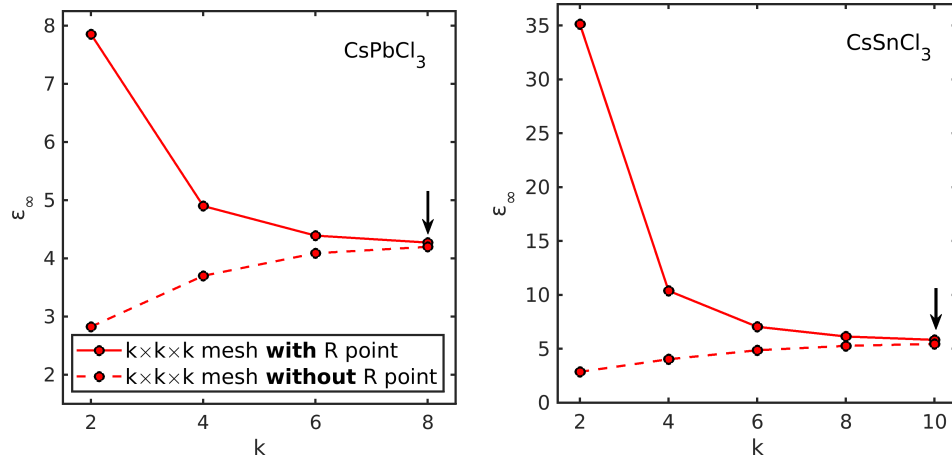


Figure 5.2 – Convergence of the high-frequency dielectric constant ϵ_{∞} of CsPbCl_3 and CsSnCl_3 with respect to the adopted \mathbf{k} -point mesh. Meshes with and without the R point are distinguished. The converged results are highlighted with an arrow.

the R point exhibit a somewhat faster convergence with respect to the number of \mathbf{k} points. However, this point describes the direct band-gap transition and is therefore indispensable for a proper description of the electronic structure. Therefore, we evaluate the dielectric function generally for \mathbf{k} -point samplings which include the R point.

The construction of hybrid functionals satisfying Koopmans' condition is based on calculations for defects in supercells [51]. For modelling the point defects, we use $2 \times 2 \times 2$ supercells (40 atoms) together with $2 \times 2 \times 2$ \mathbf{k} -point samplings. Spin polarization is explicitly included whenever unpaired electrons occur.

5.3.2 Role of semicore electrons

Preliminary to the construction of the nonempirical hybrid functionals, we devote special attention to the effect of including semicore shells among the valence electrons. To ensure consistency with the GW reference, the same PP2 pseudopotentials should be used in the hybrid functional calculations. This can be achieved with the DDH construction scheme, which relies on calculations in the primitive unit cell. However, the PP2 set of pseudopotentials becomes prohibitively demanding when dealing with defects in supercells. For the construction of hybrid functionals satisfying Koopmans' condition, we therefore make use of the lighter pseudopotentials in the set PP1.

In order to estimate the error that we introduce through neglecting the semicore electrons in PP1, we perform band-gap calculations using the two sets of pseudopotentials. In particular, we systematically vary the free parameters α_s and μ within the hybrid functional $\text{CAM}(\alpha_s, \alpha_{\ell}=1/\epsilon_{\infty}, \mu)$. The form of the functional PBE0(α) is recovered by setting $\alpha = \alpha_s$ and $\mu \rightarrow 0$. The band-gap differences originating from the different pseudopotentials are visualized

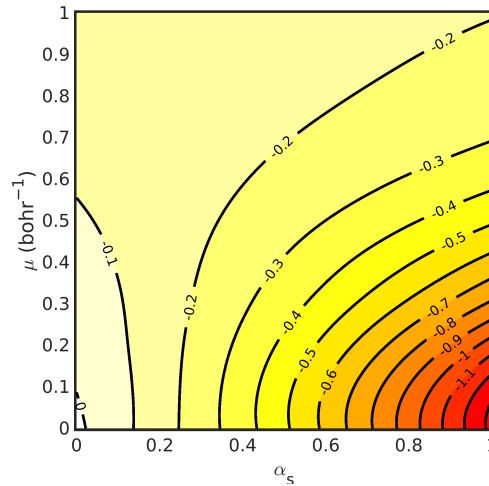


Figure 5.3 – Band-gap difference (in eV) for CsPbI₃ between calculations with pseudopotential sets PP1 and PP2, which differ by the treatment of semicore electrons. The band gaps are obtained with a CAM-type hybrid functional in which the long-range fraction of Fock exchange is set to $\alpha_\ell = 1/\epsilon_\infty$. The figure shows the band-gap difference as a function of the short-range fraction of Fock exchange α_s and the inverse screening length μ . Isovalues are shown by solid lines.

in Fig. 5.3 in the representative case of CsPbI₃. The two sets of pseudopotentials yield almost identical band gaps in the limit corresponding to the semilocal functional PBE ($\alpha_s = 0$ and $\mu = 0$). This is consistent with the fact that the two sets of pseudopotentials are generated at the PBE level and indicates that semicore states play a negligible role at this level of theory. When the fraction of Fock exchange incorporated in the functional is increased, we find that the PP1 set yields a reduction of the band gap with respect to the PP2 set. For low values of α_s , the difference in the band gap amounts to only a few tenths of an electronvolt, but it progressively increases with α_s , and reaches values larger than 1 eV for α_s approaching 1. This dependence indicates that the implicit treatment of semicore states in PP1 leads to significant discrepancies with respect to the more accurate PP2 set when the fraction of Fock exchange incorporated in the functional becomes sizeable. Similar effects were observed by Stroppa *et al.* [178] for hybrid functional calculations with pseudopotentials generated at the semilocal level.

These observations have significant consequences for the construction of nonempirical hybrid functionals. In particular, this affects the DD-RSH-CAM functionals generated in this work, which include a fraction of Fock exchange $\alpha_s = 1$ in the short range [47]. Therefore, it is only meaningful to consider DD-RSH-CAM functionals in conjunction with PP2 pseudopotentials. For the global hybrid functionals PBE0($1/\epsilon_\infty^{\text{sc}}$) and PBE0(α_K) which incorporate only small fractions of Fock exchange, the implicit treatment of core-electrons leads to smaller deviations and thus the use of the PP1 set entails smaller errors. This should be borne in mind when considering PBE0($1/\epsilon_\infty^{\text{sc}}$) and PBE0(α_K) functionals with PP1 pseudopotentials in Secs. 5.4.1 and 5.4.2.

5.4 Band gaps

5.4.1 Dielectric-dependent hybrid functionals

We first focus on the construction of dielectric-dependent hybrid functionals. The convergence of this scheme applied to PBE0(α) functionals is shown in Fig. 5.4 for the case of CsPbI₃. Generally, convergence for the dielectric constant ϵ_∞ [cf. Fig. 5.4(a)] and the band gap [cf. Fig. 5.4(b)] is reached within three to four iterations. The self-consistent update procedure is initialized through the use of the PBE functional, which corresponds to PBE0($\alpha = 0$). We remark that the PBE0($1/\epsilon_\infty^{\text{sc}}$) functional resulting from this procedure is independent of the starting point [43].

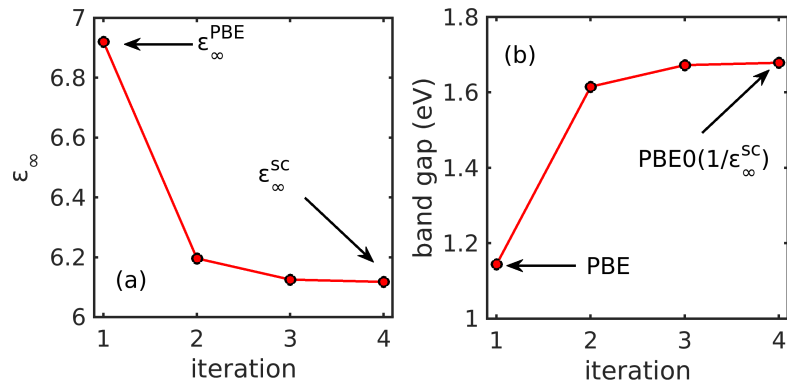


Figure 5.4 – Convergence of (a) the dielectric constant ϵ_∞ and (b) the band gap within the self-consistent DDH scheme for CsPbI₃. The values for the PBE starting point and the converged PBE0($1/\epsilon_\infty^{\text{sc}}$) are highlighted. The present results are obtained with PP1. PP2 pseudopotentials show an analogous behavior.

The band gaps obtained with the PBE0($1/\epsilon_\infty^{\text{sc}}$) functional for the present set of perovskites are shown in Table 5.3 and compared to the QSG \tilde{W} reference values. The corresponding mixing parameters $1/\epsilon_\infty^{\text{sc}}$ are given in parentheses. On average, we find a band-gap underestimation of ~ 0.4 and ~ 0.3 eV for PP1 and PP2, respectively. Such an accuracy is comparable to PBE0($1/\epsilon_\infty^{\text{sc}}$) results reported in the literature for extended sets of semiconductors and insulators [43, 47]. This provides confidence that dielectric-dependent hybrid functionals can achieve the same level of accuracy for a larger set of perovskite materials. The determined mixing parameters are almost identical for both sets of pseudopotentials. This indicates that the explicit treatment of semicore electrons only marginally affects the iterative construction scheme, even though the ensuing band gaps differ by ~ 0.1 eV.

Next, we apply the dielectric-dependent approach also to range-separated hybrid functionals. We consider the CAM-type functional, which includes a fraction of Fock exchange α_s in the short range and α_ℓ in the long-range, mediated by an inverse screening length μ . These parameters are determined through fitting of Chen’s model function [47]

$$\epsilon^{-1}(G) = 1 - (1 - \epsilon_\infty^{-1})e^{-G^2/4\mu^2} \quad (5.1)$$

Chapter 5. Band gaps of inorganic metal-halide perovskites

Table 5.3 – Band gaps (in eV) calculated through PBE0($1/\epsilon_\infty^{\text{sc}}$) and DD-RSH-CAM functionals. The determined hybrid functional parameter ($1/\epsilon_\infty^{\text{sc}}$) and ($1/\epsilon_\infty^{\text{sc}}, \mu$) are given in parentheses. The considered set of pseudopotentials is indicated. Band gaps evaluated through QSG \tilde{W} are given as reference. The mean absolute difference (MAD) is given with respect to these values.

	PBE0($1/\epsilon_\infty^{\text{sc}}$)		DD-RSH-CAM	QSG \tilde{W}
	PP1	PP2	PP2	PP2
CsPbI ₃	1.68 (0.16)	1.83 (0.17)	1.99 (0.18, 0.51)	2.27
CsPbBr ₃	2.48 (0.23)	2.65 (0.23)	2.84 (0.24, 0.53)	3.01
CsPbCl ₃	3.24 (0.27)	3.32 (0.27)	3.40 (0.28, 0.56)	3.41
CsSnI ₃	0.60 (0.10)	0.65 (0.10)	0.78 (0.12, 0.48)	1.10
CsSnBr ₃	0.82 (0.13)	0.88 (0.13)	0.99 (0.15, 0.53)	1.32
CsSnCl ₃	1.63 (0.21)	1.64 (0.21)	1.75 (0.22, 0.58)	1.79
CsGeI ₃	1.09 (0.12)	1.17 (0.12)	1.40 (0.10, 0.55)	1.67
CsGeBr ₃	1.59 (0.17)	1.66 (0.17)	1.89 (0.15, 0.58)	2.13
CsGeCl ₃	2.44 (0.22)	2.48 (0.22)	2.51 (0.21, 0.60)	2.67
MAD	0.42	0.35	0.20	

to the inverse dielectric function as obtained from linear response theory. The accuracy of the fit is shown in Fig. 5.5 for the case of CsPbI₃. We remark, that the value determined for α_ℓ corresponds to $1/\epsilon_\infty$. Since the fitting procedure is iterated within the DDH workflow (cf. Sec. 3.1.3), the final long-range fraction of Fock exchange is $\alpha_\ell = 1/\epsilon_\infty^{\text{sc}}$.

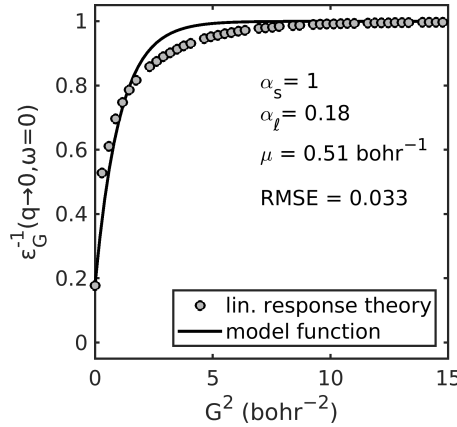


Figure 5.5 – Inverse dielectric function $\epsilon_G^{-1}(q \rightarrow 0, \omega = 0)$ of CsPbI₃ as calculated using linear response theory (circles) and fitted according to the model function (solid line). The fitted values for the parameters α_ℓ and μ and for the root-mean-square error (RMSE) are given.

The hybrid-functional parameters of the constructed DD-RSH-CAM functionals together with the obtained band-gap estimates are given in Table 5.3. The observed long-range fraction of Fock exchange is in close agreement to the one obtained with the global PBE0($1/\epsilon_\infty^{\text{sc}}$) functionals. This indicates that the long-range exchange interaction is screened with almost identical high-frequency dielectric constants $\epsilon_\infty^{\text{sc}}$ in the two approaches. Consequently, differences in the observed electronic structure originate from the different short-range description. The

calculated band gaps indicate a mean absolute difference (MAD) of 0.20 eV with respect to the QSGW reference, which corresponds to an improved description relative to PBE0($1/\epsilon_{\infty}^{\text{sc}}$). Hence, in the dielectric-dependent construction scheme, the range-separated CAM functional yields more accurate band gaps than the global PBE0 functional, in accord with the results in Ref. [47].

5.4.2 Hybrid functionals satisfying Koopmans' condition

We first apply Koopmans' condition to determine the free parameter α within the PBE0(α) functional. We consider various native defects, such as vacancies, interstitials, and antisites, but decide to focus only on halide vacancies since their single-particle energy levels are found to lie close to mid-gap. Indeed, the present construction scheme works most effectively when the hybridization of the defect states with the delocalized band states is minimized [54]. We remark that in our scheme the defect levels are obtained without structural relaxation [51, 54], thereby explaining their different location in the band gap with respect to previous studies of defects in such perovskite materials [179, 180, 181]. A graphical illustration of the halide vacancy defect is given in Fig. 5.6 (a) for the case of CsPbI₃. The defect calculations in this section are carried out with the pseudopotential set PP1 due to the computational cost entailed by the consideration of supercells.

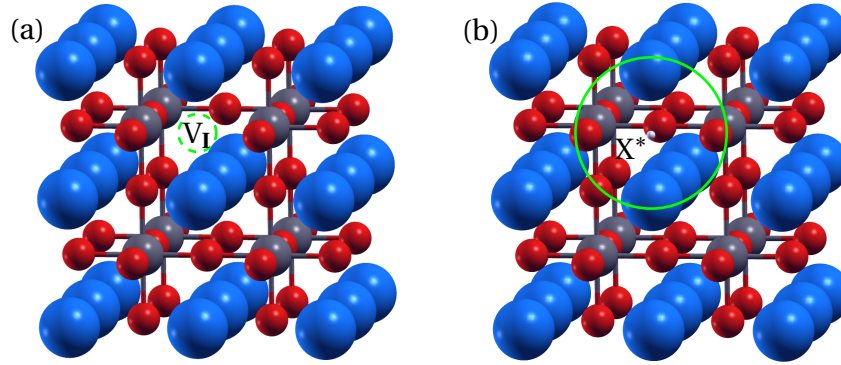


Figure 5.6 – Defective supercells of CsPbI₃ with (a) an iodine vacancy V_I and (b) an adjustable potential probe X^* . The defect sites are highlighted with green circles. Cs, Pb, I atoms are shown in blue, gray, and red, respectively. The potential probe is visualized in white.

To support the choice of the halide-vacancy defect, we use the concept of adjustable potential probes [54] as shown in Fig. 5.6 (b). We use potentials resulting from a Gaussian distribution of positive charge with width parameters σ ranging from 0.625 to 1.25 bohr. This allows us to continuously vary the defect level of the localized state across the entire band gap of the host material, as shown in Fig. 5.7. We observe that the mixing parameter satisfying Koopmans' condition α_K is 0.29 ± 0.01 irrespective of the considered defect. The uncertainty in the mixing parameter results from limitations of the construction scheme [51, 54], but yields in this case negligible band-gap deviations of ± 0.02 eV. We identify the optimal potential probe X^* by minimizing the degree of hybridization with the band edges, as described in Sec. 4.4. The

corresponding band-gap estimate is very close to that obtained with the halide vacancy (cf. Fig. 5.7). On the basis of this agreement, we focus in the following only on the halide vacancy to construct hybrid functionals satisfying Koopmans' condition.

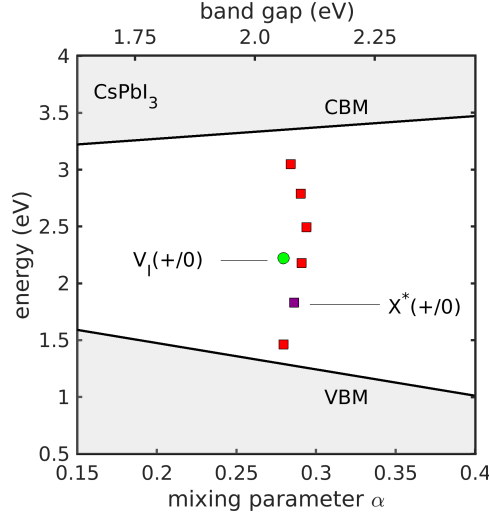


Figure 5.7 – Band edges and defect energies displayed versus the mixing parameter α for the iodine vacancy V_I (green circle) and various local potential probes (red squares) in CsPbI_3 . X^* refers to the potential probe with the smallest degree of hybridization with the band edges. The indicated band gaps are obtained with the functional $\text{PBE0}(\alpha)$.

In Table 5.4, the band gaps resulting from the constructed $\text{PBE0}(\alpha_K)$ functionals are reported and compared with $\text{QSG}\tilde{W}$ references. We find a MAD of 0.21 eV between the $\text{PBE0}(\alpha_K)$ band gaps and the GW references. We remark that the chlorine compounds show larger errors but this effect cannot trivially be related to the electronegativity or to the size of the involved ions. While the origin of these deviations is unclear at the moment, the MAD on the full set of considered compounds is consistent with values in the literature [51]. This consistency supports that this level of accuracy can be expected when considering a larger set of perovskite materials.

It is also of interest to compare the present results with those obtained with $\text{PBE0}(1/\epsilon_\infty^{\text{sc}})$ functionals (cf. Table 5.3), which share the same functional form of $\text{PBE0}(\alpha)$. The mixing parameters of the $\text{PBE0}(1/\epsilon_\infty^{\text{sc}})$ functionals are systematically lower than those of $\text{PBE0}(\alpha_K)$, and so are the corresponding estimates for the band gap. With respect to the GW references, the performance of $\text{PBE0}(\alpha_K)$ (MAD = 0.21 eV) is significantly better than that of $\text{PBE0}(1/\epsilon_\infty^{\text{sc}})$ (MAD = 0.42 eV). Hence, for the global functional $\text{PBE0}(\alpha)$, the fraction of Fock exchange solely determined through ϵ_∞ generally leads to underestimated band gaps, while the enforcement of Koopmans' condition yields better results on average. These differences suggest that the physical properties considered in the two construction schemes are not equivalent [56] and that they could potentially be exploited in a complementary fashion. However, the generality of this observation remains to be demonstrated for a larger variety of materials.

Table 5.4 – Band gaps (in eV) calculated through PBE0(α_K) functionals. The corresponding mixing parameters α_K are given in parentheses. The considered set of pseudopotentials is indicated. Band gaps evaluated through QSG \tilde{W} are given as reference. The mean absolute difference (MAD) is given with respect to these values.

	PBE0(α_K)		QSG \tilde{W}
	PP1	PP2	PP2
CsPbI ₃	2.06 (0.28)	2.28	2.27
CsPbBr ₃	2.99 (0.35)	3.24	3.01
CsPbCl ₃	3.87 (0.41)	4.00	3.41
CsSnI ₃	1.02 (0.23)	1.12	1.10
CsSnBr ₃	1.34 (0.26)	1.42	1.32
CsSnCl ₃	2.31 (0.35)	2.29	1.79
CsGeI ₃	1.46 (0.21)	1.55	1.67
CsGeBr ₃	2.03 (0.26)	2.12	2.13
CsGeCl ₃	2.91 (0.32)	2.93	2.67
MAD	0.21	0.20	

Part of the differences between the band gaps obtained with PBE0(α_K) and QSG \tilde{W} might result from the use of different pseudopotential sets in the two calculations. To evaluate this effect, we determine the band gaps with the PP2 set using the same mixing parameters as obtained from the PP1 defect calculations. We hereby rely on the fact that the mixing parameters remain almost unchanged upon varying the pseudopotential set, as seen in Table 5.3 for PBE0($1/\epsilon_\infty^{\text{sc}}$). Table 5.4 shows that this generally yields an increase of the resulting band gaps as a consequence of the trend in Fig. 5.3. However, the overall accuracy (MAD = 0.20 eV) remains similar to that achieved with PP1 (MAD = 0.21 eV) and thus the considerations made above remain unaffected.

Next, it is our interest to study the accuracy of CAM hybrid functionals when enforcing Koopmans' condition. As discussed in Sec. 5.3.2, such calculations require the explicit treatment of semicore electrons, i.e. the use of the demanding PP2 pseudopotentials. To circumvent this problem, we determine the free parameters of the CAM functional by performing defect supercell calculations with PP1 pseudopotentials. We then obtain band-gap estimates from bulk calculations of the primitive unit cell using the constructed CAM functional with either PP1 or PP2 pseudopotentials.

We illustrate this procedure for the iodine vacancy V_I in CsPbI₃ in Fig. 5.8. In the investigated CAM functionals, α_ℓ is fixed to $1/\epsilon_\infty$, while α_s and μ are varied systematically. We only consider $\alpha_s < 0.5$ due to the decreasing reliability of the PP1 pseudopotentials with increasing α_s (cf. Fig. 5.3). The parameters fulfilling Koopmans' condition are identified by the red curve within the two-dimensional (α_s, μ) space. In Ref. [51], it was found that such lines remain close to band-gap isolines, thereby providing a robust determination of the band gap irrespective of the location on the curve fulfilling Koopmans' condition (Koopmans' curve). This behavior

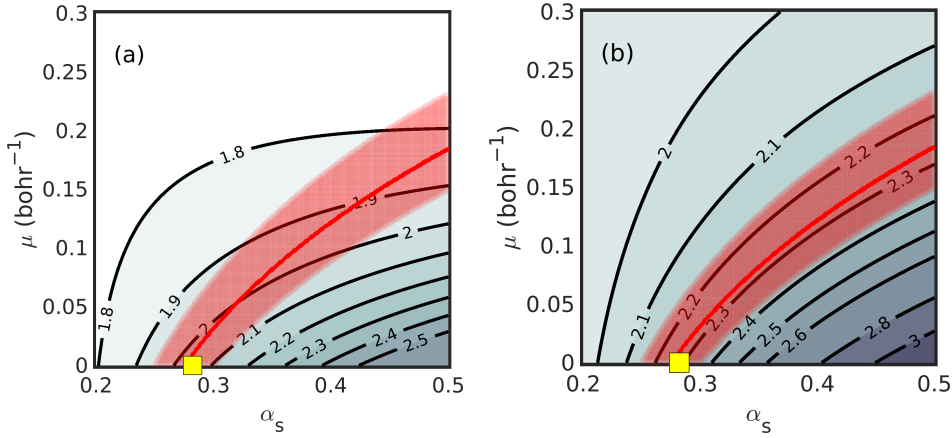


Figure 5.8 – Isocontour plots for the band gap of CsPbI_3 as a function of the short-range fraction of Fock exchange α_s and the inverse screening length μ . The parameter α_ℓ is fixed to $1/\epsilon_\infty$. The displayed band gaps are obtained with (a) PP1 and (b) PP2 pseudopotentials. The red lines indicate fulfillment of Koopmans’ condition, and the regions shaded in red deviations below 0.1 eV. The point in parameter space corresponding to the $\text{PBE0}(\alpha_K)$ functional is highlighted with a yellow square.

is not seen for PP1 pseudopotentials [Fig. 5.8(a)], but is recovered when the PP2 set is used [Fig. 5.8(b)]. In the latter case, the band gap always remains close to ~ 2.3 eV, in agreement with the band gap achieved with the global functional $\text{PBE0}(\alpha_K)$. These results suggest that the deviation of the Koopmans’ curve from a band-gap isoline for PP1 pseudopotentials is a consequence of the discrepancies pointed out in Fig. 5.3. Nevertheless, the hybrid-functional parameters determined with PP1 pseudopotentials appear to have a more extended range of validity than the band-gap values, in a similar way as seen above for $\text{PBE0}(1/\epsilon_\infty^{\text{sc}})$ functionals (cf. Table 5.3). Overall, to close this section on the use of Koopmans’ condition for determining the parameters, we conclude that the consideration of the CAM functional does not bring any improvement over the PBE0 functional. This is in agreement with the findings of Ref. [51].

5.5 Summary

In this chapter, we applied two nonempirical schemes for the construction of hybrid functionals to a set of inorganic metal-halide perovskites. We set out to determine the accuracy by which such nonempirical hybrid functionals are capable of predicting band gaps. For this purpose, we also performed state-of-the-art GW calculations, which we used as reference. The free parameters of the hybrid functionals in the first scheme were fixed through the dielectric response, while the enforcement of Koopmans’ condition on defect states was the criterion at the basis of the second scheme. Moreover, we investigated two classes of functionals: global functionals with a single undetermined parameter and range-separated CAM-type functionals involving three parameters.

The dielectric-dependent approach based on global functionals yields a mean average deviation of 0.35 eV with respect to the *GW* references. This deviation is in line with previous results in the literature on other materials [43, 47]. The consideration of range-separated functionals reduces the mean average deviation to 0.20 eV, confirming thereby that the use of this type of functional leads to a higher accuracy [47, 35]. Global hybrid functionals fulfilling Koopmans' condition also yield band gaps in good agreement with our *GW* references, as indicated by the mean average deviation of 0.20 eV. Consideration of CAM-type functionals supports the robustness of the predicted band gaps [51], and hence does not lead to any further improvement in the accuracy. Overall, the two applied schemes yield band gaps with an accuracy of ~ 0.2 eV. For this, the dielectric-dependent scheme requires the use of range-separated functionals, but plain global functionals are sufficient within the scheme based on Koopmans' condition. More generally, the differing features of the two schemes hint at the fact that reproducing the dielectric response and imposing Koopmans' condition are nonequivalent constraints [56]. This might deserve further investigation to benefit from the individual advantages of the two schemes in a combined fashion.

On the practical side, the dielectric-dependent scheme only involves bulk calculations for the primitive unit cell, whereas the scheme based on Koopmans' condition requires the consideration of localized defect states and thus the treatment of supercells of suitable size. The latter condition can imply demanding computational resources and restrict the overall flexibility of the scheme, as seen in this chapter as far as the class of pseudopotentials that could be treated. Furthermore, the use of Koopmans' condition necessitates the identification of defect states lying in the middle of the band gap. This is a material-dependent issue which complicates the incorporation of Koopmans' condition in automatized procedures.

In view of applying such nonempirical schemes to a larger class of perovskite materials, we conclude that the dielectric-dependent scheme with range-separated functionals is the most suitable, both for the accuracy achieved and for the computational cost involved. Hence, it stands out as a viable scheme to achieve accurate band gaps in the high-throughput screening of perovskite materials.

6 Band gaps of liquid water and hexagonal ice

In this chapter, we calculate the fundamental band gaps of liquid water and hexagonal ice through advanced electronic-structure methods. We compare specifically the performance of state-of-the-art *GW* calculations with nonempirical hybrid functionals. For the latter, we fix the free parameters either through the dielectric response of the material or through enforcing Koopmans' condition to localized states. The various approaches yield consistent band gaps, in good agreement with available experimental references. Furthermore, we discuss the critical aspects of each approach that underlie the band-gap predictions.

The results presented in this chapter have been submitted to Physical Review Research.

6.1 Motivation

Liquid water is an ubiquitous material in nature and has inevitably drawn great scientific attention. In particular, the electronic structure of liquid water has been the subject of numerous experimental [182, 183, 184, 185, 186, 187] and theoretical studies [60, 116, 188, 189]. These fundamental efforts enable a deeper understanding of liquid water in technological applications such as solvation processes [190, 191, 192, 193, 194] or catalytic reactions at solid-water interfaces [195, 23, 196, 59, 197, 198]. In addition to the liquid phase, also various solid phases of water have been investigated. The precise knowledge of the electronic structure of these polymorphs is relevant for atmospheric science [199, 200, 201, 202, 203], geoscience [204], astronomy [205, 206], as well as solid-state physics [207, 208, 209, 210].

It is surprising that despite this great scientific effort, the fundamental band gap of water is only known with mediocre accuracy. Indeed, the often cited study of Bernas *et al.* reports a band gap for liquid water of 8.7 ± 0.5 eV [186]. This value and its sizeable uncertainty reflect the lack of consensus among the various studies from which this band-gap estimate has been inferred. It is noteworthy that also the band gaps of the solid phases of water have not been determined with a high precision. In particular, the fundamental band gap of the most prominent ice *Ih* has been estimated to be 8.8 ± 0.4 eV [211]. Such substantial uncertainties call for further investigation.

Complementary to experimental studies, also a great deal of theoretical works have been devoted to this open question. Many-body perturbation theory in the *GW* approximation is generally considered as the most accurate computational scheme for band-gap evaluation [9, 15, 17, 18]. Various flavors of this approach have been instrumental to predict the band gap of liquid water [212, 213, 60, 195, 116, 188, 214] and ice [215, 216, 217]. However, the various studies have not reached a consensus on the band gap yet. Indeed, the reported values for liquid water range from 7.8 to 10.5 eV with an uncertainty even larger than that of the experimental measurements. Among these studies, Chen *et al.* have deployed the most advanced method consisting in quasiparticle self-consistent *GW* including vertex corrections and obtained a band gap of 8.9 eV [116]. However, such high-level *GW* calculations are computationally demanding and have remained rare. For further confirmation, it is therefore necessary to take under consideration a larger variety of electronic-structure approaches. Moreover, to allow for applications involving larger systems, it is highly desirable that such alternative methods are computationally less demanding.

Electronic-structure calculations based on nonempirical hybrid functionals [24, 31, 32, 70] can serve as a valuable alternative to *GW* calculations. In particular, dielectric-dependent hybrid (DDH) functionals have already successfully been applied to liquid water [43, 35, 61, 59]. Similar investigations based on hybrid functionals satisfying Koopmans' condition are at present still lacking. A comparison of both nonempirical hybrid-functional schemes together with high-level *GW* approaches might yield valuable insight into the fundamental band gap of water and ice.

6.2 Experimental band-gap references

Prior to deploying advanced electronic-structure calculations, it is our interest to establish robust experimental band-gap references. We infer such references through a critical review of various experimental studies in the literature. The fundamental band gap, defined as the separation between the valence-band maximum (VBM) and the conduction-band minimum (CBM), is generally determined through the separate investigation of the two band edges. The VBM is given through the ionization potential (IP) as obtained in photoemission experiments. The CBM is determined by the electron affinity (EA) or equivalently by the position of the conduction band with respect to the vacuum level (denoted V_0). These properties are generally accessed through inverse photoemission experiments or the analysis of thermodynamic data pertaining to the hydrated electron. We note that the fundamental band gap could also be inferred from the corresponding optical one [218, 219, 220]. However, this route requires a proper assessment of the excitonic binding energy for which a final consensus has not yet been reached [215, 212, 220, 221]. Therefore, we do not include optical spectroscopy experiments in our analysis of band-gap references.

First, we examine the fundamental band gap of liquid water at ambient temperature. Early studies by Delahay and coworkers reported a photoemission threshold of 9.3 ± 0.3 eV [184], which has later been revised to 10.06 eV [185]. The more recent work of Winter *et al.* indicated a very similar value of 9.9 eV [187]. Based on the latest results, we assume 10.0 ± 0.1 eV for the ionization potential of liquid water. For the unoccupied states, Bernas and collaborators reported $V_0 = -1.2$ eV [183], later revised to -0.74 eV [186]. A recent study by Ambrosio *et al.* inferred $V_0 = -0.97$ eV from thermodynamical data for the hydrated electron [193]. Overall, we estimate $V_0 = -1.0 \pm 0.2$ eV. We do not consider the value of $V_0 = -0.12$ eV proposed by Coe *et al.* [222] due to the criticism raised in Ref. [193]. Altogether, we deduce a fundamental band gap for liquid water of 9.0 ± 0.2 eV. This value is consistent with previous works by Bernas *et al.* and Painter *et al.*, which reported band gaps of 8.7 ± 0.6 eV [186] and 9 eV [223], respectively. Moreover, the present estimation is based on more recent experimental studies and subject to a smaller uncertainty. We remark that a fundamental band gap of 9.1–9.2 eV was also inferred in Ref. [189].

Next, we consider the fundamental band gap of ice. Among the various possible phases [224], we are particularly interested in hexagonal ice *Ih*. This phase is stable at ambient pressure and has been subject to numerous experimental and computational studies. To benchmark the fundamental band gap of *Ih*, we adopt in the following also results obtained for polycrystalline and amorphous ice structures. This is justified through the studies of Nordlund *et al.* [225] and Kobayashi *et al.* [219], which have demonstrated a remarkable similarity in the electronic structure of crystalline and amorphous ice based on photoemission and optical spectroscopy, respectively. Furthermore, we note that the considered experimental results have generally been obtained at a temperature of 77 K. The measurements in Refs. [226, 225, 227] have been performed at a slightly higher temperature of 90–103 K.

Chapter 6. Band gaps of liquid water and hexagonal ice

Table 6.1 – Fundamental band gaps E_g^{Expt} (in eV) of liquid water ℓ -H₂O and hexagonal ice Ih as inferred from a review of various experimental data. The given band gaps correspond to temperatures of 300 and 77 K, respectively. Band-gap corrections E_g^{corr} (in eV) are also given. These corrections account for the band-gap reduction due to nuclear quantum effects (NQE) in liquid water and to the zero-phonon renormalization (ZPR) in hexagonal ice.

	E_g^{Expt}	E_g^{corr}
ℓ -H ₂ O	9.0 ± 0.2	0.7^a
Ih	9.4 ± 0.3	1.5^b

^a Ref. [116], $T = 300$ K, ^b Refs. [235, 211], $T = 0$ K.

Early photoemission experiments by Shibaguchi *et al.* indicated an ionization potential of 10.5 eV [226]. This result has been confronted with the value of 8.7 ± 0.1 eV obtained by Baron *et al.* [228] and that of 8.8 eV by Campbell *et al.* [229]. However, it should be considered that the latter studies define the onset of the photoemission spectra according to an extended tail at lower energies. Instead, the linearly extrapolated threshold reveals a value of ~ 10 eV [229], in much better agreement with Shibaguchi *et al.* [226]. Furthermore, from the work of Pache *et al.* [230], one also infers an IP of ~ 10 eV [231]. More recent photoemission studies of Winter *et al.* [187] and Nordlund *et al.* [225] support these values for the ionization potential. Specifically, Winter *et al.* remarked that electron binding energies (and thus the IP) in ice tend to be larger by ~ 0.1 – 1.0 eV than those obtained for liquid water (10.0 ± 0.1 eV). We account for these various experimental measurements by adopting an IP estimate of 10.3 ± 0.3 eV. For the conduction-band edge, early studies of Baron *et al.* and Grand *et al.* reported rather distinct values of $V_0 = -0.9$ eV [228] and -0.1 eV [232], respectively. Later, Michaud *et al.* derived a value of $V_0 = -1$ eV [231] on the basis of the photoelectric threshold [233] and the photoconductivity [234] of hydrated electrons. Most recently, Stähler *et al.* measured $V_0 = -0.8$ eV through time-resolved photoemission experiments [227]. Overall, we take on the value of $V_0 = -0.9 \pm 0.1$ eV, only marginally higher than the one assumed for liquid water. Based on the present discussion of IP and V_0 , we infer a fundamental band gap for hexagonal ice of 9.4 ± 0.3 eV. This estimate is in overall agreement with earlier studies by Michaud *et al.* and Engel *et al.*, which reported band gaps of ~ 9 eV [231] and 8.8 ± 0.4 eV [211], respectively. The differences result from a more stringent review of the recent literature in the present work.

Overall, we adopt a band-gap reference for liquid water at 300 K of 9.0 ± 0.2 eV. For hexagonal ice at 77 K, we estimate a band gap of 9.4 ± 0.3 eV. We observe a rather small difference of 0.4 eV on average between these two phases of water. This observation indicates that the fundamental band gap of water depends only weakly on temperature and crystal structure. A similar conclusion was reached by Bernas *et al.* [186]. In this chapter, the band gap of liquid water is calculated through configurations obtained at 300 K. For hexagonal ice, we obtain the band gap through a calculation at relaxed atomic positions. The comparison of the latter with the experimental band-gap references at 77 K is justified insofar the finite temperature difference is expected to have a negligible effect. Indeed, Engel *et al.* have shown that the

calculated band gap of Ih is almost independent of temperature between 0 K and 77 K [211]. Estimated variations are limited to $\sim 0.02\text{--}0.05$ eV and are therefore disregarded [211].

After the critical review of experimental band-gap references, we discuss further effects which have to be taken into account to ensure a consistent comparison between theory and experiment. In particular, we consider nuclear quantum effects (NQE) in liquid water and zero-phonon renormalization (ZPR) in hexagonal ice. These effects originate from the quantum mechanical nature of the nuclei and generally induce a renormalization of the band gap. Since we consider classical nuclei in our structural models (cf. Sec. 6.4.1), these renormalizations are added *a posteriori* as corrections to the band gaps calculated with the advanced electronic-structure methods. A summary of the band-gap references and corrections adopted in this chapter is given in Table 6.1.

For liquid water, various studies have shown that the NQE significantly affect the electronic structure [236, 116, 188, 214]. Indeed, Chen *et al.* found a band-gap reduction of 0.7 eV due to NQE, consistently for various state-of-the-art *GW* approaches [116]. For the semilocal Perdew-Burke-Ernzerhof (PBE) functional [5], this effect reduces to 0.5 eV [116]. These results are in overall agreement with other studies in the literature. The NQE effect have been found to be 0.5 eV with the G_0W_0 @RSH method [188], 0.6 eV with the PBE0-ADMM-D3 hybrid functional [236], and 0.65 eV with *evGW* calculations [214]. Among these various values, we adopt throughout this chapter the *GW* value from Chen *et al.* for the band-gap correction due to NQE. This choice is motivated, on the one hand, by the fact that this estimate results from one of the most accurate theoretical schemes, and, on the other hand, by the fact that we adopt in this chapter the very same structural configurations obtained by Chen *et al.* [237]. Therefore, we correct the band gap of liquid water at ambient temperature by 0.7 eV due to NQE.

In analogy to liquid water, we also consider the ZPR of the band gap in the case of hexagonal ice. Monserrat *et al.* calculated a ZPR of 1.52 eV by means of DFT calculations at the semilocal and hybrid functional levels [235]. Engel *et al.* confirmed this estimate in an extended study involving various proton orderings in hexagonal ice [211]. Therefore, we adopt throughout this chapter the value of 1.52 eV for the *a posteriori* correction of the calculated band gaps in hexagonal ice.

It is noteworthy that the band-gap corrections for the two considered water phases are significantly different. Indeed, the ZPR of the band gap of hexagonal ice is larger than the NQE on the band gap of liquid water by ~ 0.8 eV. Engel *et al.* have found that the ZPR of hexagonal ice varies by only ~ 0.1 eV over the temperature range 0–240 K [211]. Therefore, the dominating part of this effect cannot solely be assigned to the temperature difference between the two phases, but should rather be related to underlying atomic structures. In particular, in the case of liquid water, the band gap reduction results from a complex interplay between the broadenings in the density of states due to the NQE and to the molecular disorder.

6.3 Theoretical schemes

In this chapter, we study the fundamental band gap of liquid water and hexagonal ice through several advanced electronic-structure methods. First, we employ the QSGW method for this purpose. Since this approach does not account for electron-hole interactions, we use also the QSG \tilde{W} scheme which includes vertex corrections in the screening (\tilde{W}). We note that QSG \tilde{W} generally yields band gaps with a high accuracy and is therefore often used as a benchmark for other electronic-structure methods (cf. Sec. 5.4). However, due to the lack of consensus among the reported GW calculations for liquid water [212, 213, 60, 195, 116, 188, 214], we do not give a particular preference to the QSG \tilde{W} scheme from the start in this chapter.

The second advanced electronic-structure method investigated in this chapter consists in dielectric-dependent hybrid (DDH) functionals. We determine such functionals through the self-consistent workflow given in Sec. 3.1.3. As underlying classes of hybrid functionals we adopt the global PBE0(α) and the range-separated CAM($\alpha_s, \alpha_\ell, \mu$) functional. For the single parameter α of the former, the DDH procedure leads to $\alpha = 1/\epsilon_\infty^{\text{sc}}$ and thus to the global DDH functional PBE0($1/\epsilon_\infty^{\text{sc}}$). For the three parameters α_s , α_ℓ , and μ of the latter, the parameter definition is performed as follows. The short-range fraction α_s is taken as a constant for which different values have been proposed in the literature. Chen *et al.* applied $\alpha_s = 1$ with the underlying idea of achieving a hybrid functional that reproduces the fully unscreened Coulomb interaction in the short range [47]. Skone *et al.* used instead an attenuated short-range exchange based on $\alpha_s = 0.25$ [35]. In this chapter, we consider both ways of fixing α_s and compare the resulting implications for the construction of range-separated DDH functionals. Moreover, we investigate the effect of adopting purely semilocal exchange in the short range as obtained by setting $\alpha_s = 0$. This definition is motivated by the success of long-range corrected hybrid functionals [90, 91, 92, 93, 94] and will be discussed in more detail in Sec. 6.5.2. The second parameter of the CAM functional, namely the long-range fraction of incorporated Fock exchange α_ℓ , is determined analogously to the global mixing parameter by setting $\alpha_\ell = 1/\epsilon_\infty^{\text{sc}}$. Finally, the inverse range-separation length μ is set to the Thomas-Fermi (TF) screening parameter as given in Eq. (3.6). For liquid water and hexagonal ice, Eq. (3.6) yields μ equal to 0.58 and 0.57 bohr $^{-1}$, respectively (cf. Sec. 6.4.1). These values can be physically interpreted as the inverse of the OH bond length, $1/(0.96 \text{ \AA}) \approx 0.55 \text{ bohr}^{-1}$, and represent in this perspective a typical length scale of the considered material. The values of μ_{TF} are also consistent with those obtained in Ref. [43]. We note that alternative definitions of the μ parameter relying on the effective TF screening [57], the Wigner-Seitz radius [35], or various fitting procedures [35, 47] have been suggested in literature. However, it has been shown that these definitions yield almost identical μ values [35, 47, 137] accompanied with insignificant effects on the band-gap estimates [35]. Therefore, we consider $\mu = \mu_{\text{TF}}$ throughout this chapter. Overall, we investigate three range-separated DDH functionals in this study, denoted as CAM($1, 1/\epsilon_\infty^{\text{sc}}, \mu_{\text{TF}}$), CAM($0.25, 1/\epsilon_\infty^{\text{sc}}, \mu_{\text{TF}}$), and CAM($0, 1/\epsilon_\infty^{\text{sc}}, \mu_{\text{TF}}$). We remark that the present functionals can be compared to similar range-separated DDH functionals in the literature, such as DD-RSH-CAM [47], DSH [57], and RS-DDH [35]. A comparison of these functionals is given in Table 6.2. The

differences are technical and originate from the definition of α_s and the determination of the range-separation parameter μ .

Table 6.2 – Comparison of the range-separated DDH functionals considered in this chapter (bold) with respect to similar approaches reported in the literature: DD-RSH-CAM [47], DSH [57], and RS-DDH [35]. The comparison is made in terms of the fraction of short-range Fock exchange α_s , the fraction of long-range Fock exchange α_ℓ , and the range-separation parameter μ .

	α_s	α_ℓ	μ
CAM (1, $1/\epsilon_\infty^{\text{sc}}$, μ_{TF})	1	$1/\epsilon_\infty^{\text{sc}}$	μ_{TF}
DD-RSH-CAM [47]	1	$1/\epsilon_\infty^{\text{sc}}$	$\mu_{\text{fit}}^{\text{sc}}$ ^a
DSH [57]	1	$1/\epsilon_\infty^{\text{sc}}$	$\mu_{\text{eff. TF}}^{\text{sc}}$ ^b
CAM (0.25, $1/\epsilon_\infty^{\text{sc}}$, μ_{TF})	0.25	$1/\epsilon_\infty^{\text{sc}}$	μ_{TF}
RS-DDH [35]	0.25	$1/\epsilon_\infty^{\text{sc}}$	$\mu_{\text{fit}}^{\text{c}}$
CAM (0, $1/\epsilon_\infty^{\text{sc}}$, μ_{TF})	0	$1/\epsilon_\infty^{\text{sc}}$	μ_{TF}

^a Fitted μ parameter within a self-consistent loop,

^b Effective TF parameter within a self-consistent loop,

^c Fitted μ parameter.

The third class of advanced electronic-structure methods investigated in this chapter consists in hybrid functionals that satisfy Koopmans' condition. For the construction of such functionals, we proceed as described in Sec. 3.2.3. To ensure a consistent comparison with the DDH functionals, we apply this procedure to the global PBE0(α) and to the range-separated CAM($\alpha_s, \alpha_\ell, \mu$) functional.

6.4 Computational aspects

6.4.1 Structural models

The calculations carried out in this chapter make use of well established structural models for liquid water [116] and hexagonal ice [238]. The properties of these models are summarized in Table 6.3. Graphical illustrations are given in Fig. 6.1.

Table 6.3 – Properties of the structural models used for liquid water ℓ -H₂O and hexagonal ice $1h$: Space group, lattice parameters a and c/a , number N of water molecules per unit cell, and mass density ρ . The settings are taken from Refs. [116, 238].

	Space group	a (Å)	c/a	N	ρ (g/cm ³)
ℓ -H ₂ O	$P1$	9.81		32	1.01
$1h$	$P6_3cm$	7.82	0.941	12	0.92

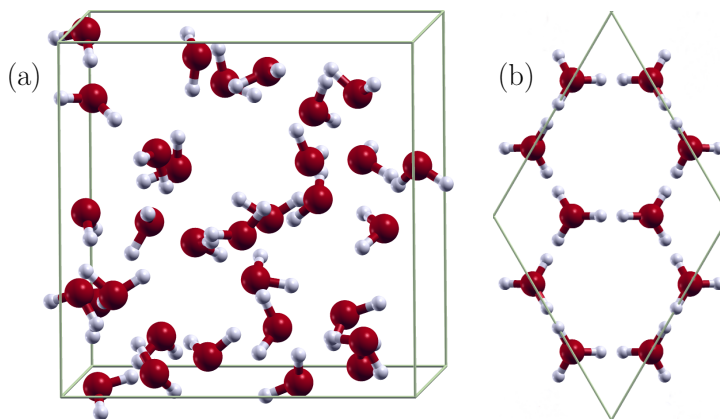


Figure 6.1 – Graphical illustration of (a) an instantaneous configuration of liquid water and (b) the Bernal-Fowler model of hexagonal ice as viewed along the c axis. Oxygen and hydrogen atoms are shown in red and white, respectively.

In the case of liquid water, we consider 20 snapshots taken from a molecular-dynamics simulation performed by Chen *et al.* [116, 237]. The atomic structure in this simulation has been shown to be well equilibrated and to be consistent with the experimental radial distribution functions [116]. The adopted snapshots are evenly spaced in time and correspond to independent configurations of 32 water molecules at ambient temperature (300 K) [116]. The density of liquid water in the considered trajectory is only marginally higher than the experimental one [239] (by $\sim 1\%$), which has been shown to negligibly affect the calculated band gaps [116]. Van der Waals interactions are incorporated in the water trajectory through the use of the revised Vydrov and Van Voorhis (rVV10) nonlocal density functional [240, 241]. The empirical parameter b had been set to 8.9, which ensures a realistic description of the structure of liquid water [242, 116]. As discussed in Sec. 6.2, we account for NQE through an a posteriori band-gap correction. It is therefore appropriate to consider configurations of liquid water in which the nuclei have been treated classically.

For hexagonal ice, we consider a unit cell as given in the Bernal-Fowler model [238]. This model comprises 12 water molecules arranged in a hexagonal lattice and has been adopted in several theoretical studies [243, 242, 211, 244, 245]. To ensure a consistent description of liquid water and hexagonal ice, we relaxed the atomic coordinates of the Bernal-Fowler model with the same rVV10 functional as used by Chen *et al.* [116]. The density of the original Bernal-Fowler model (0.92 g/cm^3) corresponds to that obtained at a temperature just below the melting point [238]. The density at this temperature differs only slightly from that obtained through extrapolation to 0 K, namely 0.93 g/cm^3 (see Ref. [246, 247] and references therein). We checked that such an increase of the density leads to negligible changes in the calculated band gaps (less than 0.01 eV at the PBE level of theory). Therefore, we adopt in this chapter the lattice constants (and thus the density) as originally proposed by Bernal and Fowler [238]. Furthermore, we remark that the present model carries a net dipole moment which is closely connected to the lattice-constant ratio c/a [243]. To investigate the effect of this dipole, we

modified this ratio such that the net dipole moment vanishes, but we found no relevant change in the band gap. Hence, we keep the unmodified c/a ratio throughout this chapter.

We note that hexagonal ice is generally a proton-disordered phase of solid water. To account for this effect, various structural models have been proposed in the literature [248]. The most stable proton-ordered configuration of Ih is referred to as XIh [244]. It has been observed below the order-disorder transition temperature of 72 K [249] and exhibits the space group $Cmc2_1$ [250]. However, Engel *et al.* have shown that the band gaps calculated using the $Cmc2_1$ model and the Bernal-Fowler model differ by less than 0.02 eV at the semilocal and hybrid-functional levels of theory [211]. Likewise, the computed band gaps for 16 distinct Ih models agree within 0.05 eV when the zero-phonon renormalization is taken into account [211]. Therefore, it is justified to focus in our investigation on the Bernal-Fowler model as a representative structural configuration of Ih .

6.4.2 Computational details

The calculations presented in this chapter are carried out with normconserving pseudopotentials to describe core-valence interactions [87, 88]. The energy cutoff of the plane-wave basis set is set at 85 Ry. The adopted \mathbf{k} -point samplings for the bulk calculations in liquid water and hexagonal ice are $1 \times 1 \times 1$ (only the Γ -point) and $2 \times 2 \times 2$, respectively. We calculate the VBM of liquid water following the procedure outlined by Ambrosio *et al.* [190]. This implies the calculation of the average electron density of states (DOS) over the adopted selection of 20 water snapshots. The VBM is then determined through linear extrapolation of the valence-band wing in the DOS as shown in Fig. 6.2.

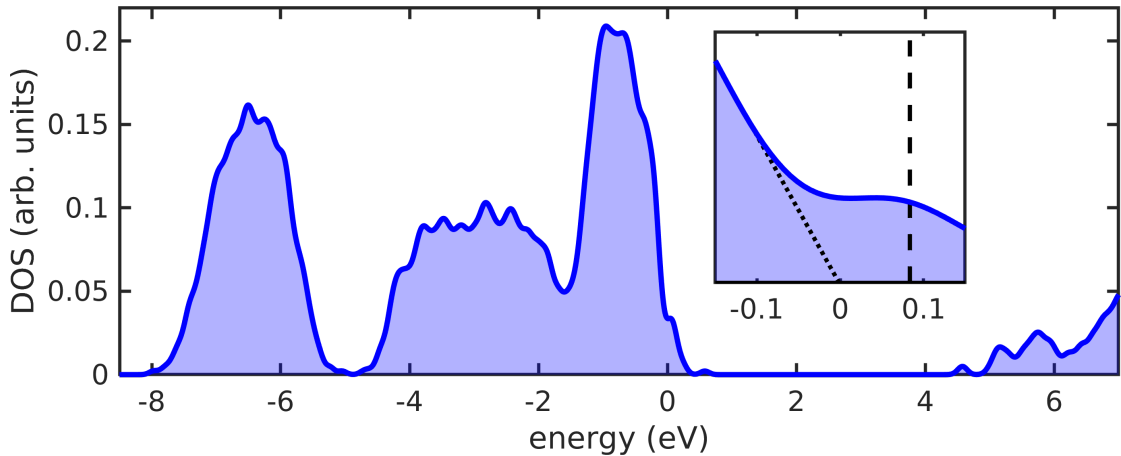


Figure 6.2 – Density of states (DOS) of liquid water as calculated with the PBE functional. The inset shows the DOS near the VBM. The dotted line indicates the linear extrapolation of the valence-band wing of the DOS. The vertical dashed line represents the highest occupied KS level obtained as an average over the 20 classical snapshots. Energies are referred to the VBM as obtained in the extrapolated limit.

This procedure is convenient since it leads to a fast convergence of the VBM with respect to the supercell size [190, 116]. It is noteworthy that the VBM determined in this way differs only marginally (~ 0.1 eV) from the average of the highest occupied KS level irrespective of the employed electronic-structure method. We determine the CBM of liquid water through the average of the lowest unoccupied KS level. This way of proceeding is justified by the work of Pendergast *et al.* [251]. For hexagonal ice, we determine VBM and CBM as the highest occupied and lowest unoccupied KS level, respectively. It is noteworthy that the VBM in hexagonal ice is located at the X point resulting in an indirect band-gap transition $X \rightarrow \Gamma$. The direct band gap at the Γ point is generally ~ 0.1 eV larger than the indirect one. The band gaps reported in the following correspond to the indirect transition.

The QSGW calculations in this chapter are performed with nonlocal commutators for the optical matrix element in the long-wavelength limit, as described in Ref. [167]. The contour deformation technique is used to evaluate the frequency dependence of the dielectric function [118]. We account for 8 real and 4 imaginary frequencies. For the calculation of the dielectric function, we apply the formula of Adler and Wiser [97, 98] using an energy cutoff $E_{\text{cut}}^{\text{eps}}$ of 12 Ry and a total number n_{band} of 2000 bands. In the QSGW calculations, we self-consistently update only the lowest 600 bands and keep the higher-lying states unchanged as obtained with the semilocal PBE functional [5]. For the vertex corrections in the screening, we use the bootstrap exchange-correlation kernel of Sharma *et al.* [109] in the efficient head-only implementation of Chen *et al.* [18, 116].

In order to ensure the convergence of the GW calculations, we separately extrapolate the band gap as a function of the cutoff $E_{\text{cut}}^{\text{eps}}$, the total number of bands n_{band} , and the number of self-consistently updated bands. These extrapolations are performed through an exponential function of the energy cutoff and through linear functions of the inverse number of total bands and of the inverse number of updated bands [117]. The performed extrapolations for the two considered phases of water are illustrated in Fig. 6.3. For hexagonal ice, the extrapolations in $E_{\text{cut}}^{\text{eps}}$ and n_{band} both yield corrections of ~ 0.08 eV. The extrapolation in the number of updated bands gives a correction of only 0.01 eV. For liquid water, the respective corrections are 0.03 eV, 0.28 eV, and 0.13 eV. The corrections associated with the number of bands are larger than in the case of hexagonal ice, due to the larger simulation cell used for liquid water (cf. Sec. 6.4.1). Hence, the QSGW band gaps are corrected by the sum of the three corrections determined above. This results in a global correction of 0.44 eV and 0.17 eV for liquid water and hexagonal ice, respectively.

For the construction of DDH functionals, it is necessary to evaluate the high-frequency dielectric constant ϵ_{∞} . To this end, we perform separate calculations using the finite electric field approach [128]. The proper convergence of ϵ_{∞} is ensured through a four times denser \mathbf{k} -point sampling in the direction of the field. For hexagonal ice, we perform an isotropic average over the trace of the dielectric tensor to account for the small anisotropy in ϵ_{∞} [252, 253].

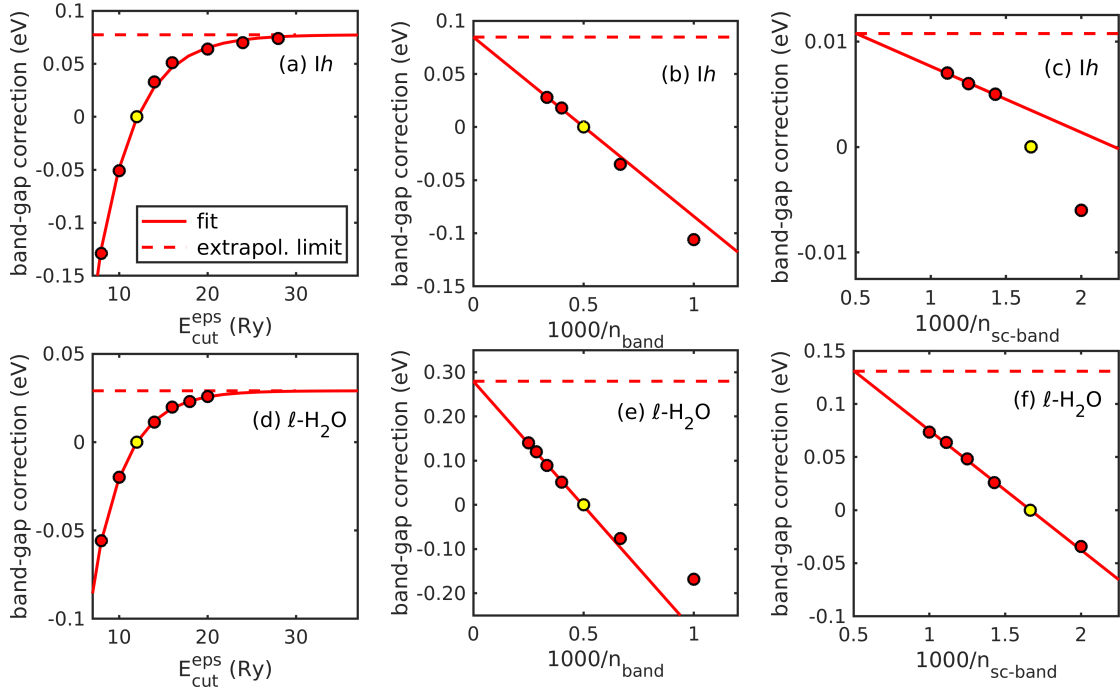


Figure 6.3 – Band-gap corrections (in eV) for hexagonal ice *Ih* (a-c) and liquid water (d-f) according to the extrapolation of the cutoff in the dielectric matrix $E_{\text{cut}}^{\text{eps}}$, the total number of bands n_{band} , and the number of updated bands $n_{\text{sc-band}}$. The yellow circle indicates the parameter value generally used in the QSGW calculations and serves as reference for the band-gap corrections. The solid and the dashed line illustrate the fit and the extrapolated limit, respectively.

The construction of hybrid functionals satisfying Koopmans’ condition is based on single-particle levels of point defects [51, 54, 115]. For liquid water, we generate such defects within the snapshots of Chen *et al.* [116]. For hexagonal ice, we generate the defects within a $2 \times 2 \times 2$ supercell based on the Bernal-Fowler model [238] (cf. Sec. 6.4.1). For both systems, a \mathbf{k} -point sampling at the sole Γ -point ensures converged single-particle levels. Spin-polarized defect calculations are performed whenever unpaired electrons occur.

6.5 Band gaps of liquid water and hexagonal ice

6.5.1 Quasiparticle self-consistent *GW*

First, we examine the band gaps of liquid water and hexagonal ice as obtained with different flavors of the QSGW approach. In particular, we consider (i) the standard QSGW scheme and (ii) QSGW \tilde{W} , which includes vertex corrections in the screening. The results of our calculations are shown in Table 6.4 together with the experimental band-gap references.

Table 6.4 – Fundamental band gaps (in eV) for liquid water ℓ -H₂O and hexagonal ice Ih as calculated with the QSGW and QSG \tilde{W} methods. The band gaps correspond to temperatures of 300 and 77 K, respectively. The reported band gaps include the corrections associated to NQE and ZPR (cf. Sec. 6.2). Band gaps inferred from experimental data are given as reference (cf. Sec. 6.2).

	QSGW	QSG \tilde{W}	Expt.
ℓ -H ₂ O	9.6	9.1	9.0 \pm 0.2^a
Ih	9.8	9.3	9.4 \pm 0.3^b

^a $T = 300$ K, ^b $T = 77$ K.

The GW schemes applied to liquid water and hexagonal ice give results that compare similarly with the corresponding experimental references. The standard QSGW method yields band gaps that are overestimated. Indeed, the calculated band gaps are higher by 0.4 eV and 0.1 eV than the upper limit of the reference range for liquid water and hexagonal ice, respectively. Similar overestimations have been observed for various other materials [17, 18] and have been attributed to the neglect of electron-hole interactions in the calculation of the screened W . We overcome this limitation by carrying out QSG \tilde{W} calculations, which include vertex corrections in the screening (\tilde{W}). In this scheme, the band gaps are smaller by 0.5 eV with respect to those obtained without vertex corrections. When comparing to experimental values, we record a very good agreement for both phases of water since the calculated band gaps fall within the reference range. Such an accuracy is in agreement with previous studies, which have found typical mean absolute errors of ~ 0.2 eV for such QSG \tilde{W} calculations [17, 18, 114].

We note that our QSG \tilde{W} calculations can be confronted with other GW studies in the literature. For liquid water, several one-shot G_0W_0 calculations have been performed. With respect to our QSG \tilde{W} scheme, this method systematically yields underestimated band gaps when semilocal results are used as starting points [212, 213, 60, 217] and overestimated band gaps when hybrid functional results are used [188]. As far as previous self-consistent GW methods are concerned, we take under consideration the recent study of Chen *et al.* [116]. These authors obtained a band gap of 8.9 eV also by means of QSG \tilde{W} calculations. The difference of 0.2 eV with respect to the present results should be attributed to small differences in the computational setup. Indeed, we evaluate the nonlocal commutators for the optical matrix element in the long-wavelength limit as described in Ref. [167] and use more stringent convergence criteria to overcome the criticism raised in Ref. [214]. The latter work reported a band gap of liquid water obtained with the eigenvalue self-consistent GW (evGW) scheme. The calculated band gap of 9.07 eV is in good agreement with the present QSG \tilde{W} band gap, despite the absence of explicit vertex corrections in the evGW approach [214]. Our results can also be compared with those of Kharche *et al.* [195]. By means of full-frequency-spectrum-only self-consistent GW calculations, these authors calculated a band gap of 9.53 eV for classical water, which was later revised to 9.7 eV [195]. Accounting for a band-gap reduction of 0.7 eV due to NQE [116], we correct their band-gap estimate to 9.0 eV. This result has been obtained without including

explicit vertex corrections, but is nevertheless in agreement with our QSG \tilde{W} band gap of 9.1 eV.

For hexagonal ice, fewer GW band-gap calculations can be found in the literature. Yim *et al.* reported a band gap of 8.9 eV obtained with one-shot G_0W_0 calculations. Similarly, Fang *et al.* found a band gap of 9.17 eV by means of a partially self-consistent GW_0 approach [216]. However, both studies did not account for the sizeable zero-phonon renormalization (ZPR) of ~ 1.5 eV (cf. Sec. 6.2). Therefore, the apparent agreement with our QSG \tilde{W} calculations results from error cancellation. In another investigation, Hahn *et al.* determined a larger band gap of ~ 10 eV using an approximate GW scheme, which incorporates a model dielectric function and lacks self-consistency [215]. When this result is corrected for ZPR, one finds a band gap of ~ 8.5 eV, to be compared with the band gap of 9.3 eV obtained in the present work.

Overall, we conclude that the QSG \tilde{W} approach used in the present work corresponds to the most elaborate theoretical framework applied so far to either liquid water or hexagonal ice. Thus, this scheme is expected to give the most accurate estimates for the band gaps of these systems.

6.5.2 Dielectric-dependent hybrid functionals

We here devote special attention to DDH functionals and to their band-gap estimates for liquid water and hexagonal ice. The free parameters of these functionals are determined through the dielectric response of the material under investigation. In this section, we therefore present the band gaps resulting from the DDH functionals together with their corresponding dielectric constants.

First, we apply the DDH procedure to the global hybrid functional PBE0(α). The dielectric constant as calculated within the self-consistent workflow is shown in Fig. 6.4(a) for the case of hexagonal ice. We observe that ϵ_∞ converges within four iterations to the self-consistent value $\epsilon_\infty^{\text{sc}}$. It is noteworthy that this specific value is independent of the considered starting point [43], as we checked using two distinct initializations, namely from results obtained with the functionals PBE and PBE0(0.7) (cf. Fig. 6.4). The calculated value of $\epsilon_\infty^{\text{sc}}$ is in agreement with its experimental counterpart showing an underestimation of only $\sim 5\%$ (Table 6.5). For liquid water, the self-consistent calculation of the dielectric constant proceeds analogously and results in a similar comparison with experiment (Table 6.5). In this case, $\epsilon_\infty^{\text{sc}}$ is only marginally affected by the considered water snapshot. We analyzed various snapshots and observed variations in $\epsilon_\infty^{\text{sc}}$ smaller than ~ 0.02 . It is sufficient to average over five different water snapshots to achieve a converged mean value with a standard deviation of less than 0.01.

Next, we consider the band gaps as obtained with the global DDH functional. The convergence of the band gap within the DDH procedure is shown in Fig. 6.4(b) for the case of hexagonal ice. Analogously to the dielectric constant, the band gap converges within four iterations

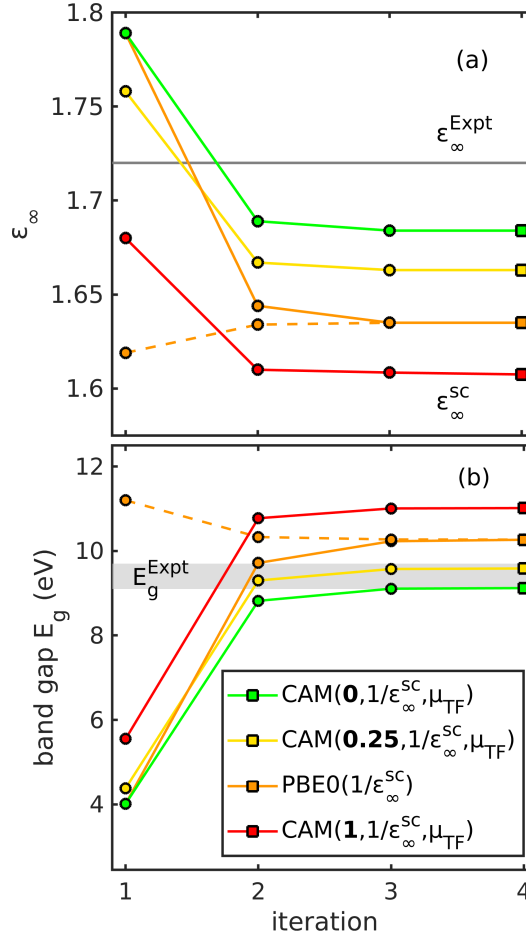


Figure 6.4 – Convergence of (a) the dielectric constant ϵ_∞ and (b) the band gap E_g within the self-consistent DDH scheme for hexagonal ice Ih. Iteration steps and converged results are visualized as circles and squares, respectively. The global hybrid functional PBE0($1/\epsilon_\infty^{\text{SC}}$) and the range-separated hybrid functionals CAM($0, 1/\epsilon_\infty^{\text{SC}}, \mu_{\text{TF}}$), CAM($0.25, 1/\epsilon_\infty^{\text{SC}}, \mu_{\text{TF}}$), and CAM($1, 1/\epsilon_\infty^{\text{SC}}, \mu_{\text{TF}}$) are examined. For the global DDH functional, the independence of the converged results from the starting point is illustrated through distinct initializations, based on results obtained with either PBE (solid line) or PBE0(0.7) (dashed line) functionals. The reported band gaps include the corrections due to ZPR (cf. Sec. 6.2). The horizontal gray line corresponds to the experimental high-frequency dielectric constant $\epsilon_\infty^{\text{Expt}}$ [254]. The shaded area indicates the interval corresponding to the experimental reference values E_g^{Expt} inferred in Sec. 6.2.

irrespective of the adopted starting point. The converged result for the band gap corresponds to the functional PBE0($1/\epsilon_\infty^{\text{SC}}$). The convergence behavior for liquid water is analogous to that of hexagonal ice shown in Fig. 6.4(b). The spread of 0.01 in $\epsilon_\infty^{\text{SC}}$ due to the statistical variety of water snapshots results in variations smaller than 0.1 eV in the band-gap estimate.

The band gaps obtained with the PBE0($1/\epsilon_\infty^{\text{SC}}$) functional for both liquid water and hexagonal ice are given in Table 6.6 together with experimental references. We observe an overestimation

6.5. Band gaps of liquid water and hexagonal ice

Table 6.5 – High-frequency dielectric constant $\epsilon_\infty^{\text{sc}}$ of liquid water ℓ -H₂O and hexagonal ice Ih as calculated self-consistently within the DDH procedure. The dielectric constants are obtained either with the global functional PBE0($1/\epsilon_\infty^{\text{sc}}$) or with the range-separated functional CAM($\alpha_s, 1/\epsilon_\infty^{\text{sc}}, \mu_{\text{TF}}$). Various settings for the short-range fraction of Fock exchange α_s are distinguished. Experimental dielectric constants are given for comparison.

	PBE0($1/\epsilon_\infty^{\text{sc}}$)	CAM($\alpha_s, 1/\epsilon_\infty^{\text{sc}}, \mu_{\text{TF}}$)			Expt.
		$\alpha_s = 1$	$\alpha_s = 0.25$	$\alpha_s = 0$	
ℓ -H ₂ O	1.69	1.66	1.72	1.74	$1.77 \pm 0.01^{\text{a}}$
Ih	1.64	1.61	1.66	1.68	1.72^{b}

^a Refs. [218, 220], ^b Ref. [254].

of the band gap for both water phases. With respect to the upper limit of the reference interval the deviations amount to 0.8 and 0.6 eV for liquid water and hexagonal ice, respectively. We attribute this band-gap overestimation to the underestimation of the dielectric constant with respect to the experimental value [cf. Fig. 6.4(a) and Table 6.5].

Table 6.6 – Fundamental band gaps (in eV) of liquid water ℓ -H₂O and hexagonal ice Ih as calculated with DDH functionals. The band gaps correspond to temperatures of 300 and 77 K, respectively. The band gaps are obtained either with the global functional PBE0($1/\epsilon_\infty^{\text{sc}}$) or with the range-separated functional CAM($\alpha_s, 1/\epsilon_\infty^{\text{sc}}, \mu_{\text{TF}}$). The value of the parameter $1/\epsilon_\infty^{\text{sc}}$ is given in parentheses. Various settings for the short-range fraction of Fock exchange α_s are distinguished. The reported band gaps include the corrections associated to NQE and ZPR (cf. Sec. 6.2). Band gaps inferred from experimental data are given as reference (cf. Sec. 6.2).

	PBE0($1/\epsilon_\infty^{\text{sc}}$)	CAM($\alpha_s, 1/\epsilon_\infty^{\text{sc}}, \mu_{\text{TF}}$)			Expt.
		$\alpha_s = 1$	$\alpha_s = 0.25$	$\alpha_s = 0$	
ℓ -H ₂ O	10.0 (0.59)	10.9 (0.60)	9.5 (0.58)	9.0 (0.57)	9.0 \pm 0.2^a
Ih	10.3 (0.61)	11.0 (0.62)	9.6 (0.60)	9.1 (0.59)	9.4 \pm 0.3^b

^a $T = 300$ K, ^b $T = 77$ K.

Our result for the band gap of hexagonal ice can be compared with that obtained by Skone *et al.*, who used a similar self-consistent approach [43]. These authors reported a band gap of 11.71 eV for hexagonal ice [43]. When this result is corrected for the ZPR, one obtains a band gap of 10.2 eV, in good agreement with the value of 10.3 eV obtained in the present work.

In the second part of this section, we apply the DDH construction procedure to the range-separated functional CAM($\alpha_s, \alpha_\ell, \mu$). This functional incorporates different fractions of Fock exchange in the short (α_s) and in the long range (α_ℓ). The transition between the two limiting regimes is mediated by the range-separation parameter μ . For the determination of these parameters, we proceed as discussed in Sec. 6.3. In particular, we consider three different

settings for the short-range fraction of Fock exchange α_s , namely α_s equal to 1, 0.25, and 0. The respective range-separated DDH functionals are then denoted CAM(0, $1/\epsilon_\infty^{\text{sc}}, \mu_{\text{TF}}$), CAM(0.25, $1/\epsilon_\infty^{\text{sc}}, \mu_{\text{TF}}$), and CAM(1, $1/\epsilon_\infty^{\text{sc}}, \mu_{\text{TF}}$).

The convergence of the DDH scheme for the three functionals considered is shown in Fig. 6.4 in the case of hexagonal ice. The convergence behavior is generally very similar to that of the global DDH functional, but the results deserve close attention. First, we focus on the self-consistently determined dielectric constants $\epsilon_\infty^{\text{sc}}$. The values resulting from the three range-separated DDH functionals are given in Table 6.5 for both liquid water and hexagonal ice. We observe a systematic variation of $\epsilon_\infty^{\text{sc}}$ as a function of α_s . More specifically, the smaller the short-range Fock exchange α_s , the higher the dielectric constant $\epsilon_\infty^{\text{sc}}$. This systematic trend manifests in deviations from the experimental references ranging from only $\sim 2\%$ for $\alpha_s = 0$ up to $\sim 6\%$ for $\alpha_s = 1$. Overall, these dielectric constants agree with experiment irrespective of α_s . However, the best agreement is clearly achieved for $\alpha_s = 0$ and the corresponding functional CAM(0, $1/\epsilon_\infty^{\text{sc}}, \mu_{\text{TF}}$).

Next, we investigate the band gaps resulting from the three range-separated DDH functionals. Our results for liquid water and hexagonal ice are given in Table 6.6. We find that also the band gap exhibits a systematic variation according to the value set for the parameter α_s . More specifically, the smaller the short-range Fock exchange α_s , the smaller the band gap obtained with the corresponding DDH functional CAM(α_s , $1/\epsilon_\infty^{\text{sc}}, \mu_{\text{TF}}$). In the following, we separately discuss the results for the three settings of α_s .

For $\alpha_s=1$ and the associated DDH functional CAM(1, $1/\epsilon_\infty^{\text{sc}}, \mu_{\text{TF}}$), we obtain strongly overestimated band gaps. With respect to the upper limit of the reference interval, the deviations amount to 1.7 and 1.3 eV for liquid water and hexagonal ice, respectively. This result is unexpected insofar the similar DD-RSH-CAM approach of Chen *et al.* provides accurate band gaps for a variety of semiconductors and insulators [47]. Similarly, we found a good agreement with experiment for a series of metal-halide perovskites in Chapter 5. The origin of the failure of this method for liquid water and hexagonal ice remains unclear at the moment and deserves further investigation.

For $\alpha_s=0.25$ and the corresponding DDH functional CAM(0.25, $1/\epsilon_\infty^{\text{sc}}, \mu_{\text{TF}}$), we observe a good agreement with the experimental references. Indeed, for hexagonal ice the computed band gap falls within the reference interval. For liquid water, we observe a small overestimation of 0.3 eV with respect to the upper limit of the range of experimental values. Interestingly, the band gaps obtained with CAM(0.25, $1/\epsilon_\infty^{\text{sc}}, \mu_{\text{TF}}$) can be confronted with the similar RS-DDH approach of Skone *et al.* [35]. These authors reported a band gap for hexagonal ice of 10.94 eV [35]. When this result is corrected for ZPR, one finds a band gap of 9.4 eV, in good agreement with the value of 9.6 eV found in the present work.

For $\alpha_s=0$ and the associated DDH functional CAM(0, $1/\epsilon_\infty^{\text{sc}}, \mu_{\text{TF}}$), we achieve the best agreement with experiment among the examined range-separated DDH functionals. Indeed, we find band-gap estimates falling within the experimental range for both phases of water.

On the basis of the agreement with experiment for the dielectric constant, we are led to elect the CAM(0, $1/\epsilon_{\infty}^{\text{SC}}$, μ_{TF}) as the most reliable range-separated DDH functional for liquid water and hexagonal ice. This assessment is further supported by the band gaps achieved with this functional, which fall within the range of experimental values for the two phases of water.

Before closing this section, we question to what extent the nature of the present DDH functionals can be considered nonempirical. The global hybrid functional PBE0($1/\epsilon_{\infty}^{\text{SC}}$) is entirely determined through the dielectric response of the material and is therefore fully nonempirical. However, for the range-separated functionals, the specific value adopted for α_s has a significant effect on the resulting band gaps. In a fully nonempirical DDH scheme, these different settings should be either irrelevant for the outcome or determined on the basis of an exact property of generalized Kohn-Sham theory [26]. This is manifestly not the case for the range-separated DDH functionals. This remaining indetermination also underlies the lack of consistency among the various range-separated DDH approaches in the literature [35, 47, 57]. Despite this open issue, we consider the functional CAM(0, $1/\epsilon_{\infty}^{\text{SC}}$, μ_{TF}) as the most reliable DDH functional on the grounds that it achieves the best agreement with the experimental dielectric constants.

6.5.3 Hybrid functionals satisfying Koopmans' condition

We now focus on hybrid functionals satisfying Koopmans' condition. For the construction of such functionals, we apply the procedure outlined in Sec. 3.2.3 to various localized states in the two investigated phases of water. We introduce such states through interstitial atoms (H_i , F_i , Cl_i , Br_i), substitutional atoms ($\text{F}_{\text{H}_2\text{O}}$, $\text{Cl}_{\text{H}_2\text{O}}$, $\text{Br}_{\text{H}_2\text{O}}$), or inorganic radicals (OH , NH_2). In the case of hexagonal ice, we also consider the Bjerrum defect pair, which results from locally disregarding the second ice rule [255, 256, 257]. More specifically, one water molecule is pivoted in such a way that one pair of neighboring oxygen atoms is formed with no intermediate hydrogen atom and another pair occurs with two intermediate hydrogen atoms [257]. For each considered localized state the degree of hybridization δ is computed [54]. This quantity measures the undesired hybridization between the localized defect state and the delocalized band-edge states. Through the minimization of δ , we can identify the most reliable localized defect states [54, 115, 258].

First, we examine the global hybrid functional PBE0(α) and determine the mixing parameter α_K which satisfies Koopmans' condition. Our results are shown in Fig. 6.5(a) for the case of hexagonal ice. We find different values of α_K for the various localized states. The $+/-$ and $0/-$ charge transitions of the hydrogen interstitial H_i determine the maximal and minimal value of α_K . Their sizeable variation can be attributed to strong hybridizations with the band-edge states. The mixing parameters obtained through the other localized states fall within a much narrower range. This property goes together with a systematically lower degree of hybridization for the involved defects. The smallest δ are observed for the radical OH , the radical NH_2 , the fluorine interstitial F_i , the fluorine substitutional $\text{F}_{\text{H}_2\text{O}}$, and the chlorine

substitutional $\text{Cl}_{\text{H}_2\text{O}}$. The Bjerrum defect pair, the bromine substitutional $\text{Br}_{\text{H}_2\text{O}}$, and chlorine interstitial Cl_i also show rather small values of δ , but yet noticeably larger than the previous five defects.

To account for the different behaviors of the various localized states, we proceed in the following way. We consider the five defects with the lowest degree of hybridization and compute the root mean square (rms) of their individual deviations from Koopmans' condition through

$$\Delta_K^{\text{rms}}(\alpha) = \sqrt{\frac{1}{5} \sum_{i=1}^5 [\Delta_K^i(\alpha)]^2}. \quad (6.1)$$

The rms deviation Δ_K^{rms} resulting from Eq. (6.1) is displayed in Fig. 6.5(b) for the case of hexagonal ice. We find that Δ_K^{rms} depends continuously on the fraction of Fock exchange α and reaches a minimum for a specific value in close proximity of the crossing points of the individual defects. Hence, this minimum accounts effectively for the different localized states and enables us to determine α_K in a robust fashion. The minimum value of Δ_K^{rms} is found to be ~ 0.2 eV, which corresponds to $\sim 2\%$ of the band gaps involved. This indicates that Koopmans' condition is effectively fulfilled for the various localized states albeit with a finite accuracy. We checked that the inclusion of the more hybridized bromine substitutional $\text{Br}_{\text{H}_2\text{O}}$ and Bjerrum defect pair among the defects considered in Eq. (6.1) affects the extracted α_K by less than 0.01 corresponding to changes of less than 0.1 eV in the band-gap estimate. We therefore consider only the five defects with the lowest δ . With the procedure outlined above, we find mixing parameters α_K of 0.47 and 0.48 for liquid water and hexagonal ice, respectively. In particular, the result for liquid water is in good agreement with the value of $\alpha = 0.45$ determined empirically by Ambrosio *et al.* [189]. In the case of liquid water, α_K is found to be almost independent of the considered water snapshot, with variations within ~ 0.01 . Therefore, it is sufficient to average over five different water snapshots to achieve a converged mean value.

The band gaps obtained with the functional $\text{PBE0}(\alpha_K)$ are compared with the experimental reference values in Table 6.7. The corresponding mixing parameter α_K are given in parentheses. For liquid water, we observe a small band-gap underestimation of 0.1 eV with respect to the lower bound of the experimental range. Similarly, we find an underestimation of 0.2 eV for hexagonal ice. This level of accuracy is in line with previous studies employing the nonempirical functional $\text{PBE0}(\alpha_K)$ for band-gap predictions [51, 54, 115].

It is of interest to compare the present results obtained with the functional $\text{PBE0}(\alpha_K)$ with those obtained with the functional $\text{PBE0}(1/\varepsilon_\infty^{\text{sc}})$ (cf. Table 6.6). Both originate from the global hybrid functional $\text{PBE0}(\alpha)$, but the parameters are determined through distinct construction schemes. We find that the mixing parameter $1/\varepsilon_\infty^{\text{sc}}$ is systematically higher than α_K . Consequently, the same holds for the respective band gaps obtained with $\text{PBE0}(1/\varepsilon_\infty^{\text{sc}})$ and $\text{PBE0}(\alpha_K)$. With respect to the experimental band-gap references, $\text{PBE0}(\alpha_K)$ shows a significantly better accord than $\text{PBE0}(1/\varepsilon_\infty^{\text{sc}})$. We note that similar considerations have been found to apply to the metal-

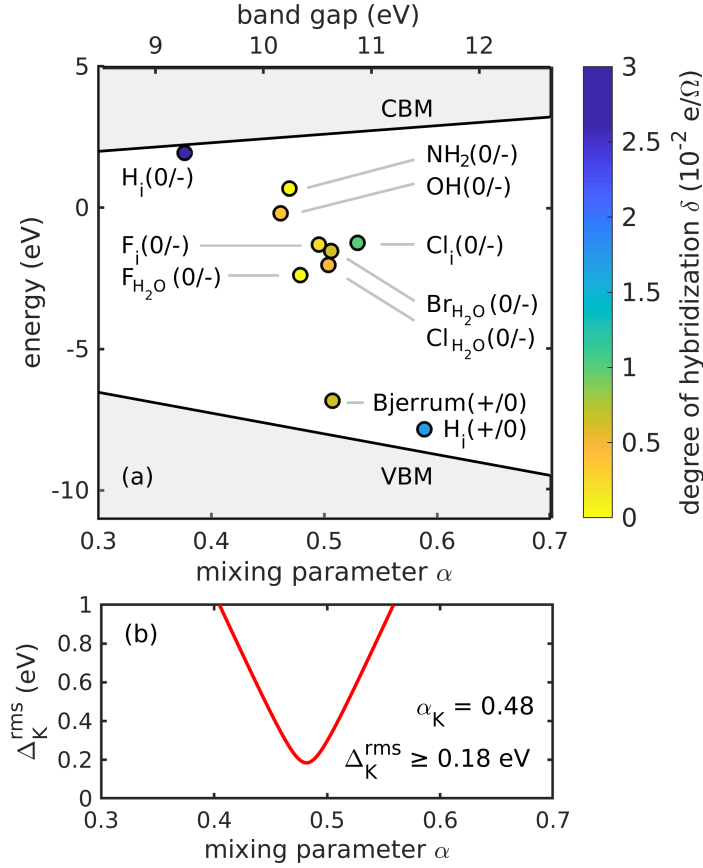


Figure 6.5 – (a) Band edges and defect energies for various localized states in hexagonal ice displayed versus the mixing parameter α incorporated in the PBE0(α) functional. The degree of hybridization δ of each localized state is visualized through the color scale. The indicated band gaps are obtained with the functional PBE0(α) prior to the application of the corrections described in Sec. 6.2. (b) rms deviation from Koopmans' condition Δ_K^{rms} as a function of the mixing parameter α . The value of α_K and the corresponding minimum of Δ_K^{rms} are indicated.

halide perovskites studied in Chapter 5. While both Koopmans' condition and the asymptotic long-range dielectric screening correspond to properties of the exact underlying generalized Kohn-Sham functional, the present results further support that these two properties are physically distinct [56]. The class of global PBE0(α) hybrid functionals described by the single parameter α is thus clearly insufficient to describe both properties at the same time, and thus prones the consideration of more elaborate hybrid functionals.

Next, we examine CAM functionals that satisfy Koopmans' condition. These functionals include three parameters α_s , α_ℓ , and μ . Since Koopmans' condition is not sufficient to fix all three parameters, we proceed in the following way. First, we narrow down the parameter space by setting α_ℓ equal to $1/\epsilon_\infty^{Expt}$. For the high-frequency dielectric constant ϵ_∞^{Expt} , we consider 1.77 [218, 220] and 1.72 [254] for liquid water and hexagonal ice, respectively. We remark that taking the experimental value for the dielectric constant introduces an empirical parameter in

Table 6.7 – Fundamental band gaps (in eV) of liquid water ℓ -H₂O and hexagonal ice Ih as calculated with hybrid functionals satisfying Koopmans' condition. The band gaps correspond to temperatures of 300 and 77 K, respectively. The band gaps are obtained either with the global functional PBE0(α_K) or with the range-separated functional CAM($\alpha_{s,K}$, $1/\epsilon_\infty^{\text{Expt}}$, μ_{TF}). The values of the parameters α_K and $\alpha_{s,K}$ are given in parentheses. The reported band gaps include the corrections associated to NQE and ZPR (cf. Sec. 6.2). Band gaps inferred from experimental data are given as reference (cf. Sec. 6.2).

	PBE0(α_K)	CAM($\alpha_{s,K}$, $1/\epsilon_\infty^{\text{Expt}}$, μ_{TF})	Expt.
ℓ -H ₂ O	8.7 (0.47)	9.2 (0.18)	9.0 ± 0.2^a
Ih	8.9 (0.48)	9.3 (0.18)	9.4 ± 0.3^b

^a $T = 300$ K, ^b $T = 77$ K.

the scheme. However, this could in principle be eliminated by taking the PBE value as a starting point and by carrying out a self-consistent cycle to ensure that the final value be consistent with the resulting hybrid functional. Setting the experimental value from the beginning ensures the physically correct screening in the long range and is sufficient for the purpose of the present investigation. Second, we treat the inverse range-separation length μ as a free parameter that we vary systematically. Third, we fix α_s through the enforcement of Koopmans' condition. The determined parameter is denoted $\alpha_{s,K}$ and depends parametrically on μ . We note that the resulting functional CAM($\alpha_{s,K}$, $1/\epsilon_\infty^{\text{Expt}}$, μ) incorporates two exact physical constraints, namely the correct long-range screening as well as Koopmans' condition [56]. The free parameter μ allows one to mediate between two extreme regimes. Indeed, for $\mu \rightarrow 0$, the present CAM functional reverts to the global hybrid functional PBE0(α_K), which is entirely determined by Koopmans' condition. Instead, for $\mu \rightarrow \infty$, the functional converges asymptotically to the functional PBE0($1/\epsilon_\infty^{\text{Expt}}$), which is entirely determined by the dielectric response. In the latter limit, the piece-wise linearity can no longer be satisfied. The continuous variation of μ allows one to study the band-gap estimate in between these two extreme cases.

For the enforcement of Koopmans' condition to the functional CAM($\alpha_{s,K}$, $1/\epsilon_\infty^{\text{Expt}}$, μ), we adopt the following procedure. We carry out an extended study on hexagonal ice and assume that an analogous analysis would also hold for liquid water insofar both phases of water exhibit very similar electronic structures. We solely consider the five localized states with the smallest degrees of hybridization, namely the radical OH, the radical NH₂, the fluorine interstitial F_i, the fluorine substitutional F_{H₂O}, and the chlorine substitutional Cl_{H₂O}. We verify that the degree of hybridization of these defects remains small when considering the range-separated CAM functional. Thereby, we ensure a reliable enforcement of Koopmans' condition and a consistent comparison with the PBE0(α_K) functional. We evaluate the deviations Δ_K^i for these five localized states and compute the rms deviation Δ_K^{rms} using Eq. (6.1). The minimum of Δ_K^{rms} defines $\alpha_{s,K}$ for each specific value of the range-separation parameter μ . It is noteworthy that the adopted construction scheme requires numerous supercell calculations at the hybrid functional level. To reduce the computational burden, we first compute Δ_K^{rms} using the Bernal-

Fowler unit cell with 12 water molecules (cf. Sec. 6.4.1). We use a grid in the two-dimensional space $(\alpha_{s,K}, \mu)$ including 6 values of $\alpha_{s,K}$ and 6 values of μ . Subsequently, we refine these results using a supercell with 96 water molecules. We generally observe small variations of Δ_K^{rms} as compared to the smaller supercell. Hence, the values of the grid obtained with the smaller supercell are adjusted using a linear interpolation of the differences achieved for a 2×2 subset of relevant points in the space (α_s, μ) .

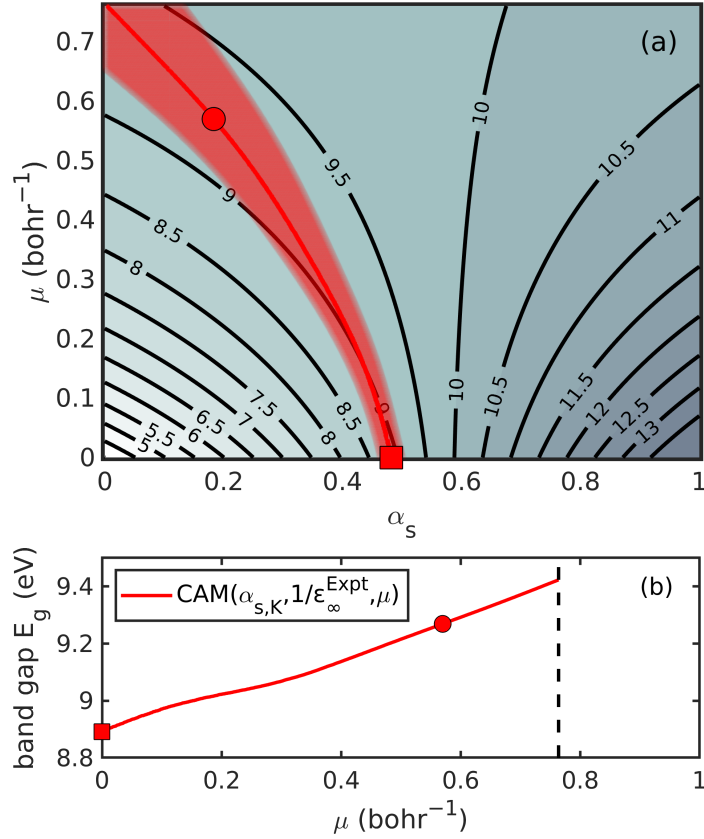


Figure 6.6 – Band gaps (in eV) of hexagonal ice *Ih* as obtained with the CAM functional: (a) iso-contour plot for the band gap as obtained with the hybrid functional $\text{CAM}(\alpha_s, 1/\epsilon_\infty^{\text{Expt}}, \mu)$. The short-range fraction of Fock exchange α_s and the screening parameter μ are varied systematically. The red line indicates Koopmans' curve $(\alpha_{s,K}, \mu)$ as obtained through the minimization of Δ_K^{rms} . The shaded region indicates deviations of less than 0.1 eV from the minimum of Δ_K^{rms} ; (b) band gaps as obtained with the hybrid functionals $\text{CAM}(\alpha_{s,K}, 1/\epsilon_\infty^{\text{Expt}}, \mu)$ along Koopmans' curve. The vertical dashed line limits the range in which Koopmans' condition can be fulfilled. Data points corresponding to the functionals $\text{PBE0}(\alpha_K)$ and $\text{CAM}(\alpha_{s,K}, 1/\epsilon_\infty^{\text{Expt}}, \mu_{\text{TF}})$ are indicated with squares and circles, respectively. The reported band gaps include the corrections resulting from the ZPR (cf. Sec. 6.2).

Based on the procedure outlined above, we determine $\alpha_{s,K}$ as a function of μ . The obtained curve $(\alpha_{s,K}, \mu)$ is denoted Koopmans' curve and is shown in Fig. 6.6(a). We observe that $\alpha_{s,K}$ decreases continuously with increasing μ . For $\mu = 0$, the range-separated CAM functional reverts to the global hybrid functional PBE0 and we thus consistently have $\alpha_{s,K} = \alpha_K$. The

upper limit for μ is reached at $\sim 0.75 \text{ bohr}^{-1}$, when $\alpha_{s,K}$ vanishes. For larger values of μ , Δ_K^{rms} shows no minimum and it is therefore no longer possible to enforce Koopmans' condition.

Next, we monitor the band gap along Koopmans' curve highlighted in Fig. 6.6(a) to identify the range of values consistent with the hybrid functionals $\text{CAM}(\alpha_{s,K}, 1/\epsilon_{\infty}^{\text{Expt}}, \mu)$. The extracted band gaps are given as a function of μ in Fig. 6.6(b). We observe an almost linear increase of the band gap with μ . For vanishing μ , we recover the band gap of 8.9 eV pertaining to the $\text{PBE0}(\alpha_K)$ functional. For the upper limit of μ , we achieve a band gap of 9.4 eV. This allows us to restrain the range of values achieved with the CAM functionals to $9.15 \pm 0.25 \text{ eV}$. We remark that these values are obtained for functionals that reproduce both Koopmans' condition and the asymptotic behavior of the Coulomb interaction. For restraining the value of the band gap even further, it is necessary to invoke additional physical constraints. Similarly to the discussion for selecting the optimal DDH functional, we could use the deviation of the calculated dielectric constant from the experimental value to identify the optimal functional along the Koopmans' curve. However, the calculated dielectric constant is found to vary little among the functionals defined in this way (1.65 ± 0.01) and can thus not be used for this purpose. Another physically motivated way to identify the optimal functional consists in realizing that the variation along the Koopmans' curve is determined by the scale of spatial variation in the screening. It is therefore reasonable to adopt the value of $\mu = \mu_{\text{TF}}$ (cf. Sec. 6.3). For hexagonal ice, $\mu_{\text{TF}} = 0.57 \text{ bohr}^{-1}$. An explicit fit of the spatially dependent dielectric constant, would give $\mu = 0.52 \text{ bohr}^{-1}$ [35], corresponding to a band-gap difference of only 0.04 eV. This leads us to favor the functional $\text{CAM}(\alpha_{s,K}, 1/\epsilon_{\infty}^{\text{Expt}}, \mu_{\text{TF}})$, which gives a band gap of 9.3 eV for hexagonal ice.

In light of the present considerations, the functional $\text{CAM}(\alpha_{s,K}, 1/\epsilon_{\infty}^{\text{Expt}}, \mu_{\text{TF}})$ satisfies Koopmans' condition, reproduces the long-range asymptotic potential, and includes the correct length-scale for the variation in the screening. This form of hybrid functional should be preferred over the functional $\text{PBE0}(\alpha)$, which does not possess sufficient free parameters to concomitantly account for all these properties. Hence, we adopt this form of CAM functional not only to predict the band gap of hexagonal ice but also that of liquid water. In the case of water, we thus adopt $\mu = \mu_{\text{TF}}$ and determine $\alpha_{s,K}$ by imposing Koopmans' condition on the same set of five defects employed for hexagonal ice. The consideration of five water snapshots is again sufficient to converge the mean value of $\alpha_{s,K}$. The calculated band gaps are given in Table 6.7 for both phases of water. We observe that the band gaps resulting from the functional $\text{CAM}(\alpha_{s,K}, 1/\epsilon_{\infty}^{\text{Expt}}, \mu_{\text{TF}})$ increase by $\sim 0.4\text{--}0.5 \text{ eV}$ with respect to those obtained with the functional $\text{PBE0}(\alpha_K)$. This result is consistent with the trend observed in Fig. 6.6(b). The agreement with experiment is very good as the band gaps obtained with this CAM functional fall within the range of the experimental reference values.

Before closing this section, it is noteworthy to compare the extension to CAM functionals with results for other materials previously reported in the literature [51, 115]. So far, Koopmans' curve has generally been found to remain close to a band-gap isoline, indicating that the range-separated functional does not improve the description achieved with the simpler global hybrid

functional (cf. Sec. 5.4.2). However, in the case of NaF, the band gap obtained with PBE0($1/\epsilon_\infty$) differed from that obtained with PBE0(α_K) by about 0.5 eV and some deviation from the isoline appeared [51]. Similarly, we here find for the two phases of water deviations from the isoline as large as 0.5 eV. This suggests that such deviations primarily occur in materials with large band gaps and low dielectric constants. More generally, from the analysis presented above [cf. Fig. 6.6(b)], such a behavior arises when the band gap achieved with the PBE0(α_K) substantially differs from that obtained with PBE0($1/\epsilon_\infty$).

6.6 Summary

In this chapter, we calculate the fundamental band gap of liquid water and hexagonal ice through advanced electronic-structure methods. We investigate specifically the performance of both state-of-the-art *GW* calculations and nonempirical hybrid functionals. The free parameters of the hybrid functionals are determined either through the dielectric response of the material or the enforcement of Koopmans' condition to localized states. We apply both construction schemes to two classes of hybrid functionals, namely the global PBE0 and the range-separated CAM functionals. The comparison of such a variety of advanced electronic-structure methods within a consistent computational setup corresponds to one of the main strengths of our work and brings valuable insight into the issue concerning the fundamental band gaps of liquid water and hexagonal ice. The results obtained in this chapter are summarized in Fig. 6.7.

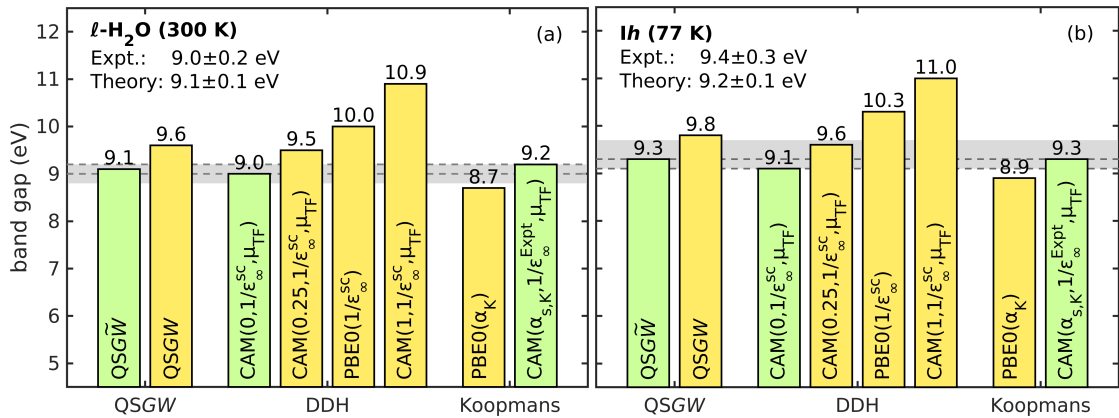


Figure 6.7 – Fundamental band gaps (in eV) of (a) liquid water ℓ -H₂O and (b) hexagonal ice I_h . Vertical bars indicate the band gaps as calculated with the various advanced electronic-structure methods. The reported band gaps include the corrections associated to NQE and ZPR (cf. Sec. 6.2). The most reliable band-gap calculations are shown in green. Based on these calculations, we infer the range of best theoretical estimates (between dashed lines). The shaded areas indicate the ranges of experimental reference values inferred in Sec. 6.2.

Table 6.8 – Parameters of all the hybrid functionals retained in this chapter describing liquid water ℓ -H₂O and hexagonal ice Ih . The fraction of short-range Fock exchange α_s , the fraction of long-range Fock exchange α_ℓ , and the range-separation parameter μ pertaining to the functional CAM($\alpha_s, \alpha_\ell, \mu$) are given. When $\alpha_s = \alpha_\ell = \alpha$, one recovers the functional PBE0(α).

	ℓ -H ₂ O			Ih		
	α_s	α_ℓ	μ	α_s	α_ℓ	μ
PBE0($1/\epsilon_\infty^{\text{sc}}$)	0.59	0.59	-	0.61	0.61	-
CAM($1, 1/\epsilon_\infty^{\text{sc}}, \mu_{\text{TF}}$)	1	0.60	0.58	1	0.62	0.57
CAM($0.25, 1/\epsilon_\infty^{\text{sc}}, \mu_{\text{TF}}$)	0.25	0.58	0.58	0.25	0.60	0.57
CAM($0, 1/\epsilon_\infty^{\text{sc}}, \mu_{\text{TF}}$)	0	0.57	0.58	0	0.59	0.57
PBE0(α_K)	0.47	0.47	-	0.48	0.48	-
CAM($\alpha_{s,K}, 1/\epsilon_\infty^{\text{Expt}}, \mu_{\text{TF}}$)	0.18	0.56	0.58	0.18	0.58	0.57

In addition, we report in Table 6.8 a summary of the parameters of all hybrid functionals retained in this chapter.

Preliminary to the theoretical investigations, we critically review various experimental studies in the literature. We discuss different estimates for the ionization potential and the electron affinity for both considered water phases. Based on the most reliable results, we infer experimental values of 9.0 ± 0.2 eV and 9.4 ± 0.3 eV for the fundamental band gaps of liquid water and hexagonal ice, respectively. These values serve as robust references for the electronic-structure methods examined in this chapter.

Then, we investigate band gaps as obtained with different state-of-the-art *GW* calculations. We show that the QSGW method yields band gaps that overestimate the experimental references. The incorporation of vertex corrections in the screening (\tilde{W}) is then instrumental to overcome the missing electron-hole interaction in W . With the resulting QSG \tilde{W} scheme, we find band gaps of 9.1 and 9.3 eV for liquid water and hexagonal ice, respectively. In comparison with the experimental references, these results are in good agreement for both phases of water. Herewith, we confirm QSG \tilde{W} being one of the most accurate schemes for band-gap predictions [17, 18].

Subsequently, we study dielectric-dependent hybrid functionals for the band gaps of liquid water and hexagonal ice. The band gaps obtained with the global DDH functional overestimate the upper limit of the reference interval by 0.6–0.8 eV. Such a poor performance is in line with a previous result for ice [43], but worse than the typical accuracy of this approach for other materials [43, 47]. Then, we study DDH functionals based on the CAM functional. We consider three range-separated DDH functionals differing in the short-range fraction of Fock exchange. Based on the comparison with experimental references for the dielectric constant, we identify the functional CAM($0, 1/\epsilon_\infty^{\text{sc}}, \mu_{\text{TF}}$) as the most reliable DDH functional. This functional incorporates pure semilocal exchange in the short-range, thereby extending

the scope of long-range corrected hybrid functionals [90, 91, 92, 93, 94]. This scheme yields band gaps of 9.0 eV and 9.1 eV for liquid water and hexagonal ice, respectively.

Finally, we investigate hybrid functionals satisfying Koopmans' condition. We find that the enforcement of this physical constraint also gives accurate band gaps. The minimization of the degree of hybridization between localized defects and delocalized band-edge states is thereby key to ensure proper band-gap predictions. First, we construct the global functional PBE0(α_K) and achieve band gaps for liquid water and hexagonal ice of 8.7 eV and 8.9 eV, respectively. These results lie lower than the onset of the range of experimental references by only 0.1–0.2 eV. This is in contrast to the global DDH functional, which is unable to attain such an accuracy. Then, we construct range-separated hybrid functionals that satisfy Koopmans' condition. In particular, we investigate the functional $\text{CAM}(\alpha_{s,K}, 1/\epsilon_{\infty}^{\text{Expt}}, \mu)$, which additionally enforces the correct long-range screening [56]. The obtained band-gap estimate exhibits a parametric dependence on the range-separation parameter μ encompassing the result of the global hybrid functional PBE0(α_K) as a lower bound. We overcome the μ dependence by invoking the scale of spatial variation of the screening, i.e. $\mu = \mu_{\text{TF}}$. This nonempirical and physically motivated setting leads to the functional $\text{CAM}(\alpha_{s,K}, 1/\epsilon_{\infty}^{\text{Expt}}, \mu_{\text{TF}})$. We employ this kind of functional for the band-gap estimates of liquid water and hexagonal ice and find 9.2 and 9.3 eV, respectively.

Overall, we show that the three advanced electronic-structure methods considered in this chapter provide consistent results for the band gaps of liquid water and hexagonal ice. Indeed, the band gaps of the most reliable schemes, namely QSG \tilde{W} , $\text{CAM}(0, 1/\epsilon_{\infty}^{\text{sc}}, \mu_{\text{TF}})$, and $\text{CAM}(\alpha_{s,K}, 1/\epsilon_{\infty}^{\text{Expt}}, \mu_{\text{TF}})$ differ by at most 0.2 eV, which corresponds to only $\sim 2\%$ of the band gaps involved. We remark that this agreement originates from a consistent computational setup and from the critical consideration of each method. In this way, our analysis allows us to resolve the discord arising from previous studies. Based on the present results, we infer best theoretical estimates of 9.1 ± 0.1 eV and 9.2 ± 0.1 eV for liquid water and hexagonal ice, respectively. The comparison of these theoretical ranges with the experimental ones obtained in Sec. 6.2 indicates a remarkable agreement. The present comparison provides strong evidence for the reliability of both experimental and theoretical estimates and reduces the residual uncertainty on the fundamental band gaps of liquid water and hexagonal ice.

Additionally to the accuracy in the band-gap predictions it is of interest to compare also the computational costs and the robustness of the examined electronic-structure methods. QSG \tilde{W} calculations require extensive computational resources and remain therefore limited to relatively small unit cells. Nevertheless, the reliability of the QSG \tilde{W} scheme has been verified not only for water and ice but also for numerous other materials. DDH functionals have the potential of replacing such high-level GW methods due to their efficient implementation in many electronic-structure codes and their fast convergence within only a few iterations. However, the present results indicate that the band gaps obtained with DDH functionals can span a large interval of values, leading to considerable uncertainty. In this chapter, we overcome this problem by taking under consideration the description of the dielectric

constant ϵ_∞ , but the validity of this way of proceeding for a larger variety of materials remains to be ascertained. Hybrid functionals satisfying Koopmans' condition also serve as a viable alternative to $QSG\tilde{W}$. This approach yields robust band-gap estimates irrespective of the considered class of hybrid functionals. However, the application of this method generally requires defect calculations at the hybrid-functional level with relatively large supercells, thereby limiting its potential.

In view of employing the present electronic-structure methods to applications involving liquid water and hexagonal ice, it is clear that the hybrid functional approaches offer significant advantages in terms of computational cost and the availability of a total-energy scheme. The present work shows that the compromise on accuracy is limited as the hybrid functional approaches achieve band gaps comparable to those obtained with the most elaborate GW scheme.

We finally remark that the results presented in this chapter are also highly relevant for the band alignment at the water/vacuum interface. Further explanations regarding this topic can be found in Appendix A.

7 Band alignment at the $\text{CaF}_2/\text{Si}(111)$ interface

In this chapter, we determine the band alignment at the $\text{CaF}_2/\text{Si}(111)$ interface through various advanced electronic-structure methods. This interface is experimentally well-studied and serves as an ideal test case to examine the accuracy of theoretical schemes. We use both global and range-separated hybrid functionals as well as GW calculations including self-consistency and vertex corrections. Our calculation procedure accounts for residual strain resulting from the small mismatch in the lateral lattice constants at the interface to minimize the systematic error in the comparison with experiment. Both the hybrid-functional and the GW schemes give band alignments in overall good agreement with the experimental characterization. However, the considered methods yield sizable variations in the calculated band offsets, which do not originate from incorrect evaluations of the band gaps but rather from different inherent relative positions of the band edges. The comparison with experiment reveals that the global hybrid functional and the quasiparticle self-consistent GW with vertex corrections give the most accurate description of the band alignment. We then determine the variation of the band offsets as a function of the amount of excess fluorine at the interface and attribute the experimental spread in the measured offsets to uncontrolled fluorine contamination.

The results presented in this chapter have been published in Ref. [111]. Further information can be found in the corresponding archive on the Materials Cloud [259].

7.1 Motivation

Why studying the band alignment at the $\text{CaF}_2/\text{Si}(111)$ interface ?

Insulator-semiconductor heterostructures are encountered in a broad variety of modern electronic devices. The precise understanding of their properties is of great practical importance [260]. However, an accurate theoretical description of such heterostructures is not trivial. It requires the appropriate prediction of the band gaps of the involved materials and the determination of their band alignment at the interface. The calculation of these quantities within density functional theory (DFT) in standard semilocal approximations [4, 5] suffers from severe band-gap underestimations [8, 261]. Advanced methods for electronic-structure calculation like the many-body perturbation theory [9, 15, 17, 18] and hybrid functionals [24, 31, 32] can overcome this deficiency and have therefore intensively been used for studying the interfacial band alignment [262, 263, 264, 261, 8, 265, 266, 267, 268, 269, 270, 21, 271].

However, two critical aspects of band-alignment calculations have been identified in the last years. First, it became apparent that a more realistic description of the band gap does not automatically imply an accurate positioning of the band-edge levels. In fact, it has been shown that different advanced electronic-structure methods tend to position the band edges differently even when they give the same band gap [36, 272, 273]. This phenomenon is not yet fully understood and has direct implications on the prediction of band offsets at heterostructures [21]. Second, we refer to the work of Grüneis *et al.* [274]. These authors proposed that *GW* calculations including higher-order diagrams are required in order to achieve an accurate description of ionization potentials (and thus band-edge levels) [274]. Since these terms are lacking in most commonly used electronic-structure methods, these approaches might yield unsatisfactory results with respect to experimental references [274]. These critical aspects put the use of many widely used methods for band-alignment calculations considerably into question.

For addressing these issues, it is necessary to determine band-edge positions with different electronic-structure methods. However, band-edge levels from periodic bulk calculations cannot directly be compared with experimental references [36]. To circumvent this limitation, theoretical schemes have been examined through their accuracy in predicting ionization potentials at surfaces [274, 18], band offsets at interfaces [21, 271] or defect levels with respect to band edges [272, 275]. While a comparison between theoretical schemes is relatively straightforward, the validation of the calculated band edges against experimental data is more difficult. Indeed, the latter requires the availability of realistic structural models accounting for the detailed surface reconstruction [18] or the specific bonding pattern at interfaces [276, 8]. In the absence of such models, it is an arduous task to draw conclusions concerning the quality of competing electronic-structure methods.

In this context, the $\text{CaF}_2/\text{Si}(111)$ interface can serve as an ideal test case. The CaF_2 layer is epitaxially grown on the silicon substrate [277] and the structural [278, 279, 280, 281, 282, 283,

284] and electronic [285, 286, 277, 287, 288, 289, 290] properties have been experimentally characterized in great detail. Furthermore, the combination of a semiconductor like Si with a wide band-gap insulator like CaF_2 leads to sizable band offsets. Therefore, differences between computational approaches are expected to be more pronounced than for heterostructures involving similar semiconductors [21, 271].

Overall, we set out to determine the band offsets at the $\text{CaF}_2/\text{Si}(111)$ interface using various advanced electronic-structure methods to examine their accuracy in comparison with the experimental characterization. In particular, we are interested to what extent hybrid functionals and *GW* methods are capable of accurately predicting the interfacial band alignment.

Should we adopt nonempirical hybrid functionals for this purpose?

For the hybrid-functional calculations, we are in principle inclined to consider nonempirical parameter definitions. However, the choice of nonempirical hybrid functionals can be problematic for the purposes of this chapter. This is due to the fact that a proper description of the band gap of the constituting bulk materials is of great importance in order to achieve meaningful results for the interfacial band offsets [8]. In case the bulk band gaps suffer from inaccuracies, the computed band offsets deteriorate accordingly. Unfortunately, we have seen in the previous chapters, that even the most sophisticated nonempirical hybrid functionals yield band gaps differing by ~ 0.2 eV from the experimental counterparts. Whereas this accuracy is comparable to state-of-the-art *GW* methods to date, it would introduce a notable uncertainty for the present study. Indeed, we can anticipate that the computed band offsets might be subject to variations of several tenth of an electronvolt due to incorrect bulk band gaps. In this case, the comparison of different electronic-structure methods becomes a difficult task. Therefore, we decide to employ empirical hybrid-functional schemes in this chapter in order to diminish systematic errors as much as possible. More specifically, we fix the hybrid-functional parameter in such a way that calculated and experimental band gap match. In light of the previous chapters, this way of proceeding is somewhat unsatisfactory but it is nevertheless appropriate for our purposes here.

7.2 Computational aspects

7.2.1 Electronic-structure methods

In this chapter, we use various advanced electronic-structure methods for determining the band alignment at the $\text{CaF}_2/\text{Si}(111)$ interface. To this end, we perform calculations for the bulk components and for an interface model, as further explained later in Sec. 7.2.3.

First, we consider hybrid functionals [24, 31, 32, 291]. In particular, we investigate global as well as range-separated hybrid functionals. For the former, we use the functional $\text{PBE0}(\alpha)$, which depends on the amount of incorporated Fock exchange α [31]. For the latter, we consider the

functional $\text{HSE}(\alpha, \mu)$ which additionally includes a range-separation parameter μ [32, 291]. For the purpose of this study, it is sufficient to vary only the mixing parameter α whereas μ is kept equal to 0.11 bohr^{-1} [291]. We remark that both functionals revert to the semilocal PBE functional [5] when $\alpha = 0$.

As second kind of advanced electronic-structure method, we use many-body perturbation theory in the GW approximation [9]. In this chapter, we perform one-shot GW calculations to correct the single-particle energies obtained from the hybrid functional calculations. In this way, the adopted GW method depends on the fraction of Fock exchange used in the preceding hybrid functional calculation. Furthermore, we consider self-consistency [15, 17, 18] and vertex corrections [18]. We account for vertex corrections through the use of the bootstrap exchange-correlation kernel [109, 18]. A summary of the electronic-structure methods investigated in this chapter is given in Table 7.1.

Table 7.1 – Advanced electronic-structure methods in this chapter: global (PBE0) and range-separated hybrid functionals (HSE); one-shot GW with ($G_0\tilde{W}_0$) and without (G_0W_0) vertex corrections using wave functions and energies either from PBE0 or from HSE; quasiparticle self-consistent GW with vertex corrections (QSG \tilde{W}). The inclusion of vertex corrections in the screening results in the notation \tilde{W} for the screened Coulomb interaction. The notation with the parameter α indicates that the fraction of Fock exchange is adapted to match the experimental band gap.

Method	Global	Range-separated
Hybrid functional:	PBE0(α)	HSE(α)
One-shot G_0W_0 :	$G_0W_0@PBE0(\alpha)$	$G_0W_0@HSE(\alpha)$
One-shot $G_0\tilde{W}_0$:	$G_0\tilde{W}_0@PBE0(\alpha)$	$G_0\tilde{W}_0@HSE(\alpha)$
QSG \tilde{W}		

7.2.2 Computational details

For all calculations, we use plane-wave basis sets and normconserving pseudopotentials to describe core-valence interactions [87, 88]. Only the outermost shells are treated among the valence states for Si ($3s^23p^2$) and F ($2s^22p^5$). In the pseudopotential of Ca, we include semicore shells ($3s^23p^64s^2$) as these states have been shown to be important in a previous GW study [292]. For the bulk calculations, we adopt the well-known primitive unit cells of Si and CaF_2 , respectively. More specifically, we model Si bulk with a face-centered cubic (fcc) cell with two Si atoms located at the reduced coordinates (0, 0, 0) and $(\frac{1}{4}, \frac{1}{4}, \frac{1}{4})$ [130]. CaF_2 bulk is described by a fcc lattice with one Ca atom at (0, 0, 0) and two F atoms at $(\frac{1}{4}, \frac{1}{4}, \frac{1}{4})$ and $(-\frac{1}{4}, -\frac{1}{4}, -\frac{1}{4})$ [292]. The structural details of the interface models are given in Sec. 7.4.1 and Sec. 7.5. The adopted \mathbf{k} -point sampling and the energy cut-off are given in Table 7.2.

We verified that the adopted parameters ensure the convergence of the total energy of the ground state within 10^{-3} eV/atom . In the particular case of silicon, a dense \mathbf{k} -point grid of $12 \times 12 \times 12$ is necessary to include the conduction-band minimum (CBM), which is not

Table 7.2 – Computational parameters used throughout this study: \mathbf{k} -point sampling, ground-state cut-off energy E_{cut} , cut-off energy $E_{\text{cut}}^{\text{eps}}$ in the dielectric matrix, and total number of bands n_{band} (occupied and unoccupied) in the dielectric matrix and in the Green's function.

	\mathbf{k} points	E_{cut} (Ry)	$E_{\text{cut}}^{\text{eps}}$ (Ry)	n_{band}
Si bulk	$8 \times 8 \times 8$	60	15	300
CaF ₂ bulk	$6 \times 6 \times 6$	100	30	500
CaF ₂ /Si interface	$8 \times 8 \times 1$	100		

located at a high-symmetry \mathbf{k} -point [130]. To avoid using such a high-density grid in the more demanding electronic-structure schemes, we proceed in the following way. We first perform advanced and semilocal calculations with a coarser $8 \times 8 \times 8$ \mathbf{k} -point mesh. The differences are evaluated and interpolated to match the denser $12 \times 12 \times 12$ \mathbf{k} -point grid. The final results are achieved by combining the interpolated corrections with a PBE calculation on the $12 \times 12 \times 12$ \mathbf{k} -point grid. This way of proceeding is appropriate since the energy corrections only weakly depend on the considered \mathbf{k} -point [12, 99]. The final band gaps differ only by ~ 0.04 eV with respect to the estimate achieved with the coarser $8 \times 8 \times 8$ \mathbf{k} -point mesh.

The GW calculations are performed with nonlocal commutators for the optical matrix element in the long-wavelength limit as described in Ref. [167]. The dielectric function is calculated with the formula of Adler and Wiser [97, 98], including an energy cut-off $E_{\text{cut}}^{\text{eps}}$ and a total number of bands n_{band} as given in Table 7.2. The frequency dependence of the dielectric function is evaluated through the contour deformation technique [118] accounting for 10 real and 10 imaginary frequencies. In the quasiparticle self-consistent GW (QS $\tilde{G}\tilde{W}$) approach [15, 17], we only update the lowest 100 bands self-consistently and keep higher-lying states as obtained at the PBE level. The update of more bands leads to indiscernible changes in the band edges. Overall, we estimate that the quasiparticle energies are converged within 0.05 eV.

7.2.3 Band-alignment scheme

In this study, we determine the band alignment following the scheme outlined in Refs. [293, 294]. A graphical representation is given in Fig. 7.1.

The band-offset determination is based on two individual bulk and on one interface calculation. The bulk models are used to position the valence-band maximum (VBM) E_{VBM} of each component relative to the average electrostatic potential V . In the interface model, the line-up of the average electrostatic potential across the interface ΔV is achieved. The valence-band offset ΔE_V is then found through

$$\Delta E_V = E_{\text{VBM}}^{\text{Si}} - E_{\text{VBM}}^{\text{CaF}_2} + \Delta V. \quad (7.1)$$

The conduction-band offset ΔE_C is then inferred from the consideration of the band gaps of the two interface components (cf. Fig. 7.1).

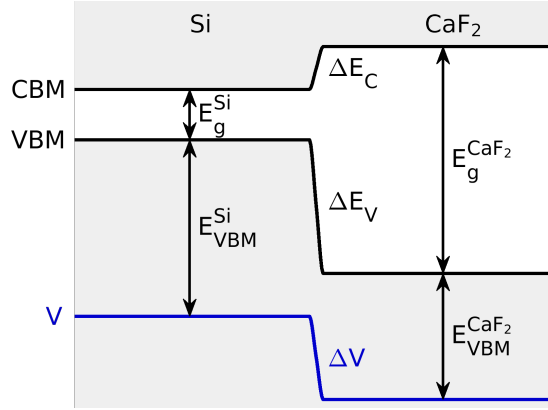


Figure 7.1 – Band-alignment scheme for the calculation of the valence-band offset ΔE_V and of the conduction band offset ΔE_C at the $\text{CaF}_2/\text{Si}(111)$ interface.

We apply this scheme to evaluate the band-alignment obtained through different electronic-structure methods following the specific procedure outlined by Alkauskas *et al.* [8]. First, we focus on the hybrid functionals, which contain a single undetermined parameter α . For each interface component, we empirically determine the optimal α for which the calculated band gap of the bulk matches its experimental counterpart. In particular, we impose an indirect band gap of 1.17 eV [130] for Si and a direct band gap of 12.0 eV [295] for CaF_2 . The latter condition is equivalent to enforcing an indirect gap of 11.7 eV. The optimal mixing parameters α_{Si} and α_{CaF_2} obtained in this way for the PBE0(α) and HSE(α) hybrid functional forms are given in Table 7.3.

Table 7.3 – Optimal mixing parameters α_{Si} and α_{CaF_2} that reproduce the experimental band gap of Si and CaF_2 , respectively. The mean value $\tilde{\alpha} = (\alpha_{\text{Si}} + \alpha_{\text{CaF}_2})/2$ is used in the interface calculation for the determination of the line-up.

	PBE0	HSE	$G_0 W_0@$		$G_0 \tilde{W}_0@$	
			PBE0	HSE	PBE0	HSE
α_{Si}	0.12	0.25	0.00	0.00	0.05	0.07
α_{CaF_2}	0.40	0.56	0.30	0.38	0.77	0.87
$\tilde{\alpha}$	0.26	0.40	0.15	0.19	0.41	0.47

The interfacial line-up is then computed with a hybrid functional defined by the mean of the mixing parameters pertaining to the two interface components [8]: $\tilde{\alpha} = (\alpha_{\text{Si}} + \alpha_{\text{CaF}_2})/2$. This approach is meaningful because the interfacial line-up potential is almost independent of the mixing parameter [8, 267, 21]. In this way, the combination of bulk and interface calculations provides us with the band offsets corresponding to a given hybrid-functional form.

Next, we consider the band alignment for the electronic-structure methods based on *GW* calculations. These calculations are performed for the bulk models of the interface components. For the line-up in the one-shot *GW* schemes, we follow the same procedure as for the hybrid

functionals since these GW schemes also depend on an underlying value of α for the starting point. A specific value $\bar{\alpha}$ is thus identified as the mean of the optimal mixing parameters of the bulk components given in Table 7.3. Since the one-shot GW calculations do not modify the charge density, we use the line-up potential achieved with the hybrid functional defined by $\bar{\alpha}$. By contrast, in the $QSG\tilde{W}$ scheme, the band-gap determination does no longer depend on the value of α of the starting hybrid functional, because of the iteration towards self-consistency. Therefore, a $QSG\tilde{W}$ calculation would in principle lead to a distinct value of the line-up ΔV . However, such high-level GW calculations are computationally demanding for large super-cells and do not lead to any sizable variation in ΔV . Indeed, Shaltaf *et al.* [261] calculated for the Si/SiO₂ interface an effect of only 0.02 eV on ΔV due to the self-consistency. This property stems from the fact that $QSGW$ only brings minor variations to the charge density and thus to the electric dipoles, as also seen in the case of small molecules [296]. In view of these considerations, we use in our $QSG\tilde{W}$ scheme the same value of ΔV as obtained with the hybrid functionals. In the $QSG\tilde{W}$ scheme, the band gaps do not match the experimental ones by construction. Hence, it should be considered that the band offsets could suffer from this drawback [8].

7.2.4 Strain effects

We now devote special attention to the strain in our description of the CaF₂/Si(111) interface. There are multiple reasons to properly account for such effects. First, in experimental conditions, the CaF₂ layer grows epitaxially upon silicon [277] with a residual mismatch, which causes this layer to be subject to compressive strain in the in-plane directions [285, 286, 277]. For the present interface, the experimental mismatch is particularly small and corresponds to 0.59% (cf. lattice constants in Table 7.4). Second, our interface modelling englobes a structural relaxation (cf. Sec. 7.4.1), which leads the relaxed model interface to exhibit lattice constants in the growth direction that differ from the targeted experimental situation. Third, we have a preference for performing the advanced calculations on bulk systems, on the one hand to take advantage of the high symmetry, and, on the other hand, to establish benchmark results for future reference. Fourth, the motivations of this study consists in comparing different advanced electronic-structure methods to experiment and it is thus important to reduce effects that could bias our conclusions as much as possible. Hence, the motivation for paying attention to strain effects arises from both experimental and computational conditions. In the following, we describe how these effects are accounted for.

We specifically distinguish between the lattice constants in the lateral directions a_{lat} and in the growth direction a_z . These quantities exhibit different values for bulk Si, bulk CaF₂, the interface model, and the strained CaF₂ layer in the experiment. A schematic illustration of the different configurations is shown in Fig. 7.2.

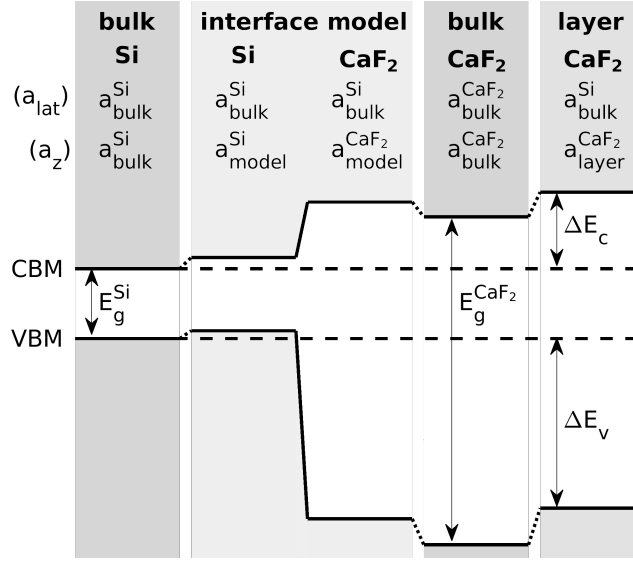


Figure 7.2 – Schematic illustration of the band alignment of bulk Si, Si and CaF_2 within the interface model, bulk CaF_2 , and the strained CaF_2 layer. The lattice constants in the lateral directions a_{lat} and in the growth direction a_z are indicated. The band gaps for Si and CaF_2 are shown in correspondence of the unstrained bulk configurations. The targeted valence-band offset ΔE_V and conduction-band offset ΔE_C , corresponding to those measured in the experimental conditions, are also indicated.

Our ultimate intention is to calculate the alignment between unstrained silicon with experimental lattice constant $a_{\text{bulk}}^{\text{Si}}$, i.e. with $a_{\text{lat}} = a_{\text{bulk}}^{\text{Si}}$ and $a_z = a_{\text{bulk}}^{\text{Si}}$, and a CaF_2 layer that is strained because of the lattice mismatch, i.e. for which $a_{\text{lat}} = a_{\text{bulk}}^{\text{Si}}$ and $a_z = a_{\text{layer}}^{\text{CaF}_2}$. The value of $a_{\text{layer}}^{\text{CaF}_2}$ is determined through the experimental values for the mismatch and the Poisson ratio of CaF_2 . For the latter, we here use the value of $\nu = 0.26$ from Ref. [297, 298]. To achieve this goal, our band alignment scheme takes advantage of (i) bulk calculations of Si and CaF_2 that are performed at their respective experimental bulk lattice constants, $a_{\text{bulk}}^{\text{Si}}$ and $a_{\text{bulk}}^{\text{CaF}_2}$, and of (ii) an interface model calculation, in which the in-plane lattice constant is fixed at the target $a_{\text{bulk}}^{\text{Si}}$, but the a_z lattice constants of both components are allowed to relax according to the electronic structure scheme used, giving $a_{\text{model}}^{\text{Si}}$ and $a_{\text{model}}^{\text{CaF}_2}$. The various lattice constants used in this chapter are compiled in Table 7.4.

To connect the two structural calculations of Si, we follow the scheme for evaluating deformation potentials proposed in Ref. [300]. We construct a superlattice in which regular Si alternates with a Si layer in which the lattice constant along the growth direction has been modified. We obtain in this way a strain-induced shift in the electrostatic potential $\Delta V(\text{Si bulk} \rightarrow \text{Si model})$. For CaF_2 , we proceed analogously. From a superlattice calculation between regular and strained CaF_2 , we obtained the effect of uniaxial strain on the electrostatic potential and on the band edges. Based on the symmetry and the linearity in the strain, we then extend the results to the specific strain transitions between the three structural configurations of CaF_2 of interest to us. More specifically, we derive in this way $\Delta V(\text{CaF}_2 \text{ model} \rightarrow \text{CaF}_2 \text{ bulk})$ and the

7.3. Band gaps and band-edge levels of bulk materials

Table 7.4 – Lattice constants (in Å) for Si and CaF₂ considered in this chapter. $a_{\text{bulk}}^{\text{Si}}$ and $a_{\text{bulk}}^{\text{CaF}_2}$ are the experimental lattice constant of bulk Si and bulk CaF₂, respectively. $a_{\text{layer}}^{\text{CaF}_2}$ is the lattice constant in the growth direction for a CaF₂ layer epitaxially grown on Si, determined through the experimental Poisson ratio. $a_{\text{model}}^{\text{Si}}$ and $a_{\text{model}}^{\text{CaF}_2}$ are lattice constants in the growth direction as found in the respective bulk regions of the relaxed model interface.

$a_{\text{bulk}}^{\text{Si}}$	$a_{\text{model}}^{\text{Si}}$	$a_{\text{model}}^{\text{CaF}_2}$	$a_{\text{bulk}}^{\text{CaF}_2}$	$a_{\text{layer}}^{\text{CaF}_2}$
5.431 ^a	5.484	5.581	5.463 ^b	5.587

^a Ref. [130], ^b Ref. [299].

strain-induced band-edge shifts between bulk CaF₂ and the strained CaF₂ layer, i.e. $\Delta E_V(\text{CaF}_2 \text{ bulk} \rightarrow \text{CaF}_2 \text{ layer})$ and $\Delta E_C(\text{CaF}_2 \text{ bulk} \rightarrow \text{CaF}_2 \text{ layer})$. We perform these calculations with the hybrid functionals PBE0(α) and HSE(α), i.e. with parameters α set as in the respective bulk phases (cf. Table 7.3). The results obtained are reported in Table 7.5.

Table 7.5 – Strain-induced shifts (in eV) of the electrostatic potential $\Delta V(\text{Si bulk} \rightarrow \text{Si model})$ and $\Delta V(\text{CaF}_2 \text{ model} \rightarrow \text{CaF}_2 \text{ bulk})$ and of the valence and conduction band levels $\Delta E_V(\text{CaF}_2 \text{ bulk} \rightarrow \text{CaF}_2 \text{ layer})$ and $\Delta E_C(\text{CaF}_2 \text{ bulk} \rightarrow \text{CaF}_2 \text{ layer})$, as obtained with the hybrid functionals PBE0(α) and HSE(α). These shifts are used for all electronic-structure methods in this chapter.

	PBE0(α)	HSE(α)
$\Delta V(\text{Si bulk} \rightarrow \text{Si model})$	−0.10	−0.10
$\Delta V(\text{CaF}_2 \text{ model} \rightarrow \text{CaF}_2 \text{ bulk})$	0.25	0.25
$\Delta E_V(\text{CaF}_2 \text{ bulk} \rightarrow \text{CaF}_2 \text{ layer})$	−0.16	−0.17
$\Delta E_C(\text{CaF}_2 \text{ bulk} \rightarrow \text{CaF}_2 \text{ layer})$	0.09	0.08

We generally observe small effects due to strain, which is consistent with the epitaxial growth found for this interface [277]. More specifically, we find strain-induced shifts in the electrostatic potential of −0.10 eV and 0.25 eV for $\Delta V(\text{Si bulk} \rightarrow \text{Si model})$ and $\Delta V(\text{CaF}_2 \text{ model} \rightarrow \text{CaF}_2 \text{ bulk})$, respectively. For the potential line-up between bulk Si and bulk CaF₂ this yields an overall correction of only 0.15 eV with respect to the value obtained through the interface model. For the band-edge shifts between bulk CaF₂ and the strained CaF₂ layer, we find with PBE0(α) a shift of −0.16 eV and 0.09 eV for the VBM and CBM, respectively. The strain corrections calculated with HSE(α) differ by at most 0.01 eV. We expect corrections of similar size for the other electronic-structure methods considered in this chapter. In particular, we apply for the one-shot *GW* schemes identical strain corrections as obtained with the underlying hybrid functional. For the QSGW scheme, we use the corrections as calculated with PBE0(α).

7.3 Band gaps and band-edge levels of bulk materials

We first focus on the bulk materials and determine band gaps and band-edge levels with respect to the average electrostatic potential. We devote special attention to the direct or

indirect nature of the band gaps. In particular, we consider the direct ($\Gamma \rightarrow \Gamma$) and the indirect ($X \rightarrow \Gamma$) band gap for CaF_2 to enable a meaningful comparison with experiment. A graphical visualization of the band structure of Si and CaF_2 is given in Fig. 7.3 as obtained at the PBE level of theory.

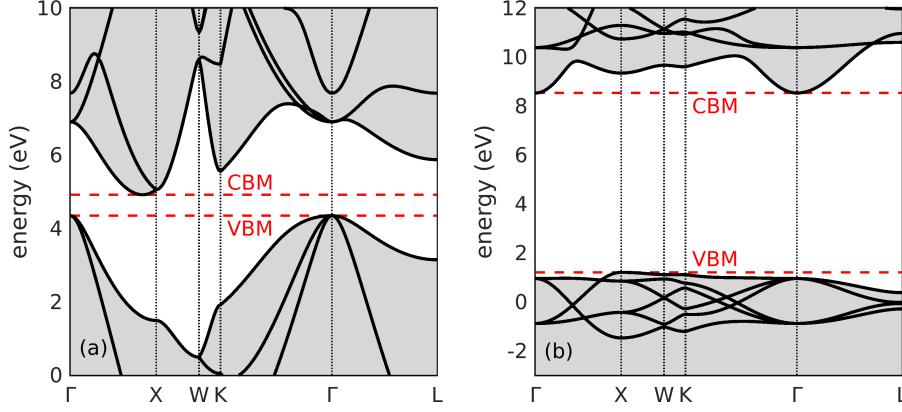


Figure 7.3 – PBE band structure of (a) Si and (b) CaF_2 . Valence-band maximum (VBM), conduction-band minimum (CBM) are indicated for each material.

A summary of the calculated band gaps is given in Table 7.6 together with experimental data for the fundamental band gap.

Table 7.6 – Band gaps (in eV) for Si and CaF_2 as calculated at various levels of theory. It is specified whether the band gaps correspond to direct or indirect transitions. All the results in this table are obtained with hybrid functionals in which $\alpha = 0.25$. The experimental data refer to fundamental band gaps.

	PBE	PBE0	HSE	$G_0W_0@$			$G_0\tilde{W}_0@$			QSG \tilde{W}	Expt.
				PBE	PBE0	HSE	PBE	PBE0	HSE		
Si (indir.)	0.57	1.79	1.17	1.17	1.54	1.41	1.11	1.44	1.33	1.28	1.17 ^a
CaF_2 (indir.)	7.33	10.11	9.30	10.41	11.51	11.28	9.28	10.07	9.98	11.47	11.8 ^b
CaF_2 (dir.)	7.58	10.37	9.57	10.72	11.80	11.57	9.59	10.37	10.28	11.76	12.0 \pm 0.1 ^c , 12.1 ^d

^a Ref. [130], extrapolated to $T = 0$ K, ^b Estimation of Shirley [301] based on Ref. [302], ^c Ref. [295], $T = 15$ K, ^d Ref. [302], $T = 90$ K.

At the PBE level the well-known band-gap underestimation is apparent. The advanced electronic-structure methods provide a more realistic description of the band gap even when the hybrid-functional parameter is set to the default value $\alpha = 0.25$ without applying any optimization. In particular, we observe that the PBE0(0.25) band gaps are generally larger than the HSE(0.25) ones, in accord with the analysis in Ref. [267]. The G_0W_0 corrections tend to level out this difference when the two hybrid functionals are used as starting points. The inclusion of vertex corrections in the G_0W_0 only yields a minor reduction of the band gap. Overall, QSG \tilde{W} gives the best agreement with experiment further supporting the high accuracy of this scheme for band-gap evaluations [15, 17, 18, 112, 114].

For a proper comparison with experiment, it is necessary to consider the band-gap renormalization due to phonons. For Si this effect is found to be 0.06 eV [154]. For CaF_2 , such an estimate is unavailable in the literature but a sizable effect on the order of ~ 0.5 eV can be expected on the basis of the result of a similar ionic compound such as MgO [156, 155]. In the band-offset calculations in which the calculated band gaps reproduce their experimental counterparts, we assume that phonon renormalization effects are implicitly accounted for through the empirical tuning of the hybrid-functional parameter α . This way of proceeding is justified as long as the phonon renormalizations affect the band edges in a similar way as the scaling of α . However, the effect of phonon renormalization should be kept in mind when assessing the accuracy of $\text{QSG}\tilde{W}$, since this scheme does not rely on any band-gap tuning.

The band gaps calculated here are in good agreement with other theoretical studies in the literature. For Si, there are numerous computational studies including the application of both hybrid-functional and GW calculations [17, 8, 261, 267, 273, 37, 21, 18, 47]. Within this variety of references, we particularly focus on the high-level GW calculations of Refs. [17] and [18]. These studies found $\text{QSG}\tilde{W}$ band gaps of 1.24 eV and 1.30 eV, respectively, in excellent agreement with our $\text{QSG}\tilde{W}$ result of 1.28 eV. For CaF_2 , several studies based on the local density approximation (LDA) for the exchange-correlation energy report an indirect band gap ranging between ~ 6.7 and 7.1 eV [301, 292, 303, 304]. These values agree well with our band gap of 7.33 eV obtained with the semilocal PBE functional. As for the more advanced electronic-structure methods, we refer to the GW calculations of Ma and Rohlfing [304], the GW calculations of Shirley [301], and to the self-consistent screened-exchange LDA (sX-LDA) calculations of Kim *et al.* [303], which yield band gaps of 11.5, 11.38, and 11.66 eV, respectively. These results are all in good agreement with our $\text{QSG}\tilde{W}$ band gap of 11.47 eV.

We then turn to band-edge levels as obtained at the various levels of theory. Our hybrid-functional results are illustrated in Fig. 7.4, where the band-edge levels are displayed as a function of the hybrid-functional parameter α .

We generally observe a linear dependence of the VBM and CBM on the fraction of incorporated Fock exchange. The corresponding band-gap opening is smaller for $\text{HSE}(\alpha)$ than for $\text{PBE0}(\alpha)$, in analogy with the results in Ref. [267]. The linearity in α is preserved when applying a one-shot GW correction, as also found in Ref. [37] for other materials. In $\text{QSG}\tilde{W}$ such dependence on the starting-point is overcome through the iteration towards self-consistency. For CaF_2 , all GW approaches provide almost symmetric band-edge corrections with respect to the hybrid-functional starting points, i.e. the upwards shift of the CBM has a similar size to the downwards shift of the VBM. Instead, for Si the VBM and CBM are both subject to a negative energy correction. Our results are generally consistent with the finding of Chen and Pasquarello that different electronic-structure methods tend to position the band edges differently [273]. This appears clearly when comparing the band edges from $\text{QSG}\tilde{W}$ with those from the hybrid functionals with optimal mixing parameters, as can be seen in Fig. 7.4 and Table 7.7. For Si, we observe that the valence-band edges as calculated with the hybrid functionals are persistently higher by 0.3 to 0.6 eV than corresponding ones in GW . For CaF_2 , no such simple statement

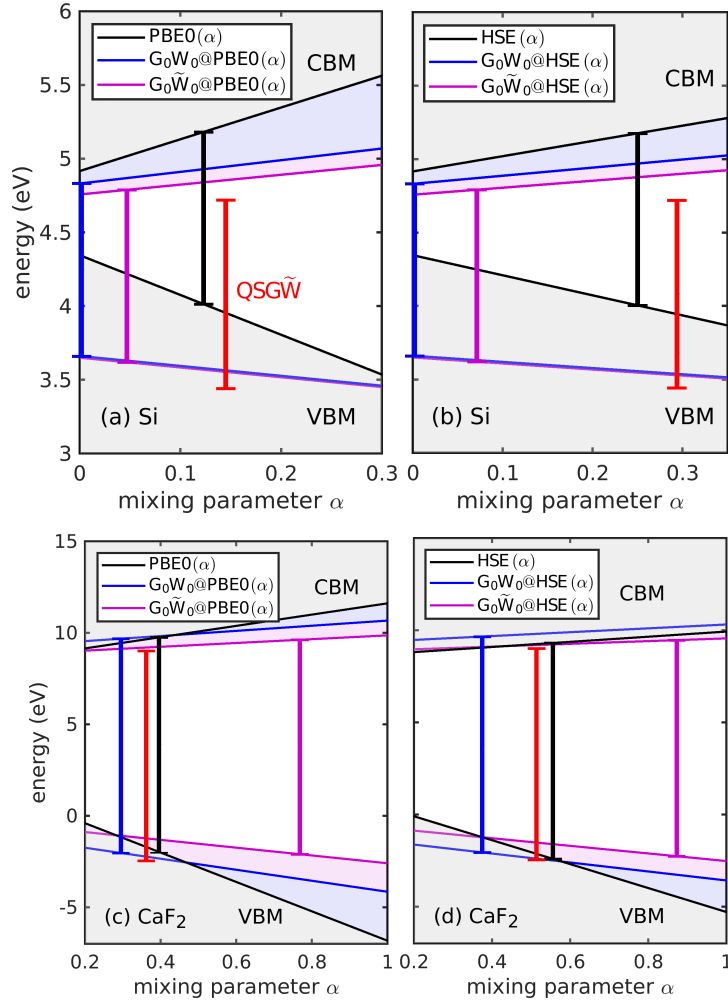


Figure 7.4 – Band-edge levels (in eV) for Si and CaF_2 as calculated through various levels of theory. The VBM and the CBM are displayed as a function of the fraction of Fock exchange α . We show the results for Si as obtained with (a) the PBE0(α) and (b) the HSE(α) functionals. The results for CaF_2 are presented analogously in (c) and (d). The band-edge levels obtained with the one-shot GW methods are also given. The vertical bars indicate the value of α needed to reproduce the experimental band gap. The red bar highlights band edges as calculated with QSGW and is positioned at the mixing parameter for which PBE0(α) and QSGW give the same band gap. The energy levels are aligned through the average electrostatic potential.

can be made. In this case, the most pronounced differences are found for the band edges obtained with the hybrid functionals. More specifically, the valence-band edge from HSE(α) is ~ 0.4 eV lower than that from PBE0(α). The GW approaches yield values lying in between those obtained with the two hybrid functionals.

Table 7.7 – Valence band-edge levels (in eV) with respect to the average electrostatic potential for Si and CaF_2 as calculated at various levels of theory. The band-edge levels are expressed as shifts with respect to the reference PBE values at 4.35 eV and 1.21 eV for Si and CaF_2 , respectively. Different calculations are aligned through the average electrostatic potential. For the parameter-dependent electronic structure methods, the fraction of incorporated Fock exchange α is tuned to reproduce the experimental band gap (cf. Table 7.3).

	PBE0(α)	HSE(α)	$G_0W_0@$		$G_0\tilde{W}_0@$		QSG \tilde{W}
			PBE0(α)	HSE(α)	PBE0(α)	HSE(α)	
Si	-0.33	-0.34	-0.68	-0.68	-0.73	-0.72	-0.90
CaF_2	-3.18	-3.61	-3.24	-3.26	-3.30	-3.47	-3.66

7.4 Band offsets at the $\text{CaF}_2/\text{Si}(111)$ interface

7.4.1 Interfacial line-up potential

For the calculation of the interfacial line-up potential ΔV , we use the so called T_4 -interface model in B-type orientation [277, 305], which is characterized by a predominance of Si-Ca bonds at the interface. The interface is charge neutral and the Ca atoms are located at the T_4 sites of the $\text{Si}(111)-(1 \times 1)$ surface. We remark that the precise interface morphology has intensively been debated in the literature [278, 285, 277, 281] resulting in clear evidence for the presently adopted T_4 -interface model [279, 289, 282, 283, 284]. Furthermore, computational studies based on this model structure successfully accounted for photoemission [306, 307] and second-harmonic generation measurements [305].

In our superlattice model, we use ~ 21 Å of Si and ~ 20 Å of CaF_2 . We carefully check that such thicknesses ensure a bulk-like electrostatic potential far from the interface. In order to mimic the epitaxial growth, the experimental lattice constant of Si is adopted for the lateral directions. We further find that the structural relaxation of the interfacial atomic positions has a significant influence on the line-up potential due to changes brought to the interface dipole. Therefore, we fully relax the structure at the PBE level until the total energy between two successive iteration steps is smaller than 10^{-5} Ry. The residual Hellmann-Feynman forces are then smaller than 10^{-4} Ry/bohr. In this structural optimization, we allow for the relaxation of both the atomic positions and the supercell size in the growth direction. The two other supercell dimensions are kept fixed. The model interface obtained in this way is used in all subsequent calculations of the interfacial line-up potential irrespective of the considered level of theory. This is justified since structural relaxations at the hybrid functional level only lead to minor changes. For instance, further relaxation with the functional PBE0(0.25) affects ΔV by 0.03 eV with respect to the value achieved with same functional but for the structure relaxed with the PBE functional. This is consistent with the results of Weston *et al.* [308].

We now study the line-up of the electrostatic potential at the $\text{CaF}_2/\text{Si}(111)$ interface. To this end, we perform calculations for the constructed interface model at the various levels of theory

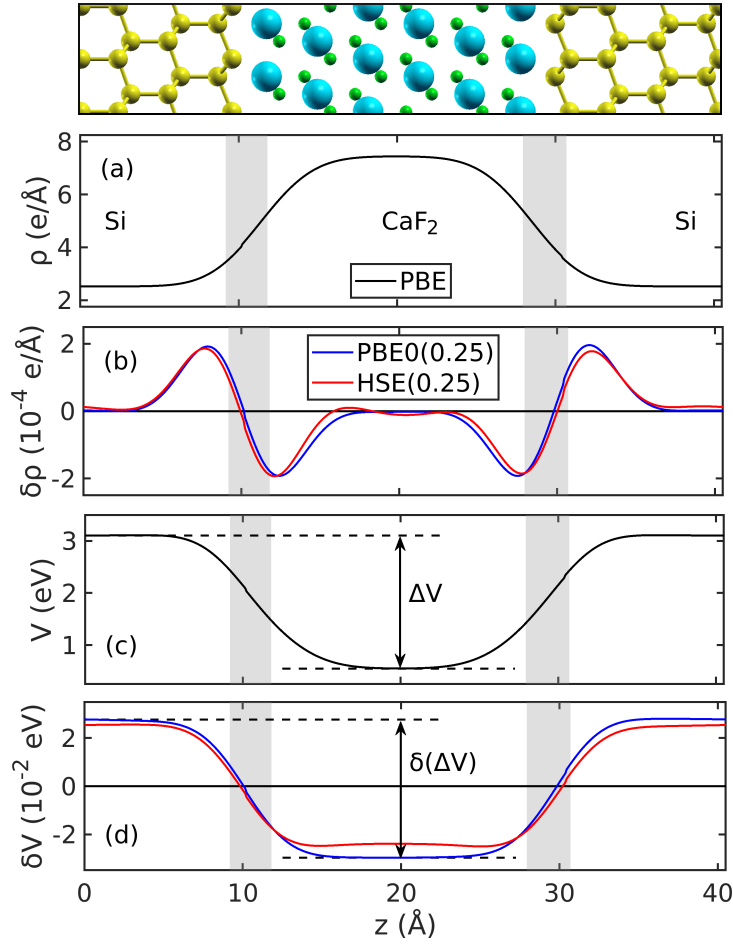


Figure 7.5 – Locally averaged (a) charge density ρ and (c) electrostatic potential V across the $\text{CaF}_2/\text{Si}(111)$ interface as obtained with the semilocal PBE functional. (b) The charge density $\delta\rho$ and (d) the electrostatic potential δV as obtained with the hybrid functionals PBE0(0.25) and HSE(0.25) with respect to PBE are also given. The interfacial line-up ΔV in PBE and its modification $\delta(\Delta V)$ in case of PBE0(0.25) are indicated. The shaded areas correspond to the transition regions between Si and CaF_2 . In the top panel, the atomic structure of the interface model is illustrated: Si, Ca, and F atoms are shown in yellow, blue, and green, respectively.

considered in this study. We note that earlier works demonstrated that electrostatic properties are already adequate at the semilocal DFT level [261, 8, 267, 21]. Therefore, we first focus on the PBE level of theory. The corresponding charge density ρ and electrostatic potential V are given in Figs. 7.5(a) and (c), respectively. For simplicity, the displayed quantities are averaged in the lateral directions and broadened with a Gaussian of width 2.5 \AA in the growth direction.

We observe that ρ and V exhibit bulk-like behavior away from the interfacial transition regions. From the difference between the plateau values in the electrostatic potential we infer a line-up potential of $\Delta V = 2.56 \text{ eV}$ at the PBE level. For the more advanced electronic-structure methods, we focus on the differences in the charge density $\delta\rho$ and in the electrostatic potential

δV with respect to PBE, as shown in Figs. 7.5(b) and (d), respectively. In particular, we display the results for the hybrid functionals PBE0(0.25) and HSE(0.25) as representative cases. We find that $\delta\rho$ and δV indeed correspond to minor modifications, namely on the order of $\sim 2 \cdot 10^{-4} \text{ e}/\text{\AA}$ and $\sim 0.03 \text{ eV}$, respectively. We observe a charge transfer from CaF_2 to Si [cf. Fig. 7.5(b)], which produces a change in the interfacial line-up potential $\delta(\Delta V)$ [cf. Fig. 7.5(d)]. This effect amounts to 0.06 eV for the functional PBE0(0.25). An almost identical value is found for the functional HSE(0.25).

To estimate the range of these deviations, we calculate $\delta(\Delta V)$ as a function of the hybrid-functional parameter α . The dependence is shown in Fig. 7.6 for both PBE0(α) and HSE(α).

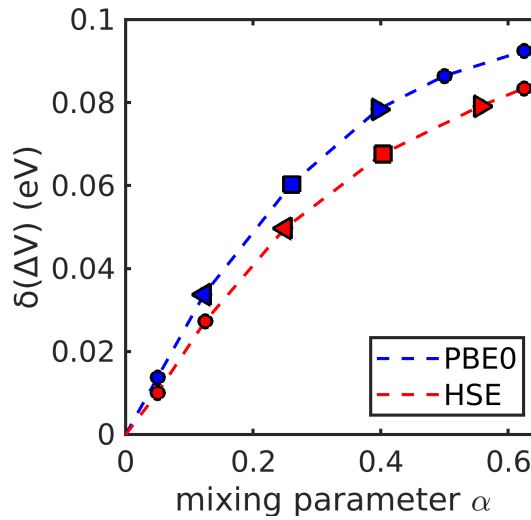


Figure 7.6 – Variation of the line-up potential $\delta(\Delta V)$ with respect to the result obtained with PBE as a function of the mixing parameter α in the hybrid functionals PBE0(α) and HSE(α). Calculations with the optimal mixing parameters for bulk Si and CaF_2 (cf. Table 7.3) are shown as triangles pointing to the left and the right, respectively. Calculations with the mean of these mixing parameters are indicated with a square. Other calculated data points are shown with circles. Dashed lines are guides to the eye.

We find a linear dependence on α at low values, but a saturation becomes apparent at higher values. Overall, the variations in the line-up potential are generally smaller than 0.1 eV conferring consistency to the applied band-alignment scheme. To overcome the remaining dependence on the parameter, we follow the procedure outlined in Ref. [8]. This consists in using the line-up potential as calculated with the mean of the optimal mixing parameters of the bulk components (cf. Table 7.3). For the hybrid functionals PBE0(α) and HSE(α), this yields almost identical line-up potentials of 2.62 eV and 2.63 eV, respectively. In the one-shot GW schemes, the line-up is obtained through the underlying hybrid functional defined with the mean value $\bar{\alpha}$ given in Table 7.3. In the QSGW scheme, we use the value of $\Delta V = 2.62 \text{ eV}$ obtained in PBE0(α) following the discussion in Sec. 7.2.3. These different choices for α lead to an uncertainty in the determination of ΔV that amounts to 0.05 eV at most.

7.4.2 Band offsets at the interface

We now have all the ingredients for the calculation of the band offsets at the $\text{CaF}_2/\text{Si}(111)$ interface. For this we combine the band-edge positions determined in Sec. 7.3 with the interfacial line-up potential calculated earlier in Sec. 7.4.1. We also account for strain effects as discussed in Sec. 7.2.4. The band offsets obtained in this way are given in Table 7.8, where they are compared with experimental data [286, 285, 290]. We remark that several differing experimental values for the band offsets can be found in the literature [285, 286, 277, 287, 288, 289, 290]. In Table 7.8, we report an interval of experimental data that encompasses the three measurements with the highest values for the valence-band offset. We expect these results to be representative of the $\text{CaF}_2/\text{Si}(111)$ interface with a low contamination of Si-F bonds, as discussed in more detail in Sec. 7.5.

Table 7.8 – Band offsets (in eV) for the $\text{CaF}_2/\text{Si}(111)$ interface as obtained at the various levels of theory considered in this chapter. Experimental data are given for comparison.

	PBE	PBE0(α)	HSE(α)	$G_0 W_0@$		$G_0 \tilde{W}_0@$		QSG \tilde{W}	Expt.
				PBE0(α)	HSE(α)	PBE0(α)	HSE(α)		
ΔE_V	5.73	8.58	9.01	8.28	8.31	8.31	8.48	8.49	8.7 ± 0.2^a
ΔE_C	0.96	1.90	1.45	2.18	2.14	2.17	1.99	1.63	1.8 ± 0.2^b

^a Refs. [286, 285, 290], ^b Based on measured ΔE_V from Refs. [286, 285, 290] and the experimental band gaps considered in this study. The effect of strain in the CaF_2 overlayer is included through strain corrections determined at the PBE0(0.40) level (cf. Table 7.5).

All advanced electronic-structure methods considered in this chapter yield a reasonable agreement with the experimental data showing errors of at most ~ 0.4 eV, corresponding to only 3% of the largest band gap involved. In particular, the highest accuracy is found for the hybrid functional PBE0(α), which yields band offsets within ~ 0.1 eV from the experimental ones. Interestingly, the high accuracy of the band alignment achieved in the PBE0(α) scheme has already been remarked previously in applications involving ionization potentials [37], band-offsets at semiconductors heterostructures [21], and band alignments at solid-water interfaces [196]. At variance, the hybrid functional HSE(α) overestimates ΔE_V by ~ 0.3 eV and hence underestimates ΔE_C by an equivalent amount. Among the GW methods, the QSG \tilde{W} achieves the highest accuracy resulting in both conduction and valence band offsets underestimated by ~ 0.2 eV. This result is particularly remarkable because the band gaps are not empirically adjusted in the QSG \tilde{W} scheme. However, the consideration of band-gap renormalization effects especially for CaF_2 might lead to a further deviation of the QSG \tilde{W} band offsets with respect to the experimental ones (cf. Sec. 7.3). For the one-shot GW methods, the agreement with respect to experiment is generally worse. In most cases, the valence-band offset is underestimated by ~ 0.4 eV irrespective of the starting point and the use of vertex corrections. The only exception is found for $G_0 \tilde{W}_0@HSE$, which yields band offsets of accuracy comparable with QSG \tilde{W} . All advanced electronic-structure methods in this chapter overcome the band-gap problem encountered in the semilocal PBE approximation (cf. Table 7.8) as

well as in previous LDA-based schemes [309, 310, 311], which yield valence-band offsets underestimated by ~ 2.0 to 2.4 eV.

Apart from the overall good agreement between theory and experiment, it is noteworthy to remark that the band offsets obtained with the various advanced electronic-structure methods show sizable variations. These variations prevalently originate from the different positioning of the band-edge levels with respect to the average electrostatic potential (cf. Sec. 7.3). The other ingredients of the modelling procedure, such as the potential line-up or the strain effects, cannot account for the size of the observed variations. At this point, it is of interest to identify which electronic-structure method provides the most reliable description of the band-edge levels.

To address this issue, we focus on the two most accurate schemes, i.e. PBE0(α) and QSG \tilde{W} . The band-offsets in these two schemes are very close (cf. Table 7.8), but the band-edge levels are noticeably different. Indeed, the band-edge levels of both Si and CaF₂ calculated in QSG \tilde{W} are deeper by 0.5–0.6 eV than the respective ones in PBE0(α). A similar situation occurs for interfaces between cubic semiconductors [21], which all belong to a similar class of materials from both the electronic and structural point of view. In the present case, this behavior is seen for two rather dissimilar materials exhibiting different crystal structure, degree of ionic bonding, and band gap. While this difference does not show up in the band offsets calculated here, it nevertheless directly affects the average electrostatic potential with respect to the vacuum level and in principle can be investigated through the comparison with experimental ionization potentials. In the case of the Si(111) surface, it has already been shown that the ionization potential calculated in the PBE0(α) scheme accurately reproduces the experimental value [37], whereas the QSG \tilde{W} result shows a significant overestimation by about 0.5 eV [18]. For silicon, Grüneis *et al.* have shown that the consideration of higher-order diagrams in GW leads to an upward shift of about 0.3 eV [274], which would compensate the discrepancy to a noticeable extent. However, the same authors have shown that such a shift is not encountered for large band-gap materials and would thus presumably not apply to the case of CaF₂. Thus, it appears clearly that further investigations are necessary to understand the overall position of the band structure with respect to the average electrostatic potential or to vacuum level.

7.5 Effect of interfacial Si-F bonding

In this section, we address the reduction of the valence-band offset at the CaF₂/Si(111) interface as the fraction of Si-F bonding increases due to excess fluorine. The possibility of a Si-F termination has been amply discussed when determining the precise interface morphology [278, 285, 277, 279]. While a predominance of Si-Ca bonds has clearly been identified at the interface [277, 279, 289, 306, 282, 283, 284, 305], evidence for a certain percentage of Si-F bonds has also been established [277, 280]. Despite the considerable efforts deployed [285, 277, 312, 280, 282, 283], the quantitative dependence of the valence-band offset on the fraction of interfacial Si-F bonding has so far remained elusive.

Having established the accuracy of advanced electronic-structure calculations, we are now in a suitable position for addressing this issue. For this purpose, we construct various interface models showing fractions of Si-F bonding corresponding to 25%, 50%, 75%, and 100% fluorine termination. To account for the intermediate fractions of fluorine termination, we double the size of the interfacial repeat unit used so far in both lateral directions, resulting in models with a total number of atoms multiplied by four. Following Refs. [286, 277], we position the F atoms at the T sites of the $\text{Si}(111)-(1 \times 1)$ surface and the Ca atoms at the T_4 sites. In particular, for each of the intermediate percentages, we consider three interface models differing in the specific arrangement of Si-F and Si-Ca bonds. Some representative examples of these models are shown in Fig. 7.7.

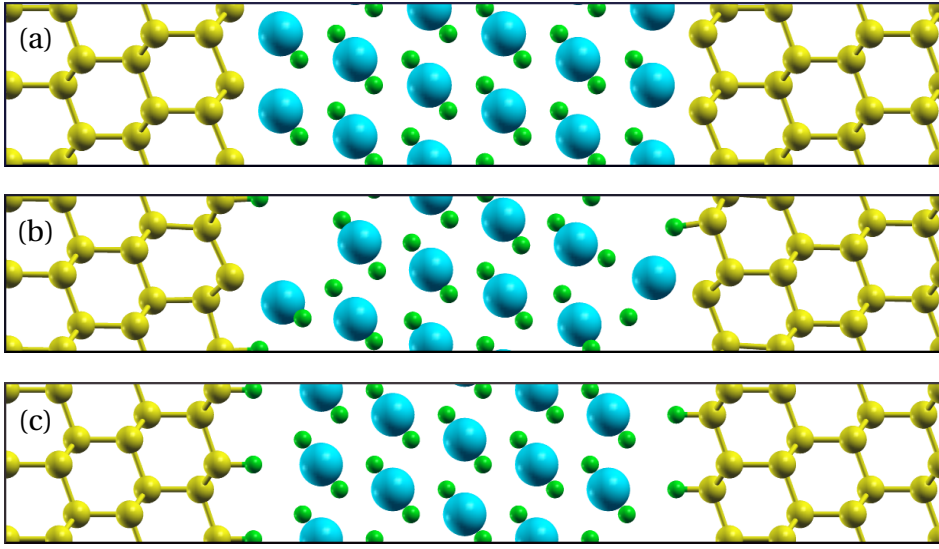


Figure 7.7 – Atomic structure of an interface model with (a) 0%, (b) 50%, and (c) 100% Si-F bonds. Si, Ca, and F atoms are shown in yellow, blue, and green, respectively.

We apply the computational setup described in Sec. 7.2, which includes a relaxation at the PBE level. We check that the considered percentages of Si-F bonds are preserved through the structural relaxation. The multiple structural models at the intermediate fractions show total energies differing by at most 0.7 eV per surface Si atom. In this way, the interface is described through a set of low-energy structural configurations. A shifted $2 \times 2 \times 1$ \mathbf{k} -point mesh is found to give converged line-up potentials. For the calculation of the band offsets, we use the hybrid functional $\text{PBE0}(\alpha)$, which has been shown in Sec. 7.4.2 to yield the highest accuracy among the electronic-structure methods considered in this study.

The results of our investigation are illustrated in Fig. 7.8, in which the valence-band offsets are displayed versus the fraction of Si-F bonding. We observe a general reduction of the valence-band offset with increasing fraction of Si-F bonding. In particular, we determine a sizable difference of 4.7 eV between pure Si-Ca and pure Si-F bonding. When considering the various structural models at a given intermediate fraction, we find valence-band offsets

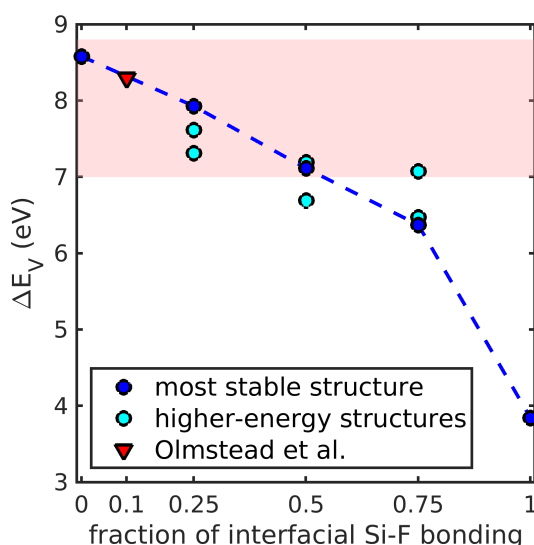


Figure 7.8 – Valence-band offset (in eV) versus the fraction of interfacial Si-F bonding. Calculated values are given as circles. The most stable and higher-energy structures are shown in blue and cyan, respectively. The dashed line is a guide to the eye. The shaded area indicates the interval of valence-band offsets measured in experiments in which the interfacial fraction of Si-F bonds has not been determined explicitly. The upper and lower bounds correspond to 8.8 eV [285] and 7.0 eV [313, 312], respectively. The experimental result of Olmstead *et al.* [277] is illustrated with a red triangle at the estimated fraction of interfacial Si-F bonding.

falling in a range of ~ 0.6 eV due to the varying bonding patterns. The descending trend of the valence-band offset is nevertheless well supported.

Our result demonstrate that the valence-band offset sensitively depends on the amount of interfacial Si-F bonding. In view of this dependence, we attribute the large spread from 7.0 eV to 8.8 eV in the experimental data [312, 313, 285, 286, 277, 287, 288, 289, 290] to different amounts of generally uncontrolled F contamination. On the basis of our calculations, we estimate that the utilized samples might contain up to 50% of Si-F bonding. In particular, in the experiment of Olmstead *et al.* [277], the fraction of Si-F bonding could be estimated resulting in a data point lying consistently with respect to the results of our calculations (cf. Fig. 7.8). This agreement supports the dependence found in Fig. 7.8.

7.6 Summary

In this chapter, we investigated the band alignment at the $\text{CaF}_2/\text{Si}(111)$ interface through various advanced electronic-structure methods based on hybrid functional and *GW* calculations. This allowed us to assess the accuracy of these theoretical schemes for an interface that has been extremely well characterized from the experimental point of view. In particular, we considered both $\text{PBE0}(\alpha)$ and $\text{HSE}(\alpha)$ hybrid-functional forms, several one-shot *GW* methods with various starting points, with or without vertex corrections, and the self-consistent $\text{QSG}\tilde{\text{W}}$

scheme. All applied schemes were empirically tuned to reproduce the experimental band gap, with the only exception being the fully *ab initio* QSG \tilde{W} . We determined the band offsets by combining the band-edge levels calculated for the bulk components with the line-up of the average electrostatic potential at the interface.

All electronic-structure methods considered in this chapter perform satisfactorily yielding band offsets within 0.4 eV from the experimental values. The highest accuracy encountered is 0.1 eV and is found for the empirically tuned PBE0(α) hybrid functional. This result is particularly interesting since it further extends the range of successful applications of this scheme [37, 21, 196]. QSG \tilde{W} is the next most accurate scheme reproducing the experimental band offsets within 0.2 eV. This is particularly remarkable since the band gap of the interface components is not imposed in this scheme, but determined in a fully *ab initio* fashion.

Apart from finding an overall good agreement with experiment, our study reveals significant differences between the band offsets calculated with the applied electronic-structure methods. Due to their size, the origin of these differences can be reconducted to the position of the band-edge levels with respect to the average electrostatic potential in each electronic-structure scheme. In particular, it is interesting to compare PBE0(α) and QSG \tilde{W} . While both schemes give band offsets agreeing within at most 0.2 eV with the experiment, the band edges with respect to the average electrostatic potential consistently differ by 0.5–0.6 eV in the two interface components. This difference does not affect the band offsets at the $\text{CaF}_2/\text{Si}(111)$ interface, but leads to different ionization potentials. In this respect, results in the literature for silicon suggest that it is the PBE0(α) scheme that yields a better agreement with the experiment [37, 18]. However, PBE0(α) is an empirical scheme and thus remains unsatisfactory. In the presence of increasing support in favor of PBE0(α) [37, 21, 196], it is legitimate to inquire whether the fully *ab initio* QSG \tilde{W} scheme still misses a crucial ingredient. Grüneis *et al.* proposed to go beyond such a *GW* scheme by including higher-order diagrams [274]. However, such corrections were found to be insignificant for large-gap materials [274] and would thus leave the band edges of CaF_2 unaffected. Therefore, it appears clearly at this stage that further investigations are necessary for allowing a consistent picture to emerge.

In the final part of this chapter, we determined the reduction of the valence-band offsets as a function of the amount of extra fluorine at the interface. Our results are consistent with the experimental characterization and offer an explanation for the large spread in the measured band offsets. The present analysis suggests that the bonding structure at the $\text{CaF}_2/\text{Si}(111)$ interface should be carefully characterized prior to the achievement of benchmark results for the band offsets.

8 Conclusions

In this thesis, we explore various routes for improving electronic-structure calculations by focusing on nonempirical hybrid functionals. In particular, we investigate dielectric-dependent hybrid functionals and hybrid functionals that satisfy Koopmans' condition as constructed for both global and range-separated functional forms. Through a series of investigations, we demonstrate that these functionals provide an accurate description of the band gaps of various semiconducting and insulating materials. The comparison with experimental references and state-of-the-art *GW* calculations confirms the validity of our conclusions.

Prior to the application of the nonempirical schemes to specific kinds of materials, we focus in Chapter 4 on conceptual developments of hybrid functionals satisfying Koopmans' condition. In particular, we identify open questions concerning the use of defect levels for the construction of these functionals. To overcome these issues, we introduce adjustable potential probes, which allow us to study the band-gap estimate as the defect level varies within the band gap. We find that the estimate is most accurate in case the defect level lies in the middle of the band gap. In contrast, we observe a notable deterioration for defect levels in the vicinity of the band edges. The monitoring of the delocalized screening charge allows us to explain this observation and in turn to achieve an improved description of the band gap. The application of this methodology to common semiconducting and insulating materials yields band gaps differing by less than 0.2 eV from experiment. In addition, our results provide guidelines for the selection of suitable potential probes even when natural defect states cannot be used. This enlarges the scope of the methodology based on the enforcement of Koopmans' condition.

Having established a conceptual balance between DDH functionals and hybrid functionals satisfying Koopmans' condition, we turn to the examination of band-gap predictions as obtained with these functionals. First, we investigate inorganic metal-halide perovskites in Chapter 5. More specifically, we study nine cubic perovskites belonging to the class CsBX_3 , with $\text{B} = \text{Ge}, \text{Sn}, \text{Pb}$ and $\text{X} = \text{Cl}, \text{Br}, \text{I}$. These compounds serve as a representative test set and allow us to perform $\text{QSG}\tilde{W}$ reference calculations due to their small unit cell. Our hybrid-functional calculations indicate that the global DDH functional exhibits an accuracy inferior to the range-separated one. This observation is inline with previous studies in the literature

corroborating range-separated DDH functionals for band-gap predictions [35, 47, 57]. The hybrid functionals fulfilling Koopmans' condition also yield band gaps in good agreement with our *GW* references. Interestingly, this statement holds irrespective of the global or range-separated functional form, thereby supporting the robustness of hybrid functionals satisfying Koopmans' condition for band-gap calculations [51]. Overall, we find that the two nonempirical schemes yield band gaps with an accuracy of ~ 0.2 eV. Based on a discussion of the required computational cost, we then elect the range-separated DDH functional as the most suitable approach for the application to high-throughput screening of larger sets of perovskite materials.

In Chapter 6, we investigate the fundamental band gaps of liquid water and hexagonal ice. Due to the large variety of conflicting experimental and theoretical studies in the literature, we proceed in two steps. First, we establish robust benchmarks through a critical review of various experimental studies. Then, we employ self-consistent *GW* calculations and nonempirical hybrid functionals to obtain state-of-the-art theoretical band-gap estimates. As a result of both steps, we consistently achieve fundamental band gaps of liquid water and hexagonal ice. Moreover, the calculations presented in this chapter provide valuable insight into the accuracy achievable with nonempirical hybrid functionals. In particular, we observe significantly overestimated band gaps when employing the global DDH functional. This result is consistent with the poor performance of this scheme seen in the study on the perovskite compounds. Once again, range-separated DDH functionals can overcome this deficiency and provide a more precise description of the band gap. However, the comparison of three different range-separated DDH functionals exhibits a critical dependence of the band-gap estimate on the specific fraction of Fock exchange incorporated in the short range. This observation hints at a lack of consistency among the existing range-separated DDH schemes and necessitates further investigation. For the hybrid functionals satisfying Koopmans' condition, we generally find good agreement with the experimental references. In case the global functional form is considered, a small band-gap underestimation of 0.1-0.2 eV is apparent. This accuracy is consistent with the results obtained in Chapter 4, Chapter 5, and Ref. [51]. In addition to the global functional, we also construct a range-separated hybrid functional that complies with the Koopmans' condition, the asymptotically correct KS potential, and the spatial variation of the screening. This nonempirical hybrid functional provides band gaps with a remarkable accuracy and guides the way towards a unification of DDH functionals and hybrid functionals enforcing Koopmans' condition.

In the last chapter of this thesis, we turn to the investigation of band-edge levels. In particular, we determine the band offsets at the $\text{CaF}_2/\text{Si}(111)$ interface. This interface can serve as an ideal test case to examine the accuracy of computational schemes due to the combination of constituents with largely different band gaps and to the precise knowledge of the interface morphology. In our study, we examine in particular global and range-separated hybrid functionals as well as *GW* calculations including self-consistency and vertex corrections. In order to diminish systematic errors, we consider in this chapter an empirical adjustment of the hybrid-functional parameters. Due to the insight gained in the previous chapters, we can infer

that the results obtained with nonempirical hybrid functionals would vary only marginally with respect to the empirical ones. Our calculations indicate that the global hybrid functional is capable of precisely describing the interfacial band offsets. The obtained accuracy is even higher than the one achieved with the highly sophisticated QSGW scheme. These promising results guide the way towards accurate band-alignment calculations with nonempirical hybrid functionals.

Finally, it is interesting to reflect on further investigations in the context of nonempirical hybrid functionals. More specifically, we focus on two aspects, namely (i) the application of nonempirical hybrid functionals to materials of particular interest, and (ii) further developments of the theoretical concepts. In the following, we address these points in more details.

First, we discuss specific materials for which the application of nonempirical hybrid functionals is expected to provide enlightening results. For instance, materials which incorporate localized d electrons such as some III-V semiconductors (GaAs, GaN, InP etc.) and transition-metal oxides (ZnO, Cu₂O, NiO, TiO₂ etc.) can be assigned to this category. In particular the latter have shown to be notoriously difficult to describe both with hybrid-functional [272] and GW calculations [101, 117, 195, 18, 196]. Therefore, it would be of great interest to examine the performance of nonempirical hybrid functionals for such materials. For DDH functionals, several successful applications have already been reported [44, 35, 136, 57, 137]. For hybrid functionals satisfying Koopmans' condition, only a few studies can be found [49, 55, 258], whereas the majority of works resort to nonempirical DFT+ U schemes [146, 147, 148] when considering materials with d electrons. A comparative study using a consistent computational setup would therefore be highly appreciated. It is noteworthy that in such an investigation one could compare not only the accuracy of the band-gap estimates but also the average positions of the d bands which are relevant for band-alignment calculations [314, 315].

Another attractive test set for nonempirical hybrid functionals represent nanoporous materials such as metal-organic frameworks (MOFs). Numerous of these compounds are investigated at present due to their possible application for photocatalytic water splitting [316, 317]. For their theoretical characterization, one could imagine an analogous investigation to our study on the metal-halide perovskites presented in Chapter 5. In particular, the application of hybrid functionals satisfying Koopmans' condition has been demonstrated recently in Ref. [316]. Similar studies employing DDH functionals are lacking at present. Therefore, it would be interesting to construct hybrid functionals based on both nonempirical schemes and to systematically compare the obtained band gaps for a representative set of MOFs. We expect that on the basis of such an examination, one could additionally identify the most appropriate functional for the high-throughput screening of large sets of MOFs.

Also amorphous materials (Ge, SiO₂, HfO₂ etc.) or binary alloys (In _{x} Ga_{1- x} N, CuIn _{x} Ga_{1- x} S₂ etc.) could be investigated by means of nonempirical hybrid functionals. These compounds are of great practical importance due to their incorporation in various microelectronic devices. Furthermore, these materials are typically studied using hybrid functionals since GW calcu-

lations are practically unaffordable due to the sizeable structural models required. It would be interesting to examine to what extent nonempirical hybrid functionals provide accurate band gaps of these systems. In particular for binary alloys, it would be fascinating to study the variation of the band gap on the concentration ratio x . This dependence is also known as band-gap bowing [318, 319] and can only be approximately described through semilocal or empirical hybrid functionals. Adopting the nonempirical hybrid-functional schemes, one could determine the amount of Fock exchange specifically for each ratio x and thus study the band-gap bowing with an unprecedented accuracy.

Certainly, there exist a variety of other materials to which nonempirical hybrid functionals could be applied as well. However, we remain here with the given examples as representatives for various other possibilities. Instead, it is our interest to discuss also conceptual developments for nonempirical hybrid functionals. In particular for hybrid functionals satisfying Koopmans' condition, one can envisage various improvements. So far, the construction of these functionals necessitates the analysis of localized defects within a supercell of the considered host material. This constraint inherits a huge computational burden which notably limits the application scope of these functionals. To overcome this drawback, it would be highly desirable to enforce Koopmans' condition without defect calculations. Interestingly, promising steps towards this goal can be found in the works of Ivady *et al.* [147, 148]. These authors focus on deriving analytical expressions for the hybrid-functional parameters that enforce Koopmans' condition. Despite the fact that this approach needs to be elaborated further, it guides the way towards enforcing Koopmans' condition at greatly reduced computational cost.

Another thought-provoking improvement of nonempirical hybrid functionals is the unification of the dielectric-dependent and the Koopmans' scheme. As we have shown in our studies on perovskites (cf. Chapter 5) and on water/ice (cf. Chapter 6), it is possible to construct such functionals based on the range-separated CAM functional. Their application to the present materials yields band-gap estimates in good agreement with experimental references and state-of-the-art *GW* calculations. However, the validity of this statement needs to be demonstrated for a larger class of semiconducting and insulating materials.

Apparently much work is still required to develop the ideas outlined in this chapter. In the mean time, we hope that the results presented in this thesis could serve as a basis for further studies employing nonempirical hybrid functionals.

Appendix A

Band alignment at the water/vacuum interface

In this Appendix, we determine the alignment of the band-edge levels of liquid water with respect to the vacuum level. This specific band alignment has provoked controversial scientific discussion [116, 188, 189] and is also highly relevant for the description of photocatalytic reactions at semiconductor/water interfaces [195, 196]. Having established a consistent description of the band gap of liquid water in Chapter 6, we are in the comfortable situation to address the band alignment at the water/vacuum interface.

Band-alignment scheme

We compute the band alignment following the scheme outlined in Refs. [293, 294]. A graphical representation of this scheme is given in Fig. 8.1.

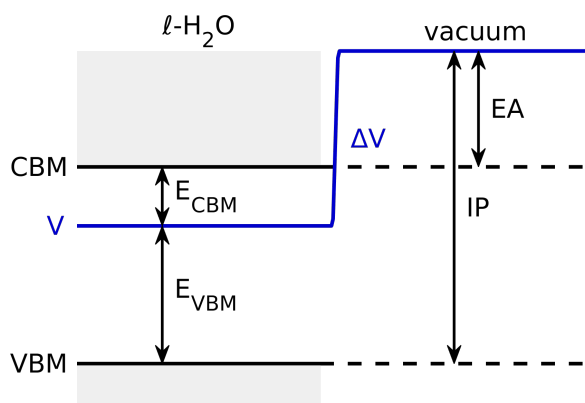


Figure 8.1 – Schematic illustration of the band alignment at the water/vacuum interface.

The determination of the band-edge positions of liquid water is based on one bulk and on one interface calculation. The former is used to position the valence-band maximum (VBM) E_{VBM} and the conduction-band minimum (CBM) E_{CBM} relative to the average electrostatic

Appendix A. Band alignment at the water/vacuum interface

potential V . The latter is instrumental to obtain the line-up ΔV of the average electrostatic potential across the water/vacuum interface. The position of the VBM with respect to the vacuum level, i.e. the ionization potential IP, is then found through $\text{IP} = -E_{\text{VBM}} + \Delta V$. In analogy, the position of the CBM relative to the vacuum level, i.e. the electron affinity EA, is given by $\text{EA} = -E_{\text{CBM}} + \Delta V$.

Band-edge positions vs. average electrostatic potential

For the bulk calculations, we focus in particular on the electronic-structure methods which yield the most reliable band-gap estimates of liquid water (cf. Sec. 6.6). These are the QSG \tilde{W} method and the nonempirical hybrid functionals CAM(0, $1/\epsilon_{\infty}^{\text{sc}}, \mu_{\text{TF}}$) and CAM($\alpha_{\text{s,K}}, 1/\epsilon_{\infty}^{\text{Expt}}, \mu_{\text{TF}}$). We do not consider the other electronic-structure methods examined in Chapter 6 since these schemes yield more inaccurate band-gap estimates, which would deteriorate the accuracy in the determined band-edge positions [8].

The computational details of the bulk calculations are given in Sec. 6.4.2 and shall not be repeated in this Appendix. We verified that the presented values for the numerical parameters ensure converged results for the band gap but also for the individual band-edge positions. Furthermore, we note that the extrapolations of the band gap as obtained with QSG \tilde{W} can be performed analogously for the VBM and the CBM. We checked that the band-edge extrapolations determined in this way are consistent with the band-gap extrapolations presented in Fig. 6.3.

The computed band-edge levels with respect to the average electrostatic potential are given in Table 8.1. We observe that both the VBM and the CBM of liquid water as obtained with QSG \tilde{W} are systematically lower by 0.3-0.6 eV with respect to the corresponding band-edge levels achieved with the nonempirical hybrid functionals. This finding could at least partially result

Table 8.1 – Band-edge levels E_{VBM} and E_{CBM} (in eV) with respect to the average electrostatic potential. The corresponding fundamental band gap E_{g} (in eV) is also given. Values obtained with QSG \tilde{W} , CAM(0, $1/\epsilon_{\infty}^{\text{sc}}, \mu_{\text{TF}}$), and CAM($\alpha_{\text{s,K}}, 1/\epsilon_{\infty}^{\text{Expt}}, \mu_{\text{TF}}$) are distinguished. In the bottom panel, the band-edge levels and the band gap include the NQE corrections $\Delta E_{\text{VBM}}^{\text{NQE}}$, $\Delta E_{\text{CBM}}^{\text{NQE}}$, and $\Delta E_{\text{g}}^{\text{NQE}}$ (see text).

	QSG \tilde{W}	CAM(0, $1/\epsilon_{\infty}^{\text{sc}}, \mu_{\text{TF}}$)	CAM($\alpha_{\text{s,K}}, 1/\epsilon_{\infty}^{\text{Expt}}, \mu_{\text{TF}}$)
E_{VBM}	−7.4	−6.8	−7.1
E_{CBM}	2.4	2.9	2.9
E_{g}	9.8	9.7	9.9
$E_{\text{VBM}} + \Delta E_{\text{VBM}}^{\text{NQE}}$	−6.9	−6.3	−6.6
$E_{\text{CBM}} + \Delta E_{\text{CBM}}^{\text{NQE}}$	2.2	2.7	2.6
$E_{\text{g}} + \Delta E_{\text{g}}^{\text{NQE}}$	9.1	9.0	9.2

from the different band-gap estimates of the three methods. However, the band-gap variations amount to only 0.1-0.2 eV and are thus insufficient to account for the full effect. We remark that similar differences in the band-edge levels obtained with *GW* and hybrid-functional schemes have been found also for Si and CaF₂ in Sec. 7.3 and for various other materials in Ref. [273].

It is noteworthy that the results presented in the top panel of Table 8.1 have been obtained with classical water snapshots. For a more realistic description of the electronic structure, it is necessary to account for nuclear quantum effects (NQE). For liquid water, these effects have been shown to reduce the fundamental band gap by $\Delta E_g^{\text{NQE}} = -0.7$ eV [116] (cf. Sec. 6.2). For the purposes of this Appendix, it is necessary to express this correction to the band gap as individual corrections to the VBM and the CBM, which we denote as $\Delta E_{\text{VBM}}^{\text{NQE}}$ and $\Delta E_{\text{CBM}}^{\text{NQE}}$, respectively. Based on the QSGW calculations of Chen *et al.* presented in Fig. 5 of Ref. [116], one can infer these corrections to be 0.47 eV and -0.23 eV, respectively. These values are consistent with other results reported in the literature [188] and ensure additionally an overall band-gap correction of -0.7 eV. Therefore we apply these NQE corrections systematically to the band-edge levels achieved with the three electronic-structure methods. The corrected band-edge levels (and band gaps) are given in the bottom panel of Table 8.1. We note that the discrepancies among the three schemes remain unaffected since $\Delta E_{\text{VBM}}^{\text{NQE}}$ and $\Delta E_{\text{CBM}}^{\text{NQE}}$ act as constant shifts to the VBM and the CBM, respectively. We adopt the corrected band-edge levels throughout this Appendix for the alignment at the water/vacuum interface.

Line-up potential at the water/vacuum interface

For the interface calculation, we consider a molecular-dynamics (MD) trajectory computed by Ambrosio *et al.* [189, 320]. In their simulation, the water/vacuum interface has been modelled through an orthorhombic supercell, which is elongated in the *c* direction and accommodates ~ 25 Å of liquid water and 40 Å of vacuum. The density of liquid water in the bulk-like region amounts to 0.995 g/cm³ which is in good agreement with experimental references [239]. The molecular configurations of the 128 incorporated water molecules are well equilibrated due to an evolution of the MD over 60 ps. Van der Waals interactions have been accounted for through the use of the revised Vydrov and Van Voorhis (rVV10) nonlocal density functional [240, 241]. The empirical parameter *b* has been set to 9.3, which ensures a realistic description of the structure of liquid water [242, 116]. Further information on the employed MD trajectory can be found in Ref. [189] and the corresponding archive on the Materials Cloud [320].

In the calculation of the line-up potential ΔV , the potential profile has been symmetrized. This effectively eliminates the bias due to the small residual electric field [189]. Upon the MD evolution, ΔV converges to a value of 3.37 ± 0.04 eV as shown in Fig. 8.2. We remark that this result has been achieved through an cumulative running average over water configurations after every time step of 0.1 ps. This corresponds to a total number of 600 snapshots which ensures a sufficient sampling of the configuration space. We note that the absolute value of ΔV cannot be compared to the result of Ambrosio *et al.* since these authors adopted a different set

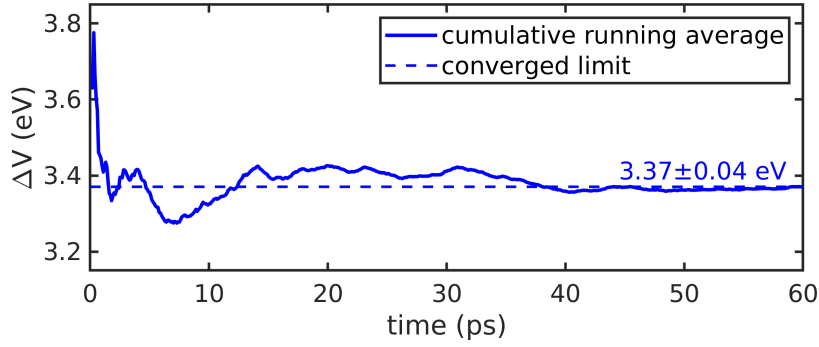


Figure 8.2 – Cumulative running average of the potential offset ΔV across the water/vacuum interface (solid line). The converged limit is also indicated (dashed line).

of pseudopotentials which critically affects the average electrostatic potential. Nevertheless, the residual uncertainty of 0.04 eV is identical to the value reported by Ambrosio *et al.* [189] which indicates that oscillations due to the finite temperature are described consistently.

For the interface calculation, we adopted in this Appendix the semilocal PBE functional. This is justified since electrostatic properties have been shown to be adequate at this level of theory [261, 8, 267, 21]. Indeed, Ambrosio *et al.* have reported a marginal variation of 0.06 eV when recalculating ΔV at the hybrid-functional level [189]. For self-consistent *GW* methods, no such result for the water/vacuum interface can be found in the literature. Nevertheless, Shaltaf *et al.* computed for the Si/SiO₂ interface a variation in ΔV of only 0.02 eV due to such *GW* calculations [261]. Therefore, we use the PBE functional for the computation of the line-up potential and adopt the value of 3.37 eV for all electronic-structure methods considered in this Appendix. We estimate that this way of proceeding introduces an uncertainty in the band alignment of at most 0.1 eV.

Band-edge positions vs. vacuum level

We now have all the ingredients for the calculation of the band alignment at the water/vacuum interface. For this, we combine the band-edge positions relative to the average electrostatic potential with the interfacial line-up. The VBM and CBM obtained in this way are given in Fig. 8.3 where they are compared with experimental references for the IP and the EA, respectively.

We find that the three considered electronic-structure methods yield band-edge levels in good agreement with the experimental references. More specifically, the QSG \tilde{W} scheme positions the CBM within the EA reference interval and the VBM only 0.2 eV below the lower bound of the IP reference interval. For the hybrid functional CAM(0, $1/\epsilon_{\infty}^{\text{sc}}, \mu_{\text{TF}}$), the CBM and the VBM lie higher than the corresponding references by 0.1 eV and 0.2 eV, respectively. The hybrid functional CAM($\alpha_{\text{s,K}}, 1/\epsilon_{\infty}^{\text{Expt}}, \mu_{\text{TF}}$) yields a CBM higher than the upper bound of the EA reference interval by 0.1 eV and a VBM falling within the IP reference interval. Overall, we find that none of the three theoretical schemes yields both band edges falling within the

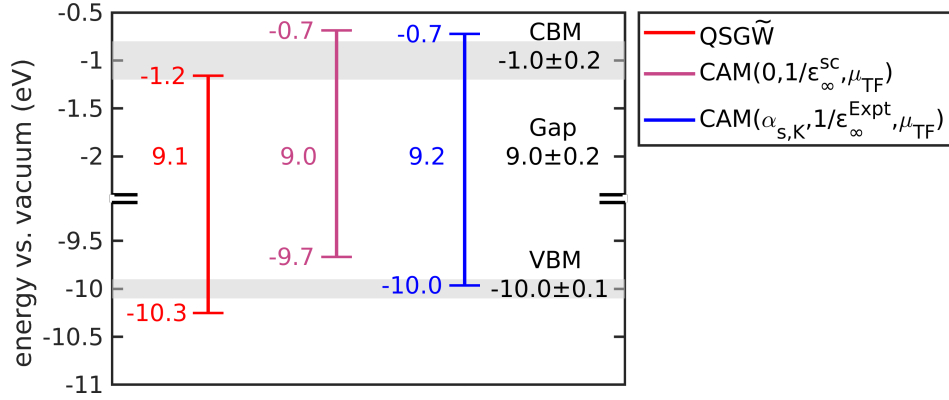


Figure 8.3 – VBM and CBM of liquid water referred to the vacuum level. The results achieved with the QSGW scheme and the nonempirical hybrid functionals CAM(0, $1/\epsilon_{\infty}^{\text{sc}}, \mu_{\text{TF}}$) and CAM($\alpha_{s,K}, 1/\epsilon_{\infty}^{\text{Expt}}, \mu_{\text{TF}}$) are shown. The shaded areas illustrate the intervals corresponding to the experimental reference values for the ionization potential IP and the electron affinity EA (cf. Sec. 6.2). The fundamental band gaps as inferred from the VBM and the CBM are also indicated. All energies are given in electronvolts.

experimental reference intervals. However, the observed deviations amount to at most 0.2 eV, which corresponds to the typical accuracy achieved with state-of-the-art electronic-structure calculations [116, 188, 189, 196].

We note that the present band alignment is consistent with other studies in the literature. In particular, for the QSGW scheme, we find band-edge positions differing only by 0.1 eV from those reported by Ziae and Bredow [214]. However, these authors combined results from calculations using different pseudopotentials which may lead to inconsistencies [189]. As far as the hybrid-functional schemes are concerned, we can compare our results with those of Ambrosio *et al.* [189]. These authors employed the empirically adjusted hybrid functional PBE0(0.45) and found the VBM and the CBM at -9.7 eV and -0.8 eV with respect to the vacuum level, respectively. These results differ only by 0.1-0.3 eV from the present values. These discrepancies can be attributed to the different value of 8.9 eV assumed for the fundamental band gap in Ref. [189].

Overall, we conclude that the QSGW scheme as well as nonempirical hybrid functionals CAM(0, $1/\epsilon_{\infty}^{\text{sc}}, \mu_{\text{TF}}$) and CAM($\alpha_{s,K}, 1/\epsilon_{\infty}^{\text{Expt}}, \mu_{\text{TF}}$) are capable of accurately predicting the band alignment at the water/vacuum interface. The residual deviations from the experimental references amount to at most 0.2 eV. The comparison with other theoretical studies in the literature further supports the conclusions drawn in this Appendix.

Bibliography

- [1] D. R. Hartree and W. Hartree. “Self-consistent field, with exchange, for beryllium”. *Proc. R. Soc. Lond. A* 150.869 (1935), pp. 9–33.
- [2] V. Fock. “Näherungsmethode zur Lösung des quantenmechanischen Mehrkörperproblems”. *Z. Physik* 61 (1930), pp. 126–148.
- [3] L. H. Thomas. “The calculation of atomic fields”. *Math. Proc. Cambridge Philos. Soc.* 23.5 (1927), pp. 542–548.
- [4] W. Kohn and L. J. Sham. “Self-Consistent Equations Including Exchange and Correlation Effects”. *Phys. Rev.* 140 (1965), A1133–A1138.
- [5] J. P. Perdew, K. Burke, and M. Ernzerhof. “Generalized Gradient Approximation Made Simple”. *Phys. Rev. Lett.* 77 (1996), pp. 3865–3868.
- [6] L. J. Sham and M. Schlüter. “Density-Functional Theory of the Energy Gap”. *Phys. Rev. Lett.* 51 (20 1983), pp. 1888–1891.
- [7] M.-Y. Zhang et al. “Hybrid functionals with system-dependent parameters: Conceptual foundations and methodological developments”. *Wiley Interdiscip. Rev.-Comput. Mol. Sci.* 10.6 (2020), e1476.
- [8] A. Alkauskas, P. Broqvist, and A. Pasquarello. “Defect Energy Levels in Density Functional Calculations: Alignment and Band Gap Problem”. *Phys. Rev. Lett.* 101 (4 2008), p. 046405.
- [9] L. Hedin. “New Method for Calculating the One-Particle Green’s Function with Application to the Electron-Gas Problem”. *Phys. Rev.* 139 (3A 1965), A796–A823.
- [10] F. Aryasetiawan and O. Gunnarsson. “The GW method”. *Rep. Prog. Phys* 61.3 (1998), pp. 237–312.
- [11] M. S. Hybertsen and S. G. Louie. “First-Principles Theory of Quasiparticles: Calculation of Band Gaps in Semiconductors and Insulators”. *Phys. Rev. Lett.* 55 (13 1985), pp. 1418–1421.
- [12] M. S. Hybertsen and S. G. Louie. “Electron correlation in semiconductors and insulators: Band gaps and quasiparticle energies”. *Phys. Rev. B* 34 (8 1986), pp. 5390–5413.

Bibliography

- [13] R. W. Godby, M. Schlüter, and L. J. Sham. “Accurate Exchange-Correlation Potential for Silicon and Its Discontinuity on Addition of an Electron”. *Phys. Rev. Lett.* 56 (22 1986), pp. 2415–2418.
- [14] F. Bruneval et al. “Many-Body Perturbation Theory Using the Density-Functional Concept: Beyond the *GW* Approximation”. *Phys. Rev. Lett.* 94 (18 2005), p. 186402.
- [15] M. van Schilfgaarde, T. Kotani, and S. Faleev. “Quasiparticle Self-Consistent *GW* Theory”. *Phys. Rev. Lett.* 96 (22 2006), p. 226402.
- [16] T. Kotani, M. van Schilfgaarde, and S. V. Faleev. “Quasiparticle self-consistent *GW* method: A basis for the independent-particle approximation”. *Phys. Rev. B* 76 (16 2007), p. 165106.
- [17] M. Shishkin, M. Marsman, and G. Kresse. “Accurate Quasiparticle Spectra from Self-Consistent *GW* Calculations with Vertex Corrections”. *Phys. Rev. Lett.* 99 (24 2007), p. 246403.
- [18] W. Chen and A. Pasquarello. “Accurate band gaps of extended systems via efficient vertex corrections in *GW*”. *Phys. Rev. B* 92 (4 2015), p. 041115.
- [19] W. Chen and A. Pasquarello. “Correspondence of defect energy levels in hybrid density functional theory and many-body perturbation theory”. *Phys. Rev. B* 88 (11 2013), p. 115104.
- [20] W. Chen and A. Pasquarello. “First-principles determination of defect energy levels through hybrid density functionals and *GW*”. *J. Phys. Condens. Matter* 27.13 (2015), p. 133202.
- [21] K. Steiner, W. Chen, and A. Pasquarello. “Band offsets of lattice-matched semiconductor heterojunctions through hybrid functionals and G_0W_0 ”. *Phys. Rev. B* 89 (20 2014), p. 205309.
- [22] X. Gonze et al. “ABINIT: First-principles approach to material and nanosystem properties”. *Comput. Phys. Commun.* 180.12 (2009), pp. 2582–2615.
- [23] M. Govoni and G. Galli. “Large Scale *GW* Calculations”. *J. Chem. Theory Comput.* 11.6 (2015), pp. 2680–2696.
- [24] A. D. Becke. “A new mixing of Hartree-Fock and local density-functional theories”. *J. Chem. Phys.* 98.2 (1993), pp. 1372–1377.
- [25] D. M. Bylander and L. Kleinman. “Good semiconductor band gaps with a modified local-density approximation”. *Phys. Rev. B* 41 (11 1990), pp. 7868–7871.
- [26] A. Seidl et al. “Generalized Kohn-Sham schemes and the band-gap problem”. *Phys. Rev. B* 53 (7 1996), pp. 3764–3774.
- [27] C. Lee, W. Yang, and R. G. Parr. “Development of the Colle-Salvetti correlation-energy formula into a functional of the electron density”. *Phys. Rev. B* 37 (2 1988), pp. 785–789.
- [28] X. Wu, A. Selloni, and R. Car. “Order- N implementation of exact exchange in extended insulating systems”. *Phys. Rev. B* 79 (8 2009), p. 085102.

-
- [29] F. Gygi. "Compact Representations of Kohn-Sham Invariant Subspaces". *Phys. Rev. Lett.* 102 (16 2009), p. 166406.
- [30] L. Lin. "Adaptively Compressed Exchange Operator". *J. Chem. Theory Comput.* 12.5 (2016), pp. 2242–2249.
- [31] J. P. Perdew, M. Ernzerhof, and K. Burke. "Rationale for mixing exact exchange with density functional approximations". *J. Chem. Phys.* 105.22 (1996), pp. 9982–9985.
- [32] J. Heyd, G. E. Scuseria, and M. Ernzerhof. "Hybrid functionals based on a screened Coulomb potential". *J. Chem. Phys.* 118.18 (2003), pp. 8207–8215.
- [33] J. Heyd, G. E. Scuseria, and M. Ernzerhof. "Erratum: Hybrid functionals based on a screened Coulomb potential [J. Chem. Phys. 118, 8207 (2003)]". *J. Chem. Phys.* 124.21 (2006), p. 219906.
- [34] W. Yang, Y. Zhang, and P. W. Ayers. "Degenerate Ground States and a Fractional Number of Electrons in Density and Reduced Density Matrix Functional Theory". *Phys. Rev. Lett.* 84 (22 2000), pp. 5172–5175.
- [35] J. H. Skone, M. Govoni, and G. Galli. "Nonempirical range-separated hybrid functionals for solids and molecules". *Phys. Rev. B* 93 (23 2016), p. 235106.
- [36] A. Alkauskas, P. Broqvist, and A. Pasquarello. "Defect levels through hybrid density functionals: Insights and applications". *Phys. Status Solidi B* 248.4 (2011), pp. 775–789.
- [37] W. Chen and A. Pasquarello. "Band-edge positions in *GW*: Effects of starting point and self-consistency". *Phys. Rev. B* 90 (16 2014), p. 165133.
- [38] T. Shimazaki and Y. Asai. "Band structure calculations based on screened Fock exchange method". *Chem. Phys. Lett.* 466.1 (2008), pp. 91–94.
- [39] T. Shimazaki and Y. Asai. "First principles band structure calculations based on self-consistent screened Hartree-Fock exchange potential". *J. Chem. Phys.* 130.16 (2009), p. 164702.
- [40] T. Shimazaki and Y. Asai. "Energy band structure calculations based on screened Hartree-Fock exchange method: Si, AlP, AlAs, GaP, and GaAs". *J. Chem. Phys.* 132.22 (2010), p. 224105.
- [41] M. A. L. Marques et al. "Density-based mixing parameter for hybrid functionals". *Phys. Rev. B* 83 (3 2011), p. 035119.
- [42] S. Refaely-Abramson et al. "Quasiparticle Spectra from a Nonempirical Optimally Tuned Range-Separated Hybrid Density Functional". *Phys. Rev. Lett.* 109 (22 2012), p. 226405.
- [43] J. H. Skone, M. Govoni, and G. Galli. "Self-consistent hybrid functional for condensed systems". *Phys. Rev. B* 89 (19 2014), p. 195112.
- [44] M. Gerosa et al. "Electronic structure and phase stability of oxide semiconductors: Performance of dielectric-dependent hybrid functional DFT, benchmarked against *GW* band structure calculations and experiments". *Phys. Rev. B* 91 (15 2015), p. 155201.

Bibliography

- [45] M. Gerosa et al. “Communication: Hole localization in Al-doped quartz SiO₂ within ab initio hybrid-functional DFT”. *J. Chem. Phys.* 143.11 (2015), p. 111103.
- [46] M. Gerosa et al. “Accuracy of dielectric-dependent hybrid functionals in the prediction of optoelectronic properties of metal oxide semiconductors: a comprehensive comparison with many-body GW and experiments”. *J. Phys. Condens. Matter* 30.4 (2017), p. 044003.
- [47] W. Chen et al. “Nonempirical dielectric-dependent hybrid functional with range separation for semiconductors and insulators”. *Phys. Rev. Materials* 2 (7 2018), p. 073803.
- [48] B. Sadigh, P. Erhart, and D. Åberg. “Variational polaron self-interaction-corrected total-energy functional for charge excitations in insulators”. *Phys. Rev. B* 92 (2015), p. 075202.
- [49] P. Deák et al. “Choosing the correct hybrid for defect calculations: A case study on intrinsic carrier trapping in β – Ga₂O₃”. *Phys. Rev. B* 95 (7 2017), p. 075208.
- [50] S. Kokott et al. “First-principles supercell calculations of small polarons with proper account for long-range polarization effects”. *New J. Phys.* 20 (2018), p. 033023.
- [51] G. Miceli et al. “Nonempirical hybrid functionals for band gaps and polaronic distortions in solids”. *Phys. Rev. B* 97 (12 2018), p. 121112.
- [52] T. J. Smart et al. “Fundamental principles for calculating charged defect ionization energies in ultrathin two-dimensional materials”. *Phys. Rev. Materials* 2 (12 2018), p. 124002.
- [53] A. R. Elmaslmane, M. B. Watkins, and K. P. McKenna. “First-Principles Modeling of Polaron Formation in TiO₂ Polymorphs”. *J. Chem. Theory Comput.* 14.7 (2018), pp. 3740–3751.
- [54] T. Bischoff, I. Reshetnyak, and A. Pasquarello. “Adjustable potential probes for band-gap predictions of extended systems through nonempirical hybrid functionals”. *Phys. Rev. B* 99 (20 2019), p. 201114.
- [55] P. Deák et al. “Optimized hybrid functionals for defect calculations in semiconductors”. *J. Appl. Phys.* 126.13 (2019), p. 130901.
- [56] L. Kronik and S. Kümmel. “Piecewise linearity, freedom from self-interaction, and a Coulomb asymptotic potential: three related yet inequivalent properties of the exact density functional”. *Phys. Chem. Chem. Phys.* 22 (29 2020), pp. 16467–16481.
- [57] Z.-H. Cui et al. “Doubly Screened Hybrid Functional: An Accurate First-Principles Approach for Both Narrow- and Wide-Gap Semiconductors”. *J. Phys. Chem. Lett.* 9.9 (2018), pp. 2338–2345.
- [58] J. C. Conesa. “Modeling with Hybrid Density Functional Theory the Electronic Band Alignment at the Zinc Oxide-Anatase Interface”. *J. Phys. Chem. C* 116.35 (2012), pp. 18884–18890.
- [59] H. Zheng, M. Govoni, and G. Galli. “Dielectric-dependent hybrid functionals for heterogeneous materials”. *Phys. Rev. Materials* 3 (7 2019), p. 073803.

-
- [60] T. A. Pham et al. “Probing the electronic structure of liquid water with many-body perturbation theory”. *Phys. Rev. B* 89 (6 2014), p. 060202.
- [61] A. P. Gaiduk et al. “First-Principles Simulations of Liquid Water Using a Dielectric-Dependent Hybrid Functional”. *J. Phys. Chem. Lett.* 9.11 (2018), pp. 3068–3073.
- [62] J. P. Perdew et al. “Density-Functional Theory for Fractional Particle Number: Derivative Discontinuities of the Energy”. *Phys. Rev. Lett.* 49 (23 1982), pp. 1691–1694.
- [63] P. Mori-Sánchez, A. J. Cohen, and W. Yang. “Many-electron self-interaction error in approximate density functionals”. *J. Chem. Phys.* 125.20 (2006), p. 201102.
- [64] M. Levy, J. P. Perdew, and V. Sahni. “Exact differential equation for the density and ionization energy of a many-particle system”. *Phys. Rev. A* 30 (5 1984), pp. 2745–2748.
- [65] V. Atalla et al. “Enforcing the linear behavior of the total energy with hybrid functionals: Implications for charge transfer, interaction energies, and the random-phase approximation”. *Phys. Rev. B* 94 (3 2016), p. 035140.
- [66] T. Stein et al. “Fundamental Gaps in Finite Systems from Eigenvalues of a Generalized Kohn-Sham Method”. *Phys. Rev. Lett.* 105 (26 2010), p. 266802.
- [67] S. Refaely-Abramson, R. Baer, and L. Kronik. “Fundamental and excitation gaps in molecules of relevance for organic photovoltaics from an optimally tuned range-separated hybrid functional”. *Phys. Rev. B* 84 (7 2011), p. 075144.
- [68] S. Lany and A. Zunger. “Generalized Koopmans density functional calculations reveal the deep acceptor state of N_O in ZnO ”. *Phys. Rev. B* 81 (2010), p. 205209.
- [69] F. Ambrosio et al. “Origin of low electron-hole recombination rate in metal halide perovskites”. *Energy Environ. Sci.* 11 (1 2018), pp. 101–105.
- [70] T. Yanai, D. P. Tew, and N. C. Handy. “A new hybrid exchange-correlation functional using the Coulomb-attenuating method (CAM-B3LYP)”. *Chem. Phys. Lett.* 393.1 (2004), pp. 51–57.
- [71] S. Refaely-Abramson et al. “Gap renormalization of molecular crystals from density-functional theory”. *Phys. Rev. B* 88 (8 2013), p. 081204.
- [72] F. Giustino. *Materials Modelling using Density Functional Theory*. Oxford: Oxford University Press, 2014.
- [73] M. Born and R. Oppenheimer. “Zur Quantentheorie der Molekeln”. *Annalen der Physik* 389 (1927), pp. 457–484.
- [74] R. M. Martin. *Electronic Structure - Basic Theory and Practical Methods*. Cambridge: Cambridge University Press, 2004.
- [75] P. Hohenberg and W. Kohn. “Inhomogeneous Electron Gas”. *Phys. Rev.* 136 (1964), B864–B871.
- [76] G. Grosso and G. P. Parravicini. *Solid State Physics*. Cambridge: Academic Press, 2003.

Bibliography

- [77] M. A. L. Marques, M. J. T. Oliveira, and T. Burnus. “Libxc: A library of exchange and correlation functionals for density functional theory”. *Comput. Phys. Commun.* 183.10 (2012), pp. 2272–2281.
- [78] J. P. Perdew and S. Kurth. “Density Functionals for Non-relativistic Coulomb Systems in the New Century”. *A Primer in Density Functional Theory*. Ed. by C. Fiolhais, F. Nogueira, and M. A. L. Marques. Berlin, Heidelberg: Springer Berlin Heidelberg, 2003, pp. 1–55.
- [79] S. H. Vosko, L. Wilk, and M. Nusair. “Accurate spin-dependent electron liquid correlation energies for local spin density calculations: a critical analysis”. *Can. J. Phys.* 58.8 (1980), pp. 1200–1211.
- [80] J. P. Perdew and A. Zunger. “Self-interaction correction to density-functional approximations for many-electron systems”. *Phys. Rev. B* 23 (10 1981), pp. 5048–5079.
- [81] J. P. Perdew and Y. Wang. “Accurate and simple analytic representation of the electron-gas correlation energy”. *Phys. Rev. B* 45 (1992), pp. 13244–13249.
- [82] D. M. Ceperley and B. J. Alder. “Ground State of the Electron Gas by a Stochastic Method”. *Phys. Rev. Lett.* 45 (1980), pp. 566–569.
- [83] F. Gygi and A. Baldereschi. “Self-consistent Hartree-Fock and screened-exchange calculations in solids: Application to silicon”. *Phys. Rev. B* 34 (6 1986), pp. 4405–4408.
- [84] H. J. Monkhorst and J. D. Pack. “Special points for Brillouin-zone integrations”. *Phys. Rev. B* 13 (1976), pp. 5188–5192.
- [85] N. Troullier and J. L. Martins. “Efficient pseudopotentials for plane-wave calculations”. *Phys. Rev. B* 43 (3 1991), pp. 1993–2006.
- [86] A. Dal Corso. “Pseudopotentials periodic table: From H to Pu”. *Comput. Mater. Sci.* 95 (2014). <http://www.quantum-espresso.org/pseudopotentials>, pp. 337–350.
- [87] D. R. Hamann. “Optimized norm-conserving Vanderbilt pseudopotentials”. *Phys. Rev. B* 88 (2013), p. 085117.
- [88] M. van Setten et al. “The PseudoDojo: Training and grading a 85 element optimized norm-conserving pseudopotential table”. *Comput. Phys. Commun.* 226 (2018), pp. 39–54.
- [89] P. Giannozzi et al. “QUANTUM ESPRESSO: a modular and open-source software project for quantum simulations of materials”. *J. Phys. Condens. Matter* 21 (2009), p. 395502.
- [90] T. Leininger et al. “Combining long-range configuration interaction with short-range density functionals”. *Chem. Phys. Lett.* 275.3 (1997), pp. 151–160.
- [91] H. Iikura et al. “A long-range correction scheme for generalized-gradient-approximation exchange functionals”. *J. Chem. Phys.* 115.8 (2001), pp. 3540–3544.
- [92] R. Baer and D. Neuhauser. “Density Functional Theory with Correct Long-Range Asymptotic Behavior”. *Phys. Rev. Lett.* 94 (4 2005), p. 043002.

-
- [93] I. C. Gerber et al. "Range separated hybrid density functional with long-range Hartree-Fock exchange applied to solids". *J. Chem. Phys.* 127.5 (2007), p. 054101.
- [94] J.-D. Chai and M. Head-Gordon. "Systematic optimization of long-range corrected hybrid density functionals". *J. Chem. Phys.* 128.8 (2008), p. 084106.
- [95] F. Bruneval and M. Gatti. "Quasiparticle Self-Consistent GW Method for the Spectral Properties of Complex Materials". *First Principles Approaches to Spectroscopic Properties of Complex Materials*. Ed. by C. Di Valentin, S. Botti, and M. Cococcioni. Berlin, Heidelberg: Springer Berlin Heidelberg, 2014, pp. 99–135.
- [96] G. Onida, L. Reining, and A. Rubio. "Electronic excitations: density-functional versus many-body Green's-function approaches". *Rev. Mod. Phys.* 74 (2 2002), pp. 601–659.
- [97] S. L. Adler. "Quantum Theory of the Dielectric Constant in Real Solids". *Phys. Rev.* 126 (2 1962), pp. 413–420.
- [98] N. Wiser. "Dielectric Constant with Local Field Effects Included". *Phys. Rev.* 129 (1 1963), pp. 62–69.
- [99] F. Gygi and A. Baldereschi. "Quasiparticle energies in semiconductors: Self-energy correction to the local-density approximation". *Phys. Rev. Lett.* 62 (18 1989), pp. 2160–2163.
- [100] J. Klimes, M. Kaltak, and G. Kresse. "Predictive GW calculations using plane waves and pseudopotentials". *Phys. Rev. B* 90 (7 2014), p. 075125.
- [101] F. Bruneval et al. "Exchange and Correlation Effects in Electronic Excitations of Cu_2O ". *Phys. Rev. Lett.* 97 (26 2006), p. 267601.
- [102] J. Vidal et al. "Strong Interplay between Structure and Electronic Properties in $\text{CuIn}(\text{S}, \text{Se})_2$: A First-Principles Study". *Phys. Rev. Lett.* 104 (5 2010), p. 056401.
- [103] S. V. Faleev, M. van Schilfgaarde, and T. Kotani. "All-Electron Self-Consistent GW Approximation: Application to Si, MnO, and NiO". *Phys. Rev. Lett.* 93 (12 2004), p. 126406.
- [104] B. Holm and U. von Barth. "Fully self-consistent GW self-energy of the electron gas". *Phys. Rev. B* 57 (4 1998), pp. 2108–2117.
- [105] W. Ku and A. G. Eguiluz. "Band-Gap Problem in Semiconductors Revisited: Effects of Core States and Many-Body Self-Consistency". *Phys. Rev. Lett.* 89 (12 2002), p. 126401.
- [106] A. Fleszar and W. Hanke. "Electronic structure of II^{B} –VI semiconductors in the GW approximation". *Phys. Rev. B* 71 (4 2005), p. 045207.
- [107] F. Bruneval, N. Vast, and L. Reining. "Effect of self-consistency on quasiparticles in solids". *Phys. Rev. B* 74 (4 2006), p. 045102.
- [108] S. Botti, D. Kammerlander, and M. A. L. Marques. "Band structures of $\text{Cu}_2\text{ZnSnS}_4$ and $\text{Cu}_2\text{ZnSnSe}_4$ from many-body methods". *Appl. Phys. Lett.* 98.24 (2011), p. 241915.
- [109] S. Sharma et al. "Bootstrap Approximation for the Exchange-Correlation Kernel of Time-Dependent Density-Functional Theory". *Phys. Rev. Lett.* 107 (18 2011), p. 186401.

Bibliography

- [110] Y.-M. Byun, J. Sun, and C. A. Ullrich. “Time-dependent density-functional theory for periodic solids: assessment of excitonic exchange–correlation kernels”. *Electronic Structure* 2.2 (2020), p. 023002.
- [111] T. Bischoff, I. Reshetnyak, and A. Pasquarello. “Band alignment at the $\text{CaF}_2/\text{Si}(111)$ interface through advanced electronic structure calculations”. *Phys. Rev. B* 101 (23 2020), p. 235302.
- [112] J. Wiktor et al. “Comprehensive modeling of the band gap and absorption spectrum of BiVO_4 ”. *Phys. Rev. Materials* 1 (2 2017), p. 022401.
- [113] C. Bhandari et al. “All-electron quasiparticle self-consistent *GW* band structures for SrTiO_3 including lattice polarization corrections in different phases”. *Phys. Rev. Materials* 2 (1 2018), p. 013807.
- [114] J. Wiktor, U. Rothlisberger, and A. Pasquarello. “Predictive Determination of Band Gaps of Inorganic Halide Perovskites”. *J. Phys. Chem. Lett.* 8.22 (2017), pp. 5507–5512.
- [115] T. Bischoff et al. “Nonempirical hybrid functionals for band gaps of inorganic metal-halide perovskites”. *Phys. Rev. Materials* 3 (12 2019), p. 123802.
- [116] W. Chen et al. “Ab initio Electronic Structure of Liquid Water”. *Phys. Rev. Lett.* 117 (18 2016), p. 186401.
- [117] C. Friedrich, M. C. Müller, and S. Blügel. “Band convergence and linearization error correction of all-electron *GW* calculations: The extreme case of zinc oxide”. *Phys. Rev. B* 83 (8 2011), p. 081101.
- [118] S. Lebègue et al. “Implementation of an all-electron *GW* approximation based on the projector augmented wave method without plasmon pole approximation: Application to Si, SiC, AlAs, InAs, NaH, and KH”. *Phys. Rev. B* 67 (15 2003), p. 155208.
- [119] R. W. Godby and R. J. Needs. “Metal-insulator transition in Kohn-Sham theory and quasiparticle theory”. *Phys. Rev. Lett.* 62 (10 1989), pp. 1169–1172.
- [120] G. Makov and M. C. Payne. “Periodic boundary conditions in ab initio calculations”. *Phys. Rev. B* 51 (7 1995), pp. 4014–4022.
- [121] S. Lany and A. Zunger. “Assessment of correction methods for the band-gap problem and for finite-size effects in supercell defect calculations: Case studies for ZnO and GaAs”. *Phys. Rev. B* 78 (23 2008), p. 235104.
- [122] C. Freysoldt, J. Neugebauer, and C. G. Van de Walle. “Fully Ab Initio Finite-Size Corrections for Charged-Defect Supercell Calculations”. *Phys. Rev. Lett.* 102 (1 2009), p. 016402.
- [123] S. E. Taylor and F. Bruneval. “Understanding and correcting the spurious interactions in charged supercells”. *Phys. Rev. B* 84 (7 2011), p. 075155.
- [124] S. Falletta, J. Wiktor, and A. Pasquarello. “Finite-size corrections of defect energy levels involving ionic polarization”. *Phys. Rev. B* 102 (4 2020), p. 041115.

-
- [125] H.-P. Komsa, T. T. Rantala, and A. Pasquarello. “Finite-size supercell correction schemes for charged defect calculations”. *Phys. Rev. B* 86 (4 2012), p. 045112.
- [126] K. Kunc and R. Resta. “External Fields in the Self-Consistent Theory of Electronic States: A New Method for Direct Evaluation of Macroscopic and Microscopic Dielectric Response”. *Phys. Rev. Lett.* 51 (8 1983), pp. 686–689.
- [127] R. Resta and K. Kunc. “Self-consistent theory of electronic states and dielectric response in semiconductors”. *Phys. Rev. B* 34 (10 1986), pp. 7146–7157.
- [128] P. Umari and A. Pasquarello. “Polarizability and dielectric constant in density-functional supercell calculations with discrete k-point samplings”. *Phys. Rev. B* 68 (8 2003), p. 085114.
- [129] C. Freysoldt, J. Neugebauer, and C. G. Van de Walle. “Electrostatic interactions between charged defects in supercells”. *Phys. Status Solidi B* 248.5 (2011), pp. 1067–1076.
- [130] O. Madelung. *Semiconductors: Data Handbook*. Springer, 1996.
- [131] P. Umari and A. Pasquarello. “Ab initio Molecular Dynamics in a Finite Homogeneous Electric Field”. *Phys. Rev. Lett.* 89 (15 2002), p. 157602.
- [132] R. W. Nunes and X. Gonze. “Berry-phase treatment of the homogeneous electric field perturbation in insulators”. *Phys. Rev. B* 63 (15 2001), p. 155107.
- [133] R. D. King-Smith and D. Vanderbilt. “Theory of polarization of crystalline solids”. *Phys. Rev. B* 47 (3 1993), pp. 1651–1654.
- [134] R. Resta. “Macroscopic polarization in crystalline dielectrics: the geometric phase approach”. *Rev. Mod. Phys.* 66 (3 1994), pp. 899–915.
- [135] I. Souza, J. Íñiguez, and D. Vanderbilt. “First-Principles Approach to Insulators in Finite Electric Fields”. *Phys. Rev. Lett.* 89 (11 2002), p. 117602.
- [136] J. He and C. Franchini. “Assessing the performance of self-consistent hybrid functional for band gap calculation in oxide semiconductors”. *J. Phys.: Condens. Matter* 29.45 (2017), p. 454004.
- [137] P. Liu et al. “Assessing model-dielectric-dependent hybrid functionals on the antiferromagnetic transition-metal monoxides MnO, FeO, CoO, and NiO”. *J. Phys.: Condens. Matter* 32.1 (2019), p. 015502.
- [138] M. Levy. “Universal variational functionals of electron densities, first-order density matrices, and natural spin-orbitals and solution of the v-representability problem”. *PNAS* 76.12 (1979), pp. 6062–6065.
- [139] M. Dauth et al. “Piecewise linearity in the GW approximation for accurate quasiparticle energy predictions”. *Phys. Rev. B* 93 (12 2016), p. 121115.
- [140] P. Mori-Sánchez, A. J. Cohen, and W. Yang. “Localization and Delocalization Errors in Density Functional Theory and Implications for Band-Gap Prediction”. *Phys. Rev. Lett.* 100 (14 2008), p. 146401.

Bibliography

- [141] J. F. Janak. “Proof that $\frac{\partial E}{\partial n_i} = \epsilon$ in density-functional theory”. *Phys. Rev. B* 18 (12 1978), pp. 7165–7168.
- [142] E. Kraisler and L. Kronik. “Fundamental gaps with approximate density functionals: The derivative discontinuity revealed from ensemble considerations”. *J. Chem. Phys.* 140.18 (2014), 18A540.
- [143] J. P. Perdew et al. “Understanding band gaps of solids in generalized Kohn–Sham theory”. *PNAS* 114.11 (2017), pp. 2801–2806.
- [144] T. Koopmans. “Über die Zuordnung von Wellenfunktionen und Eigenwerten zu den Einzelnen Elektronen Eines Atoms”. *Physica* 1 (1934), p. 104 113.
- [145] M. Cococcioni and S. de Gironcoli. “Linear response approach to the calculation of the effective interaction parameters in the LDA+ U method”. *Phys. Rev. B* 71 (2005), p. 035105.
- [146] S. Lany and A. Zunger. “Polaronic hole localization and multiple hole binding of acceptors in oxide wide-gap semiconductors”. *Phys. Rev. B* 80 (2009), p. 085202.
- [147] V. Ivády et al. “Role of screening in the density functional applied to transition-metal defects in semiconductors”. *Phys. Rev. B* 87 (20 2013), p. 205201.
- [148] V. Ivády et al. “Theoretical unification of hybrid-DFT and DFT + U methods for the treatment of localized orbitals”. *Phys. Rev. B* 90 (3 2014), p. 035146.
- [149] E. Caruso et al. “First-principles description of charge transfer in donor-acceptor compounds from self-consistent many-body perturbation theory”. *Phys. Rev. B* 90 (2014), p. 085141.
- [150] M. Weng et al. “Wannier Koopmans Method Calculations of 2D Material Band Gaps”. *J. Phys. Chem. Lett.* 9.2 (2018), pp. 281–285.
- [151] N. L. Nguyen et al. “First-Principles Photoemission Spectroscopy and Orbital Tomography in Molecules from Koopmans-Compliant Functionals”. *Phys. Rev. Lett.* 114 (2015), p. 166405.
- [152] N. L. Nguyen et al. “First-Principles Photoemission Spectroscopy of DNA and RNA Nucleobases from Koopmans-Compliant Functionals”. *J. Chem. Theory Comput.* 12.8 (2016), pp. 3948–3958.
- [153] T. Bischoff, I. Reshetnyak, and A. Pasquarello. “Adjustable potential probes for band-gap predictions of extended systems through nonempirical hybrid functionals”. *Materials Cloud Archive* (2019).
- [154] M. Cardona and M. L. W. Thewalt. “Isotope effects on the optical spectra of semiconductors”. *Rev. Mod. Phys.* 77 (2005), pp. 1173–1224.
- [155] J. P. Nery et al. “Quasiparticles and phonon satellites in spectral functions of semiconductors and insulators: Cumulants applied to the full first-principles theory and the Fröhlich polaron”. *Phys. Rev. B* 97 (2018), p. 115145.

- [156] W. R. L. Lambrecht, C. Bhandari, and M. van Schilfgaarde. "Lattice polarization effects on the screened Coulomb interaction W of the GW approximation". *Phys. Rev. Materials* 1 (2017), p. 043802.
- [157] R.-Q. Zhang et al. "A first-principles study of ultrathin nanofilms of MgO-supported TiN". *Phys. Chem. Chem. Phys.* 14 (2012), pp. 2462–2467.
- [158] T. Bischoff et al. "Nonempirical hybrid functionals for band gaps of inorganic metal-halide perovskites". *Materials Cloud Archive* (2019).
- [159] A. Kojima et al. "Organometal Halide Perovskites as Visible-Light Sensitizers for Photovoltaic Cells". *J. Am. Chem. Soc.* 131.17 (2009), pp. 6050–6051.
- [160] J. Burschka et al. "Sequential deposition as a route to high-performance perovskite-sensitized solar cells". *Nature* 499 (2013), pp. 316–319.
- [161] G. Hodes. "Perovskite-Based Solar Cells". *Science* 342.6156 (2013), pp. 317–318.
- [162] S. Razza et al. "Research Update: Large-area deposition, coating, printing, and processing techniques for the upscaling of perovskite solar cell technology". *APL Materials* 4.9 (2016), p. 091508.
- [163] W. S. Yang et al. "Iodide management in formamidinium-lead-halide-based perovskite layers for efficient solar cells". *Science* 356.6345 (2017), pp. 1376–1379.
- [164] I. E. Castelli et al. "Bandgap calculations and trends of organometal halide perovskites". *APL Materials* 2.8 (2014), p. 081514.
- [165] M. R. Filip and F. Giustino. "Computational Screening of Homovalent Lead Substitution in Organic–Inorganic Halide Perovskites". *J. Phys. Chem. C* 120.1 (2016), pp. 166–173.
- [166] S. Körbel, M. A. L. Marques, and S. Botti. "Stability and electronic properties of new inorganic perovskites from high-throughput ab initio calculations". *J. Mater. Chem. C* 4 (2016), pp. 3157–3167.
- [167] Z. H. Levine and D. C. Allan. "Linear optical response in silicon and germanium including self-energy effects". *Phys. Rev. Lett.* 63 (1989), pp. 1719–1722.
- [168] C. C. Stoumpos, C. D. Malliakas, and M. G. Kanatzidis. "Semiconducting Tin and Lead Iodide Perovskites with Organic Cations: Phase Transitions, High Mobilities, and Near-Infrared Photoluminescent Properties". *Inorg. Chem.* 52.15 (2013), pp. 9019–9038.
- [169] G. E. Eperon et al. "Formamidinium lead trihalide: a broadly tunable perovskite for efficient planar heterojunction solar cells". *Energy Environ. Sci.* 7 (2014), pp. 982–988.
- [170] M. Sebastian et al. "Excitonic emissions and above-band-gap luminescence in the single-crystal perovskite semiconductors CsPbBr₃ and CsPbCl₃". *Phys. Rev. B* 92 (2015), p. 235210.
- [171] J. B. Hoffman, A. L. Schleper, and P. V. Kamat. "Transformation of Sintered CsPbBr₃ Nanocrystals to Cubic CsPbI₃ and Gradient CsPbBr_xI_{3-x} through Halide Exchange". *J. Am. Chem. Soc.* 138.27 (2016), pp. 8603–8611.

Bibliography

- [172] L. Peedikakkandy and P. Bhargava. "Composition dependent optical, structural and photoluminescence characteristics of cesium tin halide perovskites". *RSC Adv.* 6 (2016).
- [173] I. Chung et al. "CsSnI₃: Semiconductor or Metal? High Electrical Conductivity and Strong Near-Infrared Photoluminescence from a Single Material. High Hole Mobility and Phase-Transitions". *J. Am. Chem. Soc.* 134.20 (2012), pp. 8579–8587.
- [174] C. C. Stoumpos et al. "Hybrid Germanium Iodide Perovskite Semiconductors: Active Lone Pairs, Structural Distortions, Direct and Indirect Energy Gaps, and Strong Nonlinear Optical Properties". *J. Am. Chem. Soc.* 137.21 (2015), pp. 6804–6819.
- [175] T. Krishnamoorthy et al. "Lead-free germanium iodide perovskite materials for photovoltaic applications". *J. Mater. Chem. A* 3 (2015), pp. 23829–23832.
- [176] Z.-G. Lin, L.-C. Tang, and C.-P. Chou. "Study on mid-IR NLO crystals CsGe(Br_xCl_{1-x})₃". *Optical Materials* 31.1 (2008), pp. 28–34.
- [177] G. Thiele, H. W. Rotter, and K. D. Schmidt. "Kristallstrukturen und Phasentransformationen von Caesiumtrihalogenogermanaten(II) CsGeX₃ (X = Cl, Br, I)". *Z. anorg. allg. Chem.* 545.2 (1987), pp. 148–156.
- [178] A. Stroppa and G. Kresse. "The shortcomings of semi-local and hybrid functionals: what we can learn from surface science studies". *New J. Phys.* 10.6 (2008), p. 063020.
- [179] M.-H. Du. "Density Functional Calculations of Native Defects in CH₃NH₃PbI₃: Effects of Spin–Orbit Coupling and Self-Interaction Error". *J. Phys. Chem. Lett.* 6.8 (2015), pp. 1461–1466.
- [180] J. Kang and L.-W. Wang. "High Defect Tolerance in Lead Halide Perovskite CsPbBr₃". *J. Phys. Chem. Lett.* 8.2 (2017), pp. 489–493.
- [181] J. Wiktor, F. Ambrosio, and A. Pasquarello. "Mechanism suppressing charge recombination at iodine defects in CH₃NH₃PbI₃ by polaron formation". *J. Mater. Chem. A* 6 (2018), pp. 16863–16867.
- [182] D. Grand, A. Bernas, and E. Amouyal. "Photoionization of aqueous indole: Conduction band edge and energy gap in liquid water". *Chem. Phys.* 44.1 (1979), pp. 73–79.
- [183] A. Bernas, D. Grand, and E. Amouyal. "Photoionization of solutes and conduction band edge of solvents. Indole in water and alcohols". *J. Phys. Chem.* 84.10 (1980), pp. 1259–1262.
- [184] I. Watanabe, J. B. Flanagan, and P. Delahay. "Vacuum ultraviolet photoelectron emission spectroscopy of water and aqueous solutions". *J. Chem. Phys.* 73.5 (1980), pp. 2057–2062.
- [185] P. Delahay and K. von Burg. "Photoelectron emission spectroscopy of liquid water". *Chem. Phys. Lett.* 83.2 (1981), pp. 250–254.
- [186] A. Bernas, C. Ferradini, and J.-P. Jay-Gerin. "On the electronic structure of liquid water: Facts and reflections". *Chem. Phys.* 222.2 (1997), pp. 151–160.

- [187] B. Winter et al. "Full Valence Band Photoemission from Liquid Water Using EUV Synchrotron Radiation". *J. Phys. Chem. A* 108.14 (2004), pp. 2625–2632.
- [188] A. P. Gaiduk et al. "Electron affinity of liquid water". *Nat. Commun.* 9.1 (2018), p. 247.
- [189] F. Ambrosio, Z. Guo, and A. Pasquarello. "Absolute Energy Levels of Liquid Water". *J. Phys. Chem. Lett.* 9.12 (2018), pp. 3212–3216.
- [190] F. Ambrosio, G. Miceli, and A. Pasquarello. "Redox levels in aqueous solution: Effect of van der Waals interactions and hybrid functionals". *J. Chem. Phys.* 143.24 (2015), p. 244508.
- [191] J. Wiktor, F. Bruneval, and A. Pasquarello. "Partial Molar Volumes of Aqua Ions from First Principles". *J. Chem. Theory Comput.* 13.8 (2017), pp. 3427–3431.
- [192] T. A. Pham et al. "Electronic structure of aqueous solutions: Bridging the gap between theory and experiments". *Sci. Adv.* 3.6 (2017).
- [193] F. Ambrosio, G. Miceli, and A. Pasquarello. "Electronic Levels of Excess Electrons in Liquid Water". *J. Phys. Chem. Lett.* 8.9 (2017), pp. 2055–2059.
- [194] M. Pizzochero, F. Ambrosio, and A. Pasquarello. "Picture of the wet electron: a localized transient state in liquid water". *Chem. Sci.* 10 (31 2019), pp. 7442–7448.
- [195] N. Kharche, J. T. Muckerman, and M. S. Hybertsen. "First-Principles Approach to Calculating Energy Level Alignment at Aqueous Semiconductor Interfaces". *Phys. Rev. Lett.* 113 (17 2014), p. 176802.
- [196] Z. Guo et al. "Alignment of Redox Levels at Semiconductor–Water Interfaces". *Chem. Mater.* 30.1 (2018), pp. 94–111.
- [197] A. Bouzid, P. Gono, and A. Pasquarello. "Reaction pathway of oxygen evolution on Pt(111) revealed through constant Fermi level molecular dynamics". *J. Catal.* 375 (2019), pp. 135–139.
- [198] P. Gono, F. Ambrosio, and A. Pasquarello. "Effect of the Solvent on the Oxygen Evolution Reaction at the TiO₂–Water Interface". *J. Phys. Chem. C* 123.30 (2019), pp. 18467–18474.
- [199] J. Klánová et al. "Environmental Ice Photochemistry: Monochlorophenols". *Environ. Sci. Technol.* 37.8 (2003), pp. 1568–1574.
- [200] C. S. Boxe et al. "Kinetics of NO and NO₂ Evolution from Illuminated Frozen Nitrate Solutions". *J. Phys. Chem. A* 110.10 (2006), pp. 3578–3583.
- [201] N. Takenaka and H. Bandow. "Chemical Kinetics of Reactions in the Unfrozen Solution of Ice". *J. Phys. Chem. A* 111.36 (2007), pp. 8780–8786.
- [202] A. M. Grannas et al. "An overview of snow photochemistry: evidence, mechanisms and impacts". *Atmos. Chem. Phys.* 7.16 (2007), pp. 4329–4373.
- [203] P. Llombart, E. G. Noya, and L. G. MacDowell. "Surface phase transitions and crystal habits of ice in the atmosphere". *Sci. Adv.* 6.21 (2020).
- [204] A. Liebscher. "Aqueous fluids at elevated pressure and temperature". *Geofluids* 10.1-2 (2010), pp. 3–19.

Bibliography

- [205] P. Jenniskens and D. F. Blake. “Structural transitions in amorphous water ice and astrophysical implications”. *Science* 265.5173 (1994), pp. 753–756.
- [206] L. Amiaud et al. “Measurement of the Adsorption Energy Difference between Ortho- and Para-D₂ on an Amorphous Ice Surface”. *Phys. Rev. Lett.* 100 (5 2008), p. 056101.
- [207] C. S. Cucinotta, I. Rungger, and S. Sanvito. “First Principles Study of Electron Tunneling through Ice”. *J. Phys. Chem. C* 116.42 (2012), pp. 22129–22138.
- [208] K. Thürmer and S. Nie. “Formation of hexagonal and cubic ice during low-temperature growth”. *PNAS* 110.29 (2013), pp. 11757–11762.
- [209] G. C. Sosso et al. “Unravelling the origins of ice nucleation on organic crystals”. *Chem. Sci.* 9 (42 2018), pp. 8077–8088.
- [210] N. Gerrard et al. “Strain Relief during Ice Growth on a Hexagonal Template”. *J. Am. Chem. Soc.* 141.21 (2019), pp. 8599–8607.
- [211] E. A. Engel, B. Monserrat, and R. J. Needs. “Vibrational renormalisation of the electronic band gap in hexagonal and cubic ice”. *J. Chem. Phys.* 143.24 (2015), p. 244708.
- [212] V. Garbuio et al. “Ab Initio Calculation of Optical Spectra of Liquids: Many-Body Effects in the Electronic Excitations of Water”. *Phys. Rev. Lett.* 97 (13 2006), p. 137402.
- [213] D. Lu, F. Gygi, and G. Galli. “Dielectric Properties of Ice and Liquid Water from First-Principles Calculations”. *Phys. Rev. Lett.* 100 (14 2008), p. 147601.
- [214] V. Ziaei and T. Bredow. “Probing ionization potential, electron affinity and self-energy effect on the spectral shape and exciton binding energy of quantum liquid water with self-consistent many-body perturbation theory and the Bethe–Salpeter equation”. *J. Phys.: Condens. Matter* 30.21 (2018), p. 215502.
- [215] P. H. Hahn et al. “Optical Absorption of Water: Coulomb Effects versus Hydrogen Bonding”. *Phys. Rev. Lett.* 94 (3 2005), p. 037404.
- [216] C. Fang et al. “The accurate calculation of the band gap of liquid water by means of GW corrections applied to plane-wave density functional theory molecular dynamics simulations”. *Phys. Chem. Chem. Phys.* 17 (1 2015), pp. 365–375.
- [217] W. Yim et al. “Band Gaps and Effective Oscillator Models for Solid Hydrogen and H₂O Ice at High Pressure.” *Correlations in Condensed Matter under Extreme Conditions*. Ed. by G. Angilella and A. La Magna. Springer, 2017. Chap. Band Gaps and Effective Oscillator Models for Solid Hydrogen and H₂O Ice at High Pressure.
- [218] J. M. Heller et al. “Collective oscillation in liquid water”. *J. Chem. Phys.* 60.9 (1974), pp. 3483–3486.
- [219] K. Kobayashi. “Optical spectra and electronic structure of ice”. *J. Phys. Chem.* 87.21 (1983), pp. 4317–4321.
- [220] H. Hayashi and N. Hiraoka. “Accurate Measurements of Dielectric and Optical Functions of Liquid Water and Liquid Benzene in the VUV Region (1–100 eV) Using Small-Angle Inelastic X-ray Scattering”. *J. Phys. Chem. B* 119.17 (2015), pp. 5609–5623.

- [221] N. L. Nguyen et al. "Finite-Field Approach to Solving the Bethe-Salpeter Equation". *Phys. Rev. Lett.* 122 (23 2019), p. 237402.
- [222] J. V. Coe et al. "Using cluster studies to approach the electronic structure of bulk water: Reassessing the vacuum level, conduction band edge, and band gap of water". *J. Chem. Phys.* 107.16 (1997), pp. 6023–6031.
- [223] L. R. Painter et al. "Electronic Properties of Liquid Water in the Vacuum Ultraviolet". *Phys. Rev. Lett.* 21 (5 1968), pp. 282–284.
- [224] J.-Y. Chen and C.-S. Yoo. "High density amorphous ice at room temperature". *PNAS* 108.19 (2011), pp. 7685–7688.
- [225] D. Nordlund et al. "Electronic structure effects in liquid water studied by photoelectron spectroscopy and density functional theory". *Chem. Phys. Lett.* 460.1 (2008), pp. 86–92.
- [226] T. Shibaguchi, H. Onuki, and R. Onaka. "Electronic Structures of Water and Ice". *J. Phys. Soc. Jpn.* 42.1 (1977), pp. 152–158.
- [227] J. Stähler et al. "Real-Time Measurement of the Vertical Binding Energy during the Birth of a Solvated Electron". *J. Am. Chem. Soc.* 137.10 (2015), pp. 3520–3524.
- [228] B. Baron, D. Hoover, and F. Williams. "Vacuum ultraviolet photoelectric emission from amorphous ice". *J. Chem. Phys.* 68.4 (1978), pp. 1997–1999.
- [229] M. Campbell et al. "The electronic structure of the valence bands of solid NH_3 and H_2O studied by ultraviolet photoelectron spectroscopy". *J. Electron Spectros. Relat. Phenomena* 15.1 (1979), pp. 83–90.
- [230] T. Pache et al. "The adsorption of H_2O on clean and oxygen precovered Ni(111) studied by ARUPS and TPD". *Surf. Sci.* 224.1 (1989), pp. 195–214.
- [231] M. Michaud, P. Cloutier, and L. Sanche. "Low-energy electron-energy-loss spectroscopy of amorphous ice: Electronic excitations". *Phys. Rev. A* 44 (9 1991), pp. 5624–5627.
- [232] D. Grand and A. Bernas. "On the conduction band edge energy of ice". *Chem. Phys. Lett.* 97.1 (1983), pp. 119–122.
- [233] J. V. Coe et al. "Photoelectron spectroscopy of hydrated electron cluster anions, $(\text{H}_2\text{O})_{n=2-69}^-$ ". *J. Chem. Phys.* 92.6 (1990), pp. 3980–3982.
- [234] L. Kevan. "Energy level structure and mobilities of excess electrons in aqueous and organic glasses". *J. Phys. Chem.* 76.25 (1972), pp. 3830–3838.
- [235] B. Monserrat, E. A. Engel, and R. J. Needs. "Giant electron-phonon interactions in molecular crystals and the importance of nonquadratic coupling". *Phys. Rev. B* 92 (14 2015), p. 140302.
- [236] M. Del Ben, J. Hutter, and J. van de Vondelle. "Probing the structural and dynamical properties of liquid water with models including non-local electron correlation". *J. Chem. Phys.* 143.5 (2015), p. 054506.
- [237] W. Chen et al. "Ab initio electronic structure of liquid water: Molecular dynamics snapshots". *Materials Cloud Archive* 2018.0023/v1 (2018).

Bibliography

- [238] J. D. Bernal and R. H. Fowler. “A Theory of Water and Ionic Solution, with Particular Reference to Hydrogen and Hydroxyl Ions”. *J. Chem. Phys.* 1.8 (1933), pp. 515–548.
- [239] D. E. Hare and C. M. Sorensen. “The density of supercooled water. II. Bulk samples cooled to the homogeneous nucleation limit”. *J. Chem. Phys.* 87.8 (1987), pp. 4840–4845.
- [240] O. A. Vydrov and T. Van Voorhis. “Nonlocal van der Waals density functional: The simpler the better”. *J. Chem. Phys.* 133.24 (2010), p. 244103.
- [241] R. Sabatini, T. Gorni, and S. de Gironcoli. “Nonlocal van der Waals density functional made simple and efficient”. *Phys. Rev. B* 87 (4 2013), p. 041108.
- [242] G. Miceli, S. de Gironcoli, and A. Pasquarello. “Isobaric first-principles molecular dynamics of liquid water with nonlocal van der Waals interactions”. *J. Chem. Phys.* 142.3 (2015), p. 034501.
- [243] D. R. Hamann. “H₂O hydrogen bonding in density-functional theory”. *Phys. Rev. B* 55 (16 1997), R10157–R10160.
- [244] E. A. Engel, B. Monserrat, and R. J. Needs. “Anharmonic Nuclear Motion and the Relative Stability of Hexagonal and Cubic ice”. *Phys. Rev. X* 5 (2 2015), p. 021033.
- [245] F. Ambrosio, G. Miceli, and A. Pasquarello. “Structural, Dynamical, and Electronic Properties of Liquid Water: A Hybrid Functional Study”. *J. Phys. Chem. B* 120.30 (2016), pp. 7456–7470.
- [246] A. P. Gaiduk, F. Gygi, and G. Galli. “Density and Compressibility of Liquid Water and Ice from First-Principles Simulations with Hybrid Functionals”. *J. Phys. Chem. Lett.* 6.15 (2015), pp. 2902–2908.
- [247] B. Cheng et al. “Ab initio thermodynamics of liquid and solid water”. *PNAS* 116.4 (2019), pp. 1110–1115.
- [248] T. K. Hirsch and L. Ojamäe. “Quantum-Chemical and Force-Field Investigations of Ice Ih: Computation of Proton-Ordered Structures and Prediction of Their Lattice Energies”. *J. Phys. Chem. B* 108.40 (2004), pp. 15856–15864.
- [249] Y. Tajima, T. Matsuo, and H. Suga. “Phase transition in KOH-doped hexagonal ice”. *Nature* 299.5886 (1982), pp. 810–812.
- [250] S. M. Jackson et al. “Single-Crystal Neutron Diffraction Studies of the Structure of Ice XI”. *J. Phys. Chem. B* 101.32 (1997), pp. 6142–6145.
- [251] D. Prendergast, J. C. Grossman, and G. Galli. “The electronic structure of liquid water within density-functional theory”. *J. Chem. Phys.* 123.1 (2005), p. 014501.
- [252] S. Fujita, S. Mae, and T. Matsuoka. “Dielectric anisotropy in ice Ih at 9.7 GHz”. *Ann. Glaciol.* 17 (1993), 276–280.
- [253] T. Matsuoka et al. “Precise measurement of dielectric anisotropy in ice Ih at 39 GHz”. *J. Appl. Phys.* 81.5 (1997), pp. 2344–2348.

- [254] G. P. Johari, S. J. Jones, and F. C. Frank. "Dielectric properties of polycrystalline D₂O ice Ih (hexagonal)". *Proc. R. Soc. A* 349.1659 (1976), pp. 467–495.
- [255] N. Bjerrum. "Structure and Properties of Ice". *Science* 115.2989 (1952), pp. 385–390.
- [256] M. de Koning and A. Antonelli. "On the Trapping of Bjerrum Defects in Ice Ih: The Case of the Molecular Vacancy". *J. Phys. Chem. B* 111.43 (2007), pp. 12537–12542.
- [257] I. Popov et al. "The dynamic crossover in dielectric relaxation behavior of ice Ih". *Phys. Chem. Chem. Phys.* 17 (2 2015), pp. 1489–1497.
- [258] T. J. Smart et al. "Optical absorption induced by small polaron formation in transition metal oxides: The case of Co₃O₄". *Phys. Rev. Materials* 3 (10 2019), p. 102401.
- [259] T. Bischoff, I. Reshetnyak, and A. Pasquarello. "Band alignment at the CaF₂/Si(111) interface through advanced electronic structure calculations". *Materials Cloud Archive* (2020).
- [260] A. Franciosi and C. G. Van de Walle. "Heterojunction band offset engineering". *Surf. Sci. Rep.* 25.1 (1996), pp. 1–140.
- [261] R. Shaltaf et al. "Band Offsets at the Si/SiO₂ Interface from Many-Body Perturbation Theory". *Phys. Rev. Lett.* 100 (18 2008), p. 186401.
- [262] S. Zhang et al. "Quasiparticle calculation of valence band offset of AlAs-GaAs(001)". *Solid State Commun.* 66.6 (1988), pp. 585–588.
- [263] S. B. Zhang et al. "Quasiparticle band offset at the (001) interface and band gaps in ultrathin superlattices of GaAs-AlAs heterojunctions". *Phys. Rev. B* 41 (14 1990), pp. 10058–10067.
- [264] D. Cociorva, W. G. Aulbur, and J. W. Wilkins. "Quasiparticle calculations of band offsets at AlN–GaN interfaces". *Solid State Commun.* 124.1 (2002), pp. 63–66.
- [265] M. Grüning, R. Shaltaf, and G.-M. Rignanese. "Quasiparticle calculations of the electronic properties of ZrO₂ and HfO₂ polymorphs and their interface with Si". *Phys. Rev. B* 81 (3 2010), p. 035330.
- [266] A. Wadehra, J. W. Nicklas, and J. W. Wilkins. "Band offsets of semiconductor heterostructures: A hybrid density functional study". *Appl. Phys. Lett.* 97.9 (2010), p. 092119.
- [267] H.-P. Komsa, P. Broqvist, and A. Pasquarello. "Alignment of defect levels and band edges through hybrid functionals: Effect of screening in the exchange term". *Phys. Rev. B* 81 (20 2010), p. 205118.
- [268] C. Mietze et al. "Band offsets in cubic GaN/AlN superlattices". *Phys. Rev. B* 83 (19 2011), p. 195301.
- [269] C. Mitra et al. "Quasiparticle band offsets of semiconductor heterojunctions from a generalized marker method". *Phys. Rev. B* 84 (19 2011), p. 193304.
- [270] A. Punya and W. R. L. Lambrecht. "Band offsets between ZnGeN₂, GaN, ZnO, and ZnSnN₂ and their potential impact for solar cells". *Phys. Rev. B* 88 (7 2013), p. 075302.

Bibliography

- [271] Y. Hinuma et al. “Band alignment of semiconductors from density-functional theory and many-body perturbation theory”. *Phys. Rev. B* 90 (15 2014), p. 155405.
- [272] A. Alkauskas and A. Pasquarello. “Band-edge problem in the theoretical determination of defect energy levels: The O vacancy in ZnO as a benchmark case”. *Phys. Rev. B* 84 (12 2011), p. 125206.
- [273] W. Chen and A. Pasquarello. “Band-edge levels in semiconductors and insulators: Hybrid density functional theory versus many-body perturbation theory”. *Phys. Rev. B* 86 (3 2012), p. 035134.
- [274] A. Grüneis et al. “Ionization Potentials of Solids: The Importance of Vertex Corrections”. *Phys. Rev. Lett.* 112 (9 2014), p. 096401.
- [275] W. Chen and A. Pasquarello. “Accuracy of GW for calculating defect energy levels in solids”. *Phys. Rev. B* 96 (2 2017), p. 020101.
- [276] P. Broqvist and A. Pasquarello. “First principles investigation of defects at interfaces between silicon and amorphous high-*k* oxides”. *Microelectron. Eng.* 84.9 (2007). INFOS 2007, pp. 2022–2027.
- [277] M. A. Olmstead et al. “Photoemission study of bonding at the CaF₂-on-Si(111) interface”. *Phys. Rev. B* 35 (14 1987), pp. 7526–7532.
- [278] F. J. Himpsel et al. “Structure and bonding at the CaF₂/Si(111) interface”. *Appl. Phys. Lett.* 48.9 (1986), pp. 596–598.
- [279] R. M. Tromp and M. C. Reuter. “Structure of the Si(111)-CaF₂ Interface”. *Phys. Rev. Lett.* 61 (15 1988), pp. 1756–1759.
- [280] J. D. Denlinger et al. “Growth kinetics of CaF₂/Si(111) heteroepitaxy: An x-ray photoelectron diffraction study”. *Phys. Rev. B* 51 (8 1995), pp. 5352–5365.
- [281] J. Harada et al. “X-ray scattering from surfaces and interfaces and its application to the characterization of CaF₂/Si(111) interfaces”. *J. Cryst. Growth* 163.1 (1996), pp. 31–38.
- [282] A. Klust et al. “Low-temperature interface structure of CaF₂/Si(111) studied by combining x-ray standing waves with component-resolved photoemission”. *Phys. Rev. B* 65 (19 2002), p. 193404.
- [283] C. R. Wang et al. “Temperature-dependent growth mechanisms of CaF₂ on Si(111)”. *J. Vac. Sci. Technol. A* 22.5 (2004), pp. 2182–2187.
- [284] C. Deiter et al. “Structural transitions and relaxation processes during the epitaxial growth of ultrathin CaF₂ films on Si(111)”. *Phys. Rev. B* 82 (8 2010), p. 085449.
- [285] D. Rieger et al. “Electronic structure of the CaF₂/Si(111) interface”. *Phys. Rev. B* 34 (10 1986), pp. 7295–7306.
- [286] F. J. Himpsel et al. “Determination of Interface States for CaF₂/Si(111) from Near-Edge X-Ray-Absorption Measurements”. *Phys. Rev. Lett.* 56 (14 1986), pp. 1497–1500.
- [287] P. Avouris and R. Wolkow. “Scanning tunneling microscopy of insulators: CaF₂ epitaxy on Si(111)”. *Appl. Phys. Lett.* 55.11 (1989), pp. 1074–1076.

-
- [288] A. B. McLean and F. J. Himpsel. “Band dispersion of an interface state: $\text{CaF}_2/\text{Si}(111)$ ”. *Phys. Rev. B* 39 (2 1989), pp. 1457–1460.
- [289] T. F. Heinz et al. “Electronic transitions at the $\text{CaF}_2/\text{Si}(111)$ interface probed by resonant three-wave mixing spectroscopy”. *Phys. Rev. Lett.* 63 (6 1989), pp. 644–647.
- [290] A. Izumi et al. “Study of band offsets in $\text{CdF}_2/\text{CaF}_2/\text{Si}(111)$ heterostructures using x-ray photoelectron spectroscopy”. *Appl. Phys. Lett.* 67.19 (1995), pp. 2792–2794.
- [291] A. V. Krukau et al. “Influence of the exchange screening parameter on the performance of screened hybrid functionals”. *J. Chem. Phys.* 125.22 (2006), p. 224106.
- [292] M. Verstraete and X. Gonze. “First-principles calculation of the electronic, dielectric, and dynamical properties of CaF_2 ”. *Phys. Rev. B* 68 (19 2003), p. 195123.
- [293] C. G. Van de Walle and R. M. Martin. “Theoretical study of band offsets at semiconductor interfaces”. *Phys. Rev. B* 35 (15 1987), pp. 8154–8165.
- [294] A. Baldereschi, S. Baroni, and R. Resta. “Band Offsets in Lattice-Matched Heterojunctions: A Model and First-Principles Calculations for GaAs/AlAs ”. *Phys. Rev. Lett.* 61 (6 1988), pp. 734–737.
- [295] T. Tsujibayashi et al. “Spectral profile of the two-photon absorption coefficients in CaF_2 and BaF_2 ”. *Appl. Phys. Lett.* 80.16 (2002), pp. 2883–2885.
- [296] F. Kaplan et al. “Quasi-Particle Self-Consistent *GW* for Molecules”. *J. Chem. Theory Comput.* 12.6 (2016), pp. 2528–2541.
- [297] K. Shinozaki et al. “Morphology of CaF_2 nanocrystals and elastic properties in transparent oxyfluoride crystallized glasses”. *Optical Materials* 33.8 (2011), pp. 1350–1356.
- [298] K. Liu, H. Wang, and X. Zhang. *Ductile Mode Cutting of Brittle Materials*. Springer, 2020.
- [299] R. M. Hazen and L. W. Finger. “Calcium fluoride as an internal pressure standard in high-pressure crystallography”. *J. Appl. Crystallogr.* 14.4 (1981), pp. 234–236.
- [300] C. G. Van de Walle. “Band lineups and deformation potentials in the model-solid theory”. *Phys. Rev. B* 39 (3 1989), pp. 1871–1883.
- [301] E. L. Shirley. “Many-body effects on bandwidths in ionic, noble gas, and molecular solids”. *Phys. Rev. B* 58 (15 1998), pp. 9579–9583.
- [302] G. W. Rubloff. “Far-Ultraviolet Reflectance Spectra and the Electronic Structure of Ionic Crystals”. *Phys. Rev. B* 5 (2 1972), pp. 662–684.
- [303] M. Kim et al. “Screened-exchange determination of the optical properties of large gap insulators: CaF_2 ”. *Appl. Phys. Lett.* 84.18 (2004), pp. 3579–3581.
- [304] Y. Ma and M. Rohlfing. “Quasiparticle band structure and optical spectrum of CaF_2 ”. *Phys. Rev. B* 75 (20 2007), p. 205114.
- [305] M. Bertocchi et al. “Large crystal local-field effects in second-harmonic generation of a Si/CaF_2 interface: An ab initio study”. *Phys. Rev. B* 86 (3 2012), p. 035309.

Bibliography

- [306] H. Fujitani and S. Asano. “Calculated electronic structure at the $\text{CaF}_2/\text{Si}(111)$ interface”. *Surf. Sci.* 268.1 (1992), pp. 265–274.
- [307] S. Ossicini, C. Arcangeli, and O. Bisi. “Chemical bond and electronic states at the $\text{CaF}_2\text{-Si}(111)$ and $\text{Ca-Si}(111)$ interfaces”. *Phys. Rev. B* 43 (12 1991), pp. 9823–9830.
- [308] L. Weston et al. “Accurate and efficient band-offset calculations from density functional theory”. *Comput. Mater. Sci.* 151 (2018), pp. 174–180.
- [309] S. Satpathy and R. M. Martin. “Energetics and valence-band offset of the CaF_2/Si insulator-on-semiconductor interface”. *Phys. Rev. B* 39 (12 1989), pp. 8494–8498.
- [310] M. R. Salehpour, S. Satpathy, and G. P. Das. “Electronic structure of the $\text{CaF}_2/\text{Si}(111)$ interface”. *Phys. Rev. B* 44 (16 1991), pp. 8880–8885.
- [311] S. Picozzi et al. “Highly tunable valence-band offset at the (111) Si/Si homojunction via a CaF monolayer saturated with H”. *Phys. Rev. B* 55 (24 1997), pp. 16318–16323.
- [312] F. Xu, M. Vos, and J. H. Weaver. “Influence of Au overlayers on valence-band offsets for buried $\text{CaF}_2/\text{Si}(111)$ interfaces”. *Phys. Rev. B* 39 (11 1989), pp. 8008–8011.
- [313] M. A. Olmstead et al. “Initial formation of the interface between a polar insulator and a nonpolar semiconductor: CaF_2 on $\text{Si}(111)$ ”. *J. Vac. Sci. Technol.* 4.4 (1986), pp. 1123–1127.
- [314] L. A. Ledebro and B. K. Ridley. “On the position of energy levels related to transition-metal impurities in III-V semiconductors”. *J. Phys. C: Solid State Phys.* 15.27 (1982), pp. L961–L964.
- [315] M. J. Caldas, A. Fazzio, and A. Zunger. “A universal trend in the binding energies of deep impurities in semiconductors”. *Appl. Phys. Lett.* 45.6 (1984), pp. 671–673.
- [316] G. Capano et al. “On the Electronic and Optical Properties of Metal–Organic Frameworks: Case Study of MIL-125 and MIL-125- NH_2 ”. *J. Phys. Chem. C* 124.7 (2020), pp. 4065–4072.
- [317] S. Falletta et al. “Unraveling the synergy between metal–organic frameworks and co-catalysts in photocatalytic water splitting”. *J. Mater. Chem. A* 8 (39 2020), pp. 20493–20502.
- [318] P. G. Moses and C. G. Van de Walle. “Band bowing and band alignment in InGaN alloys”. *Appl. Phys. Lett.* 96.2 (2010), p. 021908.
- [319] C. S. Schnohr et al. “Atomic-scale structure and band-gap bowing in $\text{Cu}(\text{In,Ga})\text{Se}_2$ ”. *Phys. Rev. B* 85 (24 2012), p. 245204.
- [320] Z. Guo, F. Ambrosio, and A. Pasquarello. “MD trajectories of bulk water and of the water-vacuum interface”. *Materials Cloud Archive* (2019).

Acknowledgements

At this point, I would like to thank those who contributed to the success of this PhD thesis.

My first and foremost thanks goes to Prof. Alfredo Pasquarello for the opportunity to work at CSEA. I am very grateful for his scientific guidance, his kind support and for the time and effort that he invested during the last four years.

Many thanks belong also to my friends and colleagues at EPFL. You created a stimulating and positive atmosphere that I enjoyed a lot.

Special thanks go to Tanya Castellino, Annick Evéquo, and Patricia Byron-Exarcos for helping with many administrative problems and to Florence Hagen for managing the computer system.

Furthermore, I would like to thank Westlake Church Lausanne and my wonderful home group in Ecublens for constantly reminding me what is important in life.

Finally, I am very thankful for my family. I thank my parents and grandparents for your unconditional support and for our good family life. I would like to express my very special appreciation to Marie, for all her love, that I experience everyday.

Lausanne, February 2021

Thomas Bischoff

List of Acronyms

BO	Born-Oppenheimer
DFT	density-functional theory
KS	Kohn-Sham
XC	exchange-correlation
LDA	local density approximation
GGA	generalized gradient approximation
PBE	Perdew-Burke-Ernzerhof
HF	Hartree-Fock
HSE	Heyd-Scuseria-Ernzerhof
MBPT	many-body perturbation theory
RPA	random-phase approximation
PBC	periodic boundary conditions
PP	pseudopotential
VBM	valence-band maximum
CBM	conduction-band minimum
IP	ionization potential
DOS	density of states
SOC	spin-orbit coupling
ZPR	zero-phonon renormalization
NQE	nuclear quantum effects
MAE	mean average error
FNV	Freysoldt-Neugebauer-Van de Walle

Curriculum Vitae

Personal data

Name	Thomas Bischoff
Date and place of birth	11.11.1990 in Sondershausen
Citizenship	Germany
Marital status	Married

Education

2016 – 2021	Ph.D. in Physics, École polytechnique fédérale de Lausanne, Ph.D. thesis in Computational Condensed Matter Physics
2013 – 2016	M.Sc. in Physics, Friedrich-Schiller-Universität Jena, Master thesis in Computational Condensed Matter Physics
2013 – 2016	B.Sc. in Mathematics, Friedrich-Schiller-Universität Jena, Bachelor thesis in Computational Fluid Dynamics
2010 – 2013	B.Sc. in Physics, Friedrich-Schiller-Universität Jena, Bachelor thesis in Photovoltaics
2001 – 2009	Abitur at Gymnasium Greußen

Publications related to the thesis

1. T. Bischoff, I. Reshetnyak, A. Pasquarello, *Band gaps of liquid water and hexagonal ice through advanced electronic-structure calculations*, Phys. Rev. Research (2020, submitted)
2. T. Bischoff, I. Reshetnyak, A. Pasquarello, *Band alignment at the CaF₂/Si (111) interface through advanced electronic-structure calculations*, Phys. Rev. B 101, 235302 (2020)
3. T. Bischoff, J. Wiktor, W. Chen, A. Pasquarello, *Nonempirical hybrid functionals for band gaps of inorganic metal-halide perovskites*, Phys. Rev. Materials 3, 123802 (2019)
4. T. Bischoff, I. Reshetnyak, A. Pasquarello, *Adjustable potential probes for band-gap predictions of extended systems through nonempirical hybrid functionals*, Phys. Rev. B 99, 201114(R) (2019)

Other publications

1. K. Ritter, S. Eckner, C. Preiß, G. Gurieva, T. Bischoff, E. Welter, S. Botti, S. Schorr, C. Schnohr, *Atomic scale structure and its impact on the band gap energy for $\text{Cu}_2\text{Zn}(\text{Sn},\text{Ge})\text{Se}_4$ kesterite alloys*, J. Phys. Energy 2, 035004 (2020)
2. S. Wiesendanger, T. Bischoff, V. Jovanov, D. Knipp, S. Burger, F. Lederer, C. Rockstuhl, *Effects of film growth modes on light trapping in silicon thin film solar cells*, Appl. Phys. Lett. 104, 231103 (2014)

Contributed talks at international conferences

1. T. Bischoff, I. Reshetnyak, A. Pasquarello, *Band alignment at insulator/semiconductor interfaces through advanced electronic-structure calculations*, DPG Spring meeting, March 2018, Berlin
2. T. Bischoff, I. Reshetnyak, A. Pasquarello, *Nonempirical hybrid functionals constructed through adjustable potential probes for band gap predictions of extended systems*, DPG Spring meeting, April 2019, Regensburg

Participation at international and national conferences

1. *MARVEL Site Visit*, April 2017 and 2018, Lausanne
2. *MARVEL Review and Retreat*, Sept. 2017 and 2018, Lausanne
3. *MARVEL Junior Seminar*, 2017-2020, Lausanne
4. *International Workshop on Computational Design and Discovery of Novel Materials*, Sept. 2018, Lausanne
5. *CECAM Conference: 50 years of CECAM*, Sept. 2019, Lausanne